PROBING SPIN-ISOSPIN EXCITATIONS IN PROTON-RICH NUCLEI VIA THE
^{11}C(P,N)^{11}N REACTION

By

Jaclyn Marie Schmitt

A DISSERTATION

Submitted to
Michigan State University
in partial fulfillment of the requirements
for the degree of

Physics—Doctor of Philosophy

2022

ABSTRACT

PROBING SPIN-ISOSPIN EXCITATIONS IN PROTON-RICH NUCLEI VIA THE
^{11}C$(P,N)^{11}$N REACTION

By

Jaclyn Marie Schmitt

Understanding nuclear structure and predicting nuclear properties from first principles are major goals of nuclear physics research. Many nuclear models have been created for these purposes, and benchmarking them with new data is critical for their continued development. Exotic nuclei provide fertile testing grounds for nuclear models because nuclear properties evolve and new phenomena emerge as one moves away from stability towards the driplines. In the present work, the ^{11}C$(p,n)^{11}$N reaction was measured in inverse kinematics at 95 MeV/u at the National Superconducting Cyclotron Laboratory to both provide a benchmark for current models and to lay the groundwork for future experiments. The Gamow-Teller transition strength, $B(\text{GT})$, was extracted from the measured cross section using a well-established proportionality relationship between the charge-exchange cross section and $B(\text{GT})$. The results were $B(\text{GT}) = 0.18(1)^{stat}(3)^{sys}$ to the first $\frac{1}{2}^-$ state and $B(\text{GT}) = 0.18(1)^{stat}(4)^{sys}$ to the first $\frac{3}{2}^-$ state in ^{11}N. These results are consistent with shell-model calculations after introducing a phenomenological quenching factor and with *ab-initio* Variational Monte Carlo calculations without any scaling. These results are also consistent with $B(\text{GT})$ values extracted from mirror ^{11}B(n,p) and ^{11}B$(t,^3\text{He})$ reactions, assuming isospin symmetry. Additionally, this experiment demonstrates the feasibility of using the (p,n) probe in inverse kinematics to extract $B(\text{GT})$ from transitions to proton-rich unbound nuclei, although improved background suppression will be critical in future experiments.

ACKNOWLEDGMENTS

Many forces must come together to make nuclear physics experiments like this one successful, from scientists to laboratory staff to funding agencies, and explicitly acknowledging every one is simply not possible. Nevertheless, there are several people I would like to extend special thank-yous to.

Of course, I first want to thank my advisor, Remco Zegers, for many things. Thank you for teaching me how to be a scientist and guiding me through the myriad of challenges posed by this project. Even when I unintentionally made you relive the "factor of four" debacle of 2017 (although this time it was a factor of two), you didn't bat an eyelash and kept pushing me forward. Thank you for helping me grow as a researcher by providing early hands-on experience in the lab, promoting participation in other experiments, and sending me to conferences. And thank you for always encouraging me to broaden my horizons by supporting my participation in student leadership, outreach, and *two* internships. I realize I'm very lucky to have been able to pursue all of these opportunities in graduate school.

I would also like to thank the members of my guidance committee–Daniel Bazin, Alex Brown, Hiro Iwasaki, and Kendall Mahn–for your support and encouragement at every committee meeting for the last six years.

I owe Jorge Pereira a special thank-you as well. Thank you for all of the hours you spent teaching me how to use LENDA and all of the associated hardware and software. Thank you for all of your patience as I asked for help with the Pixie modules, nscope, SpecTcl, R00TLe,... the list goes on. I'm also very grateful for the large role you played in making my thesis experiment happen.

I also want to give a shout-out to all of the past and current members of the charge-

exchange group. Thank you Shumpei for always being a dependable group member and answering my random questions. All of my senior charge-exchange classmates were great role models: Sam, thank you for all of your help with the Geant4 simulation (and group meetings were never quite as entertaining after you left); Chris, thank you for guiding me through my first data analysis experience; and Rachel, thank you for helping set up my experiment and teaching me how to do supernova simulations. To my current CE classmates, Felix, Cavan, and Zarif, thanks for the fun times in journal club, and good luck with the rest of your degrees.

Thank you to everyone who helped with the experiment: Jorge, for managing the S800; Ron, Giordano, and Jorge for DAQ support; Bingshui, Rachel, and Charlie for helping build the new LENDA frames and mount all of the LENDA bars; Juan for writing convenient bash scripts; the cyclotron and A1900 staff for delivering the beam; and everyone who took shifts. Thank you to the University of Notre Dame and Hope College for the large neutron detectors, and to Alyssa for spending an entire summer reviving them. Thank you to all of our theory friends: Alex Brown here at MSU for providing shell-model support, and Garrett King, Maria Piarulli, and Saori Pastore at WUSTL for providing *ab-initio* calculations. This work was supported by the US National Science Foundation PHY-1565546 (Operation of the NSCL), PHY-1430152 (JINA Center for the Evolution of the Elements), and PHY-1913554 (Windows on the Universe: Nuclear Astrophysics at the NSCL).

Last, I want to thank my Clemson friends, Cass, Sharon, and Eric. Even though we were scattered around the country, thinking about you guys kept me warm in this cold state. And finally, my parents and my sisters. Your limitless support made the challenges easier to overcome and the successes all the more rewarding.

TABLE OF CONTENTS

LIST OF TABLES

LIST OF FIGURES

xvii

Chapter 1

Introduction

Although the concept of atoms as the fundamental building blocks of matter has been around for millennia, our knowledge of the existence of the atomic nucleus did not come until Rutherford's famous gold foil experiment in the early 1900s [1, 2, 3, 4, 5]. Since the discovery of the nucleus, the field of nuclear physics has grown immensely and has had broad impacts on our understanding of the universe and on society. Since Arthur Eddington first suggested that the Sun is powered by nuclear fusion in 1920 [6], the field of nuclear astrophysics has advanced such that nuclear physicists now understand complex astrophysical phenomena such as supernovae, x-ray bursts, and neutron stars in great detail. Since Wilhelm Roentgen discovered x rays, the first radiation used for radiology, in 1895 [7], technology developed by nuclear physicists has been adapted into modern medical tools such as PET imaging and proton radiation therapy.

Progress in the field of nuclear physics has not slowed down, and the National Research Council has defined four questions that are central to current nuclear physics research [8]:

1. How did visible matter come into being and how does it evolve?

2. How does subatomic matter organize itself and what phenomena emerge?

3. Are the fundamental interactions that are basic to the structure of matter fully understood?

4. How can the knowledge and technical progress provided by nuclear physics best be used to benefit society?

The study of nuclear structure is critical to answering all of these questions. The first nuclear structure model was the liquid drop model proposed by George Gamow [9], which modeled the nuclear binding energy as a function of the number of neutrons and protons. Then in the 1940s, Maria Goeppert Mayer, Otto Haxel, J. Hans D. Jensen, and Hans Suess took quantum-mechanical effects into account to create the shell model [10, 11], which serves even now as the paradigm of our understanding of nuclear structure and provides a basis for more advanced models [8, 12].

Today, a myriad of advanced models are available for understanding and predicting nuclear properties, and they are typically grouped into three categories. Density functional theory (DFT) models nuclei as densities and currents rather than individual nucleons and is usually used for (medium-) heavy nuclei. Configuration-interaction models can be thought of as extensions of the shell model first introduced in the 1940s and are used for light to medium-heavy nuclei. *Ab-initio* methods are used to predict properties of the lightest nuclei by solving the nuclear many-body problem from individual nucleons and their interactions.

Benchmarking these nuclear models with experimental data is critical to their development. Rare isotopes, or isotopes with an excess of protons or neutrons, are excellent testing grounds for nuclear models. As one moves away from stability, the nucleons become very loosely bound, causing new phenomena to emerge such as halos [13, 14, 15] and novel decay modes [16, 17]. Light rare isotopes ($A \leq 12$) are particularly useful because they are more experimentally accessible due to lying only a few nucleons from stability, and because they can be used to benchmark both configuration-interaction models and *ab-initio* calculations.

A famous rare isotope is ^{11}Be, whose ground state exhibits a halo structure and demon-

strates parity inversion [18, 19]. Its isospin-symmetric partner ^{11}N also exhibits parity inversion for its ground state, but unlike ^{11}Be is unbound. Isospin symmetry dictates that these nuclei should have identical structures. The Coulomb force breaks this symmetry, but the effects are generally small and well-understood. It is interesting to consider whether "boundness" also impacts the symmetry between the two systems.

The primary goal of this thesis was to explore this question by measuring the Gamow-Teller transition strength, $B(\mathrm{GT})$, from ^{11}C to ^{11}N and to compare the result to previously measured $B(\mathrm{GT})$ for mirror transitions from ^{11}B to ^{11}Be. The Gamow-Teller transition strength is a property of a nuclear transition that is sensitive to the structure of the nuclei involved and can therefore be used to compare the structure of ^{11}N and ^{11}Be. In this work, $B(\mathrm{GT})$ for ^{11}C$\rightarrow^{11}$N transitions was extracted from the measured ^{11}C(p,n) cross section.

A secondary goal of this thesis was to further develop the (p,n) reaction to prepare for the "FRIB era." FRIB, or the Facility for Rare Isotope Beams, is a new accelerator facility that will provide access to rare isotopes never studied before. Charge-exchange reactions are one of many techniques that can be used to study rare isotopes. The (p,n) reaction is the simplest charge-exchange probe, making the extraction of structure information more straightforward than for composite charge-exchange probes. A (p,n) reaction on a proton-rich nucleus produces a proton-rich nucleus farther from stability than the target nucleus, offering unique opportunities and providing access to unbound nuclei beyond the proton dripline (the line beyond which nuclei are no longer bound).

Chapter 2 introduces the nuclear structure theories used in this work and describes a brief history of and the motivation for studying ^{11}N. Chapter 3 defines $B(\mathrm{GT})$, describes how charge-exchange reactions are used to extract $B(\mathrm{GT})$, and gives a brief history of and motivation for further developing the (p,n) reaction. Chapter 4 explains the nuclear reaction

calculations used in the analysis of the data. Chapter 5 describes the experiment, and Chapters 6 and 7 explain the analysis of the data. Chapter 8 presents the extraction of $B(\text{GT})$, and Chapter 9 discusses the results. Chapter 10 presents work done on an array of neutron detectors that will supplement the existing array used for this experiment, LENDA (Low Energy Neutron Detector Array). Chapter 11 presents the results of a study done for next-generation neutron detectors at Oak Ridge National Laboratory. Chapter 12 concludes with a summary of the work done and prospects for future work.

Chapter 2

Nuclear Structure

The nuclear shell model can be regarded as the foundation of nuclear structure and a standard of comparison for other models. The simplest implementation of the shell model is the independent particle model, where the nucleons are modeled as independent particles in a potential created by the other nucleons. It is the basis of more advanced configuration-interaction (CI) models, which include the effects of individual nucleons' interactions. The independent particle model and the configuration-interaction model used in this work are described in Section 2.1.

A major goal of nuclear physics is to describe nuclei from first principles, without relying on phenomenological models such as CI models. In other words, the goal is to develop a single coherent picture from which all nuclei can be described. Whereas any given CI model can be used for only a limited range of nuclei, *ab-initio* methods can, at least in principle, model any nucleus entirely from a realistic nucleon-nucleon interaction. *Ab-initio* calculations are extremely computationally demanding, however, and they have only recently become possible for light nuclei. There are many types of *ab-initio* methods, and Section 2.2 introduces the method used in this work, Variational Monte Carlo (VMC) calculations.

As discussed in the introduction, exotic nuclei exhibit fascinating new phenomena, and these new phenomena are challenging to model. As models are improved to capture these new phenomena, they must be benchmarked with new measurements. In this work, the exotic
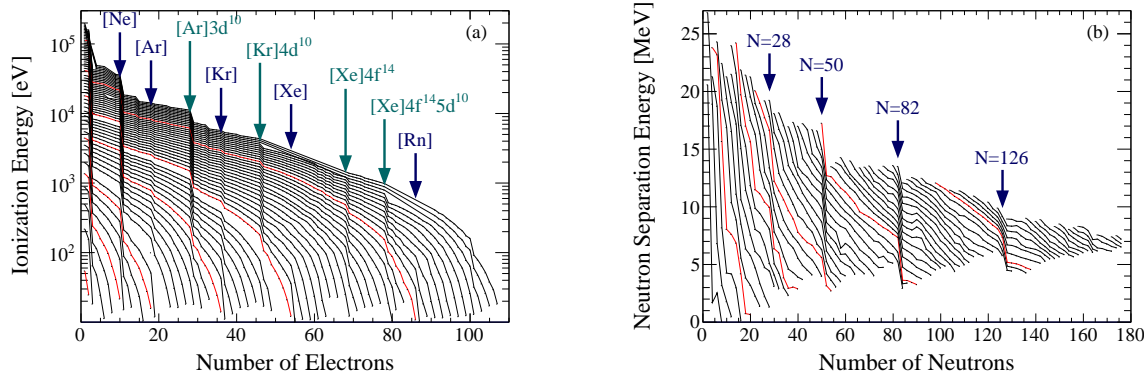
Figure 2.1: (a) Ionization energy vs. electron number [20]. Each line represents an element. Electron configurations are indicated with arrows. (b) Neutron separation energy vs. neutron number [21, 22]. Each line represents an element. The smaller magic numbers 2, 8, and 20 are not shown, but the larger magic numbers are indicated with arrows.

nucleus ^{11}N is used to benchmark both shell-model and VMC calculations. Section 2.3 gives a brief history of ^{11}N and explains why it is interesting to study.

2.1 The Shell Model

Atomic structure can be understood well by modeling electrons as independent particles in the Coulomb potential created by the nucleus. The electron energy levels are grouped into shells, and this shell structure defines the observed periodic table trends. The noble gases have full shells and are especially inert, whereas alkali metals and halogens have one extra or one missing electron relative to a full shell and are especially reactive. One signature of this shell structure is the electron ionization energy, illustrated in Figure 2.1(a). As electrons are removed, the ionization energy increases because inner electrons are closer and therefore more tightly bound to the positively-charged nucleus. At certain electron numbers, however, the ionization energy increases much more dramatically than the previous electron numbers. This increase indicates that that electron is much closer to the nucleus than the previous electron and is therefore part of the next shell.

6

As nuclear data were collected, patterns emerged that indicated that the nucleus has an analogous shell structure. One such pattern is shown in Figure 2.1(b). The neutron-separation energy is analogous to the electron ionization energy; it is the energy it takes to remove the last neutron from the nucleus. There are large drops in the neutron-separation energies at certain neutron numbers, again indicating the next full shell has been reached. The proton-separation energy exhibits a similar pattern. The proton- and neutron-numbers where nuclei exhibit phenomena indicative of strong binding relative to their neighbors are called "magic numbers."

The simplest form of the shell model is the independent particle model, where each nucleon is modeled as an independent particle in a central potential well. The potential well is created by the forces from all of the other nucleons in the nucleus, and its shape is typically something like:

$$V(r) = V^{WS}(r; R, a) - \frac{dV^{WS}}{dr}(r; R_{SO}, a_{SO})(\mathbf{L} \cdot \mathbf{S}) + V^C(r; R_C) \qquad (2.1)$$

The first term has a Woods-Saxon shape, $V^{WS}(r; R, a) = \frac{1}{1+\exp\left(\frac{r-R}{a}\right)}$, where R is the radius of the potential and a is the diffuseness, which parameterizes the sharpness of the well edge. A diagram of a typical Woods-Saxon shape is shown in Figure 2.2. This shape can be understood qualitatively from properties of the strong force. The strong force has a very short range, so each nucleon only affects its immediate neighbors. As a result, the force felt by each nucleon inside the nucleus is fairly constant, and the potential well has a flat bottom. The nucleons on the surface feel a weaker force since they have fewer neighbors, so the potential smoothly falls off to zero at the edge of the nucleus.

The second term is a spin-orbit coupling term. If a nucleon's spin is aligned with its orbital
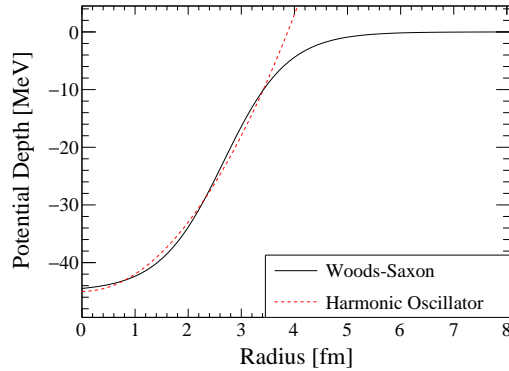
Figure 2.2: Typical Woods-Saxon shape compared to a harmonic oscillator.

angular momentum, then the nucleon feels a stronger force. This is a surface-peaked effect, so the radial component is usually written as the derivative of a Woods-Saxon potential. The spin-orbit coupling effect is large and must be included to reproduce the observed magic numbers. The Nobel Prize in Physics in 1963 was awarded to Maria Goeppert Mayer, Otto Haxel, J. Hans D. Jensen, and Hans Suess for explaining the observed magic numbers by adding a spin-orbit coupling term to the Woods-Saxon potential.

The third term is a Coulomb term to account for the repulsive force between protons. The Coulomb force raises the proton single-particle energies relative to their neutron counterparts. It is also long-range, so its effect increases as more protons are added, causing heavier nuclei to need more neutrons than protons to be stable.

The nuclear wave function can be determined by solving the Schrödinger Equation with the potential $V(r)$ in Eq. 2.1. The result is that the nucleons are arranged in a series of orbitals as shown in Figure 2.3, and the orbitals are grouped into shells. The gaps between the shells correspond to the observed magic numbers: 2, 8, 20, 28, 50, 82, and 126. Each orbital is labeled as nl_j, where n is the energy, l is the orbital angular momentum, and $j = l + s$ is the total angular momentum, where s is the spin. The symbols for l use the spectroscopic convention: s for $l = 0$, p for $l = 1$, d for $l = 2$, f for $l = 3$, etc. An orbital can hold $2j + 1$
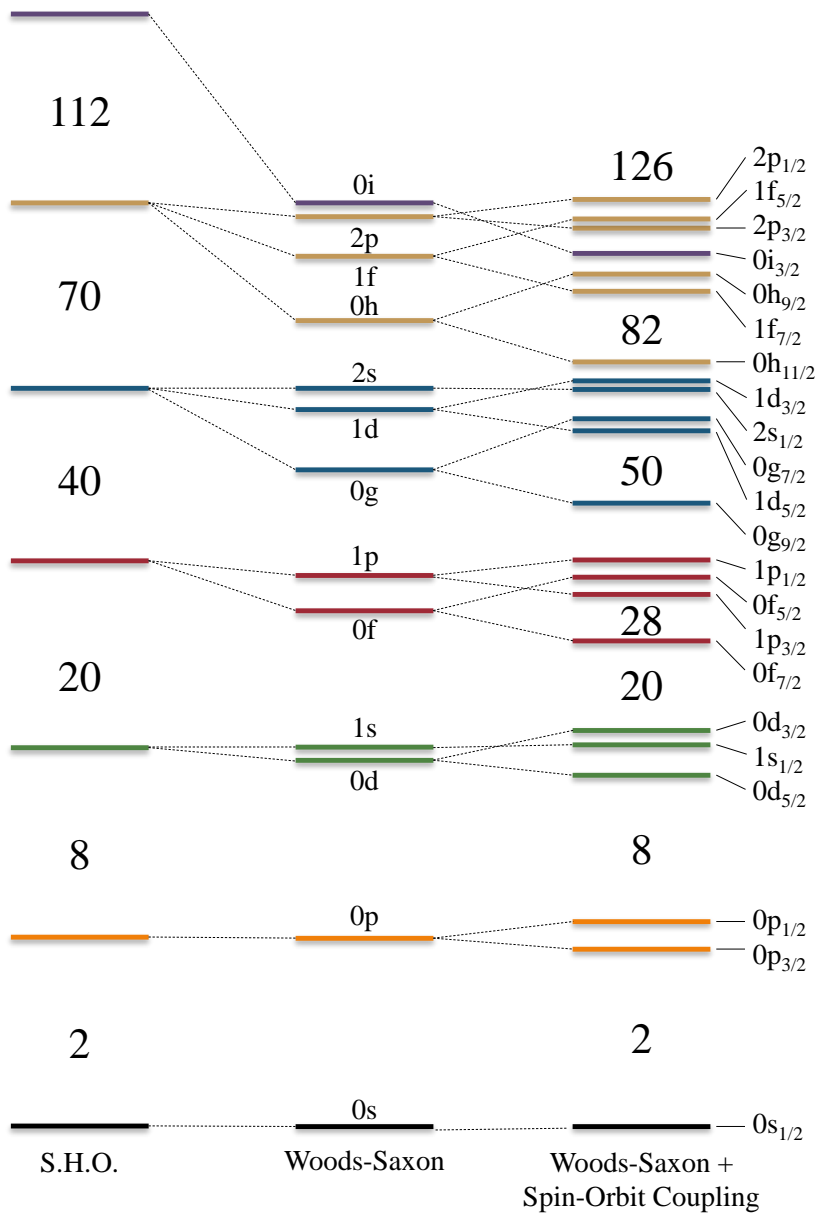
Figure 2.3: Diagram of the nucleon orbitals adapted from Ref. [23].
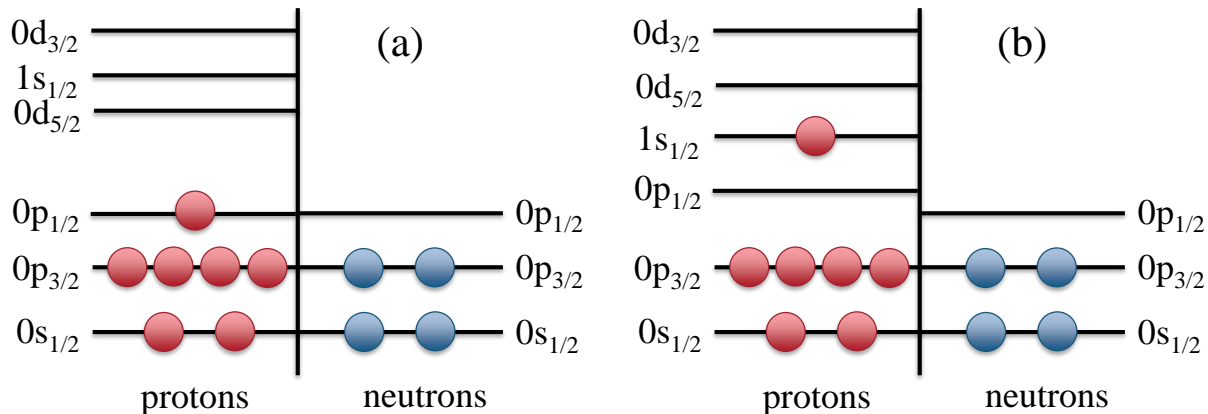
Figure 2.4: (a) Configuration that dominates the ^{11}N ground state according to the independent particle model. (b) Configuration that actually dominates the ^{11}N ground state.

nucleons, each with a different angular momentum projection $m_j = j, j - 1, ..., -j + 1, -j$. More detailed descriptions of the independent particle model can be found in textbooks such as Refs. [12, 23, 24]. A diagram of the shell structure of ^{11}N, the nucleus that is the focus of this work, according to the independent particle model is shown in Figure 2.4(a).

The independent particle model is only accurate for closed-shell nuclei near stability with one valence nucleon. For other nuclei, and especially for exotic nuclei, interactions between the nucleons can significantly affect the nuclear structure. For example, loose-binding effects cause the $0s_{1/2}$ orbital in ^{11}N to have a lower energy than in neighboring nuclei near stability. In fact, the effects are so strong that the valence proton prefers to occupy the $0s_{1/2}$ orbital rather than the $0p_{1/2}$ orbital, resulting in a ground state configuration closer to what is shown in Figure 2.4(b). Therefore, the ^{11}N ground state has spin-parity $J^\pi = \frac{1}{2}^+$ rather than the $J^\pi = \frac{1}{2}^-$ expected from the independent particle model. This is called parity inversion.

To understand and predict phenomena such as parity inversion, interactions between individual nucleons must be included in nuclear models. This class of calculations is called "configuration-interaction (CI)" methods, and descriptions can be found in Refs. [25, 26, 22,

27]. The configuration-interaction code used in this work is Oxbash [28]. The general steps of any CI calculation are:

1. Define the model space and select a basis scheme.

2. Define the interaction and calculate the Hamiltonian matrix elements.

3. Find the Hamiltonian matrix eigenvalues and eigenvectors.

The first step is the selection of a "model space," which is the set of orbitals included in the calculation. Larger model spaces will yield more accurate calculations because more configuration mixing can be taken into account. However, adding orbitals becomes computationally expensive fast. Because the core is mostly inert, only the valence orbitals and those directly above it are usually included in the model space. The nucleus of interest for this work is relatively light, so the model space used in this work, called the *spsdpf* model space, includes all orbitals up to and including $0f_{7/2}$.

The model space defines the basis states. A basis state, or configuration, is a group of singe-particle states, such as that shown in Figure 2.4. The basis-state wave function $\Psi(r_1, r_2, ...r_n)$ for n particles is the product of the single-particle wave functions $\psi_i(r_i)$:

$$\Psi(r_1, r_2, ...r_n) = \psi_1(r_1)\psi_2(r_2) \cdots \psi_n(r_n) \tag{2.2}$$

where the subscript i indicates the single-particle orbital defined by n, l, j, and sometimes m_j or isospin t depending on the scheme (discussed next). Nucleons are fermions, so the basis-state wave function must be antisymmetrized:

$$\Psi(r_1, r_2, ...r_n) = \sum_P (-1)^P P \psi_1(r_1)\psi_2(r_2) \cdots \psi_n(r_n) \tag{2.3}$$

11

where P is an operator that permutes the space and spin coordinates of the particles. The basis states can be constructed in a few different ways, including the M-scheme, where the basis states have a fixed total angular momentum projection M, the J-scheme, where the basis states have a fixed total angular momentum J, and the $J-T$ scheme, where the basis states have a fixed J and total isospin T. Oxbash can use the J-scheme or the $J-T$ scheme. In this work, the $J-T$ scheme, also called "isospin formalism," was used.

The next step in a CI calculation is to define the Hamiltonian and find its matrix elements. The Hamiltonian is usually written in the form:

$$H = \sum_i (T_i + U_i) + \sum_i \sum_{j>i} V_{ij} \tag{2.4}$$

where the sums over i, j are sums over nucleons. T_i is the kinetic energy of the ith particle, U_i is the potential energy of the ith particle in the central field, and V_{ij} is the interaction between the ith and j^{th} particles. The $\langle T_i + U_i \rangle$ single-particle matrix element is also called a single-particle energy (SPE), and it can be calculated theoretically using e.g. Hartree-Fock methods or estimated from experimental data.

The configuration-interaction matrix element can be written as a sum of two-body matrix elements (TBMEs):

$$TBME = \langle \alpha\beta | V | \alpha\beta \rangle \tag{2.5}$$

where α and β are single-particle wave functions, and $|\alpha\beta\rangle$ is the two-body anti-symmetrized

wave function:

$$|\alpha\beta\rangle = \frac{1}{\sqrt{2}} \left[\psi_\alpha(\mathbf{r_1})\psi_\beta(\mathbf{r_2}) - \psi_\beta(\mathbf{r_1})\psi_\alpha(\mathbf{r_2}) \right] \tag{2.6}$$

The TBMEs can be calculated either theoretically using a two-body nucleon-nucleon (NN) interaction V or from fits to experimental data.

The SPEs and TBMEs together are called the "interaction." The interaction used in this work was the *wbp* interaction, which Warburton and Brown created by fitting the SPEs and TBMEs to data [29].

Finally, the last step of the CI method is to diagonalize the Hamiltonian matrix to get the eigenvalues and eigenfunctions. The most common diagonalization method is the Lanczos method [30, 31]. The resulting eigenvalues are the energies of the nuclear states, and the resulting eigenfunctions, which are linear combinations of the basis states, are the wave functions of the nuclear states.

2.2 *Ab-initio* Methods

Whereas configuration-interaction methods use a mean-field potential with two-body corrections, *ab-initio* methods use nucleon-nucleon interactions to solve the nuclear many-body problem. In this work, the NV2+3-Ia* and NV2+3-IIb* interactions were used with the Variational Monte Carlo (VMC) method to calculate B(GT) for the transitions of interest. These calculations were done by collaborators at Washington University in St. Louis (WUSTL), and details of the calculations can be found in Ref. [32]. For more general re-

views of Quantum Monte Carlo methods, see Refs. [33, 34, 35]. This section presents a brief overview of the interaction and VMC method used for these calculations.

The equation to solve is the many-body Schrödinger Equation:

$$H\Psi(J^{\pi}; T, T_z) = E\Psi(J^{\pi}; T, T_z) \tag{2.7}$$

where J^{π} is the spin-parity, T is the isospin, and T_z is the isospin projection of the state of interest. The Hamiltonian has the form:

$$H = \sum_i T_i + \sum_i \sum_{j>i} v_{ij} + \sum_i \sum_{j>i} \sum_{k>j} V_{ijk} \tag{2.8}$$

where T_i is the one-body non-relativistic kinetic energy operator, v_{ij} is the two-body interaction, and V_{ijk} is the three-body interaction. For any *ab-initio* method, the two main ingredients are (1) the interactions, v_{ij} and V_{ijk}, and (2) the computational method used to solve the Schrödinger Equation.

There are two major categories of interactions: phenomenological interactions and interactions derived from effective field theories. Phenomenological interactions are derived from fits to large sets of nucleon-nucleon scattering data. A famous phenomenological two-body interaction is the Argonne v_{18} two-body potential, "AV18." This potential has the form:

$$v_{ij} = \sum_p v_p(r_{ij}) O_{ij}^p \tag{2.9}$$

where the sum over p is the sum over operators. AV18 includes a total of 18 operators O_{ij}^p, which can be separated into three categories, charge-independent (CI), charge-dependent

(CD), and charge-symmetry breaking (CSB):

$$O_{ij}^{CI} = [1, \boldsymbol{\sigma_i} \cdot \boldsymbol{\sigma_j}, S_{ij}, \mathbf{L} \cdot \mathbf{S}, \mathbf{L}^2, \mathbf{L}^2(\boldsymbol{\sigma_i} \cdot \boldsymbol{\sigma_j}), (\mathbf{L} \cdot \mathbf{S})^2)] \otimes [1, \boldsymbol{\tau_i} \cdot \boldsymbol{\tau_j}] \qquad (2.10)$$

$$O_{ij}^{CD} = [1, \boldsymbol{\sigma_i} \cdot \boldsymbol{\sigma_j}, S_{ij}] \otimes T_{ij} \qquad (2.11)$$

$$O_{ij}^{CSB} = \tau_{z_i} + \tau_{z_j} \qquad (2.12)$$

where $\boldsymbol{\sigma_i}$ and $\boldsymbol{\tau_i}$ are the spin and isospin of nucleon i, $\mathbf{L}$ is the relative angular momentum between nucleons i and j, $\mathbf{S}$ is the total spin of nucleons i and j, $S_{ij} = 3\boldsymbol{\sigma_i} \cdot \hat{r}_{ij} \boldsymbol{\sigma_j} \cdot \hat{r}_{ij} - \boldsymbol{\sigma_i} \cdot \boldsymbol{\sigma_j}$ is the tensor operator, and $T_{ij} = 3\tau_{z_i}\tau_{z_j} - \boldsymbol{\tau_i} \cdot \boldsymbol{\tau_j}$ is the isotensor operator. In total, this model has 42 parameters that were obtained from a fit to 1787 pp and 2514 np observables plus the nn scattering length and deuteron binding energy.

The AV18 model is often paired with a three-body interaction to account for higher order effects such as the Δ nucleon excitation. Two common three-body interactions are the Urbana IX (UIX) and the Illinois-7 (IL7) 3N models:

$$V_{ijk}^{UIX} = V_{ijk}^{2\pi,P} + V_{ijk}^{R} \qquad (2.13)$$

$$V_{ijk}^{IL7} = V_{ijk}^{2\pi,P} + V_{ijk}^{2\pi,S} + V_{ijk}^{3\pi,\Delta R} + V_{ijk}^{R} + V_{ijk}^{R,T=3/2} \qquad (2.14)$$

The $V_{ijk}^{2\pi,P/S}$ terms are two-pion exchange P/S-wave terms. V_{ijk}^{R} is a short-range phenomenological term. $V_{ijk}^{3\pi,\Delta R}$ accounts for three-pion rings with one or two Δs, and $V_{ijk}^{R,T=3/2}$ is a small additional repulsive term. See Ref. [33] and references therein for more about these terms. Each V_{ijk}^{x} term has a strength A^x, and the A^xs were found by fits to data in conjunction with the AV18 two-body interaction.

Although relatively straightforward to create and use, phenomenological models have two

important disadvantages. First, due to their phenomenological nature, assessing theoretical uncertainties in calculations that use these models is not possible. Additionally, there is no systematic way to improve these models. Nuclear effective field theories (EFTs) provide alternative ways to construct the interactions v_{ij} and V_{ijk} that do not suffer from these disadvantages. A detailed discussion of nuclear EFTs can be found in Refs. [36, 37].

Briefly, a nuclear EFT starts with the general QCD Lagrangian. First, the quark, gluon, heavy meson, and other nucleon substructure degrees of freedom that are not relevant for the low-energy nuclear system of interest are integrated out. Then the Lagrangian is rewritten as an expansion of p/Λ_b. p is the typical momentum scale of the nuclear system (usually about the mass of the pion), and Λ_b is the "breakdown scale," which is defined by the degrees of freedom that have been integrated out (usually about 1 GeV). The rewritten Lagrangian must be consistent with the symmetries and symmetry breakings of QCD. For example, approximate chiral symmetry defines the symmetries for chiral EFT (χEFT). The resulting interaction V of the EFT Lagrangian has the form:

$$V = \sum_\nu V^\nu(\{C_i^\nu\}) \left(\frac{p}{\Lambda_b}\right)^\nu \tag{2.15}$$

where V^ν is the contribution at order ν and $\{C_i^\nu\}$ are low-energy couplings (LECs) that encode the unresolved physics associated with the degrees of freedom that have been integrated out. The LECs are determined from fits to data. The lowest order ν is called leading order (LO). Terms commonly included in LO are $C_\mathbf{1}\mathbf{1}$, $C_{\boldsymbol{\sigma}}\boldsymbol{\sigma_i} \cdot \boldsymbol{\sigma_j}$, $C_{\boldsymbol{\tau}}\boldsymbol{\tau_i} \cdot \boldsymbol{\tau_j}$, $C_{\boldsymbol{\sigma\tau}}\boldsymbol{\sigma_i} \cdot \boldsymbol{\sigma_j}\boldsymbol{\tau_i} \cdot \boldsymbol{\tau_j}$, and the one-pion exchange potential, $\propto \frac{\boldsymbol{\sigma_i}\cdot\mathbf{q}\boldsymbol{\sigma_j}\cdot\mathbf{q}}{\boldsymbol{q}^2+m_\pi^2}\boldsymbol{\tau_i} \cdot \boldsymbol{\tau_j}$, where $\mathbf{q} = \mathbf{p} - \mathbf{p}'$ and $\mathbf{p}$, $\mathbf{p}'$ are the relative nucleon momenta before and after the interaction. Adding higher-order terms

increases accuracy. Next-to-leading order is denoted by NLO, next-to-next-to-leading order by NNLO or N^{2}LO, next-to-next-to-next-to-leading order by N^{3}LO, etc.

In this work, two modified Norfolk local chiral interactions, NV2+3-Ia* and NV2+3-IIb*, were used for v_{ij} and V_{ijk}. NV2 is a two-body interaction derived from χEFT that uses nucleons, pions, and Δ-isobars as degrees of freedom. There are four versions of this interaction: NV2-Ia, NV2-IIa, NV2-Ib, and NV-IIb. The "I" and "II" indicate the energy range of data used to fit the LECs. The "a" and "b" indicate the R_S and R_L used in v_{ij}. (R_S is the contact term Gaussian parameter and R_L is the pion-range operator cutoff radius. See Refs. [38, 39, 40, 41, 42].) The NV2 two-body interactions were combined with a three-body interaction constructed up to N^{2}LO in the same chiral expansion, indicted by the "+3". The three-body LECs were determined from fits to trinucleon energies. Finally, the "*" indicates that this is the second generation of the NV2+3 interaction. In the second generation interaction, B(GT) from tritium β-decay was added to the trinucleon data used to fit the three-body LEC parameters. See Refs. [38, 39, 40, 41, 42] for details about these interactions.

After the Hamiltonian is defined, the next step is to implement an *ab-initio* method to solve the Schrödinger Equation. These methods include, for example, quantum Monte Carlo (QMC), no-core shell model (NCSM), coupled cluster (CC), and in-medium similarity renormalization group (IM-SRG). Variational Monte Carlo (VMC), a type of QMC method, was used by our WUSTL collaborators in this work.

VMC starts with a trial function Ψ_T that is close to the ground-state wave function of interest, Ψ_0. The energy of that trial function, E_V, is given by Eq. 2.16, and it is an upper limit of the true ground-state energy E_0. E_V is minimized by varying parameters of Ψ_T.

The result of the minimization is the ground state energy E_0 and wave function Ψ_0.

$$E_V = \frac{\langle \Psi_T | H | \Psi_T \rangle}{\langle \Psi_T | \Psi_T \rangle} \geq E_0 \tag{2.16}$$

The $\langle \rangle$ in Eq. 2.16 indicate integrals over all nucleon positions $\mathbf{r_i}$ and sums over all spins $\boldsymbol{\sigma_i}$ and isospins $\boldsymbol{\tau_i}$. With such a large parameter space, standard numerical integration techniques are only tractable for the smallest systems. VMC uses Monte Carlo integration with importance sampling to perform the integral for larger systems.

As the name suggests, Monte Carlo integration is a method of evaluating an integral via Monte Carlo sampling. An integral of a function f can be estimated according to Eq. 2.17, where the sum over i is the sum over uniformly sampled x_i.

$$I = \int f(x)dx \approx \frac{1}{N} \sum_{i=1}^{N} f(x_i) \tag{2.17}$$

If the function f is concentrated in a small range of x, then sampling the whole x space uniformly is very inefficient. The algorithm efficiency can be increased by sampling x_i from a probability distribution $p(x)$ that is similar to $f(x)$. This is called "importance sampling:"

$$I = \int f(x)dx = \int g(x)p(x)dx \approx \frac{1}{N} \sum_{i=1}^{N} g(x_i) \tag{2.18}$$

where $g(x) = f(x)/p(x)$ and x_i are sampled from $p(x)$.

After multiplying the integrand in the numerator by Ψ_T/Ψ_T, Eq. 2.16 can be rewritten as:

$$E_V = \frac{\sum_{\sigma\tau} \int d\mathbf{R} P(\mathbf{R}, \sigma, \tau) \frac{H\Psi_T(\mathbf{R},\sigma,\tau)}{\Psi_T(\mathbf{R},\sigma,\tau)}}{\sum_{\sigma\tau} \int d\mathbf{R} P(\mathbf{R}, \sigma, \tau)} \tag{2.19}$$

where $P(\mathbf{R}, \sigma, \tau) = \Psi_T^\dagger \Psi_T$. A VMC algorithm samples a set of points $\mathbf{X_i}$ in $[\mathbf{R}, \sigma, \tau]$ space from the distribution $p(\mathbf{X}) = \frac{P(\mathbf{X})}{\sum_{\sigma\tau} \int d\mathbf{R} P(\mathbf{X})}$ and evaluates $g(\mathbf{X_i}) = \frac{H\Psi_T(\mathbf{X_i})}{\Psi_T(\mathbf{X_i})}$. The average of $g(\mathbf{X_i})$ is an estimate of E_V.

2.3 ^{11}N: History and Motivation

^{11}N is a proton-unbound exotic nucleus with seven protons and four neutrons. As discussed in Chapter 1, ^{11}N demonstrates parity inversion of the ground state, which is evidence of shell structure evolution and makes this nucleus an interesting test case for nuclear models. Additionally, it is the mirror nucleus of ^{11}Be, a famous halo nucleus that also demonstrates parity inversion of the ground state.

^{11}N was first observed by Benenson et $al.$ via the ^{14}N(^{3}He,^{6}He) reaction in 1974 [43]. They observed one peak with a mass excess of 25.23(10) MeV and a width of 740(100) keV and interpreted it as the $\frac{1}{2}^-$ first excited state. The next observation of ^{11}N did not come until 20 years later, when Guimarães et $al.$ measured the same reaction at the Sector-Focusing Cyclotron of the Institute for Nuclear Study, University of Tokyo in 1995 [44]. They resolved two low-energy peaks and postulated that these were the $\frac{1}{2}^+$ ground state and $\frac{1}{2}^-$ first excited state.

Axelsson et $al.$ used a more direct reaction technique called resonant scattering, i.e. ^{10}C+p, to study ^{11}N at the Grand Accélérateur National d'Ions Lourds (GANIL) in 1996 [45]. They observed three states, and, by assuming mirror symmetry with the known states in ^{11}Be, inferred that these states were the $\frac{1}{2}^+$ ground state, the $\frac{1}{2}^-$ first excited state, and the $\frac{5}{2}^+$ second excited state. Calculations of the excitation function with the assumed J^πs yielded a good fit to the data, confirming the J^π assignments. The radii of the nuclear and

Coulomb potentials had to be increased from 1.2 fm to 1.4 fm. This potential was used to deduce spectroscopic factors of 0.7-0.9 for these three states, indicating that the states have a ^{10}C+p single-particle structure. Broad resonances at higher excitation energies were also observed and given tentative J^π assignments.

Azhari *et al.* measured the ^{9}Be(^{12}N,^{11}N) reaction at the NSCL in 1998 [46]. Two states were observed, however, only the relative energies were measured, so the identities of the measured states were unclear.

Also in 1998, Lépine-Szily *et al.* studied the ^{12}C(^{14}N,^{15}C)^{11}N reaction at GANIL [47, 48]. The ground state was not observed, but they observed and measured energies and widths of five states, the first two of which were determined to be the $\frac{1}{2}^-$ first excited state and the $\frac{5}{2}^+$ second excited state. The energies and widths of these states matched theoretical predictions by Fortune [49] and Barker [50] well. The other three states were only tentatively assigned J^π. An R-matrix analysis confirmed that the $\frac{1}{2}^-$ state is a $p_{1/2}$ resonance and the $\frac{5}{2}^+$ is a $d_{5/2}$ resonance.

Soon after in 2000, Oliveira *et al.* did a similar experiment to measure ^{10}B(^{14}N,^{13}B)^{11}N at GANIL [51]. They measured many states, including the ground state, and extracted the energies and widths. By comparing the ground state width to a prediction based on ^{11}Be spectroscopic factors, they estimated that the ground state has a 50% d-wave admixture. They confirmed the previous J^π assignments of the $\frac{1}{2}^-$ and $\frac{5}{2}^+$ states and made tentative J^π assignments for higher-lying states. They also suggested a $K = 1/2$ band starting with the $\frac{1}{2}^-$ first excited state.

Also in 2000, Markenroth *et al.* reanalyzed the data from Axelsson *et al.* in conjunction with new resonant scattering data from the NSCL [52]. They again confirmed the $\frac{1}{2}^+$, $\frac{1}{2}^-$, and $\frac{5}{2}^+$ assignments for the first three states. They used an optical model to calculate

theoretical cross sections and found that the calculations best matched the data with the level ordering $1s_{1/2}$, $0p_{1/2}$, and $0d_{5/2}$, which is consistent with the known level inversion. The experimental energy difference between the $0d_{5/2}$ and $1s_{1/2}$ states agreed with theoretical prediction by Fortune $et\ al.$ [49]. Again, broad resonances were observed at higher excitation energies, but could only be speculatively discussed.

Markenroth $et\ al.$ also addressed the possibility of core-excitation admixtures, i.e. ^{10}C[2^+]$\otimes\pi$, playing a role in the ground state parity inversion. Energies are not sensitive to core-excitations, so their contribution is not well-constrained, and theoretical predictions vary dramatically. The simplicity of the resonant scattering probe compared to the stripping reactions usually used for this type of study allowed Markenroth $et\ al.$ to use the width measured in this experiment to conclude that the ground state has no large core-excitation admixtures.

In 2003, Guimarães $et\ al.$ repeated their measurement of 1995 with an isotopically enriched target [53]. They measured angular distributions of the first two states for the first time and further confirmed their J^π assignments using DWBA calculations. They also extracted a spectroscopic factor of 0.1-0.2 for the ground state, which suggests a large d-wave admixture. They also measured higher-lying states and made tentative J^π assignments.

Casarejos $et\ al.$ did another ^{10}C+p experiment in 2006 at the CYCLONE facility at Louvain-la-Neuve [54]. They did an R-matrix analysis to extract the energies and widths of the first two peaks. They compared their results to previous experimental and theoretical results, but refrained from drawing strong conclusions due to differing definitions of reported energies and widths confusing the comparison. They also extracted spectroscopic factors and compared them to theoretical calculations and to the mirror ^{11}Be spectroscopic factors, but again did not use them to draw strong conclusions about ^{11}N structure.

^{11}N was not revisited experimentally for 10 years until Kumar *et al.* measured ^{10}C$+p$ at the ISAC rare-isotope beam facility at TRIUMF in 2017 [55]. The focus of this work was establishing low-energy elastic scattering as a method of constraining the nuclear force prescription for *ab-initio* calculations.

^{11}N was studied most recently by Webb *et al.* at the NSCL in 2019 by impinging an ^{13}O beam on a ^{9}Be target [56]. A strong $\frac{1}{2}^-$ peak and a weaker $\frac{3}{2}^-$ peak were observed, and their energies and widths were extracted. The focus of this work was ^{12}O, and ^{11}N structure was only discussed in the context of being an intermediate step for ^{12}O $2p$ decay.

Regarding the first $\frac{1}{2}^-$ and $\frac{3}{2}^-$ states, which are the focus of this work, previous works generally agree from spectroscopic-factor analyses and mirror-symmetry arguments that the first $\frac{1}{2}^-$ state in ^{11}N is a single-particle state with a ^{10}C$\otimes\pi(p_{1/2})$ structure, and Refs. [52] and [56] suggest that the first $\frac{3}{2}^-$ state couples strongly to an excited ^{10}C$[2_1^+]$ core.

A more direct measure of the nuclear structure of ^{11}N and a comparison to the same measure in ^{11}Be would shed light on the question of the effect of "unboundness" on isospin symmetry. In this work, the Gamow-Teller transition strength, $B(\text{GT})$, is used for that purpose. Measuring $B(\text{GT})$ from the ground state of ^{11}C, which has a p-shell configuration, would be a more direct probe of the p-shell contents of ^{11}N than has been done so far. The $B(\text{GT})$ values can then be compared to those from ^{11}B to isospin symmetric states in ^{11}Be. The Gamow-Teller transition strength has already been extracted for ^{11}B[g.s.]$\rightarrow^{11}$Be* transitions from ^{11}B(n,p)-type reactions, including ^{11}B(n,p) [57], ^{11}B($d,^2$He) [58], and ^{11}B($t,^3$He) [59]. Any differences between the $B(\text{GT})$ of the proton-rich and neutron-rich cases would indicate how and to what extent "boundness" affects mirror symmetry.

Chapter 3

Charge-Exchange Reactions

Charge-exchange (CE) reactions are reactions in which the participating nuclei exchange a proton and a neutron. The isospin changes by one unit, $\Delta T = 1$ (isovector), the spin may or may not change, $\Delta S = 1$ (spin-transfer) or $\Delta S = 0$ (non-spin-transfer), and any amount of angular momentum can be transferred, $\Delta L = 0$ (monopole), $\Delta L = 1$ (dipole), $\Delta L = 2$ (quadrupole), etc.

CE reactions are an effective method of populating and studying exotic nuclei. With radioactive beams at intermediate energies ($\approx$100 MeV/A), CE reactions can take an already-exotic nucleus even further from stability via a single-step, direct reaction mechanism. CE reactions have proven to be very useful probes of the spin-isospin response of nuclei; see Refs. [60, 61, 62, 63] for reviews. Gamow-Teller (GT) transitions ($\Delta L = 0$, $\Delta S = 1$, $\Delta T = 1$) are spin-isospin transitions that connect states via the Gamow-Teller operator, $\sigma\tau_{\pm}$, and they are the focus of this work.

As discussed in the last chapter, ^{11}C[g.s.] is a p-shell nucleus. The Gamow-Teller transition strength B(GT) to ^{11}N can provide information about the p-shell content of states in ^{11}N. Section 3.1 introduces the B(GT) quantity and explains how it can be used to learn about nuclear structure. Section 3.2 explains how B(GT) is extracted from the CE cross section using a proportionality relationship. Last, Section 3.3 presents a brief history of the (p,n) reaction and how it is further developed in this work.

3.1 The Gamow-Teller Transition Strength

Before discussing how CE reactions are used to extract $B(\text{GT})$, this section first defines $B(\text{GT})$ and explains how it provides structure information. $B(\text{GT})$ is defined as the reduced matrix element of the initial and final states $|i\rangle$ and $|f\rangle$ with the Gamow-Teller operator:

$$B(\text{GT}_\pm) = \frac{|\langle f|| \sum_k \sigma_k \tau_{k\pm} ||i\rangle|^2}{2J_i + 1} \tag{3.1}$$

where the sum over k is the sum over nucleons, the $\pm$ indicates a transition in the $\beta^\pm$ direction, and J_i is the total angular momentum of the initial state.

A more intuitive understanding of $B(\text{GT})$ can be obtained by considering its relationship to the β-decay half-life:

$$ft_{1/2} = \frac{C}{B(\text{F}) + (g_A/g_V)^2 B(\text{GT})} \tag{3.2}$$

where $ft_{1/2}$ is the ft-value or comparative half-life. f is the phase-space factor, which very roughly goes as Q^5, where Q is the Q-value of the β-decay. $t_{1/2}$ is the half-life of the decay, g_V and g_A are the weak-interaction vector and axial-vector coupling constants, and C is a combination of fundamental constants. $B(\text{F})$ is the Fermi transition strength, which is similar to $B(\text{GT})$, but with the spin operator σ rather than the $\sigma\tau$ operator. It is generally negligible except for the transition to the isobaric analog state, where it dominates.

The ft-value can be thought of as a half-life corrected for the effects of charge and decay energy. A transition between two states has a shorter half-life if the Q-value is larger; the ft-value removes this effect and is defined only by the nuclear structure. The smaller the
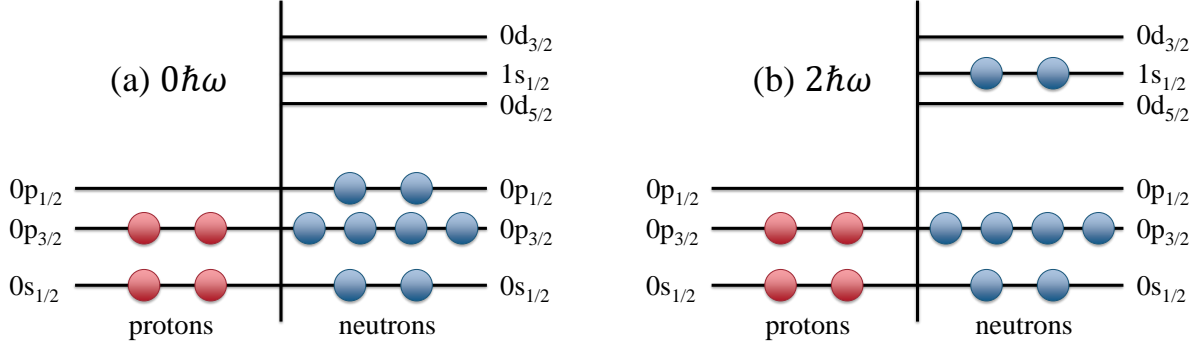
Figure 3.1: Examples of (a) $0\hbar\omega$ and (b) $2\hbar\omega$ configurations for ^{12}Be, adapted from Ref. [65]. In reality, the shell gap between the p- and sd-shells disappears for nuclei far from stability.

comparative half-life, the more the overlap between the initial and final states, and the larger the $B(\mathrm{GT})$.

The work by Meharchand *et al.* [64] is an excellent example of how $B(\mathrm{GT})$ can be used to extract nuclear structure information. Meharchand *et al.* extracted $B(\mathrm{GT})$ from the ^{12}B(^{7}Li,^{7}Be)^{12}Be CE reaction to study the first two 0^+ states in ^{12}Be. Based on the independent particle model, one might expect the ground state, or the 0^+_1 state, to have a $0\hbar\omega$ configuration, where all nucleons are in the s- and p-shells. An example of such a configuration is shown in Figure 3.1(a). Similarly, one would expect the 0^+_2 state to have a $2\hbar\omega$ configuration, where two nucleons are in the sd-shell, and an example is shown in Figure 3.1(b).

However, the shell gap between the p- and sd-shells disappears in nuclei far from stability. This causes the $0\hbar\omega$ and $2\hbar\omega$ configurations to mix, so the first two 0^+ states are each a superposition of $0\hbar\omega$ and $2\hbar\omega$ configurations.

The structure of the neighboring nucleus ^{12}B is relatively well-known to be mostly p-shell. Therefore a GT transition from ^{12}B to ^{12}Be only populates states containing p-shell ($0\hbar\omega$) configurations, and the $B(\mathrm{GT})$ value for each transition contains information about the p-shell content of each ^{12}Be state. This is illustrated in Figure 3.2.
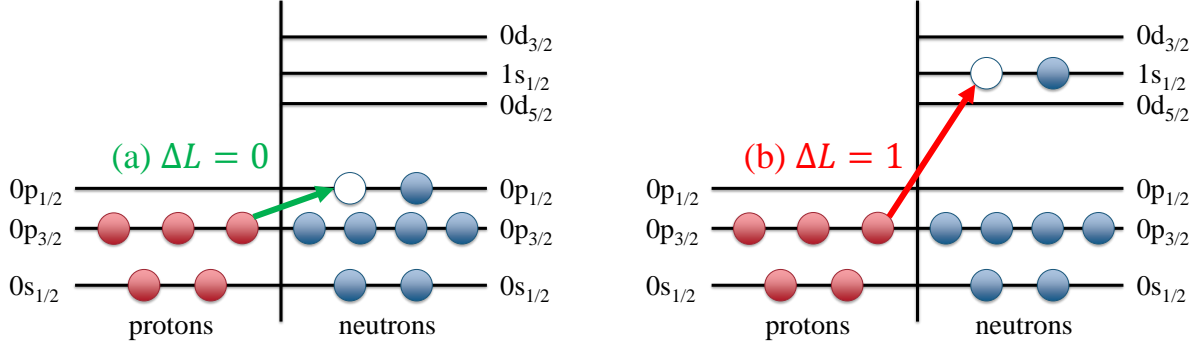
Figure 3.2: Examples of transitions from ^{12}B to (a) $0\hbar\omega$ and (b) $2\hbar\omega$ configurations in ^{12}Be, adapted from Ref. [65]. GT transitions do not change L, so a p-shell nucleon must stay in the p-shell, and GT transitions will only populate states that contain $0\hbar\omega$ configurations.

In reality, nuclear states are not just one or two configurations, but also include small contributions from higher-order configurations ($4\hbar\omega$, $6\hbar\omega$, etc.). To capture the effects of these higher-order configurations, Meharchand et $al.$ modeled the nuclei in the shell-model code Oxbash and modified the calculations until they reproduced the measured ratio $\frac{B(GT)[0_2^+]}{B(GT)[0_1^+]}$. The final calculations showed that the p-shell contribution was $25(5)\%$ for the 0_1^+ ground state and $60(5)\%$ for the 0_2^+ excited state.

One more important concept related to $B(\text{GT})$ is quenching, which is the phenomenon that measured $B(\text{GT})$ values are systematically lower than shell-model predictions. A review can be found in Ref. [66]. One possible quenching mechanism is configuration mixing with 2p2h configurations via the tensor interaction. Configuration mixing would move part of the strength to high excitation energies, making it difficult to observe experimentally. Another possible explanation is coupling between the particle-hole and $\Delta(1232)$-isobar nucleon-hole states. Part of the strength would go to exciting the Δ resonance, also known as the Δ baryon, which is essentially an excited state of the nucleon itself and has spin $\frac{3}{2}$ and isospin $\frac{3}{2}$. Chou et $al.$ [67] found a phenomenological expression for the quenching factor in $A = 1-39$
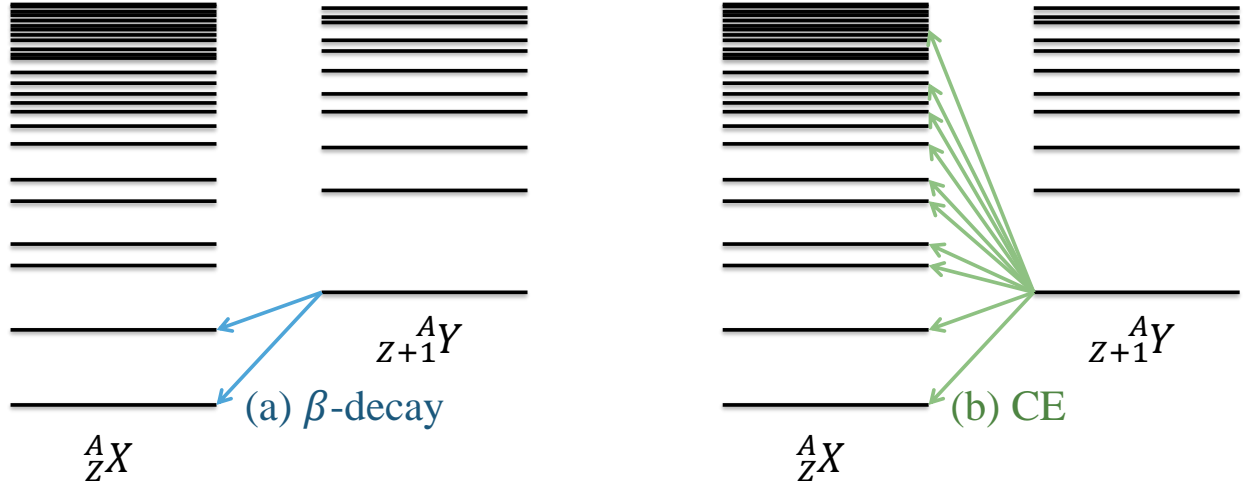
Figure 3.3: (a) β-decay from parent nucleus Y can only populate states in the daughter nucleus X that are energetically accessible according to the Q-value of the decay. (b) Charge-exchange reactions don't have such a limitation and can populate excited states above the decay threshold.

nuclei, and this was applied to the shell-model calculations done in this work:

$$q = 1 - 0.19 \left(\frac{A}{16} \right)^{0.35} \tag{3.3}$$

$$q^2 = 0.69 \text{ for } A = 11 \tag{3.4}$$

3.2 The Proportionality Relationship

The Gamow-Teller transition strength, $B(\text{GT})$, is traditionally measured via β-decay. However, β-decay is limited by the decay Q-value, and high-lying excited states (and nuclei that do not β-decay) cannot be studied. As illustrated in Figure 3.3, CE reactions do not have this limitation and can populate high-lying excited states.

Although β-decay is mediated by the weak force and CE reactions are mediated by the strong force, the operators involved in each process are very similar. The central isovector spin-flip ($\Delta S = 1$) and non-spin-flip ($\Delta S = 0$) terms in the effective nucleon-nucleon

27

interaction that mediate (p,n) reactions are:

$$\sum_i V_{\sigma\tau}(r_{ip})(\boldsymbol{\sigma}_i \cdot \boldsymbol{\sigma}_p)(\boldsymbol{\tau}_i \cdot \boldsymbol{\tau}_p) \tag{3.5}$$

$$\sum_i V_{\tau}(r_{ip})(\boldsymbol{\tau}_i \cdot \boldsymbol{\tau}_p) \tag{3.6}$$

where the sum i is the sum over target nucleons and p is the proton. These operators are similar to the operators that mediate GT and Fermi β-decay:

$$G_A \sum_i \boldsymbol{\sigma}_i \tau_i^{\pm} \tag{3.7}$$

$$G_V \sum_i \tau_i^{\pm} \tag{3.8}$$

The similarity of the operators suggests that the β-decay transition strength might be proportional to the CE cross section. In 1987, Taddeucci et $al.$ derived a rigorous theoretical framework for such a proportionality relationship [68]:

$$\left.\frac{\mathrm{d}\sigma}{\mathrm{d}\Omega}(q=0)\right|_{\Delta L=0} = \hat{\sigma}_{GT} B(GT) \tag{3.9}$$

where $\left.\frac{\mathrm{d}\sigma}{\mathrm{d}\Omega}(q=0)\right|_{\Delta L=0}$ is the $\Delta L = 0$ component of the CE cross section extrapolated to zero momentum transfer ($q = 0$, where $\mathbf{q} = \mathbf{k_f} - \mathbf{k_i}$), and $\hat{\sigma}_{GT}$ is the proportionality constant called the unit cross section.

Taddeucci et $al.$ derived this proportionality relationship by (1) modeling the cross section in the Distorted Wave Born Approximation (DWBA), (2) assuming $\Delta L = 0$, and (3) applying the eikonal approximation to the distorted waves. As a result, the unit cross

section can be factorized into three independent terms:

$$\hat{\sigma} = KN^D |J_{\sigma\tau}|^2 \tag{3.10}$$

$K = \frac{E_i E_f}{(\hbar^2 c^2 \pi)^2} \frac{k_f}{k_i}$ is a kinematical factor containing information about the masses and energies of the particles, where E_i and E_f are the initial and final reduced energies, and k_i and k_f are the incoming and outgoing wave momenta. $N^D = \frac{\sigma_{DWBA}}{\sigma_{PWBA}}$ is the ratio of the distorted wave to the plane wave cross section called the distortion factor, and $J_{\sigma\tau}$ is the volume integral of the nucleon-nucleus interaction.

The three approximations made in deriving the proportionality relationship require the CE reaction to fulfill several conditions. Essentially, the reaction must be done at intermediate energies, and the $\Delta L = 0$ component of the cross section must be extracted and extrapolated to $q = 0$.

First, for the proportionality relationship to hold, the reaction should take place in a single step, i.e. $p \to n$ via a meson exchange, as opposed to multistep processes such as the case in which the proton picks up a neutron and the deuteron deposits a proton. Single-step processes dominate at intermediate energies, about 100 MeV/u.

Next, the $\Delta L = 0$ component of the CE cross section must be extracted. In reality, the total angular momentum $J = L + S$ is the good quantum number, not L and S. When looking at $\Delta J^\pi = 1^+$ states, there are two possible $\Delta L + \Delta S$ combinations: $\Delta L = 0, \Delta S = 1$ and $\Delta L = 2, \Delta S = 1$. The tensor interaction can enhance the $\Delta L = 2, \Delta S = 1$ component and cause it to interfere coherently and incoherently with the $\Delta L = 0, \Delta S = 1$ component. The incoherent contribution can be separated out by doing a Multipole Decomposition Analysis (MDA), which is explained in Section 8.2.1. The coherent contribution, however, cannot be

easily removed. It can be estimated by turning on and off the tensor interaction in reaction theory codes but is generally a source of uncertainty in this type of experiment.

Last, the eikonal approximation, also called the high-energy or Glauber approximation, is a high-energy approximation ($E \gg V$) that assumes the projectile follows a straight-line trajectory. (See texts such as Refs. [69] and [70] for more about the eikonal approximation.) This approximation requires distortion effects to be minimized and $q = 0$. Distortion effects can be minimized by doing the reaction at intermediate energies, and the cross section at $q = 0$ can be found by extrapolation, which is explained later. Qualitatively, the $q = 0$ requirement can be thought of as matching the conditions of β-decay, where relatively little momentum is transferred to the β-particle [60].

The most direct evidence supporting the proportionality relationship comes from a comparison of measured cross sections to cross sections predicted from the proportionality relationship using known $B(\text{GT})$ from β-decay. Examples from Ref. [68] are given in Figure 3.4, and the proportionality relationship is indeed valid for these test cases. For more information about the proportionality relationship, see Ref. [68].

Note that CE reactions induce both GT and Fermi transitions, and a similar proportionality relationship holds for Fermi transitions. To the extent that isospin is a good quantum number, the only state populated by a Fermi transition is the isobaric analog state (IAS). The IAS is the only state that can have both GT and Fermi contributions. (If the IAS is 0^+, then it only has a Fermi contribution.) Since the vast majority of the Fermi strength is contained in the excitation of the IAS, it is safe to assume that other $\Delta L = 0$ transitions are associated with a Gamow-Teller transition. In the case of $^{11}\text{C}(p,n)$, $|T_z|$ increases, so there is no IAS of the $^{11}\text{C}[\text{g.s.}]$ in the final nucleus ^{11}N, and $\Delta L = 0, \Delta S = 0$ contributions will be very small.
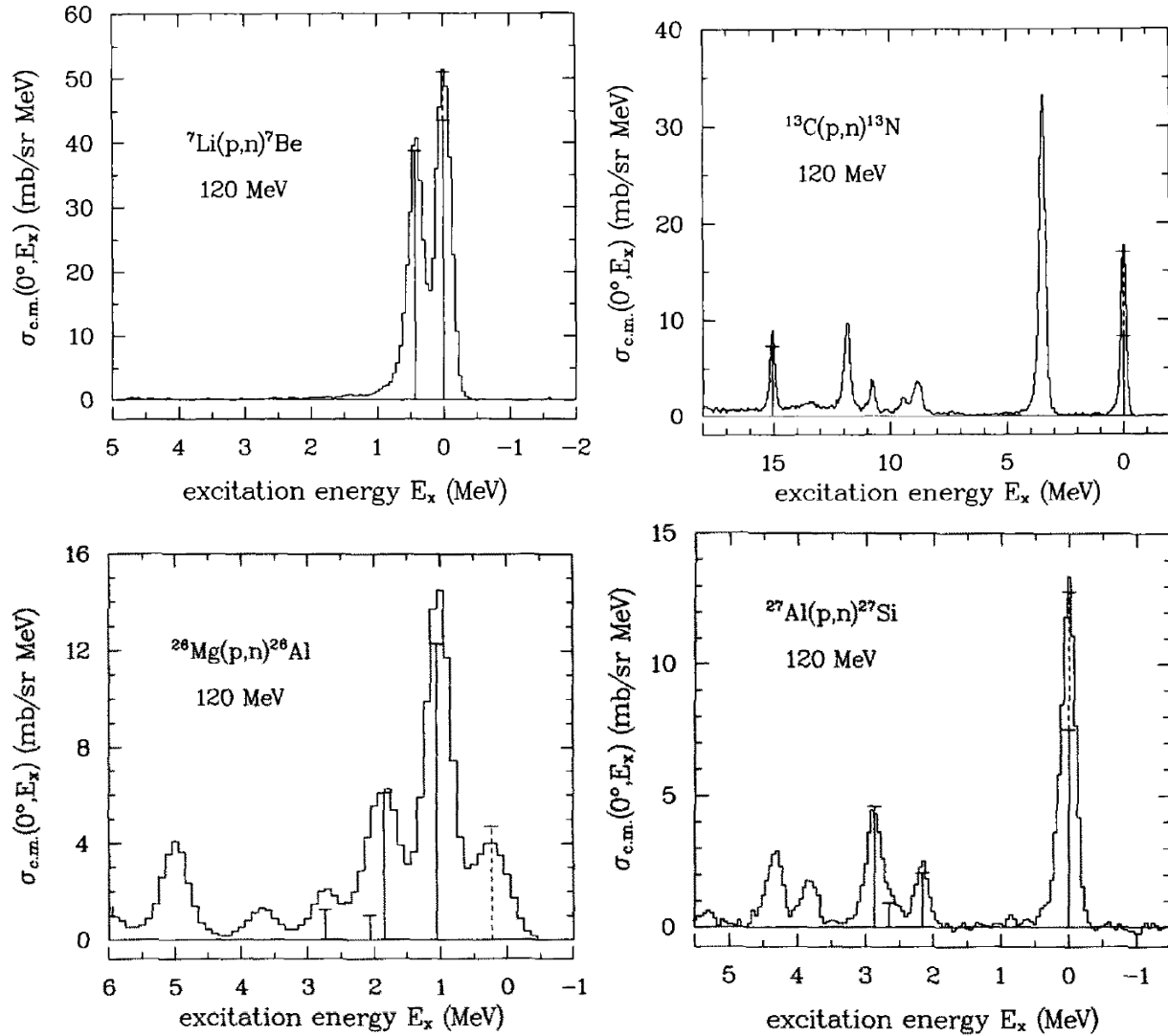
Figure 3.4: Evidence supporting the proportionality relationship [68]. The vertical bars indicate the cross section calculated from the proportionality relationship with $B(\text{GT})$ from β-decay. The dashed portion indicates the Fermi contribution. The bars match the data well, indicating that the proportionality is valid.

31

Finally, at very high excitation energies ($\approx$30 MeV), isovector monopole resonances also contribute to the $\Delta L = 0$ cross section [71], but such high excitation energies are not studied in this work.

3.3   The (p,n) Reaction: History and Motivation

The story of the (p,n) experimental technique used in this work begins in 1961, when Anderson *et al.* used the ^{51}V(p,n) reaction to discover the isobaric analog state (IAS) [72, 73]. A transition to the IAS is an isospin transition and is analogous to Fermi β-decay. People soon realized that the (p,n) reaction could also be used to populate spin-isospin transitions analogous to Gamow-Teller β-decay [74].

At first, the (p,n) reaction was used to probe the nucleon-nucleon interaction, in particular the spin and spin-isospin parts of the effective two-body force, V_τ and $V_{\sigma\tau}$. The ratio of the IAS cross section to a Gamow-Teller state cross section was used to deduce $V_{\sigma\tau}/V_\tau$, as in e.g. Refs. [75, 76]. The $B(GT)$ values obtained from β-decay to those states was a critical ingredient in the connection between the cross sections and $V_{\sigma\tau}/V_\tau$.

In 1975, Wharton *et al.* argued that there should be some kind of correlation between the $\Delta L = 0$ part of the CE cross section and $B(GT)$ using (^{6}Li, ^{6}He) data [77]. However, the beam energy was low, and multi-step processes obscured the proportionality. Doering *et al.* soon after measured a Gamow-Teller resonance in an $N > Z$ nucleus for the first time and stated that the CE and Gamow-Teller β-decay operators are similar and should therefore have roughly proportional strength functions [78].

Motivated by previous works that used the (p,n) reaction to study $V_{\sigma\tau}/V_\tau$, Goodman *et al.* in 1980 suggested that essentially the opposite could be done [79]. Instead of using

the known GT strength to extract $V_{\sigma\tau}/V_\tau$, use the known NN interaction to extract the GT strength. This concept would enable the extraction of $B(\text{GT})$ to states inaccessible to β-decay. The theoretical framework for proportionality was more rigorously developed by Taddeucci et $al.$ in 1987 [68]. The ability to extract $B(\text{GT})$ in regions inaccessible to β-decay has become very useful for understanding nuclear structure [63] and astrophysical phenomena [80, 81].

Because of the difficulties associated with creating and using a target of unstable nuclei, (p,n) studies were initially restricted to stable nuclei. This changed in the 1990s when rare-isotope beams became available. By impinging the rare-isotope beam on a hydrogen target, the (p,n) reaction in inverse kinematics could be used to study unstable nuclei. One of the first test cases for the (p,n) reaction in inverse kinematics was the $^6\text{He}(p,n)^6\text{Li}$ reaction done at GANIL in 1996 to study halo structures in $A = 6$ nuclei [82, 83].

Several experiments followed using the (p,n) reaction in inverse kinematics to study halo structures in light nuclei, including $^6\text{He}(p,n)$ at the National Superconducting Cyclotron Laboratory (NSCL) [84] and at the China Institute of Atomic Energy [85], $^{11}\text{Li}(p,n)$ at RIKEN [86, 87, 88], and $^{14}\text{Be}(p,n)$ at RIKEN [89].

While all of these experiments used the (p,n) reaction in inverse kinematics to probe exotic nuclear structure, none actually extracted $B(\text{GT})$. The first successful experiment that extracted $B(\text{GT})$ from unstable nuclei via the (p,n) reaction in inverse kinematics was the $^{14}\text{Be}(p,n)$ experiment done by Satou et $al.$ at RIKEN [90, 91]. Satou et $al.$ measured the cross section, extracted $B(\text{GT})$ based on Taddeucci's framework, and showed that the result matched the $B(\text{GT})$ measured from β-decay.

Programs to further develop the (p,n) reaction in inverse kinematics as a probe of the spin-isospin response of unstable nuclei are actively being developed at both RIKEN and

the NSCL. At the NSCL (now the Facility for Rare Isotope Beams, FRIB), Sasano *et al.* in 2011 established a new technique using the missing-mass method to measure the (p,n) reaction in inverse kinematics [92, 93]. The ^{56}Ni,^{55}Co(p,n) reactions were measured and the $B(GT)$ values extracted to benchmark electron capture rate approximations used in supernova simulation codes. Lipschutz *et al.* extracted $B(GT)$ from the ^{16}C(p,n) reaction and established the same technique as a probe of isovector giant resonances [94].

At RIKEN, in 2015, Kobayashi *et al.* extracted $B(GT)$ from the ^{8}He(p,n) reaction [95]. In 2016, Yasuda *et al.* used the technique developed by Sasano *et al.* to measure the ^{132}Sn(p,n) reaction [96]. The resulting $B(GT)$ from this experiment was used to put constraints on the Landau-Migdal parameter, which characterizes the strength of the short range component of the spin-isospin interaction [97]. Most recently, a new neutron detector array, called the Particle Analyzer Neutron Detector Of Real-time Acquisition (PANDORA), was developed to measure spin-isospin responses of neutron dripline nuclei. PANDORA was tested at the HIMAC facility in Chiba with the ^{6}He(p,n) reaction and at RIKEN with the ^{11}Li(p,n) and ^{14}Be(p,n) reactions [98].

All of the (p,n) experiments listed so far have been primarily focused on stable and neutron-rich unstable nuclei. However, the (p,n) reaction would also be useful for studying proton-rich unstable nuclei. As mentioned in Chapter 1, the (p,n) reaction on a proton-rich nucleus produces a proton-rich nucleus farther from stability, providing access to unbound nuclei beyond the proton dripline via a simple reaction mechanism.

A proton-rich nucleus that would be particularly interesting to study with the (p,n) reaction is ^{100}Sn, the heaviest known $N = Z$ doubly-magic bound nucleus. The $B(GT)$ of its β^+-decay to ^{100}In is the largest known $B(GT^+)$ [99], suggesting a robust shell closure at $N = Z = 50$. A ^{100}Sn(p,n) experiment could extract $B(GT)$ in the β^- direction to the unbound

^{100}Sb, which would be a valuable test of isospin symmetry. However, measuring (p,n) on such a heavy, proton-rich nucleus is not yet feasible because sufficient beam intensities cannot presently be obtained. This work is part of the NSCL/FRIB charge-exchange program and seeks to further extend the missing-mass (p,n) technique established by Sasano *et al.* to proton-unbound nuclei in preparation for future studies on nuclei such as ^{100}Sn.

Chapter 4

Theoretical Cross Sections

As discussed in Section 3.2, $B(\text{GT})$ is proportional to the $\Delta L = 0$ cross section extrapolated to zero momentum transfer ($q = 0$). In this work, the $\Delta L = 0$ cross section was extracted from the measured cross section via a Multipole Decomposition Analysis (MDA). The critical ingredients for doing an MDA are theoretical cross sections. In this chapter, the theoretical cross sections used for the MDA are calculated in the Distorted Wave Born Approximation (DWBA) using the code DW81 [100]. The MDA is discussed later in Section 8.2.1.

4.1   The Distorted Wave Born Approximation

In general, nuclear reaction cross sections are calculated from the wave function of the target+projectile system, and the wave function of the system is found by solving the Schrödinger Equation. In most cases, the equation cannot be solved exactly, but many approximations have been derived. One such approximation is the "Distorted Wave Born Approximation (DWBA)." This section sketches a brief derivation of the DWBA, and a full description can be found in texts such as Refs. [69] and [70].

The goal is to calculate the cross section of the reaction that takes place when an incoming projectile nucleus interacts with a heavy target nucleus. (In inverse kinematics, the roles are reversed, but it doesn't matter since the calculations are done in the center-of-mass frame.) ψ is the total wave function describing the projectile+target system, and it can be found by

solving the Schrödinger Equation:

$$[H - E]\psi = 0 \tag{4.1}$$

where E is the energy and $H = T + V$ is the Hamiltonian with kinetic energy operator T and potential V.

When the distance between the projectile and the target becomes very large, $r \to \infty$, the solution is the sum of the incoming plane wave and the outgoing spherical wave:

$$\psi(r \to \infty) = e^{ik_i z} + f(\theta, \phi)\frac{e^{ik_f r}}{r} \tag{4.2}$$

where $e^{ik_i z}$ is the incoming plane wave with momentum k_i and $\frac{e^{ik_f r}}{r}$ is the outgoing spherical wave with momentum k_f. The coefficient $f(\theta, \phi)$ in front of the outgoing spherical wave is called the "scattering amplitude," and this coefficient contains all of the physics of the reaction.

The differential cross section of a nuclear reaction is defined as the ratio of the scattered angular flux to the incident flux, and it can be written in terms of the scattering amplitude as:

$$\frac{d\sigma}{d\Omega}(\theta, \phi) = \frac{k_f}{k_i}|f(\theta, \phi)|^2 \tag{4.3}$$

By solving the Schrödinger Equation and applying the boundary conditions in Eq. 4.2, one can show that the scattering amplitude is completely determined by the potential V:

$$f(\theta, \phi) = -\frac{\mu}{2\pi\hbar^2} \int e^{-i\mathbf{k}' \cdot \mathbf{r}'} V(\mathbf{r}')\psi^+(\mathbf{k}, \mathbf{r}')d\mathbf{r}'$$

$$= -\frac{\mu}{2\pi\hbar^2}\langle\phi^{(-)}|V|\psi\rangle \tag{4.4}$$

where ϕ is the plane wave solution for $V = 0$, and the $^{(-)}$ superscript indicates the complex conjugate.

Next, for convenience, we define a transition matrix, or T-matrix, with elements T_{fi}, and write $f(\theta, \phi)$ in terms of these matrix elements:

$$T_{fi} = \langle\phi^{(-)}|V|\psi\rangle \tag{4.5}$$

$$f(\theta, \phi) = -\frac{\mu}{2\pi\hbar^2}T_{fi} \tag{4.6}$$

Therefore if we can find the transition matrix elements, we can calculate the cross section. The rest of this section explains how the DWBA is used to write T_{fi} in terms of knowns, eliminating the unknown ψ.

The homogeneous solution to the Schrödinger Equation with $V = 0$ is the plane wave ϕ. To find the inhomogeneous solution ψ, we define a new operator called the "Green's integral operator" $\hat{G}^+ = [E - T]^{-1}$ that can be applied to both sides of the Schrödinger Equation:

$$[H - E]\psi = 0$$

$$[E - T]\psi = V\psi$$

$$[E - T]^{-1}[E - T]\psi = [E - T]^{-1}V\psi$$

$$\psi = \hat{G}^+V\psi \tag{4.7}$$

Then the total solution is the sum of the homogeneous and inhomogeneous solutions. This

is called the "Lippmann-Schwinger Equation:"

$$\psi = \phi + \hat{G}^+ V \psi \tag{4.8}$$

The Lippmann-Schwinger Equation is an implicit equation since ψ appears on both sides. The exact solution can be written as a "Born series:"

$$\begin{aligned}
\psi &= \phi + \hat{G}^+ V [\phi + \hat{G}^+ V [\phi + \hat{G}^+ V [\cdots]]] \\
&= \phi + \hat{G}^+ V \phi + \hat{G}^+ V \hat{G}^+ V \phi + \hat{G}^+ V \hat{G}^+ V \hat{G}^+ V \phi + \cdots
\end{aligned} \tag{4.9}$$

Then the transition matrix elements can also be written as a series:

$$\begin{aligned}
T_{fi} &= \langle \phi^{(-)} | V | \psi \rangle \\
&= \langle \phi^{(-)} | V | \phi + \hat{G}^+ V \phi + \hat{G}^+ V \hat{G}^+ V \phi + \hat{G}^+ V \hat{G}^+ V \hat{G}^+ V \phi + \cdots \rangle \\
&= \langle \phi^{(-)} | V | \phi \rangle + \langle \phi^{(-)} | V \hat{G}^+ V | \phi \rangle + \langle \phi^{(-)} | V \hat{G}^+ V \hat{G}^+ V | \phi \rangle + \cdots
\end{aligned} \tag{4.10}$$

If V is weak, then the first term in this series is a sufficiently precise estimate, and this is called the "Plane Wave Born Approximation (PWBA)."

$$T_{fi}^{PWBA} = \langle \phi^{(-)} | V | \phi \rangle \tag{4.11}$$

If the potential can be broken up into two parts, $V = U_1 + U_2$, where U_1 is an optical potential that cannot cause any transitions, then the Lippmann-Schwinger Equation

becomes:

$$\psi = \phi + \hat{G}_0^+(U_1 + U_2)\psi$$

$$= \chi + \hat{G}_1^+ U_2 \psi \tag{4.12}$$

where $\hat{G}_0^+ = [E - T]^{-1}$, $\hat{G}_1^+ = [E - T - U_1]^{-1}$, and χ is the solution with $V = U_1$ only, called the "distorted wave." This is again an implicit equation that can be expanded into a Born Series:

$$\psi = \chi + \hat{G}_1^+ U_2[\chi + \hat{G}_1^+ U_2[\chi + \hat{G}_1^+ U_2[...]]]$$

$$= \chi + \hat{G}_1^+ U_2 \chi + \hat{G}_1^+ U_2 \hat{G}_1^+ U_2 \chi + \hat{G}_1^+ U_2 \hat{G}_1^+ U_2 \hat{G}_1^+ U_2 \chi + ... \tag{4.13}$$

Then the transition matrix elements can be written in terms of the distorted wave χ scattered by U_2, and again expanded into a series:

$$T_{fi} = \langle \chi^{(-)} | U_2 | \psi \rangle$$

$$= \langle \chi^{(-)} | U_2 | \chi + \hat{G}^+ U_2 \chi + \hat{G}^+ U_2 \hat{G}^+ U_2 \chi + \hat{G}^+ U_2 \hat{G}^+ U_2 \hat{G}^+ U_2 \chi + \cdots \rangle$$

$$= \langle \chi^{(-)} | U_2 | \chi \rangle + \langle \chi^{(-)} | U_2 \hat{G}^+ U_2 | \chi \rangle + \langle \chi^{(-)} | U_2 \hat{G}^+ U_2 \hat{G}^+ U_2 | \chi \rangle + \cdots \tag{4.14}$$

If U_2 is weak relative to U_1, then the series can be truncated after the first term, and we get the first order "Distorted Wave Born Approximation (DWBA):"

$$T_{fi}^{DWBA} = \langle \chi^{(-)} | U_2 | \chi \rangle \tag{4.15}$$

4.1.1 The Optical Potential

The optical potential U_1 is the elastic scattering potential that distorts the incoming and outgoing waves in the DWBA. In this work, U_1 is a sum of several potentials: the Coulomb potential, plus an attractive nuclear potential, plus a surface-peaked spin-orbit potential:

$$
\begin{aligned}
U_1(r) = & U_C(r; r_C) - \\
& V f(r; r_v, a_v) - iW f(r; r_w, a_w) + \\
& \frac{1}{r} (\mathbf{L} \cdot \mathbf{S}) \left[V_{so} \frac{\mathrm{d}}{\mathrm{d}r} f(r; r_{vso}, a_{vso}) - iW_{so} \frac{\mathrm{d}}{\mathrm{d}r} f(r; r_{wso}, a_{wso}) \right]
\end{aligned}
\tag{4.16}
$$

The first term is the Coulomb potential with radius r_C. The second two terms are the attractive nuclear potential with a Woods-Saxon shape $f(r; r_x, a_x)$, real depth V, and imaginary depth W. The last two terms are the surface-peaked spin-orbit potential with real depth V_{so} and imaginary depth W_{so}. The Woods-Saxon potential is:

$$
f(r; r_x, a_x) = \frac{1}{1 + \exp(\frac{r - r_x}{a_x})}
\tag{4.17}
$$

where r_x is the radius of the potential and a_x is the diffuseness.

The optical potential parameters ideally come from fitting elastic scattering data measured with the desired projectile and target at the desired incident energy. However, no such data exist for most unstable nuclei, and this is the case for $^{11}C(p,n)^{11}N$. To solve this problem, global potentials that provide the necessary parameters as functions of target A, target Z, and projectile energy have been created by fitting data from many experiments. The global potential by Madland was used for the calculations done for this work [101]. This

Table 4.1: Optical potential parameters for ^{11}C(p,n) at 94 MeV/A [101]. The imaginary spin-orbit part was neglected.

Potential	V	r_v	a_v	W	r_w	a_w
p - central	-26.2	1.22	0.70	-7.0	1.43	0.50
p - spin-orbit	-20.1	0.99	0.66			
n - central	-29.1	1.20	0.70	-6.6	1.46	0.47
n - spin-orbit	-22.2	0.99	0.67			

potential is an extension of that by Schwandt and Kaitchuck [102] to include a larger mass and energy range. The parameters are given in Table 4.1.

The optical potential not only distorts the incoming and outgoing waves, but also defines how the nucleons are bound in the target nucleus. If the optical potential was exact, then the eigenenergies of the optical potential would be the single-particle energies of each orbital. However, due to higher-order effects not included in the spherical potential model, the single-particle energies are in reality shifted from these eigenenergies. To account for these shifts, the DW81 program takes single-particle energies as inputs and adjusts the real depth V until the single-particle energies are reproduced.

The single-particle energies were calculated using Oxbash with the Skyrme SK20 interaction. The core nucleus ^{10}C is proton-rich, so many of the orbitals are unbound. DW81 does not provide a means to calculate wave functions for unbound nucleons that are properly normalized, so the energies were artificially lowered to -1.0 MeV. This artificial binding does not significantly affect the resulting angular distribution shapes.

4.1.2 Transition Potential

The potential U_2 is the effective interaction between the projectile nucleon and the target nucleus that describes the coupling between the initial and final states. If the projectile p is one nucleon, then U_2 is the overlap of the initial and final target states $|i\rangle$ and $|f\rangle$ with the

projectile-target interaction:

$$U_2 = \langle f | \sum_j V_{pj}(1 - P_{pj}) | i \rangle \tag{4.18}$$

where the sum over j is the sum over nucleons in the target and P_{pj} is the permutation operator to properly include antisymmetrization. This expression for the nuclear transition potential U_2 can be factorized into a reaction part and a structure part. The reaction part can be calculated from the effective nucleon-nucleon interaction, and the structure part can be calculated from the one-body transition densities. See Ref. [60] for details about this factorization.

The effective nucleon-nucleon interaction $V_{NN}(r_{12})$ is a sum of central (C), spin-orbit (LS), and tensor (T) components:

$$V_{NN}(r_{12}) = V^C(r_{12}) + V^{LS}(r_{12})(\mathbf{L} \cdot \mathbf{S}) + V^T(r_{12})S_{12} \tag{4.19}$$

where r_{12} is the relative position of the two nucleons, $S_{12} = 3(\boldsymbol{\sigma_1} \cdot \hat{\mathbf{r}})(\boldsymbol{\sigma_2} \cdot \hat{\mathbf{r}}) - \boldsymbol{\sigma_1} \cdot \boldsymbol{\sigma_2}$ is the tensor operator, and each $V^x(r)$ is sum of Yukawa potentials $Y(x) = e^{-x}/x$ with amplitudes V_i^x and ranges R_i:

$$V^C(r) = \sum_{i=1}^N V_i^C Y\left(\frac{r}{R_i}\right) \tag{4.20}$$

$$V^{LS}(r) = \sum_{i=1}^N V_i^{LS} Y\left(\frac{r}{R_i}\right) \tag{4.21}$$

$$V^T(r) = \sum_{i=1}^N V_i^T r^2 Y\left(\frac{r}{R_i}\right) \tag{4.22}$$

The V_i and R_i parameters can be determined from fits to data. The effective nucleon-nucleon interaction used for these calculations was that of Franey and Love at 140 MeV [103].

The one-body transition densities (OBTDs) contain all of the relevant nuclear structure information. The OBTDs are weighting factors for 1p-1h contributions to the reduced matrix element of the operator of interest, in this case the Gamow-Teller transition operator. The OBTDs were calculated in the *spsdpf* model space with the *wbp* interaction using the code Oxbash [28]. The Oxbash OBTDs (when calculated using isospin formalism) are:

$$a(\Delta j, \Delta t) = \frac{\langle f|||[a_{k1}^+ \otimes \tilde{a}_{k2}]^{\Delta j, \Delta t}|||i\rangle}{\sqrt{(2\Delta j + 1)(2\Delta t + 1)}} \tag{4.23}$$

where Δj and Δt are the changes in angular momentum and isospin from the initial to the final state, and $k_{1,2}$ are the orbitals of the particle and hole. The DW81 code uses a different OBTD convention, the so-called z-coefficients, so the Oxbash result needs to be multiplied by a factor before it can be used by DW81:

$$z = a(\Delta j, \Delta t) \times \langle t_i, t_{zi}, \Delta t, \Delta t_z | t_f, t_{zf}\rangle \times \frac{\sqrt{2\Delta t + 1}}{\sqrt{(2j_i + 1)(2t_f + 1)}} \tag{4.24}$$

4.2 Theoretical Excitation-Energy Spectrum

Figure 4.1 shows the ^{11}C(p,n)^{11}N theoretical differential cross sections at $0°$ as a function of the ^{11}N excitation energy. The first two negative parity states, $\frac{1}{2}^-$ at 0.311 MeV and $\frac{3}{2}^-$ at 2.026 MeV, have the largest cross sections at $0°$. The calculations do not include the intrinsic widths of the states, so even with smearing from the experimental resolution
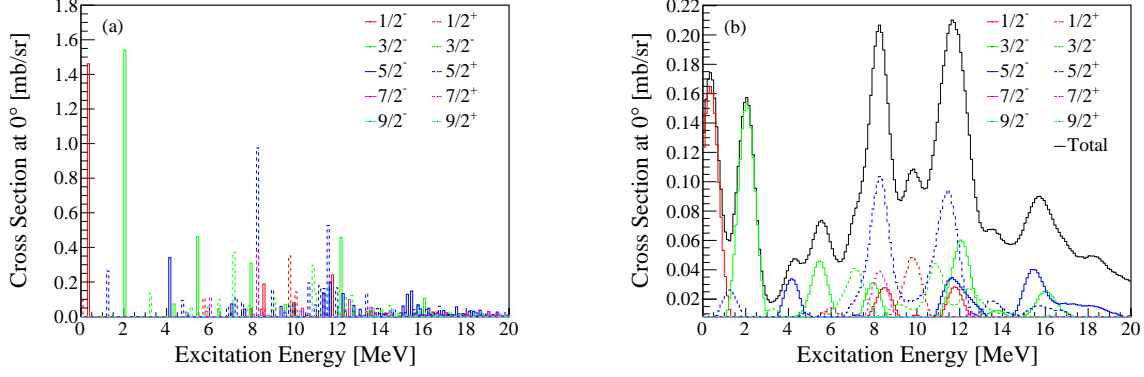
Figure 4.1: (a) Theoretical cross section, including $\frac{1}{2}^{\pm}, \frac{3}{2}^{\pm}, \frac{5}{2}^{\pm}, \frac{7}{2}^{\pm}, \frac{9}{2}^{\pm}$ states. (b) Same as (a), smeared with the experimental resolution.

applied, the states at higher excitation energies are expected to be significantly wider than suggested by Figure 4.1(b).

4.3 Theoretical Angular Distributions

As previously mentioned, the $\Delta L = 0$ component of the measured cross section must be determined to extract $B(\mathrm{GT})$. This is done using a procedure called a Multipole Decomposition Analysis (MDA), and the theoretical angular distributions are necessary ingredients for an MDA. In an MDA, the measured angular distribution is fit to a sum of theoretical angular distributions, where each theoretical angular distribution is a characteristic ΔL shape. In this section, the characteristic ΔL shapes for the $^{11}\mathrm{C}(p,n)$ reaction are calculated. The actual MDA is done in Section 8.2.1.

The spin-parity of $^{11}\mathrm{C}[\mathrm{g.s.}]$ is $J^{\pi} = \frac{3}{2}^{-}$. The $\Delta S = 0$ component is small in this case, so only $\Delta S = 1$ transitions were considered. The selection rules for the different angular momentum transfer components are shown in Table 4.2, with all possible final-state spin-parities given in the last column. The first $\frac{1}{2}^{-}$, $\Delta J = 1$ state was selected as the $\Delta L = 0$ shape, the first $\frac{1}{2}^{+}$, $\Delta J = 1$ state was selected as the $\Delta L = 1$ shape, and the seventh $\frac{7}{2}^{-}$,

Table 4.2: Selection rules from ^{11}C[g.s.] for the different angular momentum transfer components.

Shape	J_i^π	ΔL	ΔS	ΔJ	J_f^π
$\Delta L = 0$	$\frac{3}{2}^-$	0	1	1	$\frac{1}{2}^-$, $\frac{3}{2}^-$, $\frac{5}{2}^-$
$\Delta L = 1$	$\frac{3}{2}^-$	1	1	0,1,2	$\frac{1}{2}^+$, $\frac{3}{2}^+$, $\frac{5}{2}^+$, $\frac{7}{2}^+$
$\Delta L = 2$	$\frac{3}{2}^-$	2	1	1,2,3	$\frac{1}{2}^-$, $\frac{3}{2}^-$, $\frac{5}{2}^-$, $\frac{7}{2}^-$, $\frac{9}{2}^-$
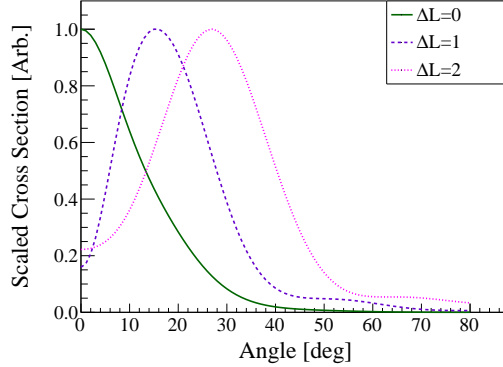
Figure 4.2: $\Delta L = 0, 1, 2$ shapes calculated with DW81. These are used in the MDA in Section 8.2.1.

$\Delta J = 3$ state was selected as the $\Delta L = 2$ shape for the MDA. These shapes are shown in Figure 4.2.

There are three main sources of error in the ΔL shapes:

- OBTDs

- Optical potential parameters

- NN interaction parameters

The different states shown in Figures 4.3, 4.4, and 4.5 serve as an estimation of the shape uncertainty due to the OBTDs. Changing the state used for the MDA did not significantly change the final result, so the error from the OBTDs was neglected.

The error from the uncertainty in the optical potential parameters and the NN interaction parameters were estimated by using parameters from different models. Shapes using optical

46

potential parameters from ^{12}C$+p$ scattering [104] (as opposed to the global potential) are shown in Figures 4.6, 4.7, and 4.8 for $\Delta L = 0, 1, 2$, respectively. Shapes using NN interaction parameters from the Franey-Love interaction at 100 MeV [103] (as opposed to 140 MeV) are shown in Figures 4.9, 4.10, and 4.11 for $\Delta L = 0, 1, 2$, respectively. For both the different optical potential and the different NN interaction, the results do not significantly differ from the original case.
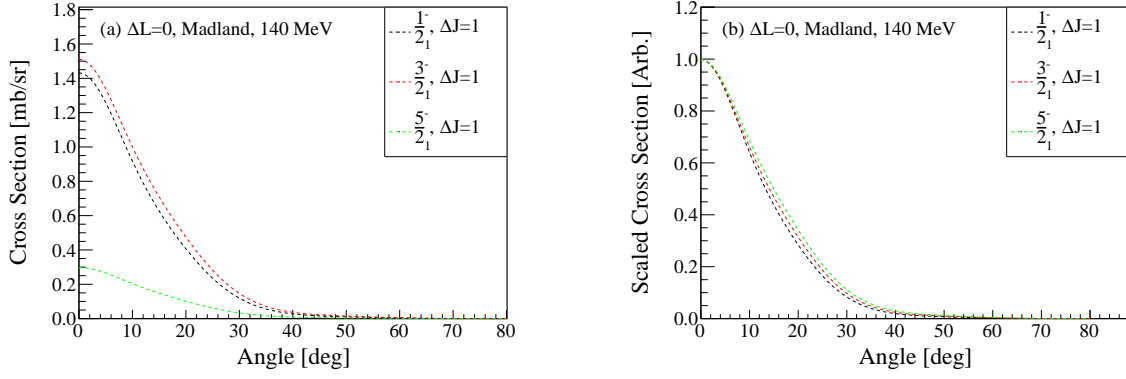
Figure 4.3: (a) DWBA $\Delta L = 0$ cross sections. (b) Scaled version of (a).
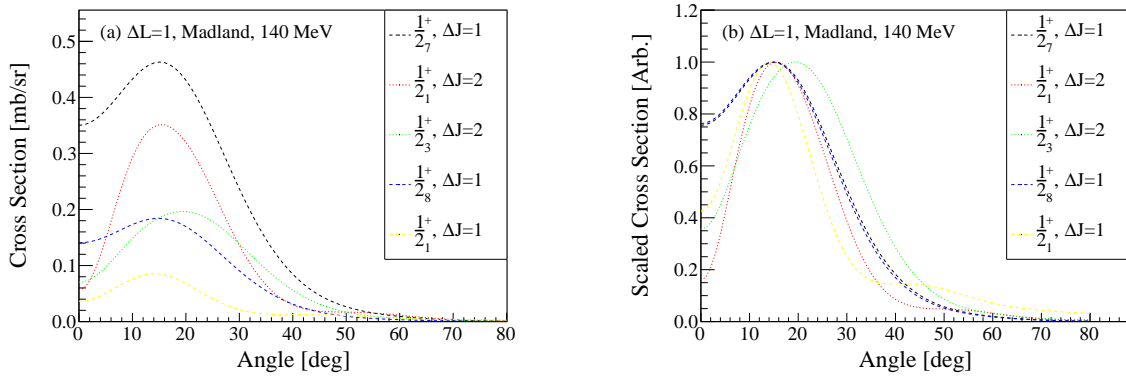
Figure 4.4: (a) DWBA $\Delta L = 1$ cross sections. (b) Scaled version of (a).
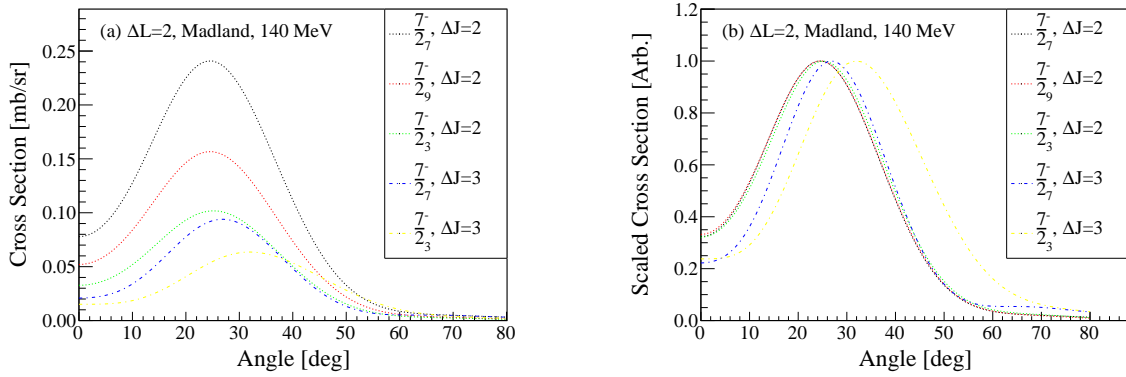
Figure 4.5: (a) DWBA $\Delta L = 2$ cross sections. (b) Scaled version of (a).
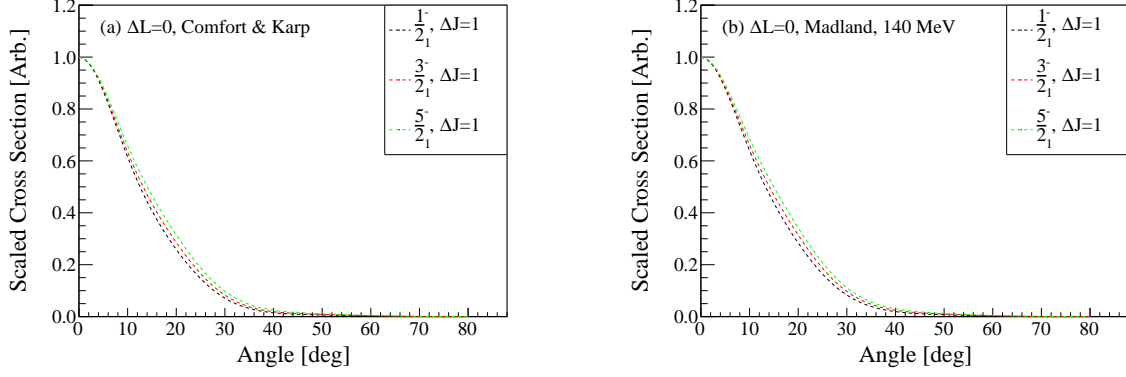
Figure 4.6: (a) Scaled $\Delta L = 0$ cross sections with optical potential parameters from Ref. [104]. (b) Scaled $\Delta L = 0$ cross sections with the original optical potential parameters.
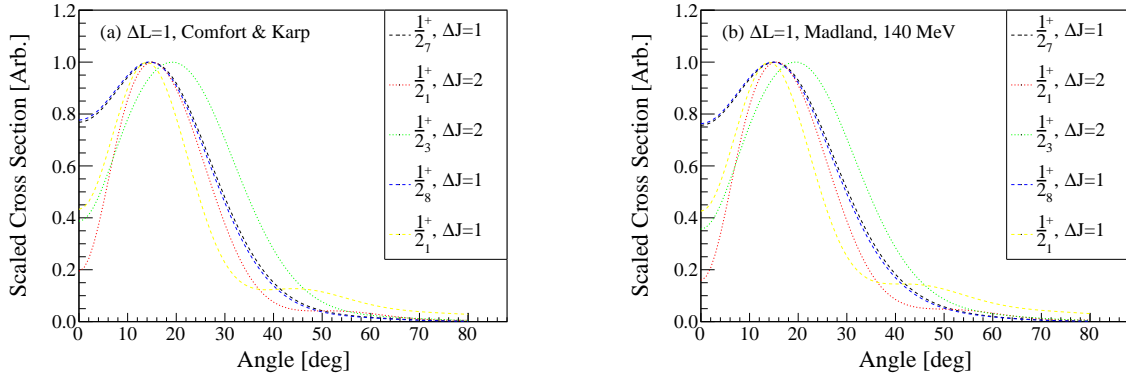
Figure 4.7: (a) Scaled $\Delta L = 1$ cross sections with optical potential parameters from Ref. [104]. (b) Scaled $\Delta L = 1$ cross sections with the original optical potential parameters.
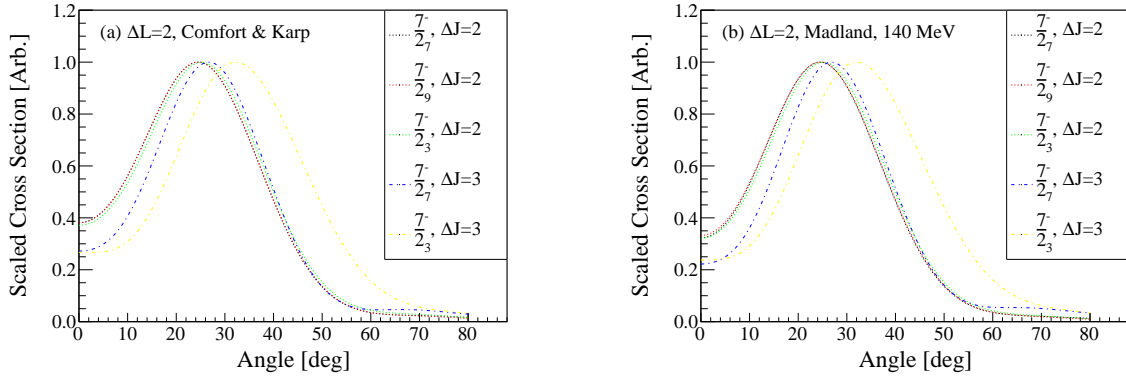
Figure 4.8: (a) Scaled $\Delta L = 2$ cross sections with optical potential parameters from Ref. [104]. (b) Scaled $\Delta L = 2$ cross sections with the original optical potential parameters.

49
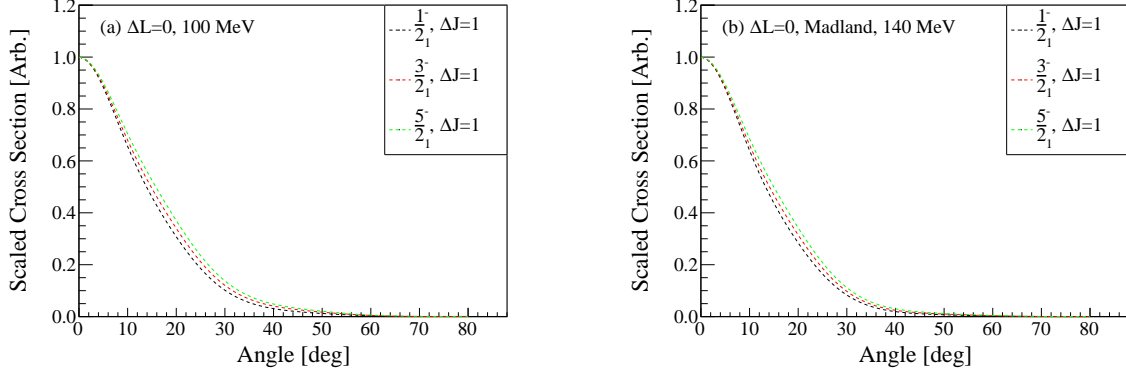
Figure 4.9: (a) Scaled $\Delta L = 0$ cross sections with the 100 MeV NN interaction [103]. (b) Scaled $\Delta L = 0$ cross sections with the original NN interaction.
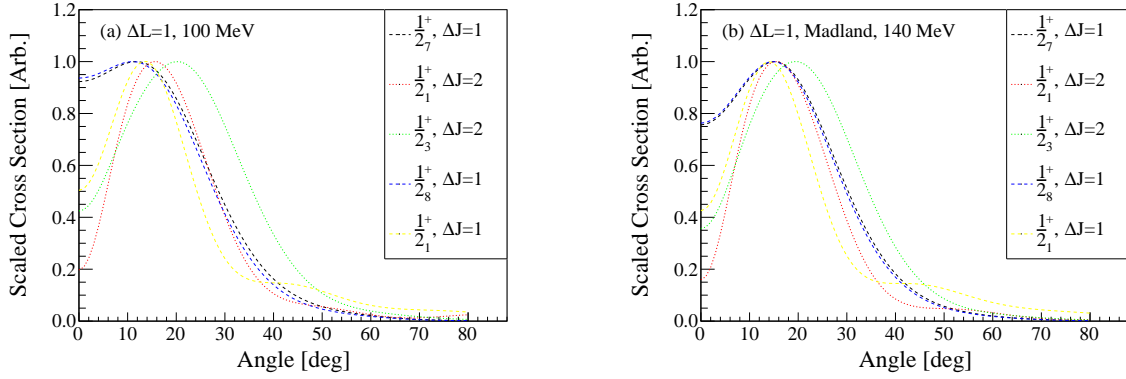
Figure 4.10: (a) Scaled $\Delta L = 1$ cross sections with the 100 MeV NN interaction [103]. (b) Scaled $\Delta L = 1$ cross sections with the original NN interaction.
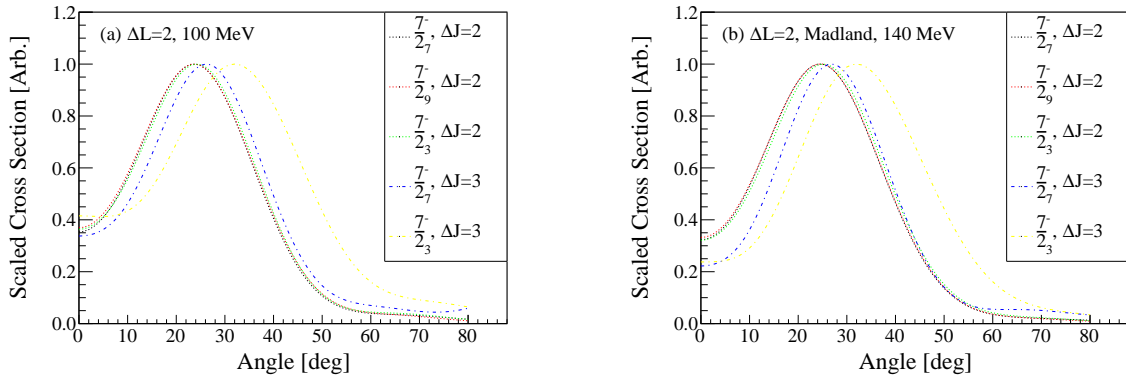
Figure 4.11: (a) Scaled $\Delta L = 2$ cross sections with the 100 MeV NN interaction [103]. (b) Scaled $\Delta L = 2$ cross sections with the original NN interaction.

Chapter 5

Experiment

The goal of this work was to extract the Gamow-Teller transition strength, $B(\text{GT})$, from the $^{11}\text{C}(p,n)^{11}\text{N}$ and $^{12}\text{N}(p,n)^{12}\text{O}$ cross sections. Figure 5.1 shows a diagram of the $^{11}\text{C}(p,n)^{11}\text{N}$ reaction. The experimental method used to measure this reaction was the "missing mass method," where the ejectile excitation energy and center-of-mass scattering angle are calculated from the projectile, target, and recoil momenta. In this experiment, the ^{11}N or ^{12}O excitation energy and center-of-mass scattering angle were reconstructed from the measured neutron energy and angle. This reconstruction is illustrated in Figure 5.2 for $^{11}\text{C}(p,n)^{11}\text{N}$. Then, from the excitation energies and scattering angles, the differential cross sections were determined. This chapter describes the experiment done to measure the cross sections.

The experiment (e17018) was run at the National Superconducting Cyclotron Laboratory (NSCL) in November 2018. The rare-isotope beam of ^{11}C and ^{12}N was created at the
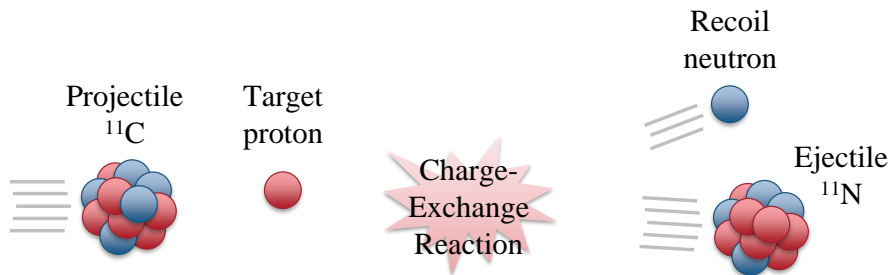
Figure 5.1: Diagram of the charge-exchange reaction $^{11}\text{C}(p,n)^{11}\text{N}$. In the missing mass method, the ejectile momentum is reconstructed from known projectile, target, and recoil momenta.
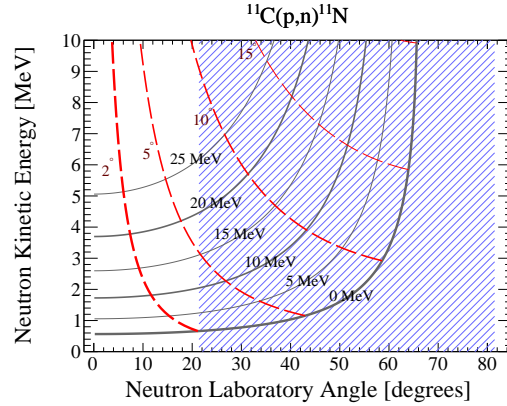
Figure 5.2: Reaction reconstruction for ^{11}C(p,n)^{11}N at about 100 MeV/u. The solid black lines are lines of constant ^{11}N excitation energy, and the dashed red lines are lines of constant center-of-mass scattering angle. The blue shaded region is the region covered by LENDA.

Coupled Cyclotron Facility (CCF) via projectile fragmentation, explained in Section 5.1. The beam impinged on the Ursinus liquid hydrogen target, which is described in Section 5.2. The heavy residual nuclei were detected and identified by the S800 Spectrograph, and the S800 is described in Section 5.3. Neutrons were detected by the Low Energy Neutron Detector Array (LENDA), Section 5.4. Last, an overview of the data acquisition system is given in Section 5.5.

5.1   Beam Production

The rare-isotope cocktail beam of ^{11}C and ^{12}N was created via projectile fragmentation, as illustrated in Figure 5.3. In projectile fragmentation, a primary stable beam is accelerated to an intermediate energy and impinged on a production target. The stable beam is fragmented into a variety of smaller species, including rare isotopes. The rare isotopes of interest are usually separated out by a fragment separator to create the secondary beam desired for the experiment.

In this experiment, an ^{16}O primary beam was created via the electron cyclotron resonance
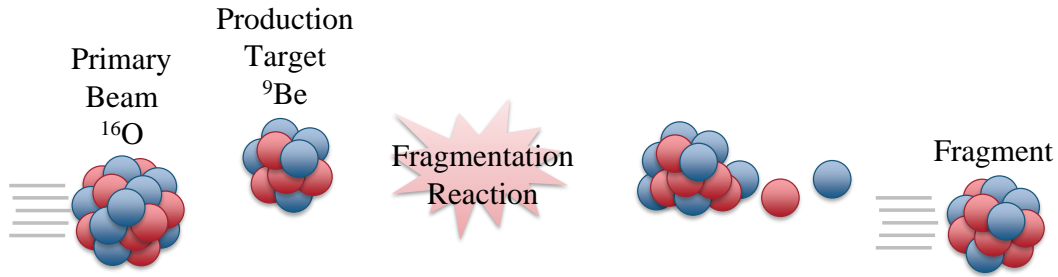
Figure 5.3: Diagram of the fragmentation reaction used to produce the rare-isotope beam in this experiment. An ^{16}O primary beam impinged on a ^{9}Be production target to create a secondary beam of ^{11}C and ^{12}N.
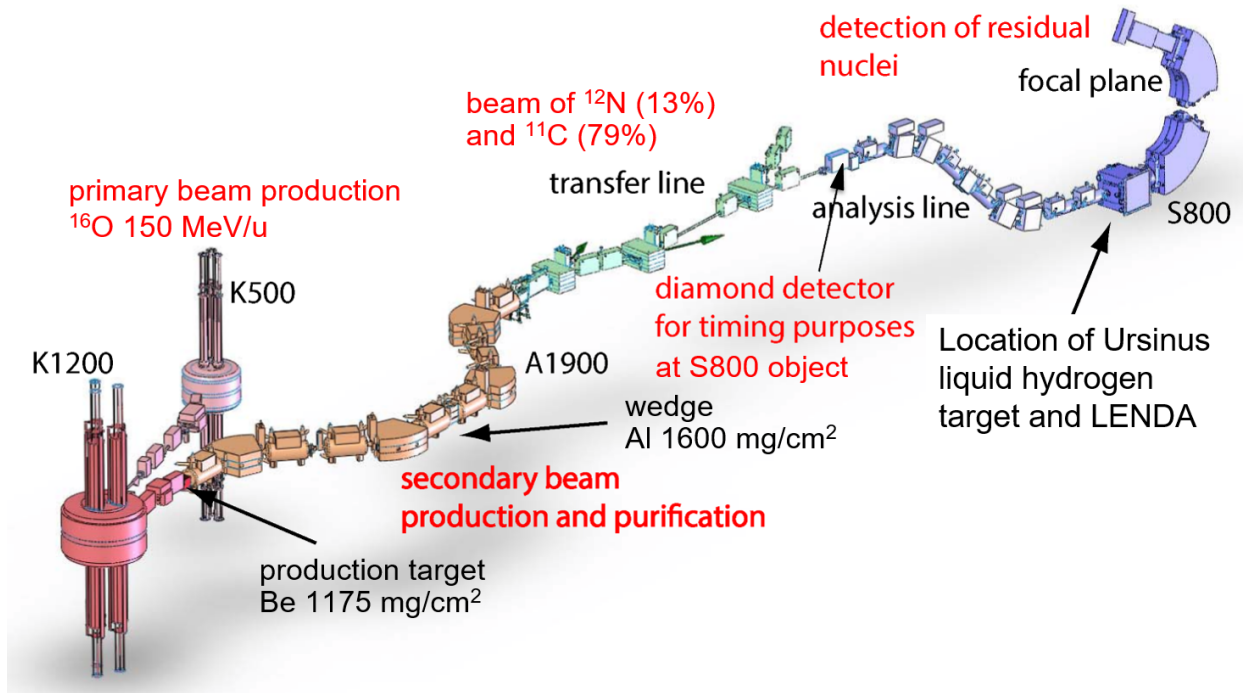
Figure 5.4: E17018 at the National Superconducting Cyclotron Laboratory (NSCL). See text for details. (The Ursinus liquid hydrogen target and the Low Energy Neutron Detector Array (LENDA) are not shown.)

Table 5.1: Beam rates for each rigidity setting. The beam rate was measured by the S800 object detector and corrected to get the absolute beam rate. The beam rate uncertainty is about 8%.

Rigidity Setting [Tm]	Measured Beam Rate [Hz]	Absolute Beam Rate [Hz]
2.3290	3.7e+06	4.9e+06
2.4900	2.8e+06	3.7e+06
2.8000	2.5e+06	3.2e+06
3.0000	4.1e+06	5.5e+06
2.5915	2.5e+03	3.1e+03

(ECR) method by the Superconducting Source for Ions (SuSI) [105]. Then it was accelerated to 150 MeV/u by the K500 and K1200 coupled cyclotrons [106]. Next, the primary beam impinged on a 1175 mg/cm^2 beryllium production target. The entire beamline for e17018 is illustrated in Figure 5.4.

The secondary rare-isotope beam was purified by the A1900 fragment separator [107] with a 1600 mg/cm^2 aluminum wedge and a 0.5% momentum acceptance. The resulting secondary beam was a cocktail beam of 78% ^{11}C, 14% ^{12}N, 7% ^{10}B, and <1% ^{13}O. The beam rates measured at the A1900 focal plane at the beginning of the experiment were 41,600 $\frac{\text{pps}}{\text{pnA} \, ^{16}\text{O}}$ for ^{11}C and 4,910 $\frac{\text{pps}}{\text{pnA} \, ^{16}\text{O}}$ for ^{12}N (A1900 Run 7795).

The beam rate was measured during the experiment by the S800 object detector. The raw measured rates and the corrected absolute rates are given in Table 5.1. A plastic scintillator is usually used at the S800 object, however, the rates in this experiment were too high to use plastic. In experiment e10003 [94], the plastic object scintillator suffered significant radiation damage from an incident beam rate of 2-3 MHz of ^{16}C. Therefore, a diamond detector [108] was used at the S800 object instead.

Each beam particle was identified according to the time difference between the particle's S800 object detector signal and the nearest RF signal. Because all beam particles have the same momentum coming out of the A1900, different species have different velocities.
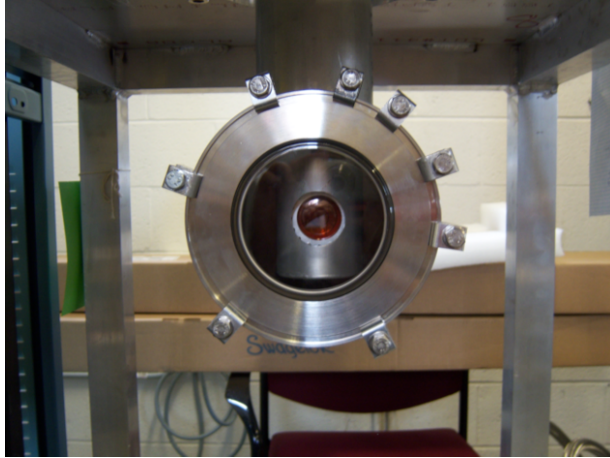
Figure 5.5: Ursinus liquid hydrogen target. The orange circle in the center is the Kapton foil.

With different velocities, they take different amounts of time to travel the same distance. Therefore the time to reach the S800 object relative to the RF signal was used to identify beam particles.

5.2 Liquid Hydrogen Target

The secondary beam was sent to the S3 experimental vault and impinged on the Ursinus liquid hydrogen target, where the (p,n) reaction took place. A photo of the target is shown in Figure 5.5. The liquid hydrogen is contained by two Kapton foils, each 125 μm thick. Kapton is a polyimide (a type of polymer) film that can withstand extreme temperatures [109]. The target has a radius of 3.5 cm and a thickness of 7 mm. (The foils actually bulge outwards when the target is full of liquid, so the thickness is slightly more than 7 mm. This will be discussed later in Section 7.4.) The liquid hydrogen had a temperature of about 16 K and a pressure of about 830 torr. The hydrogen areal density was 50.9(2) mg/cm^2.

A liquid target has important advantages compared to solid and gas targets. Plastic foils such as polyethylene $(CH_2)_n$ suffer from significant C background. The only background from

a liquid target is that from the foils containing the liquid. These foils are very thin, so their background contribution is negligible. Gas targets, while background-free, cannot be made as dense as solid and liquid targets. Therefore a liquid target results in a higher luminosity without the C background. A denser target does have the disadvantage of more energy straggling, and therefore a worse beam energy resolution. However, in this experiment, the energy straggling (0.08%) was small compared to the beam spread (0.3%).

5.3   S800 Spectrograph

After a reaction occurred in the target, the heavy residual nucleus went to the S800 Spectrograph [110]. The S800 consists of two quadrupoles and a sextupole for beam focusing and two dipoles for spectroscopy.

The S800 can be run in two modes: focus mode or dispersion-matching mode. In focus mode, the beam is focused at the target, and in dispersion-matching mode, the beam is dispersed at the target. In this experiment, it was important to have the beam focused on the target for two reasons. First, if the beam was not focused, then the beam spot could have been too large for the liquid hydrogen target. Second, a small beam spot on the target was necessary to accurately determine the neutron angle. The S800 also has better momentum acceptance in focus mode than in dispersion-matching mode. The energy resolution in the S800 is worse in focus mode, but that was not important for this experiment because the S800 was not used to reconstruct the reaction. Detailed descriptions of each mode can be found in Ref. [111].

The reactions of interest were ^{11}C$(p,n)^{11}$N and ^{12}N$(p,n)^{12}$O, however, ^{11}N and ^{12}O are unbound. They immediately decay by particle emission, so the S800 measured their decay

Table 5.2: S800 magnetic-rigidity settings.

Rigidity Setting [Tm]	Reaction+Decay Channel
2.3290	$^{11}\text{C}(p,n)^{11}\text{N} \rightarrow {}^{10}\text{C}+p$
2.4900	$^{12}\text{N}(p,n)^{12}\text{O} \rightarrow {}^{10}\text{C}+2p$
2.8000	$^{11}\text{C}(p,n)^{11}\text{N} \rightarrow 2\alpha+3p$
3.0000	$^{12}\text{N}(p,n)^{12}\text{O} \rightarrow 2\alpha+4p$
2.5915	^{11}C and ^{12}N (Unreacted beam)

products, not ^{11}N and ^{12}O themselves. ^{11}N decays by one-proton emission to $^{10}\text{C}+p$. If the ^{10}C is created in an excited state above 3.354 MeV, then it further decays to $2\alpha+2p$. ^{12}O decays by two-proton emission to $^{10}\text{C}+2p$. Again, the ^{10}C will either survive or decay to $2\alpha+2p$ depending on its excitation energy. Therefore the S800 was tuned to detect both ^{10}C and α particles for each reaction. The rigidity settings of the S800 for each decay channel are shown in Table 5.2. (Rigidity is a measure of a particle's momentum and charge, or how much the particle's trajectory will be bent by a magnetic field.)

A suite of detectors measured the residual nuclei at the focal plane of the S800, and these detectors are illustrated in Figure 5.6. The cathode readout drift chambers (CRDCs), described in Section 5.3.1, measured the positions and angles of the residual nuclei. The ionization chamber, Section 5.3.2, measured the energy losses. The focal-plane scintillator, Section 5.3.3, measured the times, and the hodoscope, Section 5.3.4, measured the total energies of the residual nuclei after passing through all of the other detectors.

5.3.1 Cathode Readout Drift Chambers (CRDCs)

The cathode readout drift chambers (CRDCs) measured the position of the residual nucleus at two points along the beam path. CRDC1 was located at the focal plane of the spectrograph, and CRDC2 was 1.061 m downstream. The positions measured by the CRDCs were used for various corrections to the data.
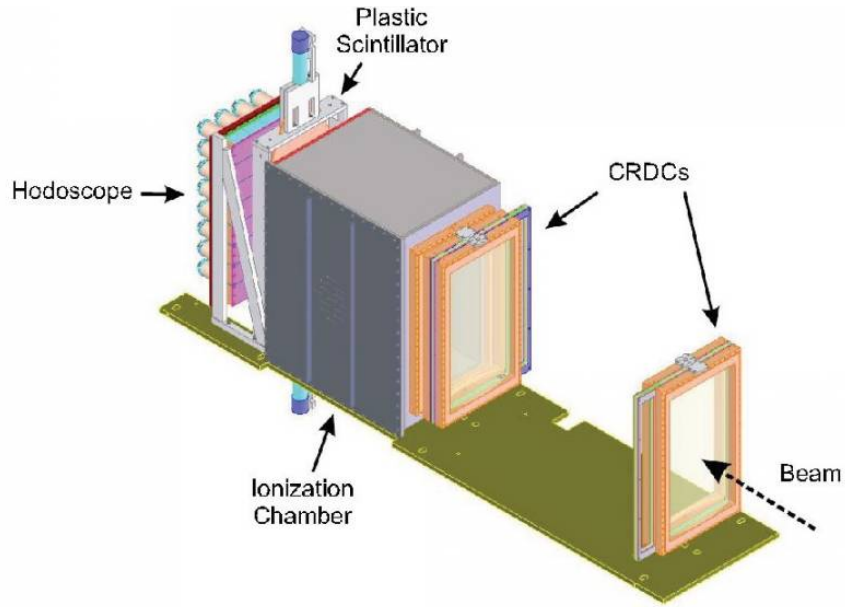
Figure 5.6: Diagram of the S800 focal-plane detectors, taken from Ref. [111]. The cathode readout drift chambers (CRDCs) measured the position and angle, the ionization chamber measured the energy loss, the plastic scintillator measured the time, and the hodoscope measured the remaining energy of each residual nucleus.
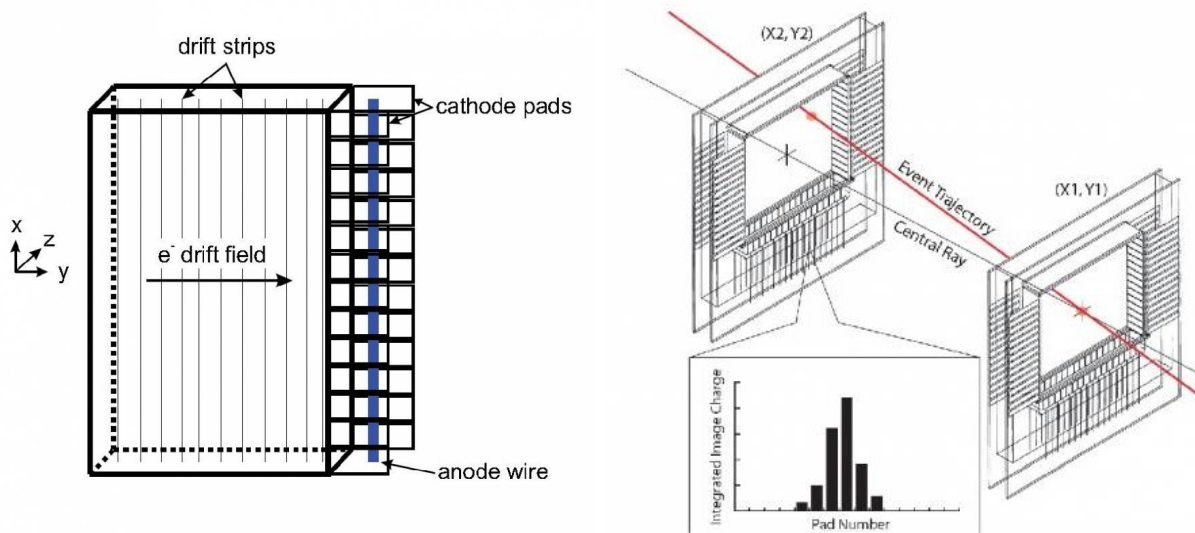
Figure 5.7: (Left) Illustration of the S800 CRDCs principle of operation, taken from Ref. [111]. See text for details. (Right) Diagram of position and angle reconstruction by the S800 CRDCs, taken from Ref. [111].

The principle of operation of the CRDCs is illustrated in Figure 5.7 (Left). Each chamber was filled with 80% CF_4 and 20% C_4H_{10} gasses at about 40 torr. An electric field was applied across the chamber in the y-direction. When an ion passed through the chamber, the gas was ionized, and the freed electrons drifted to the anode wire and created a signal in the cathode pads. The anode voltages were 970 V for CRDC1 and 1000 V for CRDC2 for the ^{10}C rigidity settings, and 1070 V for both CRDCs for the α-particle rigidity settings. For more information about the CRDCs, see Ref. [111].

The CRDC x-position (position in the dispersive direction) was calculated from the distribution of charge on the pads. The y-position (position in the non-dispersive direction) was calculated from the electrons' drift time, where the reference time was provided by the *E1 up* signal (top PMT of S800 focal-plane scintillator). Then the angles were reconstructed from the positions in the two CRDCs as shown in Figure 5.7 (Right).

5.3.2 S800 Ionization Chamber

The ionization chamber measured the energy loss of the residual nucleus, which was used for particle identification.

An ionization chamber is a chamber filled with a gas that has electrodes on either side that create a uniform electric field. When a charged particle passes through the chamber, it ionizes the gas, and the newly created free electrons and positive ions drift to the anode and cathode where they create a signal. The number of ion pairs, and hence the signal size, is proportional to the energy loss of the particle. The energy loss is proportional to the squared charge of the particle for a fixed energy, so the proton number Z of fully stripped ions can be deduced from the energy loss. For more information about ionization chambers, see Ref. [112].

The S800 ionization chamber consists of 16 stacked ionization chambers filled with P10 gas at about 300 torr. The anode voltage was set to 200 V for this experiment. For more information about the S800 ionization chamber, see Ref. [111].

5.3.3   S800 Focal-Plane Scintillator

The S800 focal-plane scintillator is a plastic scintillator that measured the time of the residual nucleus. The top photomultiplier tube (PMT), called *E1 up*, provided the reference time for each event in the experiment, i.e., the S800 object, the RF, and the LENDA times-of-flight were all measured relative to *E1 up*. The object and RF times-of-flight were used for beam-particle and reaction-product identification. The LENDA time-of-flight was used to calculate the energy of the neutron.

A plastic scintillator is a solid solution of a fluorescent molecule dissolved in plastic. When a charged particle passes through a plastic scintillator, it excites the fluorescent molecules. The fluorescent molecules promptly de-excite and emit visible photons. A plastic scintillator is usually coupled to a photomultiplier tube (PMT), which is a device that converts the emitted photons into an electronic signal that can be recorded and analyzed. The excitation occurs in less than a nanosecond, and the de-excitation occurs with a half-life on the order of a few nanoseconds. The resulting fast signal makes plastic scintillators ideal for timing measurements. For more information about plastic scintillators and PMTs, see Ref. [112].

The S800 focal-plane scintillator, called *E1*, is a 5-mm-thick BC-400 or BC-404 plastic scintillator read out by an EMI 98807B PMT on each end. Both PMTs were set to 1480 V for the ^{10}C rigidity settings and to 1710 V for the α-particle rigidity settings. The scintillator's timing resolution is about 100 ps for a point-like beam spot in the focal plane, and about 1 ns
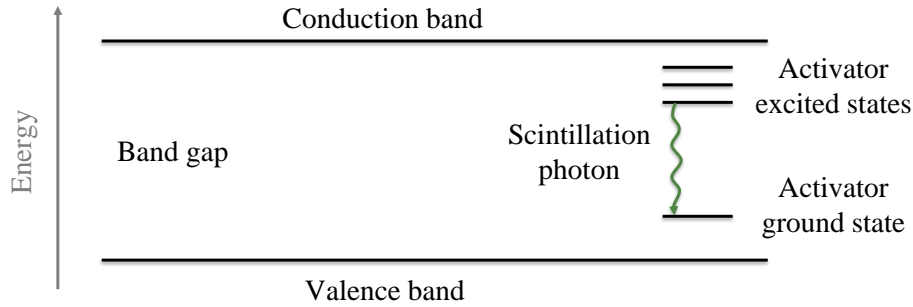
Figure 5.8: Illustration of the energy band structure of an inorganic scintillator with an activator, adapted from Ref. [112]. The scintillation photon comes from the de-excitation of an electron through the activator states.

when the whole focal plane is illuminated. For more information about the S800 focal-plane scintillator, see Ref. [111].

5.3.4 S800 Hodoscope

The hodoscope is an array of scintillators that measured the total energy of the residual nuclei after they passed through the other focal-plane detectors. The hodoscope multiplicity and energy were used for particle identification in the α-particle rigidity settings.

The S800 hodoscope is an array of CsI(Na) detectors. A CsI(Na) detector is an inorganic CsI crystal with Na activators. An inorganic crystal lattice only allows electrons in certain energy ranges: the valence (low-energy) band and the conduction (high-energy) band. There is a gap between these two energy bands, called the band gap, where electrons are not allowed. However, if a small amount of an impurity, called an activator, is added to the crystal lattice, then discrete allowed states appear in the band gap near each activator. This energy band structure is illustrated in Figure 5.8.

When a charged particle passes through an inorganic crystal with activators, electrons in the crystal are excited from the valence band to the conduction band. This leaves holes in the valence band, which quickly travel to activator sites and ionize them. Then electrons in

61

the conduction band migrate through the crystal until they encounter an ionized activator, where they de-excite via the excited states in the band gap. A visible photon is emitted, and it travels through the material to a PMT, where it is converted to an electronic signal. The inorganic crystal scintillation process is slower than that of plastic scintillators but yields more photons. Therefore, due to their higher light yields, inorganic scintillators are generally better for energy measurements. For more information about inorganic scintillators, see Ref. [112].

The S800 hodoscope consists of an 8×4 array of CsI(Na) scintillators. These scintillators are 5.1 cm thick, which is thick enough to completely stop any residual nuclei. The scintillators are each coupled to one Hamamatsu R1307 PMT. All PMTs were set to 330 V for both the ^{10}C and α-particle rigidity settings. For more about the S800 hodoscope, see Ref. [111].

5.4   LENDA

The Low Energy Neutron Detector Array (LENDA) [113, 114] measured both the position and time-of-flight of the neutron. The neutron angle was calculated from the LENDA bar position relative to the target, and the neutron energy was calculated from its time-of-flight and flight distance from the target to the detector.

LENDA is an array of plastic scintillation detectors. As previously discussed, plastic scintillators have a very good timing resolution, which is crucial for neutron time-of-flight measurements such as this experiment.

Additionally, plastic is good for measuring neutrons because it has a high hydrogen content. When a neutron passes through the detector, it scatters off and transfers momentum to a nucleus in the detector material. The energy of that recoil nucleus is proportional to the

number of fluorescent molecules that it excites and hence the number of scintillation photons produced. Therefore the size of the signal is maximized when the recoil nucleus energy is maximized. According to two-body kinematics, a neutron can transfer more energy to light nuclei than to heavy nuclei, so an incident neutron can transfer the most energy to hydrogen, the lightest nucleus. Due to its high hydrogen content, plastic yields large signals and is an ideal material for neutron detection. For more about plastic proton recoil scintillators for neutron detection, see Ref. [112].

LENDA is an array of 24 detectors, each consisting of a 2.5×4.5×30 cm BC-408 plastic scintillator coupled to a Hamamatsu H6410 PMT on each end. The plastic scintillator is wrapped in several layers:

1. Inner layer: filter paper

2. Middle layer: aluminum foil

3. Outer layer: black electrical tape

The filter paper and aluminum foil reflect any escaped photons back into the scintillator, and the black electrical tape blocks all ambient photons from entering the scintillator and creating noise.

Figure 5.9 shows LENDA set up for the experiment. The LENDA bars were positioned about 1 m from the target in the angle range $\theta_{LENDA} \approx 21° - 81°$, where θ_{LENDA} is the azimuthal angle with the beam line as the z-axis. The angles were selected based on the reaction kinematics (Figure 5.2), and the distance was selected to balance angular resolution with geometrical efficiency. The LENDA bars were slightly separated to minimize multiple scattering.
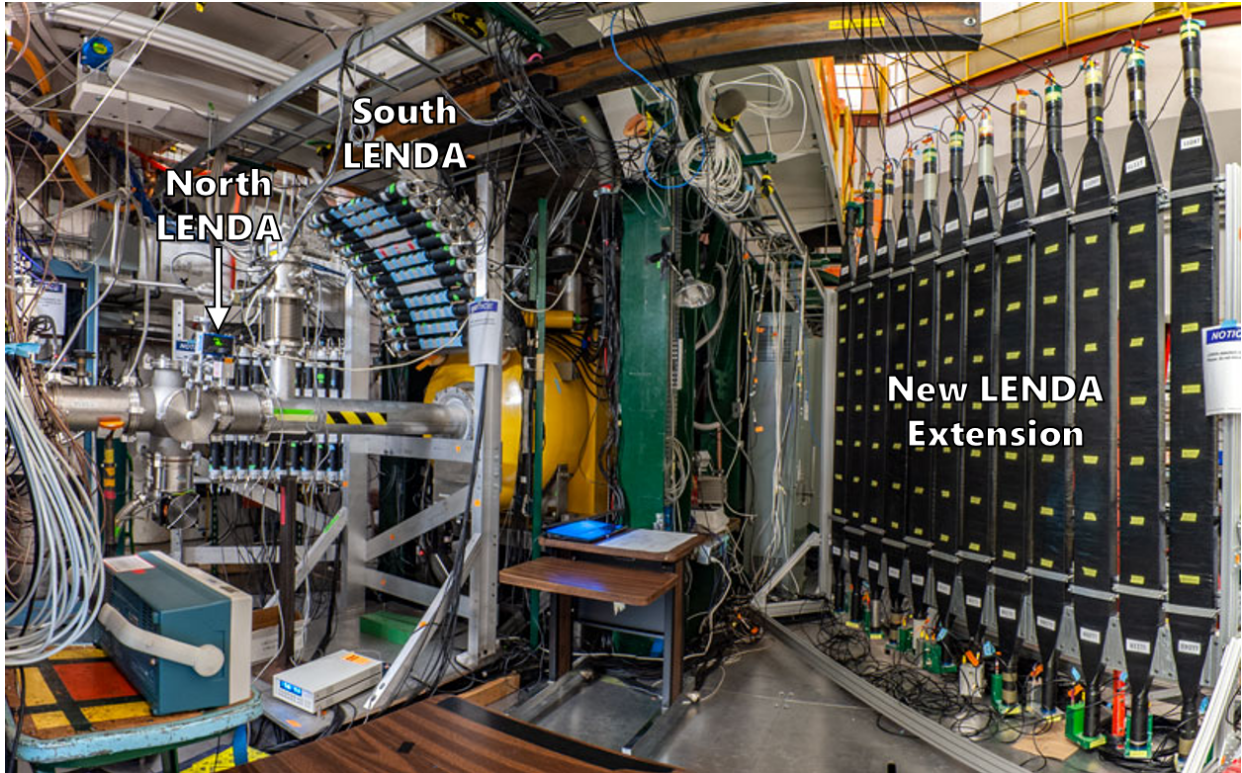
Figure 5.9: E17018 experimental setup [Photo credit: S. Noji]. The beam enters from the left. North LENDA was placed to the left of the beamline (from the beam's point of view), and South LENDA was placed above the beamline. The new LENDA extension was placed to the right of the beamline; see Chapter 10 for information about these detectors.

North LENDA was placed to the left of the beamline (from the beam's point of view), and South LENDA was placed above the beamline. The detectors were originally named according to which side of the beamline they would be on, north or south, but it was not possible to position the arrays according to their assigned cardinal directions in this experiment. Due to constraints from the South LENDA frame, the North LENDA array was shifted backwards relative to South LENDA. This resulted in three holes in LENDA's forward angle coverage. One of the North LENDA bars (NL12) was placed to the right of the beamline at a farther distance to cover one of those holes.

5.5 Data Acquisition System

The purpose of the data acquisition system (DAQ) was to find coincidences between LENDA and the S800 focal plane, and an electronics diagram is shown in Figure 5.10. The S800 DAQ is described in detail in Ref. [111]. The LENDA PMT signals were sent to XIA 14-bit 250 MHz Pixie 16 digital pulse processors [115]. The *E1 up* signal served as the reference channel for all other channels in each Pixie module. For details about LENDA digital pulse processing, see Ref. [114].

The Pixie-16 modules were each connected to a Har-Link–to–LEMO module, also known as a breakout module. The Har-Link–to–LEMO module provided an *or* gate between all Pixie channels in output *o7*. Then an *or* gate between all *o7* signals was created via NIM logic modules and sent to the S800 DAQ. This signal is the *Secondary Raw Trigger*, essentially the LENDA trigger. The S800 Universal Logic Module (ULM) trigger electronics looked for coincidences between the *Secondary Raw Trigger* and *E1 up*. When it found a coincidence, it created the *Master Live* signal, essentially the S800-LENDA coincidence signal. The *Master Live* signal served as the external trigger to let the LENDA digital data acquisition system (DDAS) know that a coincidence took place (*i4*).

In addition to the *Master Live* signal, the S800 DAQ sent two other signals to the LENDA Har-Link–to–LEMO modules. First, the *S800 Clock* served as the LENDA DDAS external clock so that LENDA used the same clock as the S800 (*i3*). Second, the *IMP SYNC* signal synchronized the S800 and LENDA DAQs (*i7*).

Various signals, labeled "PP" in Figure 5.10, were patched to Data-U6 from the S3 vault for diagnostic purposes. These included the *Secondary Raw Trigger*, the delayed fast trigger

of the first channel in each module ($o0$), the external trigger gate ($o3$), and the LENDA top/bottom coincidence gate ($o4$).
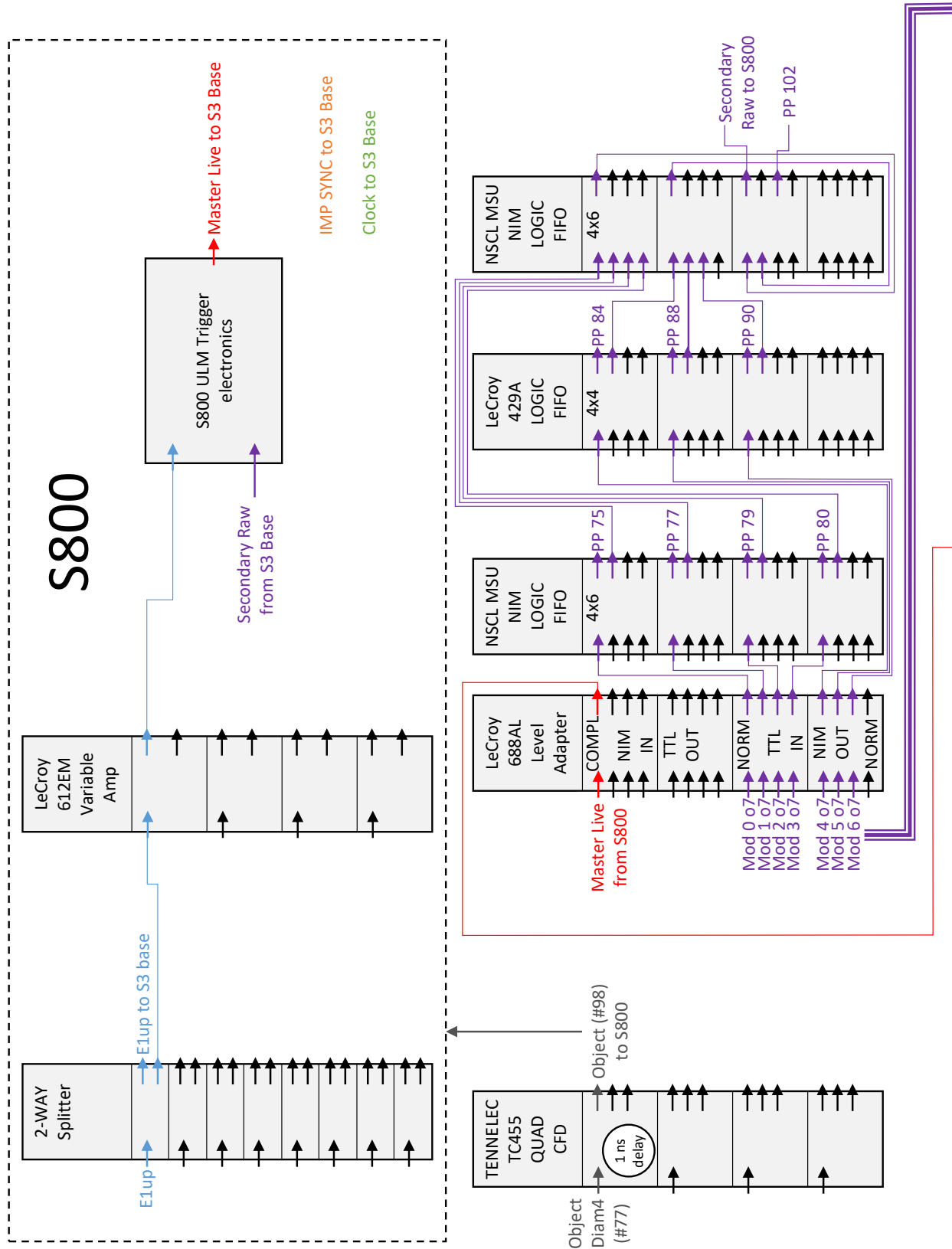
Figure 5.10: E17018 LENDA DAQ electronics diagram. See text for details.
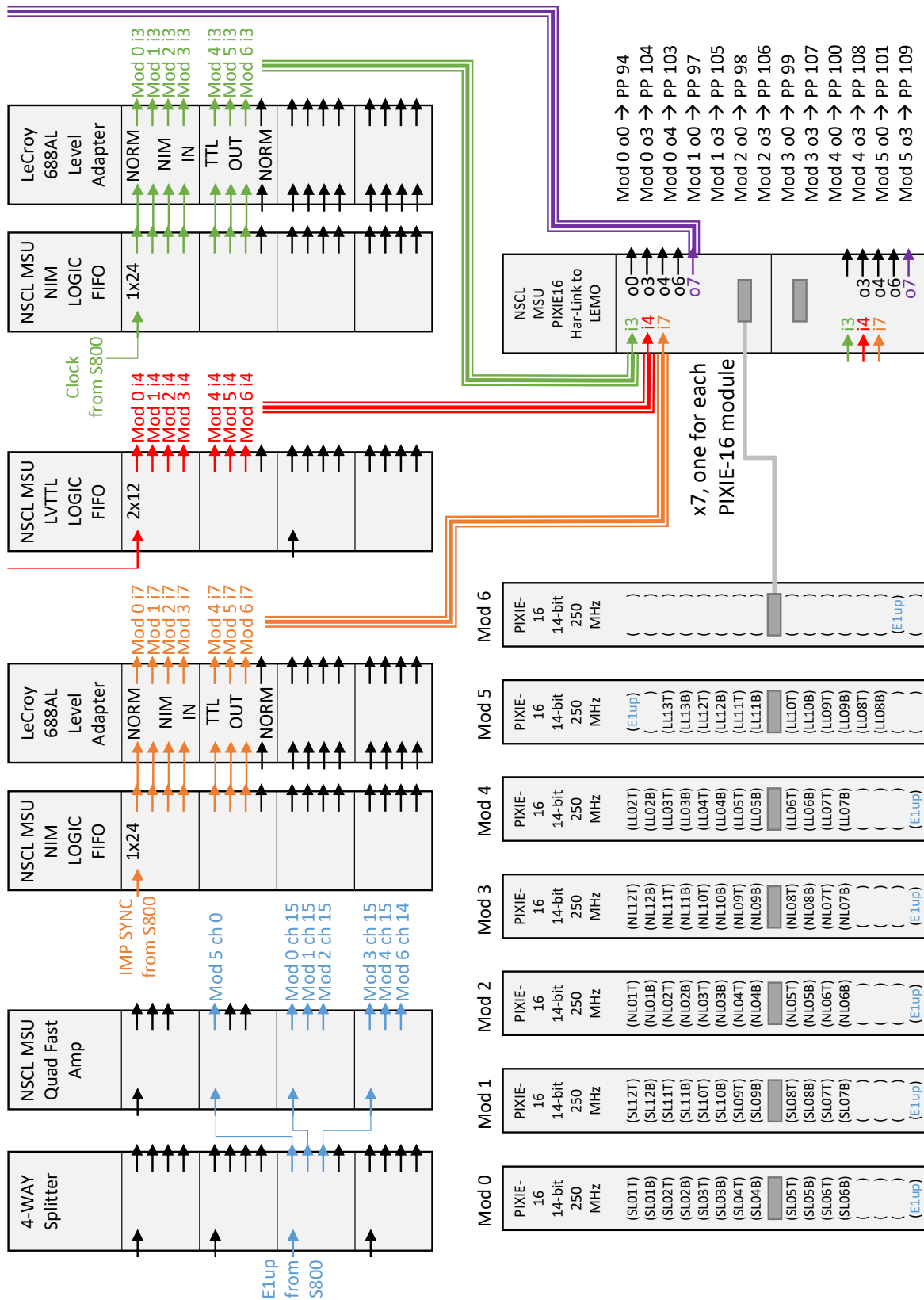
Figure 5.10 (cont'd)

Chapter 6

Data Analysis I

In this chapter, the quantities necessary for the missing mass calculation are extracted from the raw experimental data. Recall that in the missing mass method, the ejectile (reaction product, ^{11}N or ^{12}O) excitation energy and center-of-mass scattering angle are calculated from the known projectile (beam particle, ^{11}C or ^{12}N), target (proton), and recoil (neutron) momenta (Figure 5.1). The missing mass calculation ingredients are:

- beam identity and energy (Section 6.1)

- reaction product identity (Section 6.2)

- neutron angle and time-of-flight (Section 6.3)

To extract these ingredients, the detectors were calibrated, cuts were defined to clean the data, and corrections were applied to eliminate artificial correlations. The analysis was done using the R00TLe analysis code [116], built from the ROOT Data Analysis Framework [117].

6.1   Beam Identity and Energy

This section presents the beam particle identification and the beam energy determination. The beam particle was identified by its time-of-flight to the S800 object relative to the RF signal (Section 6.1.1). The beam energy was determined from the S800 focal-plane position

and angle measured by the CRDCs in the unreacted beam setting. First, the CRDCs were calibrated, and the focal-plane positions and angles were calculated (Section 6.1.2). Then the focal-plane positions and angles were used to reconstruct the energies and angles of the beam particles at the target (Section 6.1.3). Last, the beam particles' energies and angles at the target were used to determine the beam profile (Section 6.1.4) and average energy (Section 6.1.5).

6.1.1 Beam Identification

The secondary beam used for this experiment was a cocktail beam consisting of four species, ^{11}C, ^{12}N, ^{10}B, and ^{13}O, and the beam particle was identified on an event-by-event basis. The A1900 fragment separator selected particles with the same rigidity, so particles with different masses and charges had different velocities as they exited the A1900. As a result, each species took a different amount of time to reach the S800 object detector, so each particle was identified by the time difference between its S800 object signal and the nearest RF signal, TOF_{obj-RF}.

The absolute object time T_{obj} and the absolute RF signal time T_{RF} were not directly measured in the experiment. All times were measured with respect to one reference time T_{ref}, the *E1 up* signal (top PMT of S800 focal-plane scintillator). Therefore TOF_{obj-RF} was calculated from the object time-of-fight TOF_{obj} and the RF time-of-flight TOF_{RF} relative to *E1 up*:

$$TOF_{RF} = T_{RF} - T_{ref} \tag{6.1}$$

$$TOF_{obj} = T_{obj} - T_{ref} \tag{6.2}$$

$$TOF_{obj-RF} = T_{obj} - T_{RF}$$

$$= TOF_{obj} - TOF_{RF} \tag{6.3}$$

TOF_{obj} and TOF_{RF} were corrected on a run-by-run basis for drifts in the detectors' timing throughout the experiment by subtracting an offset ΔTOF_{run}:

$$TOF = TOF - \Delta TOF_{run} \tag{6.4}$$

$$\Delta TOF_{run} = \overline{TOF}_{run} - \overline{TOF}_0 \tag{6.5}$$

where $\overline{TOF}_{run}$ is the mean of the tallest peak during the current run and $\overline{TOF}_0$ is the mean of the tallest peak during the first run. Figure 6.1 shows the TOF spectra before and after the offsets were added. The change was subtle, but the peaks did get narrower. The ranges of good TOF_{RF} and TOF_{obj} were selected by eye, and they are shown in Figure 6.2 for TOF_{RF} and in Figure 6.3 for TOF_{obj}. These gates did not cut any good events, i.e. $\epsilon_{obj-RF} = 100\%$.

The first TOF_{obj} and TOF_{RF} hits that occurred in the selected ranges were used to calculate TOF_{obj-RF}. The result was a few sets of peaks shifted a certain number of RF periods from each other, shown in Figure 6.4(a). Each peak corresponds to a different secondary beam particle: the tallest peak in each set is ^{11}C, followed by ^{12}N, and then a small amount of ^{10}B and ^{13}O contamination. The beam-identification gates were determined by eye. The efficiency of the beam-identification gates was determined by fitting each peak to a Gaussian curve and taking the ratio of the area under the curve inside the gate A_{inside}
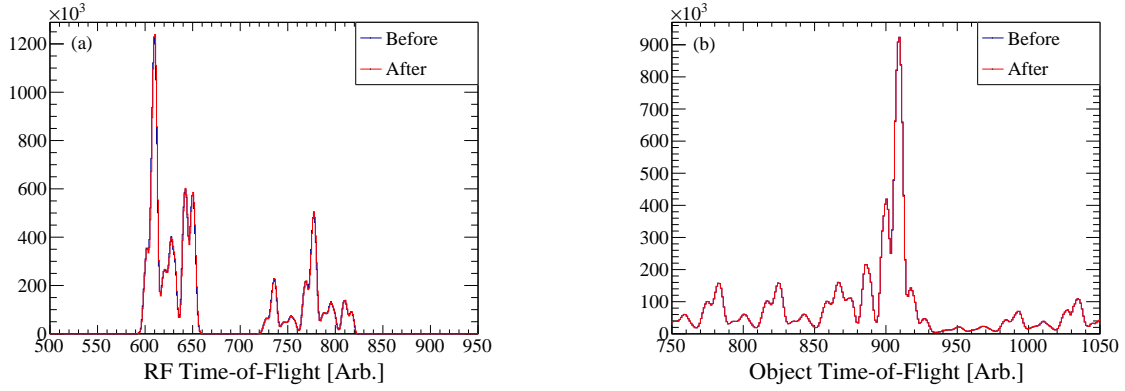
Figure 6.1: (a) RF and (b) S800 object time-of-flight spectra before and after the offset correction.
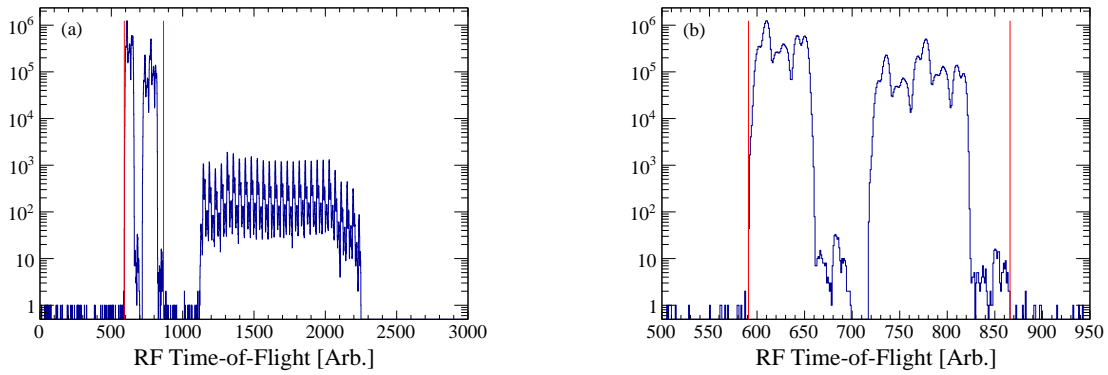
Figure 6.2: (a) RF time-of-flight spectrum. The red lines indicate the range of good events. (b) Zoomed-in version of (a).
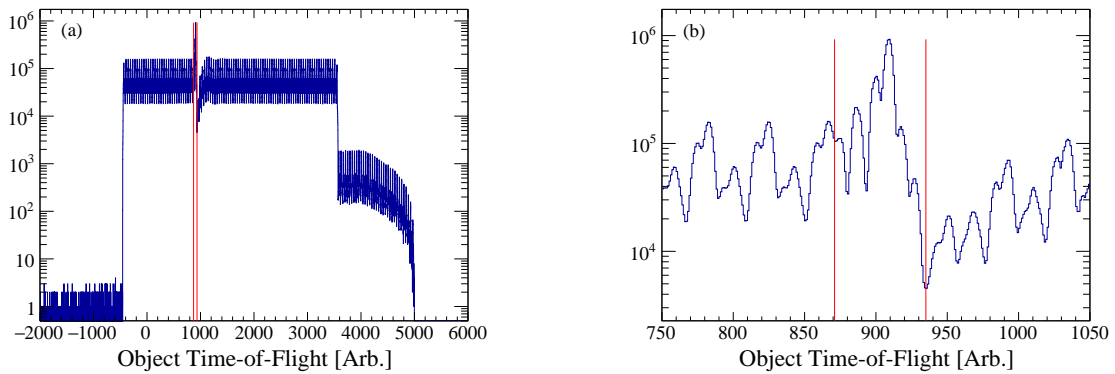
Figure 6.3: (a) S800 object time-of-flight spectrum. The red lines indicate the range of good events. (b) Zoomed-in version of (a).
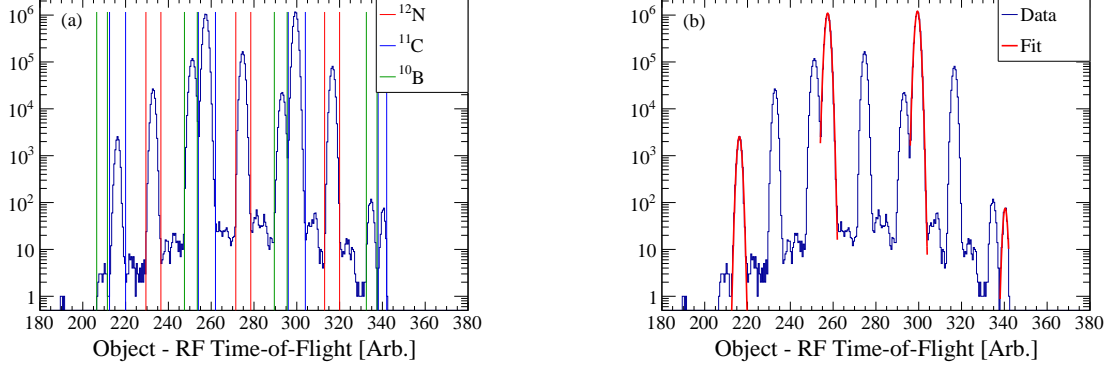
Figure 6.4: (a) TOF_{obj-RF} spectrum used for beam-particle identification. Red, blue, and green lines indicate the beam-identification gates for ^{12}N, ^{11}C, and ^{10}B, respectively. (b) Same spectrum as (a), but the red lines are the fits used to determine the ^{11}C beam-identification gate efficiency.

Table 6.1: Beam identification gate efficiencies, ϵ_{beamID}.

Rigidity [Tm]	Beam	ϵ_{beamID}
2.3290	^{11}C	99.9866 %
2.4900	^{12}N	99.9991 %
2.8000	^{11}C	99.9745 %
3.0000	^{12}N	99.9986 %

to the total area under the curve A_{total}:

$$\epsilon_{beamID} = \frac{A_{inside}}{A_{total}} \tag{6.6}$$

The fits for ^{11}C are shown in Figure 6.4(b), and the resulting efficiencies are shown in Table 6.1. Virtually all good counts were accepted.

6.1.2 S800 CRDCs Calibrations

The CRDCs measured the position of the particle at two different locations at the end of the S800 Spectrograph. The CRDC positions were used to calculate the focal-plane parameters. First, the CRDC energies and positions were calibrated (Sections 6.1.2.1 and 6.1.2.2). Then

focal-plane parameters were calculated from the CRDC positions (Section 6.1.2.3). Finally, the CRDCs' efficiency was determined (Section 6.1.2.4).

6.1.2.1 CRDCs Energy Calibration

The signal from each CRDC pad was a trace of up to four points called "samples," and the raw pad energy E_{pad} was the average of all the samples. The calibrated pad energies E_{pad}^{cal} were calculated as:

$$E_{pad}^{cal} = slope_{pad}(E_{pad} - pedestal_{pad}) \tag{6.7}$$

where $slope_{pad}$ is the scaling factor between raw energy and calibrated energy and $pedestal_{pad}$ is the raw energy's offset from zero.

The pedestals were measured in a dedicated pedestals run where the CRDC thresholds were set very low so that the pads triggered on noise. The pedestal of each pad was taken as the average pad energy over all events in the pedestals run. The raw and calibrated data from the pedestals run are shown in Figures 6.5 and 6.6 for CRDC1 and CRDC2, respectively.

The slopes were found by gain-matching the average pedestal-corrected energy of each pad $\overline{E}_{pad}$ to the average pedestal-corrected energy of all pads $\overline{E}_{All\ pads}$:

$$slope_{pad} = \frac{\overline{E}_{All\ pads}}{\overline{E}_{pad}} \tag{6.8}$$

The CRDCs' absolute energies were not needed for this analysis, so the average energy was not matched to any physical energy. There was no special run taken to determine the slopes; a regular run near the middle of the experiment was chosen to get the most representative energy calibration for all of the runs. The run was a 2.4900 Tm run, and gates on ^{12}N beam
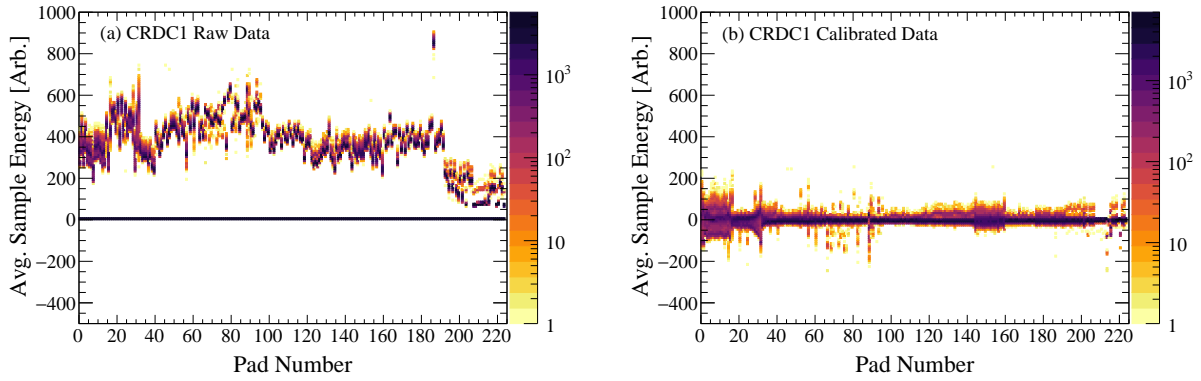
Figure 6.5: CRDC1 pad energies from the pedestals run (a) before and (b) after the pedestals calibration.
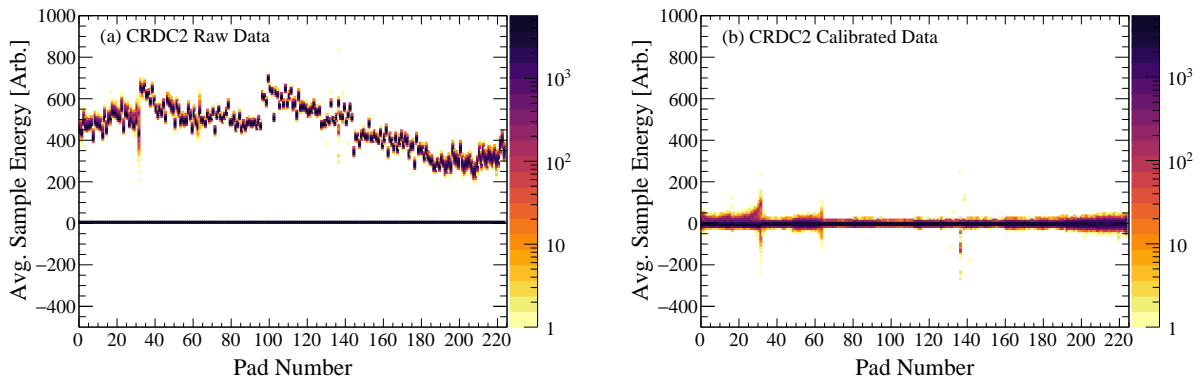
Figure 6.6: CRDC2 pad energies from the pedestals run (a) before and (b) after the pedestals calibration.

particles and ^{10}C reaction products were applied. Note that the blocker was in place for the 2.4900 Tm rigidity setting, so the 2.4300 Tm rigidity setting was used to find the slope of the pads that were blocked (pads 0-35 in CRDC1 and pads 0-20 in CRDC2). Any pads with zero counts were assigned a slope of 1.0. The results are shown in Figures 6.7 and 6.8 for CRDC1 and CRDC2, respectively. The pad gains drifted slightly throughout the experiment, but that effect was neglected. Because the CRDCs were not used to reconstruct the reaction, good position and angle accuracy were not needed for this analysis.

75
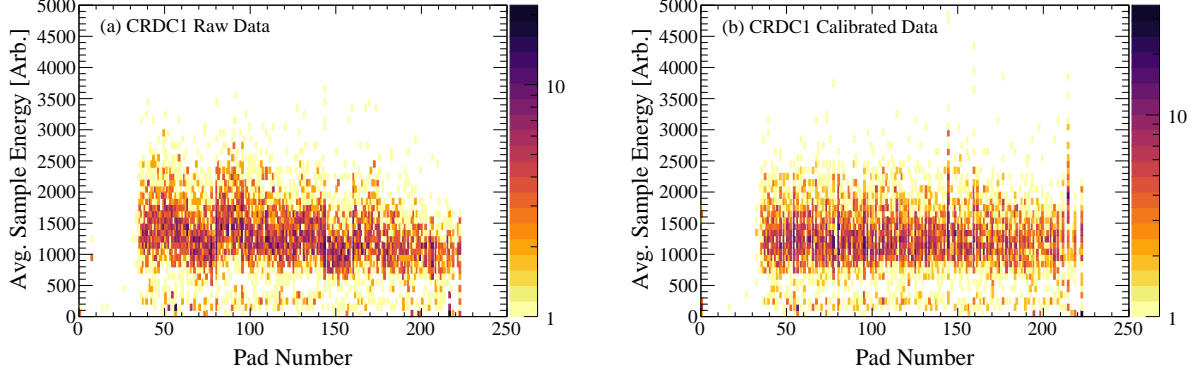
Figure 6.7: CRDC1 pad energies from a 2.4900 Tm run gated on ^{12}N beam particles and ^{10}C reaction products (a) before and (b) after gain matching.
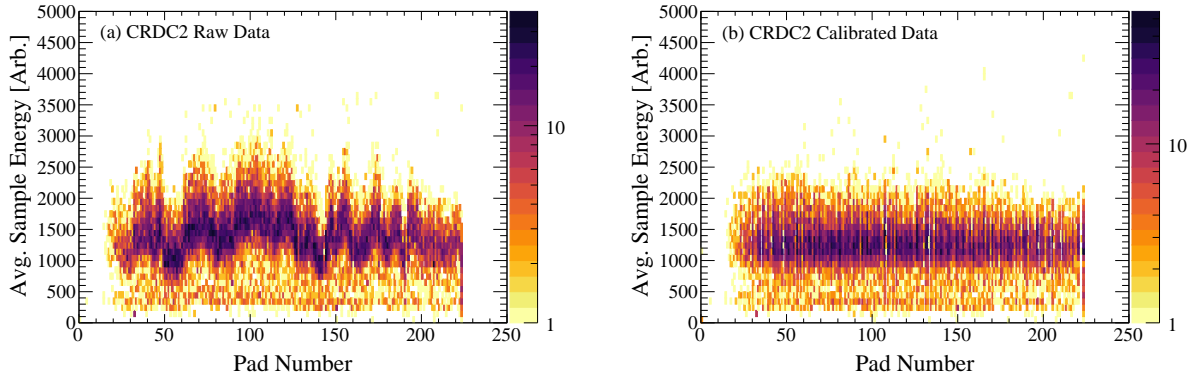
Figure 6.8: CRDC2 pad energies from a 2.4900 Tm run gated on ^{12}N beam particles and ^{10}C reaction products (a) before and (b) after gain matching.

6.1.2.2 CRDCs Position Calibration

The calibrated CRDC positions x_{CRDC} and y_{CRDC} were calculated as:

$$x_{CRDC}[\text{mm}] = 2.54 \left[\frac{\text{mm}}{\text{pad}}\right] \times X_{COG}[\text{pad}] + x_{offset}[\text{mm}] \tag{6.9}$$

$$y_{CRDC}[\text{mm}] = slope_y \left[\frac{\text{mm}}{\text{arb. time unit}}\right] \times TAC[\text{arb. time unit}] + y_{offset}[\text{mm}] \tag{6.10}$$

where units are shown in brackets for clarity. The CRDC x-position was calculated from the pad center-of-gravity X_{COG}, which is the average pad number weighted according to the pad energies. The x-slope was fixed because each pad is 2.54 mm wide. The CRDC
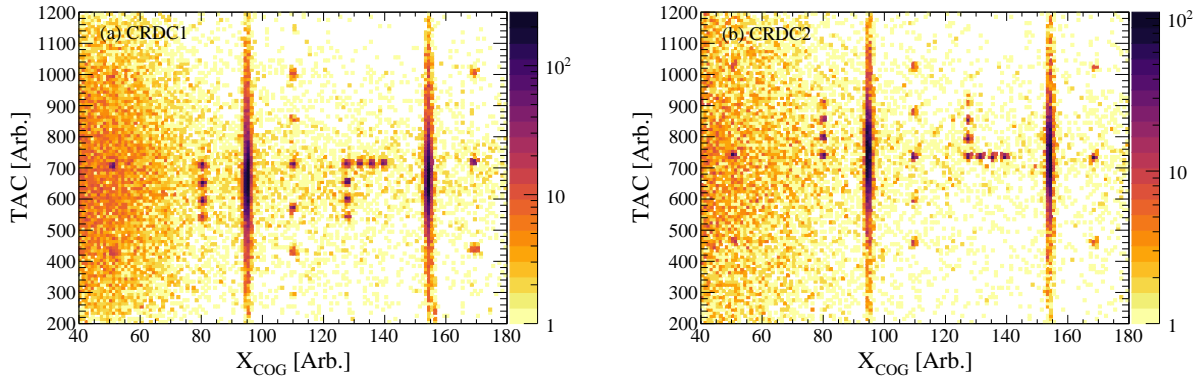
Figure 6.9: CRDC position calibration data from the mask runs for (a) CRDC1 and (b) CRDC2. These mask runs were done before the experiment began, and additional mask runs were done immediately after the experiment began and before it ended.

y-position was calculated from the drift time TAC, which is the time measured by the anode wire minus the reference time measured by $E1\ up$.

Dedicated runs, called mask runs, were taken for each CRDC position calibration. A mask is a metal plate with holes at known locations. In each mask run, a mask was placed over the CRDC being calibrated. The resulting CRDC position spectra have sharp peaks where the mask holes are, as shown in Figure 6.9. The position was calibrated by matching each peak to a known hole position in the mask.

Some CRDC pads have been known to occasionally malfunction, affecting the quality of the X_{COG} measurement. While these so-called "bad pads" could be removed from the analysis, their effect was inconsequential for this experiment again because the CRDCs were not used to reconstruct the reaction. Therefore no bad pads were removed.

The y-slope was corrected for drifts in TAC gains on a run-by-run basis. The average TAC of events gated on the beam particle and reaction product of interest was found for each run. The slope was adjusted such that the average y_{CRDC} did not change from its
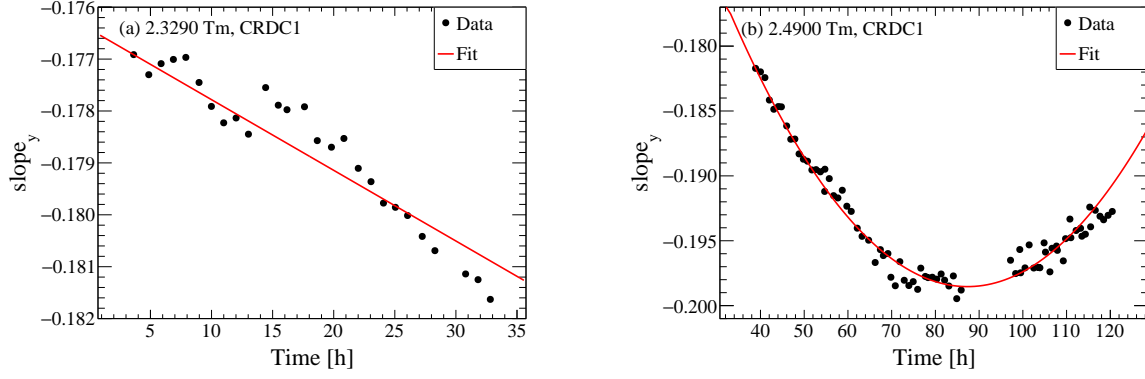
Figure 6.10: CRDC1 y-slope as a function of time for the (a) 2.3290 Tm runs and the (b) 2.4900 Tm runs.
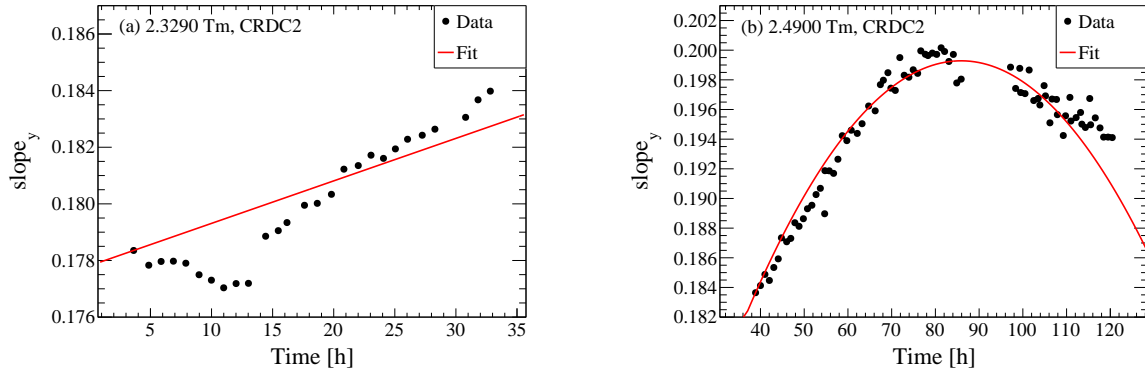
Figure 6.11: CRDC2 y-slope as a function of time for the (a) 2.3290 Tm runs and the (b) 2.4900 Tm runs.

value in the first run:

$$slope_y = slope_y \times \frac{\overline{TAC}_0}{\overline{TAC}_{run}} \tag{6.11}$$

where $\overline{TAC}_0$ and $\overline{TAC}_{run}$ are the average TAC for the first and current runs, respectively. The run-by-run adjusted slopes were fit as a function of time, and the fits were fixed to the mask runs where possible. The fits are shown in Figures 6.10 and 6.11, and the fit value was used as the final $slope_y$.

6.1.2.3 Focal-Plane Position and Angle

The focal-plane parameters were calculated from the calibrated CRDC positions and from the gap between the CRDCs, $gap = 1.061$ m:

$$xfp = x_{CRDC1}, \quad x\text{-position (dispersive) in the focal plane} \tag{6.12}$$

$$yfp = y_{CRDC1}, \quad y\text{-position (non-dispersive) in the focal plane} \tag{6.13}$$

$$afp = \text{atan}\left(\frac{x_{CRDC2} - x_{CRDC1}}{gap}\right), \quad \text{dispersive angle in the focal plane} \tag{6.14}$$

$$bfp = \text{atan}\left(\frac{y_{CRDC2} - y_{CRDC1}}{gap}\right), \quad \text{non-dispersive angle in the focal plane} \tag{6.15}$$

6.1.2.4 CRDCs Efficiency

The collective efficiency of both CRDCs was calculated as:

$$\epsilon_{CRDC} = \frac{\text{Events with a good } X_{COG} \text{ in both CRDCs}}{\text{Total number of events}} \tag{6.16}$$

with gates on the beam particle and reaction product of interest applied. Gating on the reaction product of interest ensured that the efficiency measurement was not biased by light ions or other background that could make the efficiency look worse than it actually is. Because the corrected E_{IC}-TOF_{obj} PID required focal-plane corrections, and hence a CRDC measurement, the uncorrected E_{IC}-TOF_{obj} PID was used to identify the reaction product. See Section 6.2.4 for more about the PID gates.

The efficiencies are given in Table 6.2. There was a large discrepancy between the two ^{10}C rigidity settings: ϵ_{CRDC} was 97% for the 2.3290 Tm setting but 34% for the 2.4900 Tm setting. This was due to scattering off the beam blocker in the 2.4900 Tm rigidity setting, i.e.,

Table 6.2: CRDC efficiencies ϵ_{CRDC}. The 2.3290 Tm ϵ_{CRDC} was used for the 2.4900 Tm rigidity setting.

Rigidity [Tm]	Beam	Reaction Product	ϵ_{CRDC}
2.3290	^{11}C	^{10}C	97 %
2.4900	^{12}N	^{10}C	97 %
2.8000	^{11}C	α	23 %
3.0000	^{12}N	α	18 %

^{10}C nuclei hit the blocker then scattered back into the focal-plane detectors. This hypothesis is supported by the fact that the majority of the bad events had a good CRDC2 X_{COG}. The S800 acceptance correction already accounted for the effect of the blocker (discussed in Section 6.2.1). Therefore the 2.3290 Tm value was used for the 2.4900 Tm rigidity setting. The efficiencies for the α-particle rigidity settings were very low because the CRDC anode voltage was too low for the smaller α-particle signals.

6.1.3 S800 Inverse Map and the Target Parameters

The energy and angle of the particles at the target were reconstructed from the focal-plane parameters with the S800 Inverse Map. The algorithm described in Ref. [118] calculates the transfer matrix of the S800 ion optics from the target to the focal plane, then inverts that matrix. The inverted matrix S^{-1} is called the "S800 Inverse Map," and instructions for how to calculate the map can be found in Ref. [111]. The S800 Inverse Map was applied to the focal-plane parameters to get the target parameters:

$$\begin{bmatrix} ata & yta & bta & dta \end{bmatrix} = S^{-1} \begin{bmatrix} xfp & afp & yfp & bfp \end{bmatrix} \tag{6.17}$$

Table 6.3: Beam profile.

	^{12}N	^{11}C	^{10}B
σ_{KE} [MeV]	4.4	3.7	2.8
σ_{ata} [deg]	0.5	0.5	0.5
σ_{yta} [mm]	3.8	4.1	4.1
σ_{bta} [deg]	0.3	0.3	0.4

where the target parameters are:

$$dta = \frac{KE - KE_0}{KE_0} = \text{ deviation from the central energy at the target} \tag{6.18}$$

$$yta = y\text{-position at the target} \tag{6.19}$$

$$ata = \text{ dispersive angle at the target} \tag{6.20}$$

$$bta = \text{ non-dispersive angle at the target} \tag{6.21}$$

6.1.4 Beam Profile

The beam profile was measured by sending the beam to the S800 focal plane in the unreacted beam setting, 2.5915 Tm. These data were taken with an empty target cell so there would be no extra spreading from straggling in the liquid hydrogen. Scattering in the Kapton foils was negligible. The spread in the beam kinetic energy, *ata*, *yta*, and *bta* are shown in Table 6.3 for each beam species.

6.1.5 Beam Energy

The average beam energy at the reaction point was determined in three steps. First, the beam energy *after* the target was reconstructed from the S800 focal-plane parameters in the unreacted beam setting, 2.5915 Tm (Section 6.1.5.1). Second, the beam energy after the target was used in conjunction with the Geant4 Simulation Toolkit [119] to determine

the beam energy *before* the target (Section 6.1.5.2). Third, the beam energy *at the reaction point* was determined by using the beam energy before the target again in conjunction with the simulation (Section 6.1.5.3).

6.1.5.1 After the Target

The unreacted beam particles were measured in the S800 focal plane after passing through the empty target cell (Run 188) and after passing through the full target cell (Run 198). The kinetic energy of the beam after passing through the target KE_{beam}^{after} was calculated as follows. Units are given in brackets for clarity. First, the central momentum p_0 was written in terms of the rigidity $B\rho_0$ and the charge $q = Z$ (equal to the atomic number for fully stripped ions):

$$B\rho_0[Tm] = \frac{p_0}{q} = \frac{p_0[MeV/c]}{Z[e^+]} \times \frac{10^6}{c[m/s]}$$

$$p_0[MeV/c] = (10^{-6}c[m/s]) \times B\rho_0[Tm] \times Z[e^+] \tag{6.22}$$

Then the central kinetic energy KE_0 was calculated from p_0, where m is the mass of the beam particle:

$$KE_0[MeV] = \sqrt{(p_0[MeV/c])^2 + (m[MeV/c^2])^2} - m[MeV/c^2] \tag{6.23}$$

Table 6.4 gives the beams' central momenta and kinetic energies for the unreacted beam setting. Last, KE_{beam}^{after} was calculated from dta, the fractional deviation from KE_0:

$$KE_{beam}^{after} = (1 + dta)KE_0 \tag{6.24}$$

82

Table 6.4: The rigidity $B\rho_0$, central momentum p_0, and central kinetic energy KE_0 for the unreacted beam setting.

Beam Particle	$B\rho_0$ [Tm]	p_0 [MeV/c]	KE_0 [MeV]
^{12}N	2.5915	5438	1251
^{11}C	2.5915	4661	1010
^{10}B	2.5915	3885	777

Table 6.5: The beam's fractional deviation from the central kinetic energy dta and kinetic energy KE_{beam}^{after} after passing through the empty target cell and the full target cell.

Beam Particle	Empty Cell dta [%]	Empty Cell KE_{beam}^{after} [MeV]	Full Cell dta [%]	Full Cell KE_{beam}^{after} [MeV]
^{12}N	2.8558	1287	-0.0782	1250
^{11}C	2.9343	1039	-0.0410	1009
^{10}B	2.8547	799	-0.1694	775

Table 6.5 gives the beam energies after the empty and full targets.

6.1.5.2 Before the Target

To find the beam energy before the target KE_{beam}^{before}, the beam was simulated with the Geant4 Simulation Toolkit [119] using the profile found in Section 6.1.4. The beam was simulated several times with a variety of input energies passing through the empty target cell. The simulated energies after the cell were plotted as a function of the input energies and fit to a line, as illustrated in Figure 6.12. That fit function was used to calculate the input energy that yielded the actual measured KE_{beam}^{after}.

Note that the empty cell was simulated as a vacuum between the Kapton foils, however, the empty cell was filled with hydrogen gas during the real empty cell measurement. The energy loss in the gas was negligibly small, < 0.027 MeV according to LISE^{++}. Also note that the beam could have slightly changed between the empty cell run and the rest of the experiment because it took a few hours for the target to cool. This created an unknown
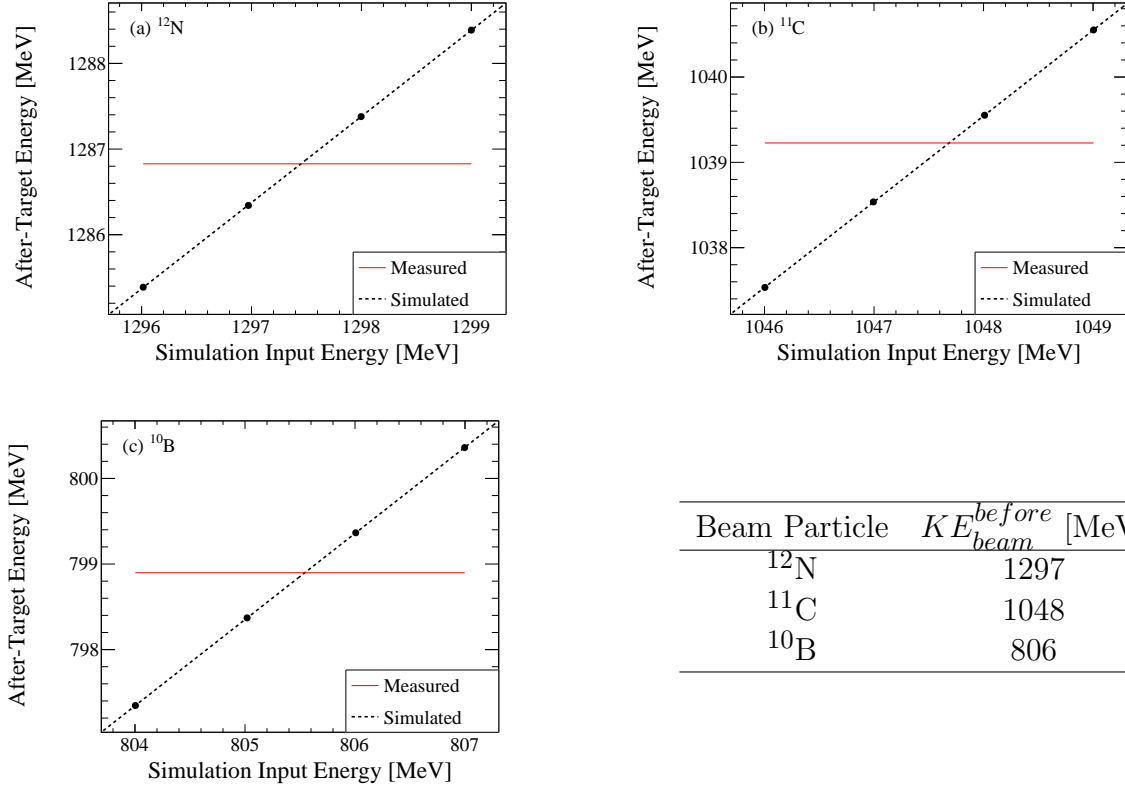
Figure 6.12: Kinetic energy of the beam after the empty target as a function of the beam energy before the target for (a) ^{12}N, (b) ^{11}C, and (c) ^{10}B. The measured KE_{beam}^{after} is given by the solid red line. The black points show the simulation results, and the black dashed line is a fit to these points. The intersection of the fit and the measured KE_{beam}^{after} provides the actual KE_{beam}^{before}.

amount of uncertainty in the beam energies, however, this uncertainty was neglected because the final result was not very sensitive to the beam energy.

6.1.5.3 At the Reaction Point

Finally, the beam energy at the reaction point was determined, again using the Geant4 simulation. The beam was simulated passing through the full target with energy KE_{beam}^{before} and the profile found in Section 6.1.4. In each simulated event, the charge-exchange reaction occurred at a random point in the target along the beam axis, and the energy of the beam

Table 6.6: Beam energies at the reaction point KE_{beam}.

Beam Particle	KE_{beam} [MeV]
^{12}N	1274
^{11}C	1029

at the reaction point KE_{beam} was recorded. The average KE_{beam} from the simulation was used as the beam energy in the missing mass calculation. The results are shown in Table 6.6.

6.2 Reaction Product Identity

When the beam impinged on the liquid hydrogen target, many other reactions were possible in addition to charge-exchange reactions, including for example knockout or transfer reactions. The products of these other reactions often reached the S800 and triggered background events. To eliminate these background events, the reaction products were identified, and all events without the correct charge-exchange reaction product, ^{10}C or an α-particle, were removed. This process of identifying the reaction product, called particle identification (PID), was done with the S800 focal-plane detectors.

First, the S800 momentum and angular acceptances were determined from the measured rigidity and angle in the S800 focal plane (Section 6.2.1). Then the S800 object time-of-flight and ionization chamber energy were corrected (Section 6.2.2) and the hodoscope's energy was calibrated (Section 6.2.3). Next, the PID gates were created from the corrected object time-of-flight, corrected ionization chamber energy, and hodoscope multiplicity and calibrated energy (Section 6.2.4).
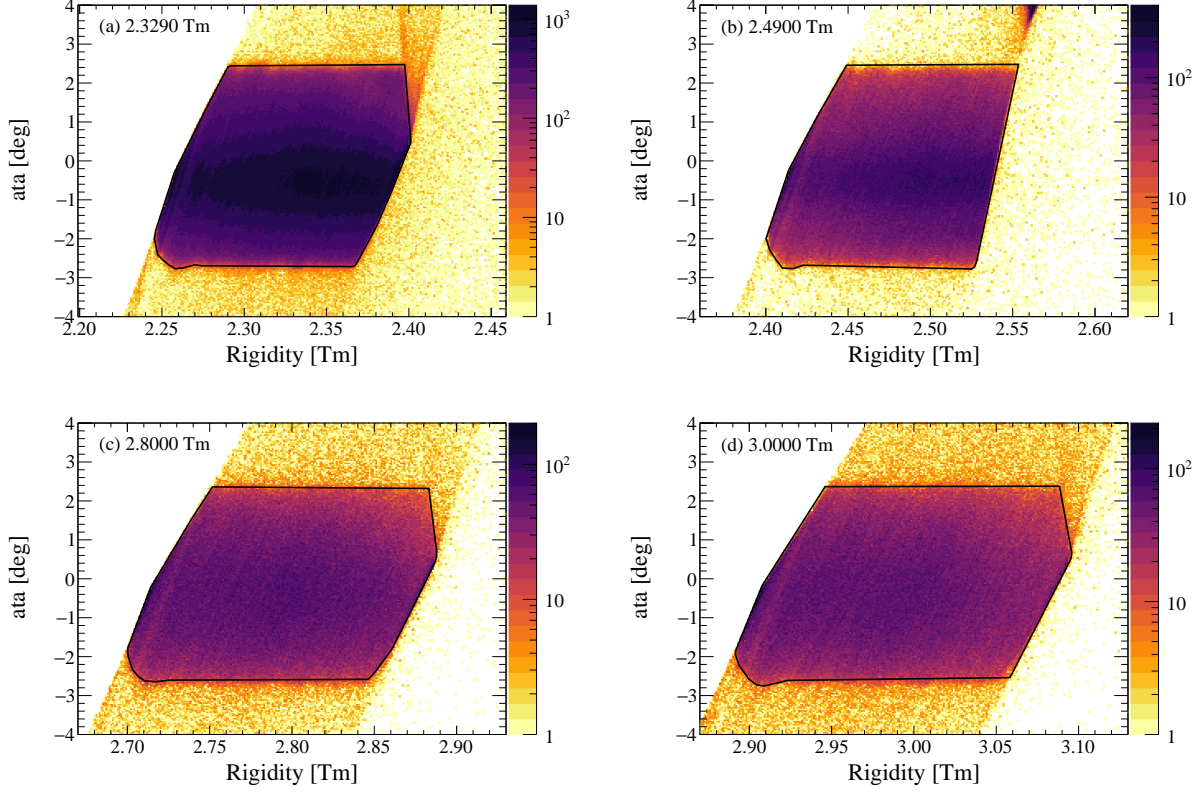
Figure 6.13: Dispersive angle *ata* vs. rigidity $B\rho$ in the S800 focal plane. The (a) 2.3290 Tm and (c) 2.8000 Tm settings are gated on the ^{11}C beam, and the (b) 2.4900 Tm and (d) 3.0000 Tm settings are gated on the ^{12}N beam. The S800 acceptance cuts are shown in black outlines.

6.2.1 S800 Acceptance

The S800 momentum acceptance is the range of momenta that the S800 can measure in the focal plane. If a reaction product is created with a momentum outside this range, then the S800 spectrograph dipoles either bend it too much or not enough, and the particle does not reach the focal plane. Similarly, the S800 also only accepts a small range of scattering angles. If the reaction product exits the target with a large angle, then it does not reach the focal plane.

The S800 acceptance for each rigidity setting was defined by the cuts in *ata* and $B\rho$ shown in Figure 6.13. The 2.3290 Tm and 2.8000 Tm data were gated on the ^{11}C beam, and the

2.4900 Tm and 3.0000 Tm data were gated on the ^{12}N beam. No gate on reaction product was applied. The 2.4900 Tm acceptance was chopped at high $B\rho$ because the blocker was inserted to prevent the beam from hitting the focal plane.

The S800 was tuned to the average rigidity of the ^{10}C and α particles resulting from the ^{11}N and ^{12}O decay, however, the ^{10}C and α-particle momentum and angular distributions were wider than the S800 acceptance. As a result, events with reaction products in the tails of the momentum or angular distributions were lost. This effect was taken into account using the Geant4 simulation and is discussed in Section 7.2.2.

6.2.2   S800 Focal-Plane Corrections

Particle identification was done with the energy loss in the ionization chamber E_{IC} and object time-of-flight TOF_{obj}. The $E_{IC} - TOF_{obj}$ PID plot is shown in Figure 6.22(a) for the 2.3290 Tm rigidity setting. Each peak is a different reaction product, and although distinct, they significantly overlap, making the identity of the reaction product ambiguous for many events. This overlap was reduced by applying corrections to E_{IC} and TOF_{obj}.

To first order, particles with higher energy were bent less in the S800 and hit the top of the focal plane. Particles with higher energy also had a larger energy loss and a shorter time-of-flight. Hence E_{IC} and TOF_{obj} were correlated with xfp. E_{IC} and TOF_{obj} had higher-order correlations with the other focal-plane parameters as well. These correlations were removed to reduce the smearing in E_{IC} and TOF_{obj} by applying the following corrections, with the scintillator energy E_{scint} included for completeness:

$$TOF_{obj}^{corr} = TOF_{obj} + C_{obj}^{xfp} \times xfp + C_{obj}^{afp} \times afp \tag{6.25}$$

$$E_{IC}^{corr} = E_{IC} + C_{IC}^{xfp} \times xfp + C_{IC}^{afp} \times afp \tag{6.26}$$

$$E_{Scint}^{corr} = E_{scint} + C_{scint}^{xfp} \times xfp + C_{scint}^{xfp^2} \times xfp^2 + C_{scint}^{afp} \times afp \qquad (6.27)$$

The C-coefficients are the correction parameters, and they were tuned such that the xfp- and afp-correlations disappear. The scintillator required a second-order xfp term because its PMTs measure light output better if the particle is closer to one PMT or the other.

The xfp correlations are shown in Figures 6.14, 6.15, and 6.16, and the afp correlations are shown in Figures 6.17, 6.18, and 6.19, before and after the correction for the 2.3290 Tm rigidity setting. Gates on the beam particle and reaction product of interest were applied. In the α-particle rigidity settings, a significant fraction of events had two α particles in the focal plane. Because a second particle would convolute the correlations, an extra gate was applied to only allow events where a single α particle was accepted.

6.2.3   Hodoscope Calibrations

The hodoscope was used for PID in the α-particle rigidity settings. The crystal energies are calibrated in Section 6.2.3.1, and the positions are calibrated in Section 6.2.3.2.

6.2.3.1   Hodoscope Energy Calibration

Only relative hodoscope energies were needed for the PID. One crystal with good statistics, crystal 6, was used to fix the energy scale. Then the rest of the crystals' energy spectra were calibrated to match crystal 6. The results of the calibration are shown in Figure 6.20. There was a change in crystal 15 at Run 397, so this crystal had two sets of calibration parameters.
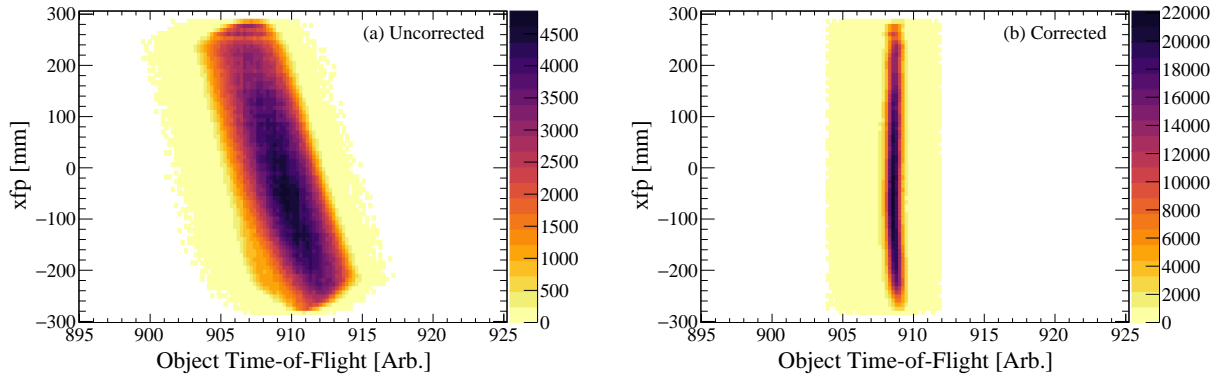
Figure 6.14: (a) Corrected and (b) uncorrected $TOF_{obj} - xfp$ correlation for the 2.3290 Tm rigidity setting.
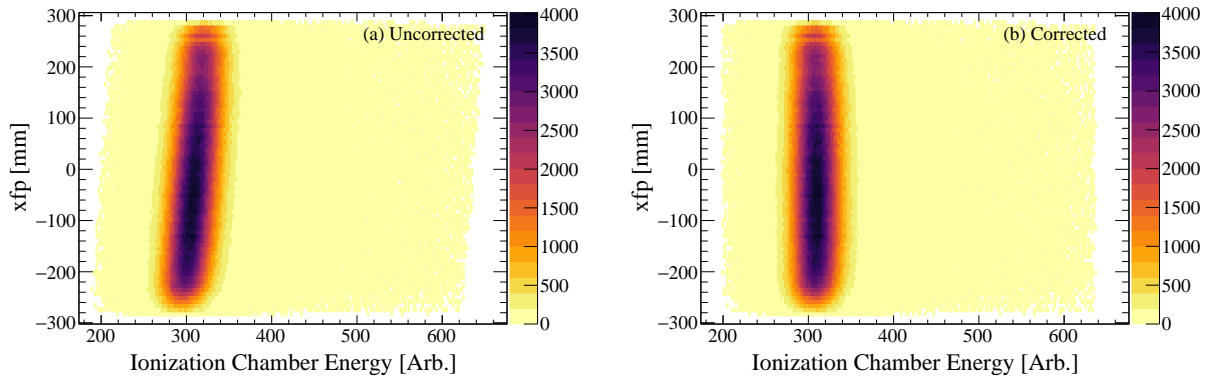
Figure 6.15: (a) Corrected and (b) uncorrected $E_{IC} - xfp$ correlation for the 2.3290 Tm rigidity setting.
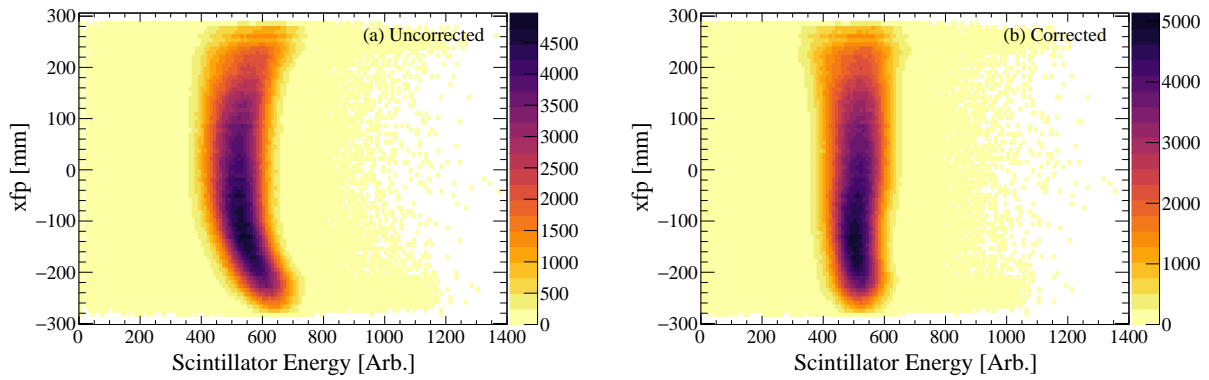
Figure 6.16: (a) Corrected and (b) uncorrected $E_{Scint} - xfp$ correlation for the 2.3290 Tm rigidity setting.
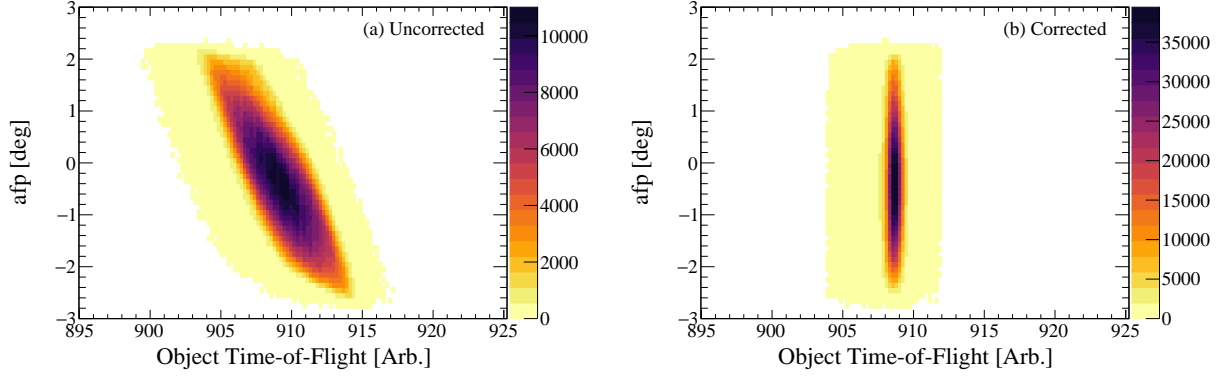
Figure 6.17: (a) Corrected and (b) uncorrected $TOF_{obj} - afp$ correlation for the 2.3290 Tm rigidity setting.
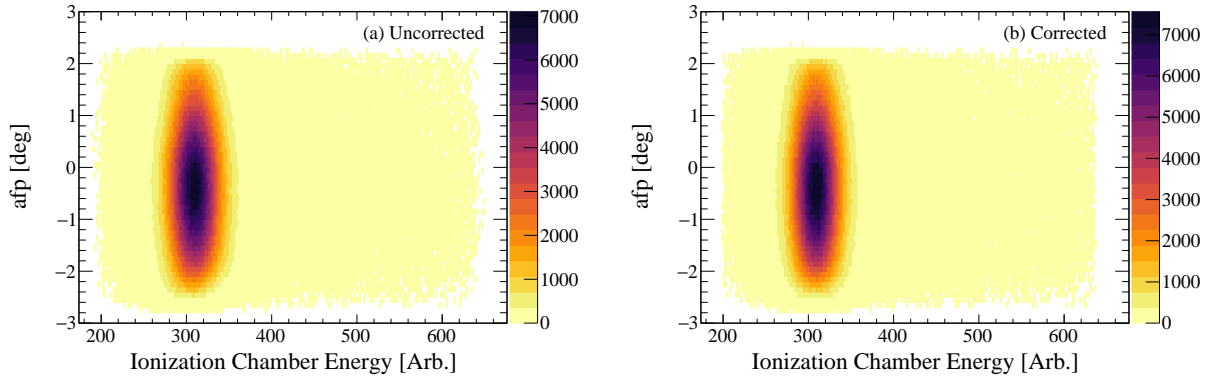
Figure 6.18: (a) Corrected and (b) uncorrected $E_{IC} - afp$ correlation for the 2.3290 Tm rigidity setting.
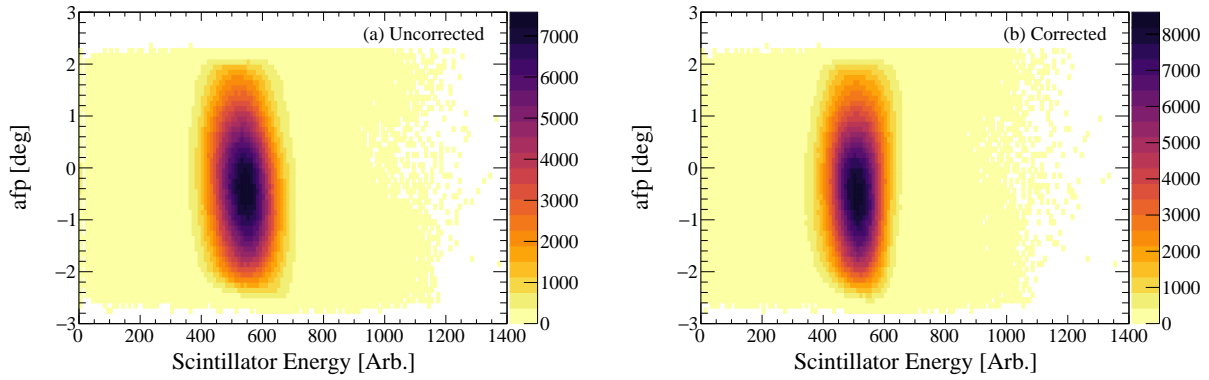
Figure 6.19: (a) Corrected and (b) uncorrected $E_{Scint} - afp$ correlation for the 2.3290 Tm rigidity setting.
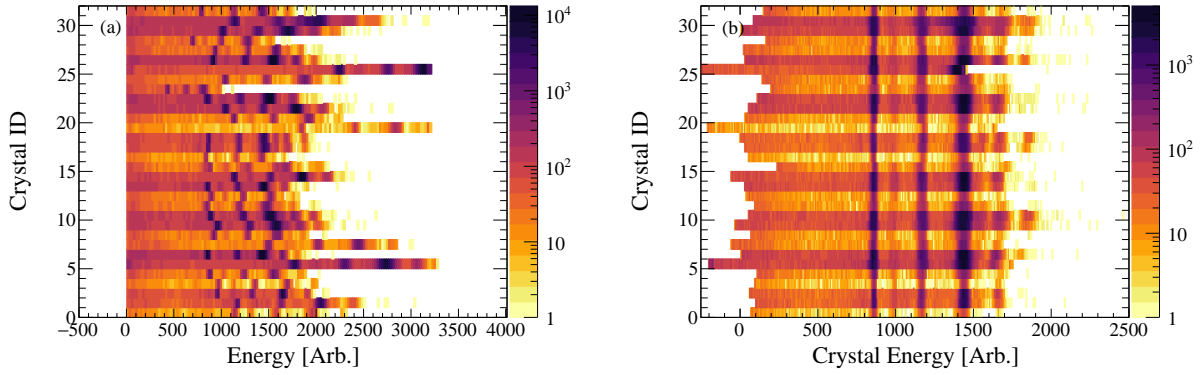
Figure 6.20: Hodoscope energy spectra (a) before and (b) after calibration.

6.2.3.2 Hodoscope Position Calibration

The hodoscope crystal positions were determined by using the CRDCs. The set of all hodoscope crystal positions was known from the geometry of the detector, but the location of each individual crystal was unknown. The crystals were not ordered according to their ID number; they were arranged such that the best crystals were in the center. The average CRDC x- and y-positions of events in each crystal were used to determine the relative position of each crystal, which could then be matched to one of the known crystal positions. The average CRDC x- and y-positions for events gated on each crystal is shown in Figure 6.21. Data from the 3.0000 Tm rigidity setting gated on the ^{12}N beam were used for this calibration. The hodoscope position was not actually used in the analysis, but is included for completeness.

6.2.4 Particle Identification

As previously discussed, charge-exchange reactions were not the only reactions occurring in the target. Reaction products from other reactions created a large amount of background. The S800 focal-plane detectors provided the information necessary to identify the reaction product and remove this background.

91
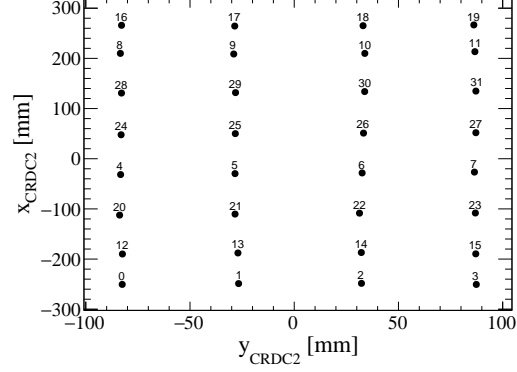
Figure 6.21: Average CRDC positions for each hodoscope crystal. The marker labels indicate the crystal ID number. From this, the crystal ID was assigned to a known crystal location.

The reaction products were identified based on their energy loss in the ionization chamber E_{IC} and object time-of-flight TOF_{obj}. E_{IC} is proportional to the square of the charge z^2 according to the Bethe-Bloch Equation [112]:

$$-\frac{dE}{dx} = \frac{4e^4 z^2}{m_0 v^2} NZ \left[\ln\left(\frac{2m_0 v^2}{I}\right) - \ln\left(\frac{1-v^2}{c^2}\right) - \frac{v^2}{c^2} \right] \tag{6.28}$$

where

$$\frac{dE}{dx} = \text{linear stopping power}$$

$$v = \text{velocity of primary particle}$$

$$ze = \text{charge of primary particle}$$

$$N = \text{number density of absorber atoms}$$

$$Z = \text{atomic number of absorber atoms}$$

$$m_0 = \text{electron rest mass}$$

TOF_{obj} is proportional to the mass-to-charge to ratio:

$$B\rho = \frac{p}{q} = \frac{mv}{q} = \frac{m \times (distance/TOF)}{q}$$

$$TOF = \frac{distance}{B\rho}\frac{m}{q} \tag{6.29}$$

The ions were fully stripped in this experiment, so the square of the charge and the charge-to-mass ratio uniquely defined an isotope. Therefore, each isotope had a different E_{IC} and TOF_{obj}.

Figures 6.22 and 6.23 show the PIDs for the 2.3290 Tm and 2.4900 Tm rigidity settings, respectively. Each peak represents a different reaction product. The corrected $E_{IC}-TOF_{obj}$ PID gate was applied to the data used for the missing mass calculation, but two other gates were needed to determine various correction parameters: the uncorrected $E_{IC} - TOF_{obj}$ PID and the uncorrected $E_{IC} - TOF_{RF}$ PID. Additionally, the corrected $E_{Scint} - TOF_{obj}$ PID was used for determining the acceptances of the PID gates.

The E_{IC} tails are likely from pileup. Because the TOF_{obj} matches the main peaks, the E_{IC} high-energy tail events are almost certainly good events. The cause of the TOF_{obj} tail is not clear, however, gates on the E_{IC} high-energy tail events yielded kinematics plots that look the same as those of the good events in the main peak and were therefore included.

The PIDs for the 2.8000 Tm and 3.0000 Tm rigidity settings are shown in Figures 6.24 and 6.25, respectively. Because the ^{11}N and ^{12}O decay into $2\alpha+3p$ and $2\alpha+4p$, respectively, either one or both of the resulting α particles were detected in the S800 focal plane. The α peak in the $E_{IC} - TOF_{obj}$ PID contained both one- and two-α-particle events.

The hodoscope was used to create gates on events where a single α particle was detected in the focal plane. If only one α particle reached the focal plane, then only one hodoscope
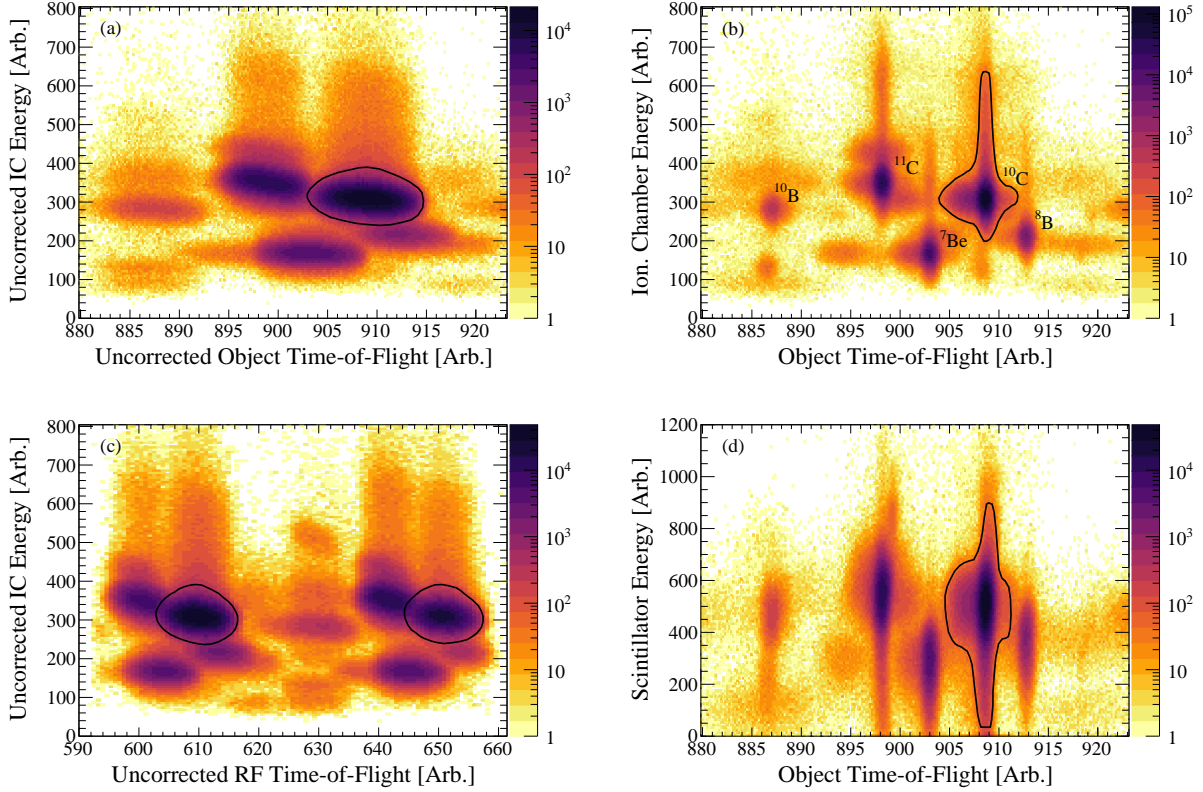
Figure 6.22: PIDs used for the 2.3290 Tm rigidity setting: (a) Uncorrected $E_{IC} - TOF_{obj}$ PID. (b) Corrected $E_{IC} - TOF_{obj}$ PID. (c) Uncorrected $E_{IC} - TOF_{RF}$ PID. (d) Corrected $E_{Scint} - TOF_{obj}$ PID.

crystal was hit (hodoscope multiplicity = 1), and the energy deposited in the crystal was the energy of one α particle. If two α particles reached the focal plane, then they either hit the same hodoscope crystal or two different hodoscope crystals. If they both hit the same crystal, then the hodoscope multiplicity was still one, but the energy was twice that of the one-α-particle case. If they hit two different crystals, then the hodoscope multiplicity was 2, and the energy of each hit was the energy of one α particle. Therefore, single-α-particle events can be identified with two additional gates:

- hodoscope multiplicity=1

- $E_{IC} - E_{hod}$ gate on one-α-particle events (shown in Figures 6.24 and 6.25)

94
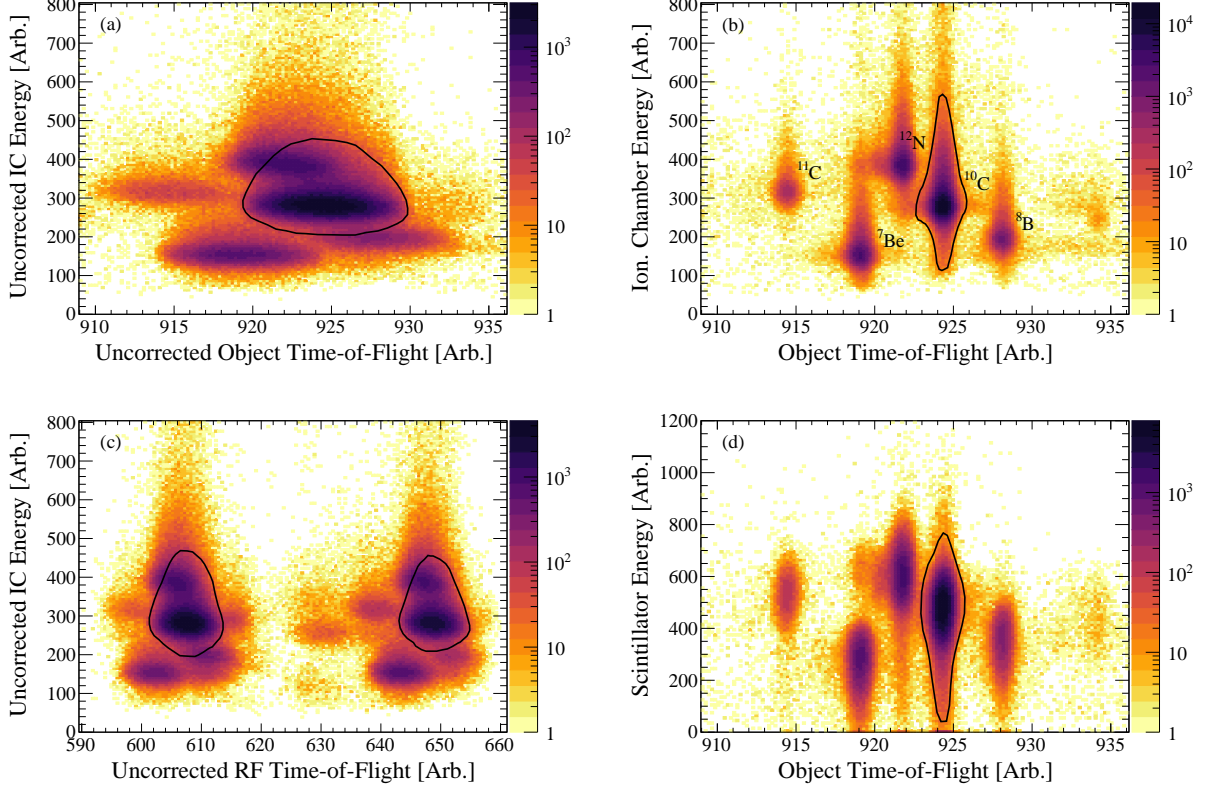
Figure 6.23: PIDs used for the 2.4900 Tm rigidity setting: (a) Uncorrected $E_{IC} - TOF_{obj}$ PID. (b) Corrected $E_{IC} - TOF_{obj}$ PID. (c) Uncorrected $E_{IC} - TOF_{RF}$ PID. (d) Corrected $E_{Scint} - TOF_{obj}$ PID.

Finally, the ^{10}B events were also necessary for the LENDA time-of-flight corrections in the α-particle rigidity settings, and that gate is also shown in Figures 6.24 and 6.25.

The fraction of events lost due to the particle identification gates was used in efficiency corrections (discussed in Section 7.2.3). Data gated on the beam particle and reaction product of interest using the $E_{scint} - TOF_{obj}$ PID was used to determine the ionization chamber efficiency ϵ_{IC}. No events had undefined E_{IC}, so $\epsilon_{IC} = 100\%$. The hodoscope efficiency was not needed because the hodoscope gates were used only to determine corrections and were not actually applied to the data.

Then the only efficiency that needed to be considered from the particle identification was that of the PID gates. Because the peaks have long tails, a simple 2D Gaussian was not an
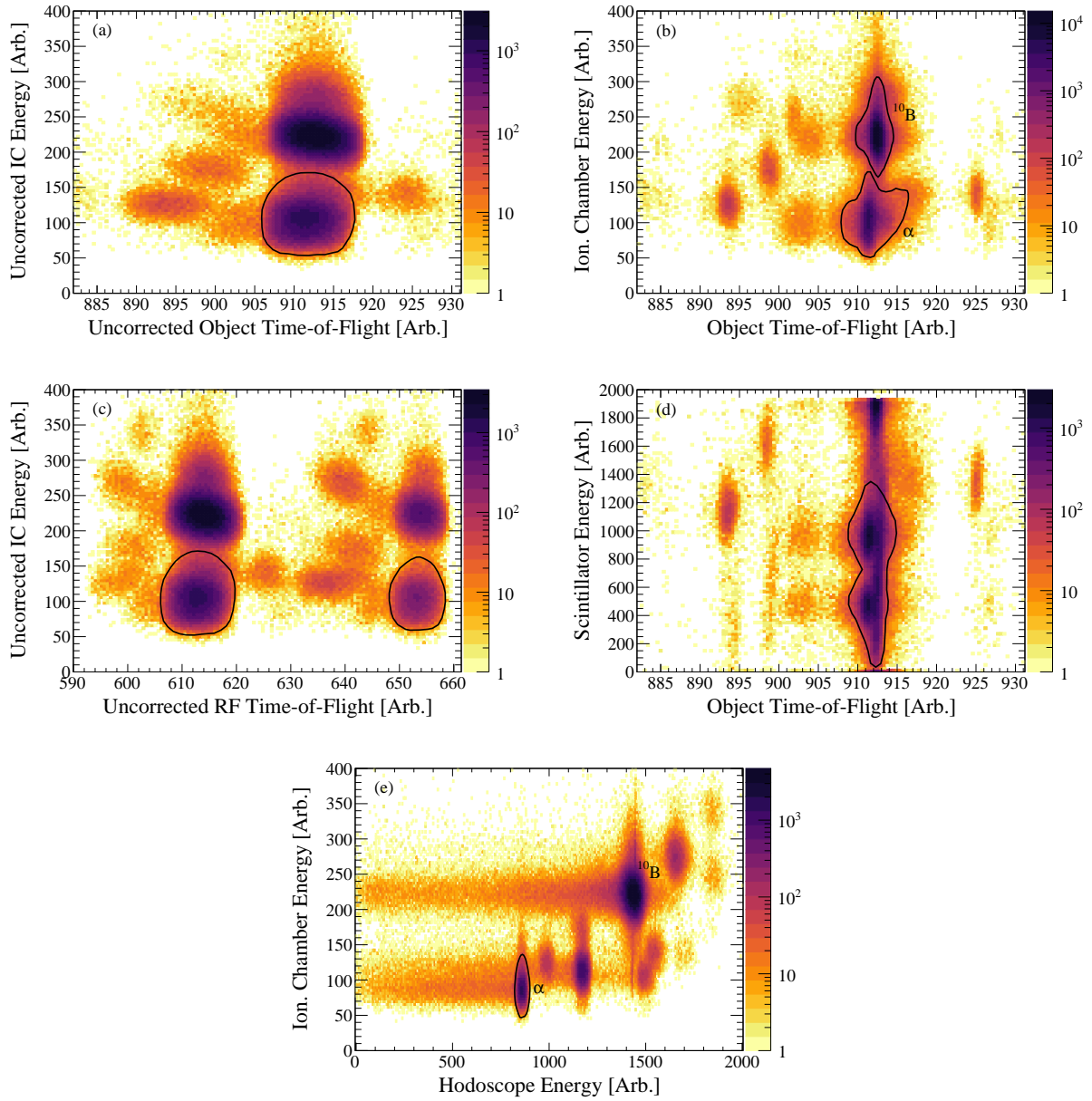
Figure 6.24: PIDs used for the 2.8000 Tm rigidity setting: (a) Uncorrected $E_{IC} - TOF_{obj}$ PID. (b) Corrected $E_{IC} - TOF_{obj}$ PID. (c) Uncorrected $E_{IC} - TOF_{RF}$ PID. (d) Corrected $E_{scint} - TOF_{obj}$ PID. (e) Corrected $E_{IC} - E_{hod}$ PID.
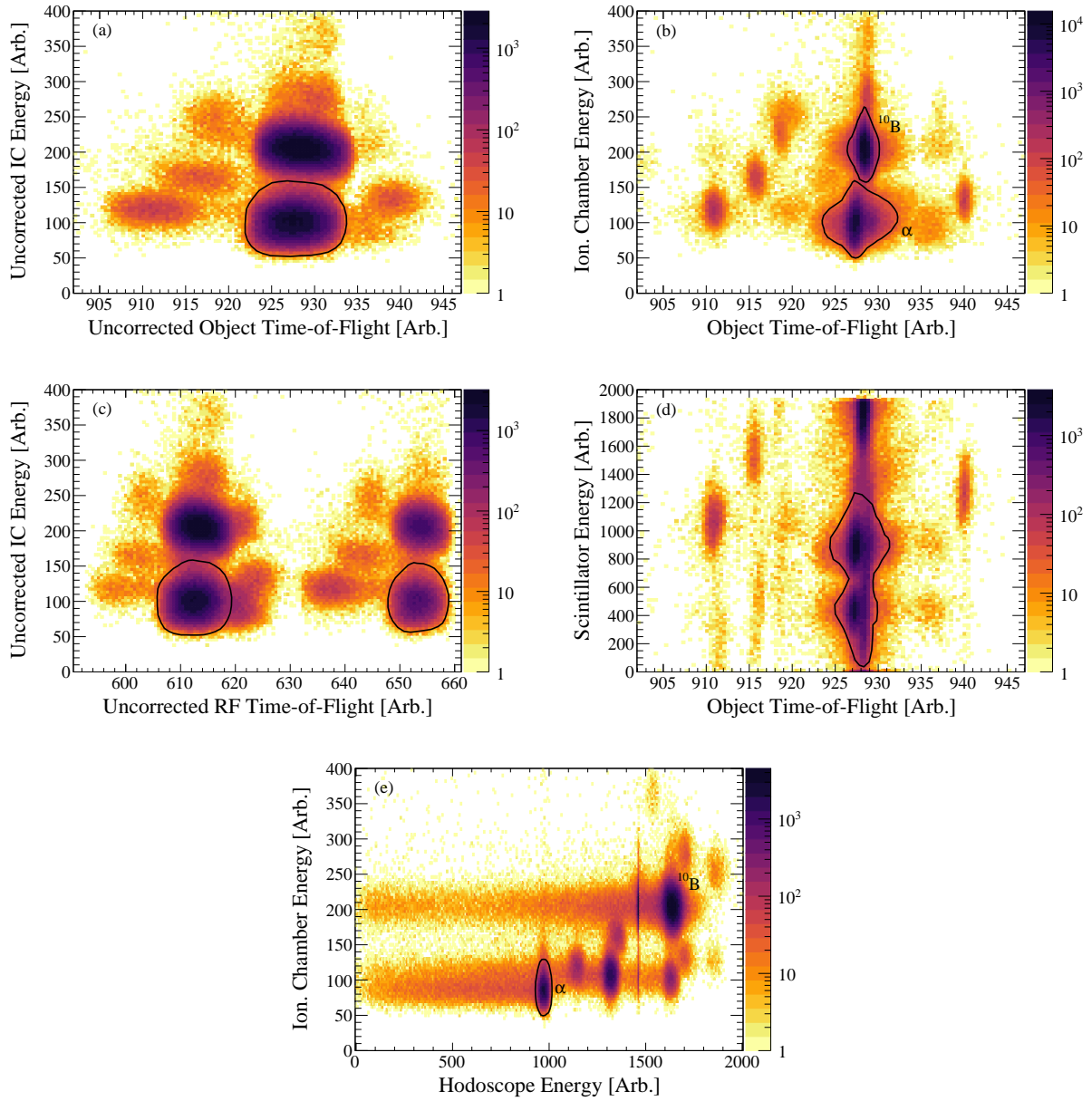
Figure 6.25: PIDs used for the 3.0000 Tm rigidity setting: (a) Uncorrected $E_{IC} - TOF_{obj}$ PID. (b) Corrected $E_{IC} - TOF_{obj}$ PID. (c) Uncorrected $E_{IC} - TOF_{RF}$ PID. (d) Corrected $E_{scint} - TOF_{obj}$ PID. (e) Corrected $E_{IC} - E_{hod}$ PID.
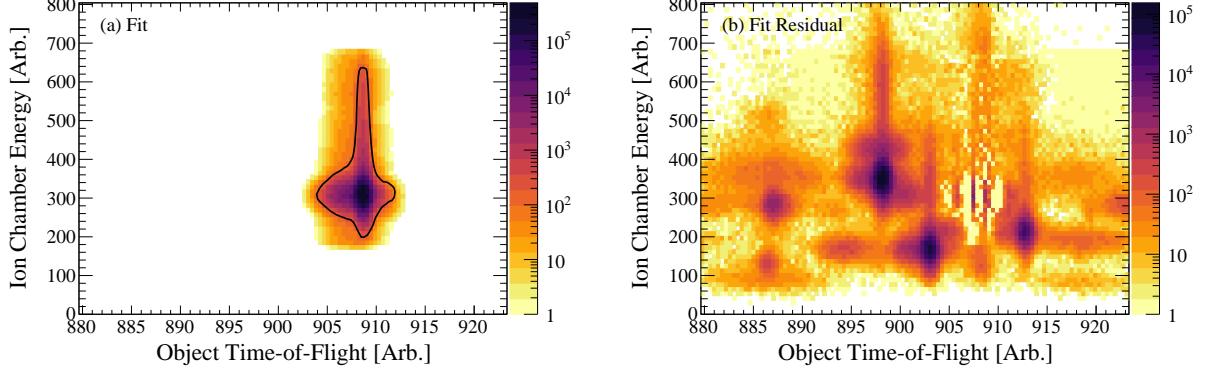
Figure 6.26: (a) Fit used to determine the PID efficiency of the $E_{IC} - TOF_{obj}$ PID for the 2.3290 Tm rigidity setting. (b) The fit residual (the data minus the fit).

Table 6.7: $E_{IC} - TOF_{obj}$ PID gate efficiencies, ϵ_{PID}.

Rigidity Setting	Beam Particle	Reaction Product	ϵ_{PID}
2.3290 Tm	^{11}C	^{10}C	99.7 %
2.4900 Tm	^{12}N	^{10}C	98.9 %
2.8000 Tm	^{11}C	α	98.4 %
3.0000 Tm	^{12}N	α	99.1 %

accurate model of their shapes. Instead, each spectrum was split into projections onto the TOF_{obj} axis, and the projections were fit with the sum of two 1D Gaussians. Figure 6.26 shows the fit result and residual for the 2.3290 Tm rigidity setting. Although the residual is not flat, the fluctuations are small and on average zero, indicating that the number of counts in the fit was accurate.

The efficiencies of the $E_{IC} - TOF_{obj}$ PID gates ϵ_{PID} were calculated as the ratio of fit events inside the cut N_{in}^{fit} to the total number of fit events N_{tot}^{fit}:

$$\epsilon_{PID} = \frac{N_{in}^{fit}}{N_{tot}^{fit}} \tag{6.30}$$

The ϵ_{PID} are given in Table 6.7. Efficiencies of the other PID gates are not needed because they are only used to do other corrections and are not actually applied to the data used in the missing mass calculation. The uncertainty in the efficiency is negligible.

6.3 Neutron Angle and Time-of-Flight

The neutron angle and time-of-flight were measured by the Low Energy Neutron Detector Array (LENDA). The angle was calculated from the LENDA bar positions, and the time-of-flight was measured with respect to *E1 up*. First, the LENDA bar positions were calibrated with a laser tracker (Section 6.3.1). Then the LENDA light output was calibrated (Section 6.3.2) and used to apply cuts to clean the data (Section 6.3.3). Next, the LENDA time-of-flight was corrected (Section 6.3.4). Finally, some additional cuts were applied to the LENDA multiplicity, neutron kinetic energy, and LENDA light output to further clean the data (Section 6.3.5).

6.3.1 LENDA Position Calibration

The position of each LENDA bar was measured with a high-precision 3-D coordinate measurement machine (FARO Laser Tracker/X with CAM2X software) [120]. The origin of the alignment coordinate system was set to the center of the target, 40 inches upstream from the flange of the S800 quad gate valve.

6.3.2 LENDA Light-Output Calibration

The LENDA light output is the light generated in the detector by the incident particle, and it is proportional to the energy deposited by the particle. The light output was used for making cuts to clean the data. Three radioactive sources provided five calibration points for each LENDA photomultiplier tube (PMT):

- ^{241}Am: two low-energy photopeaks at 26.3446 keV and 59.5409 keV

- ^{137}Cs: a γ ray with a Compton edge at 441.1047 keV

- ^{22}Na: annihilation γ ray with a Compton edge at 340.6667 keV and another γ ray with a Compton edge at 849.6913 keV

The photopeaks were fit with Gaussian curves that had a light-output-dependent standard deviation, and the Compton edges were identified as the location of the 2/3 maximum of the end of the Compton continuum. The energy spectra for SL01T, the top PMT of SL01, are shown in Figure 6.27.

Figure 6.28 shows the light-output calibration for SL01T before and after the experiment. The changes in the LENDA light-output calibrations before and after the experiment were generally small. The light-output calibration was used to define a light-output threshold, and this threshold defined the efficiency of the LENDA bars. The uncertainty in the LENDA efficiency from the change in the light-output calibration was taken into account by using the Geant4 simulation and is discussed in Section 7.2.2.4.

6.3.3   LENDA Light-Output Cuts

The light output of each LENDA event was used to clean the data. Cuts were applied to eliminate events with low light output, which had poor resolution (Section 6.3.3.1), and cuts were applied to eliminate events with high light output, which were contaminated with charged particles (Section 6.3.3.2).

6.3.3.1   Low-Light-Output Threshold

Events with low light output had poor timing resolution and were removed. The light-output threshold was set as high as possible without cutting charge-exchange events. The lowest neutron kinetic energy that could be measured in this experiment was $KE_n = 0.573$ MeV, based on the kinematics of the reaction and the LENDA bar positions. According to Eq. 6.31 [114],
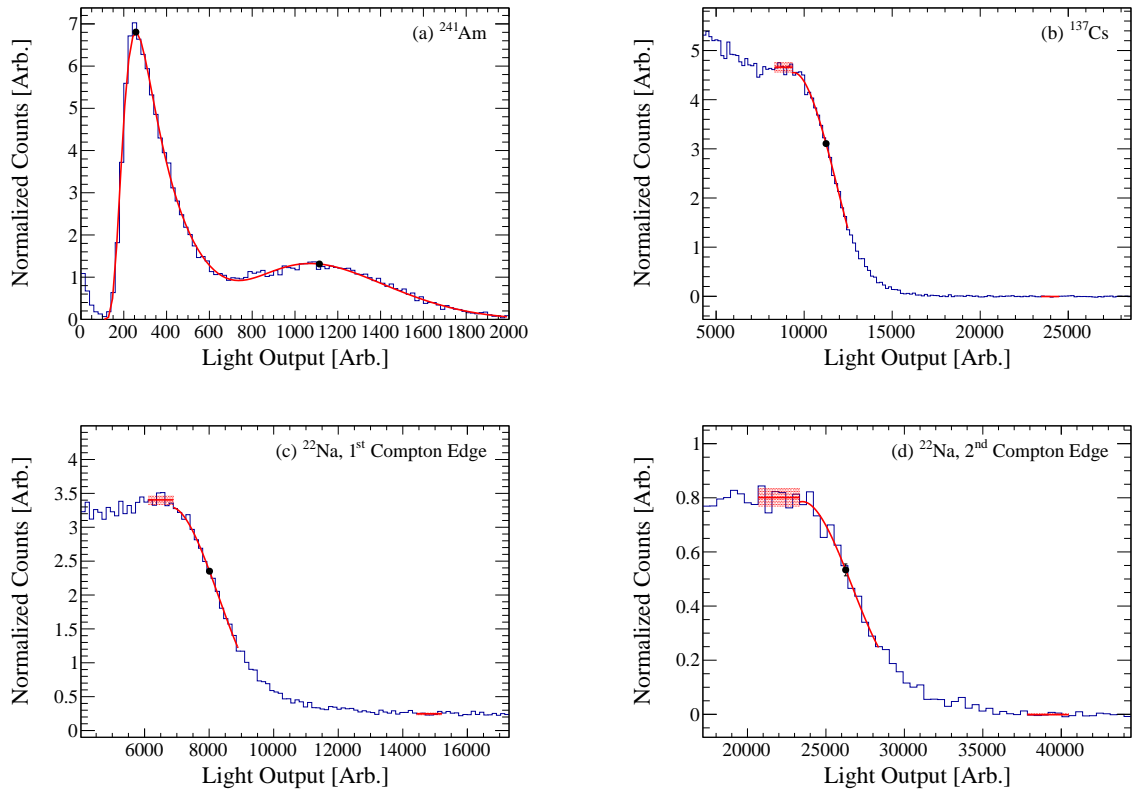
Figure 6.27: Energy spectra for SL01T light-output calibration before the experiment: (a) ^{241}Am photopeaks, (b) ^{137}Cs Compton edge, (c) ^{22}Na first Compton edge, (d) ^{22}Na second Compton edge. The red curves are the fits, and the black points indicate the photopeak or Compton edge location. The red rectangles show the uncertainty in the maximum and minimum used to determine the 2/3 maximum for the Compton edge.
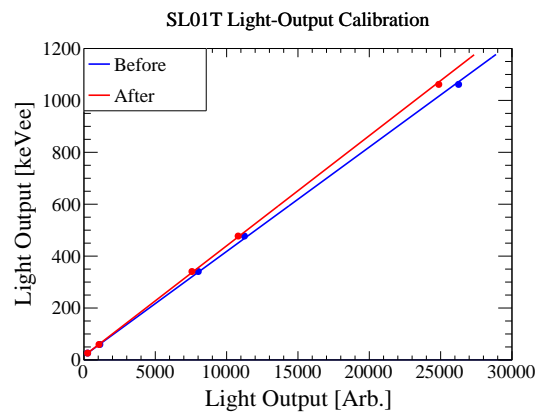
Figure 6.28: Light output calibrations for the SL01T PMT before (blue) and after (red) the experiment.

a neutron with kinetic energy 0.573 MeV can yield a maximum light output of 99.8 keVee in a LENDA bar. This value served as a maximum for the light-output threshold to prevent charge-exchange events with the lowest neutron kinetic energy from being entirely removed.

$$LO_{max} = \begin{cases} 18.53 + 95.08 KE_n + 81.58 KE_n^2, & KE_n < 3 \text{ MeV} \\ \\ 518.1 KE_n - 499.5, & KE_n > 3 \text{ MeV} \end{cases} \tag{6.31}$$

The random-coincidence background subtraction (discussed later in Section 7.2.1.2) also put constraints on the light-output threshold. The random-coincidence background model was created from data with neutron time-of-flight $TOF_n > 125$ ns, or $KE_n < 0.335$ MeV. The 125 ns time-of-flight limit corresponds to a minimum light-output threshold of 59 keVee. This minimum light-output threshold ensured that the random-coincidence background model contained no good events and was not overestimated.

Therefore the constraints on the light-output threshold LO_{min} were:

1. $LO_{min} < 99.8$ keVee, otherwise regions of KE_n where good charge-exchange events can occur would be cut.

2. $LO_{min} > 59$ keVee, otherwise good charge-exchange events would leak into the random-coincidences sampling region $TOF_n > 125$ ns.

A light-output threshold of $LO_{min} = 65$ keVee was chosen, equivalent to $KE_n = 0.371$ MeV or $TOF_n = 119$ ns. This selection kept the threshold as low as possible while leaving some wiggle room for uncertainties in the conversion from kinetic energy to light output.

6.3.3.2 High-Light-Output Cut

There were many events with very high light output at low "neutron" kinetic energies, which were actually charged particles. These were removed with a light-output cut that is a function of the kinetic energy, namely, Eq. 6.31 plus 3000 keVee. A more restrictive light-output cut was applied later (discussed in Section 6.3.5.3).

6.3.4   LENDA Time-of-Flight Corrections

The neutron time-of-flight required several corrections. The raw LENDA time-of-flight was the difference between the LENDA time and the *E1 up* time. The S800 focal-plane corrections were again applied because of the artificial correlations between the *E1 up* time and the focal-plane position and angle (Section 6.3.4.1). Each channel of the Pixie-16 modules introduced its own offset, called the jitter (Section 6.3.4.2). The time of the LENDA signal was also dependent on the light output, and this effect is called walk (Section 6.3.4.3). All of these corrections collectively put the γ flash at 0 ns.

Once the γ flash was corrected to 0 ns, the time-of-flight was shifted so that the γ flash was in the proper place according to the speed of light. Eq. 6.32 shows how all of these corrections ware implemented to get the corrected time-of-flight. Finally, the LENDA time-of-flight resolution was found (Section 6.3.4.4).

$$
\begin{aligned}
TOF_{corr} = {} & TOF_{raw} - C_{xfp} \times xfp - C_{afp} \times afp \\
& - jitter \\
& + C_{walkA}(LO + C_{walkB} - \sqrt{LO^2 + C_{walkC} \times LO + C_{walkD}}) \\
& + d/c
\end{aligned}
\tag{6.32}
$$

where

$$TOF_{corr} = \text{corrected time-of-flight}$$

$$TOF_{raw} = \text{raw time-of-flight (the LENDA time minus the } E1 \ up \text{ time)}$$

$$C_i = \text{correction parameters}$$

$$xfp = x\text{-position in the focal plane}$$

$$afp = \text{dispersive angle in the focal plane}$$

$$jitter = \text{offset of the } \gamma \text{ flash from zero}$$

$$LO = \text{average light output of the LENDA bar}$$

$$d = \text{distance from the target to the LENDA bar}$$

$$c = \text{speed of light}$$

Gates on the beam particles of interest were applied to the data to do these corrections. Additionally, a gate on the ^{10}C reaction product was applied to the ^{10}C rigidity settings and a gate on the ^{10}B reaction product was applied to the α-particle rigidity settings. ^{10}B, not α particles, were used because α-particle events did not yield a γ flash.

Slightly different light-output cuts were applied to the data used to do these corrections than what was described in the previous section (Section 6.3.3). Here, the cuts applied were 65 keVee $< LO <$ 6000 keVee, with a constant light-output maximum rather than a maximum that is a function of kinetic energy. The kinetic energy is a function of the time-of-flight–the variable being corrected–so it could not be used to define a cut.
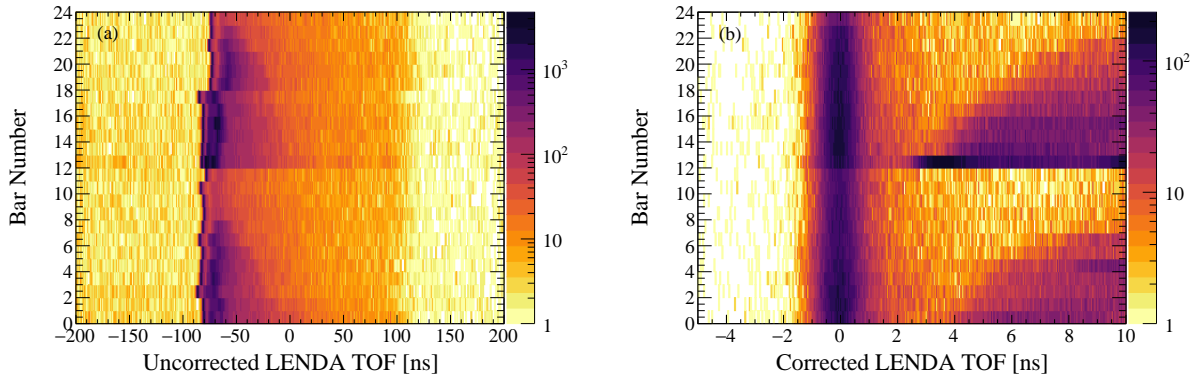
Figure 6.29: LENDA time-of-flight spectra (a) before and (b) after the jitter correction for the first set of 2.3290 Tm runs. Note that (b) is zoomed in relative to (a).

6.3.4.1 S800 Focal-Plane Corrections

Just like the object time-of-flight, the LENDA time-of-flight was corrected for position and angle in the focal plane since the reference time was the *E1 up* signal. The same signal from the same detector was used, so the parameters that were found for the object time-of-flight only needed slight adjustments for the LENDA time-of-flight corrections.

6.3.4.2 Jitter

The offset of the γ flash from zero, called the jitter, was different for each Pixie-16 channel. The jitter was found separately for each rigidity setting since the offsets depended on the experimental conditions. Additionally, during the 2.3290 Tm runs, the data acquisition system (DAQ) had to be restarted multiple times. Whenever the DAQ restarted, the jitters changed. Hence a new set of jitter corrections was made each time the DAQ restarted, a total of four sets for four groups of 2.3290 Tm runs. Figure 6.29 shows the time-of-flight spectra for each LENDA bar before and after the jitter correction for the first set of 2.3290 Tm runs.
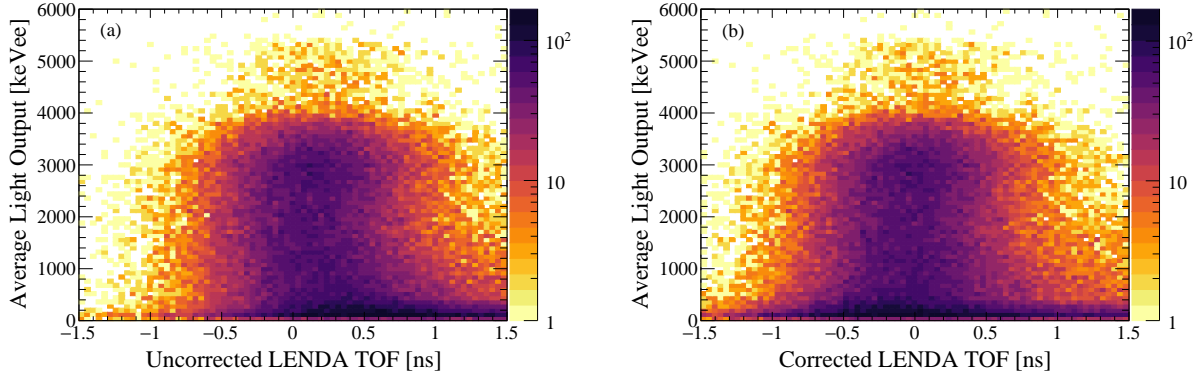
Figure 6.30: LENDA light output vs. time-of-flight (a) before and (b) after the walk correction.

6.3.4.3 Walk

Walk is the dependence of a signal's time on its light output. This effect can be minimized by passing the signal through a filter such as a constant fraction discriminator (CFD). In this analysis, multiple filters were applied to the LENDA pulses to minimize walk; see Ref. [114] for information about these filters. Although the filters greatly reduced walk, they did not eliminate it completely. Therefore a walk correction was still applied to the data.

The first set of 2.3290 Tm runs had the most γ-flash statistics and was used to determine the walk correction. This effect is intrinsic to the LENDA detectors themselves, so it was only done once and not separately for each rigidity setting. A slant asymptote was used to model the time-of-flight as a function of light output. The light output vs. time-of-flight before and after the walk correction are shown in Figure 6.30.

6.3.4.4 LENDA Time-of-Flight Resolution

LENDA's time-of-flight resolution was found as a function of light output, given by Eq. 6.33. LO is the light output and a_i are the parameters determined from a fit to the data, shown in Figure 6.31. The first set of 2.3290 Tm runs was used to determine the resolution. A
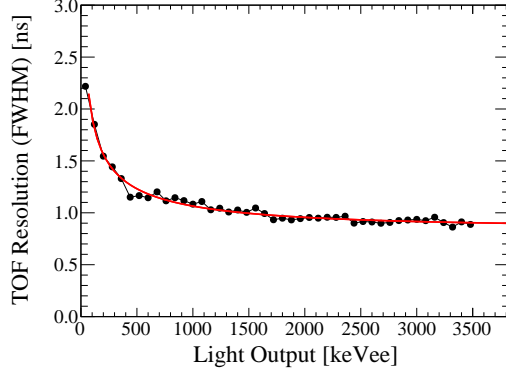
Figure 6.31: LENDA time-of-flight resolution as a function of light output. The black points are the data, and the solid red line is the fit.

resolution of up to about 1 ns (FWHM) was achieved for higher light outputs.

$$FWHM(LO) = a_0 + a_1(LO)^{a_2} + a_3(LO)^{a_4} \tag{6.33}$$

6.3.5 Additional Cuts

Finally, a few final cuts were applied to the data: a cut on the LENDA multiplicity (Section 6.3.5.1), cuts on the neutron kinetic energy (Section 6.3.5.2), and a second cut on light output (Section 6.3.5.3).

6.3.5.1 LENDA Multiplicity

Two or more LENDA bars were occasionally hit in the same event due to various sources of background. Good charge-exchange reactions only resulted in one neutron, and because it was not possible to identify which hit was the charge-exchange neutron, events with more than one LENDA bar hit were removed. The efficiency of the multiplicity cut ϵ_{mult} was
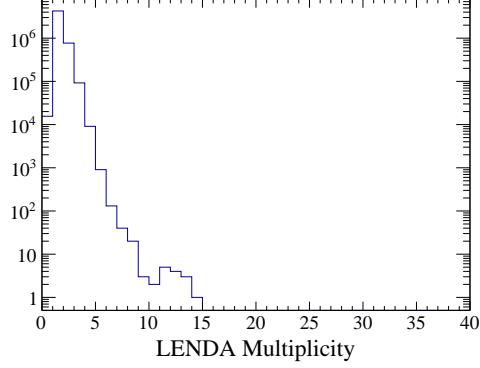
Figure 6.32: LENDA multiplicity for the 2.3290 Tm rigidity setting.

taken as the number of events with more than one LENDA bar:

$$\epsilon_{mult} = \frac{\text{Number of events with LENDA multiplicity} > 1}{\text{Total number of events}} \tag{6.34}$$

Gates on the beam particle and reaction product of interest were applied the data before evaluating the multiplicity-gate efficiency. The multiplicity plot for the 2.3290 Tm rigidity setting is shown in Figure 6.32, and the results are given in Table 6.8. The error in ϵ_{mult} was negligible.

6.3.5.2 Kinetic Energy Cuts

The light-output threshold was set to 65 keVee. According to Eq. 6.31, neutrons with kinetic energy less than 0.37 MeV cannot create a light output above this threshold in LENDA. Therefore events with $KE_n < 0.37$ MeV were background and hence removed.

Charged particles began to significantly contaminate the data at neutron kinetic energies above 9 MeV, so events with $KE_n > 9$ MeV were removed.

Table 6.8: LENDA multiplicity cut efficiency ϵ_{mult} for each rigidity setting.

Rigidity Setting	Beam	Reaction Product	ϵ_{mult}
2.3290 Tm	^{11}C	^{10}C	83 %
2.4900 Tm	^{12}N	^{10}C	84 %
2.8000 Tm	^{11}C	α	86 %
3.0000 Tm	^{12}N	α	81 %

6.3.5.3   Second High-Light-Output Cut

Although the charged particle bands at very high light output were removed by the previous light-output cut, a significant amount of background was still present at high light outputs. This background was removed by directly applying Eq. 6.31 as the light-output maximum. A scaling factor was included to compensate for the degradation of the light-output calibration at high light output values. The propagation of the uncertainty in this scaling factor is described in Section 7.2.1.4.

Chapter 7

Data Analysis II

In the last chapter, the data were cleaned, and the beam energy, neutron angle, and neutron time-of-flight were determined. In this chapter, these quantities are used to calculate the differential cross section. First, the reaction was reconstructed using the missing mass method (Section 7.1), and the total number of reactions was calculated (Section 7.2). Next, the number of incident beam particles (Section 7.3) and target density (Section 7.4) were determined. Finally, all of these quantities were used to calculate the cross section (Section 7.5). Statistical errors were propagated automatically by the ROOT software, and systematic errors were determined and propagated manually.

7.1   The Missing Mass Method

The missing mass method is the reconstruction of the ejectile excitation energy and the center-of-mass scattering angle from the recoil kinetic energy and laboratory angle using two-body kinematics. Only the z-component of the projectile (^{11}C or ^{12}N beam) momentum was used for the calculation in this analysis. The projectile's total energy E_{proj} and momentum p_{proj} were calculated from the kinetic energies KE_{beam} found in Section 6.1.5:

$$E_{proj} = KE_{beam} + m_{proj} \tag{7.1}$$

$$p_{proj} = \sqrt{E_{proj}^2 - m_{proj}^2} \tag{7.2}$$

The target (proton) was stationary and had zero momentum:

$$E_p = m_p \tag{7.3}$$

$$p_p = 0 \tag{7.4}$$

The recoil (neutron) angle was measured by LENDA. The LENDA bar angles were calculated from the bar positions, which were calibrated in Section 6.3.1. Because only the z-component of the beam momentum was used, only the angle relative to the z-axis (the beam axis) was needed to reconstruct the reaction. The neutron angle θ was calculated as the LENDA bar angle θ_{LENDA} plus a random smearing $\Delta\theta$:

$$\theta = \theta_{LENDA} + \Delta\theta \tag{7.5}$$

The smearing was included to account for the 4.5 cm width of the LENDA bar, and it was selected uniformly from $-1.29° \leq \Delta\theta \leq 1.29°$.

Then the neutron energy E_n and momentum p_n were calculated from the neutron path length d (Section 6.3.1) and time-of-flight TOF_{corr} (Section 6.3.4):

$$\beta_n = \frac{d}{c \times TOF_{corr}} \tag{7.6}$$

$$\gamma_n = \frac{1}{\sqrt{1 - \beta_n^2}} \tag{7.7}$$

$$KE_n = (\gamma_n - 1)m_n \tag{7.8}$$

$$E_n = \gamma_n m_n \tag{7.9}$$

$$p_n = \sqrt{E_n^2 - m_n^2} \tag{7.10}$$

The missing mass is defined as the total mass of the ejectile, i.e. $m_{missing} = m_{ejec} + E_x$. Finally, E_{proj}, p_{proj}, θ, E_n, p_n, and all of the masses m_i, were used to find $m_{missing}$ and hence the excitation energy E_x:

$$p_{ejec}^2 = p_{proj}^2 + p_n^2 - 2p_{proj}p_n\cos\theta$$

$$E_{ejec} = E_{proj} + m_p - E_n$$

$$m_{missing} = \sqrt{E_{ejec}^2 - p_{ejec}^2}$$

$$E_x = m_{missing} - m_{ejec} \tag{7.11}$$

and the center-of-mass scattering angle θ_{CM}:

$$\beta_{proj} = \frac{p_{proj}}{E_{proj} + m_p}$$

$$\gamma_{proj} = \frac{1}{\sqrt{1 - \beta_{proj}^2}}$$

$$p_{n_z} = p_n \cos\theta$$

$$p_{n_r} = p_n \sin\theta$$

$$p_{n_z}^{CM} = \gamma_{proj}(p_{n_z} - \beta_{proj}E_n)$$

$$p_{n_r}^{CM} = p_{n_r}$$

$$p_n^{CM} = \sqrt{(p_{n_z}^{CM})^2 + (p_{n_r}^{CM})^2}$$

$$\theta_{CM} = \arcsin\frac{p_n}{p_n^{CM}}\sin\theta \tag{7.12}$$

The data in the lab frame are shown in Figure 7.1(a), and the data transformed into the center-of-mass frame are shown in Figure 7.1(b). The neutron lab angle resolution was defined by the 4.5 cm bar width. The neutron lab kinetic energy resolution was defined by
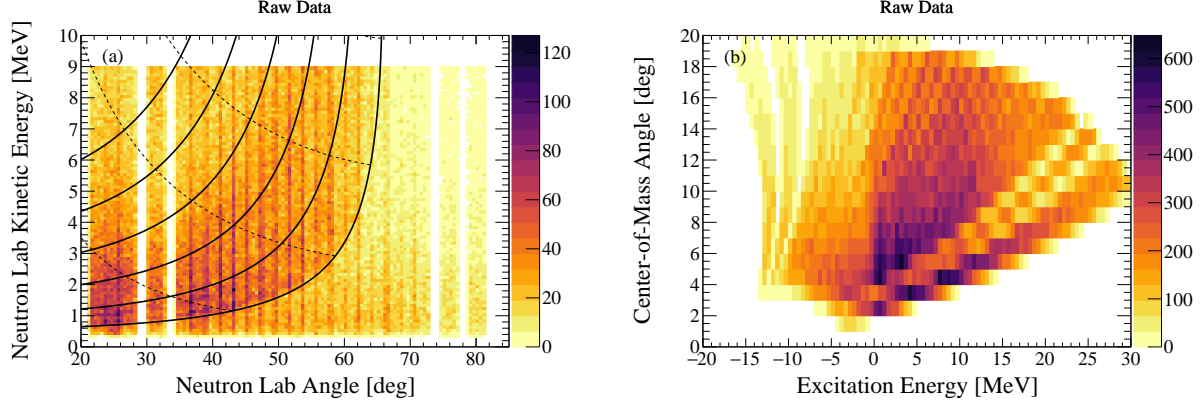
Figure 7.1: Raw data N_{raw} in (a) the laboratory frame and (b) the center-of-mass frame for the 2.3290 Tm setting. All corrections, calibrations, and cuts from Ch. 6 are applied.

the LENDA bar distance from the target ($\approx$1 m), the thickness of the LENDA bar (2.5 cm), and the LENDA timing resolution ($0.9 - 2.0$ ns).

7.2   Reaction Rate

The result of the missing mass calculation in the previous section was the raw counts N_{raw} as a function of excitation energy and center-of-mass scattering angle (Figure 7.1). In this section, the total number of reactions N_{rxn} is calculated. First, all remaining background was subtracted from N_{raw} to get the measured counts N_{meas} (Section 7.2.1). Then N_{meas} was corrected for the LENDA and S800 acceptance to get N'_{rxn} (Section 7.2.2). Last, N'_{rxn} was corrected for all of the other detector efficiencies and analysis cuts to get the total number of reaction counts N_{rxn} (Section 7.2.3).
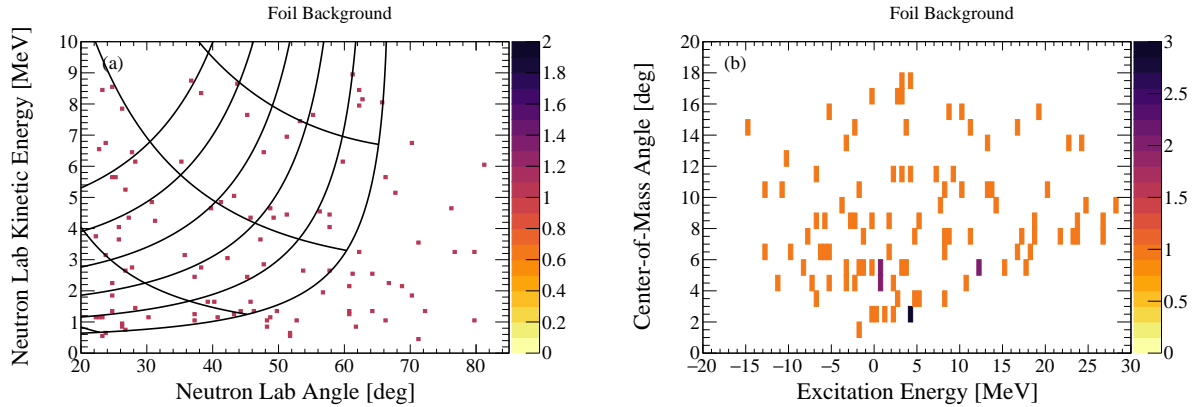
Figure 7.2: Foil background measurement for the 2.4900 Tm rigidity setting in (a) the laboratory frame and (b) the center-of-mass frame.

7.2.1 Background Subtraction

Even after all of the cleaning discussed in Ch. 6, more background remained to be subtracted. This background had three sources: the foil of the target (Section 7.2.1.1), random coincidences (Section 7.2.1.2), and non-charge-exchange reactions (Section 7.2.1.3).

7.2.1.1 Foil Background

Although the foil was thin, reactions could still occur inside it. The foil background contribution was measured by sending the beam through the empty target cell. An empty cell run was taken for the 2.3290 Tm and 2.4900 Tm rigidity settings (Runs 410 and 411). The DAQ was restarted between these runs and the other 2.3290 Tm runs, so a jitter correction could not be done for the 2.3290 Tm empty cell run. As a result, the LENDA TOF corrections could not be completed, and the 2.3290 Tm empty cell data could not be used. However, the 2.4900 Tm empty cell data showed that the foil background was small, Figure 7.2. No foil background model could be made from this data, so the hydrogen in the foil was included in the target thickness calculation. The contribution from other elements in the foil was negligible compared to uncertainties from other background components.

114

7.2.1.2 Random Coincidences

To simplify the random-coincidence background subtraction, a normalized time-of-flight TOF_{1m} was defined. A normalized time-of-flight enabled meaningful comparison of the different LENDA bars' time-of-flight spectra and could be universally related to a kinetic energy. The normalized time-of-flight TOF_{1m} was defined as what the time-of-flight would have been if the LENDA bar was exactly 1 m from the target:

$$TOF_{1m} = \frac{TOF_{corr}}{d} \tag{7.13}$$

where TOF_{corr} is the corrected neutron time-of-flight and d is the distance from the target to the LENDA bar.

A random coincidence event is an event where the neutron detected by LENDA and the ^{10}C detected by the S800 were completely uncorrelated. Because the neutron and ^{10}C were uncorrelated, they could have come from the same beam bunch or from different beam bunches. There is no preference as to whether or not they came from the same beam bunch; a random coincidence between a neutron and ^{10}C in bucket X is just as likely to occur as a random coincidence between a neutron in bucket X and a ^{10}C in bucket Y. Hence the random coincidence time-of-flight spectrum is periodic with a period equal to the RF period.

The light-output threshold applied earlier in the analysis ensured that there were no charge-exchange events beyond $TOF_{1m}^{max} \approx 119$ ns. Therefore all events with $TOF_{1m}^{max} > 119$ ns were random coincidences. The random-coincidence background model was created from a TOF_{1m} window starting at $TOF_{1m} = 130$ ns with a width equal to the normalized RF time. Figure 7.3 shows the TOF_{1m} spectra for all LENDA bars, with the black lines indicating the sample window. NL12 (Bar Number 0) had a significantly shorter window
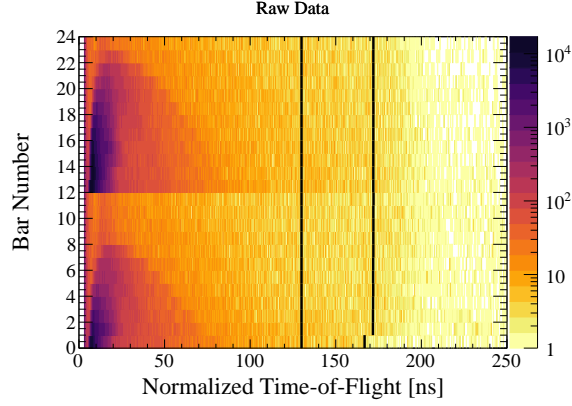
Figure 7.3: Normalized time-of-flight spectrum for each LENDA bar for the 2.3290 Tm setting. The black lines indicate the random coincidence sampling window. The light output maximum cut is not applied so the data at large TOF_{1m} can be seen.
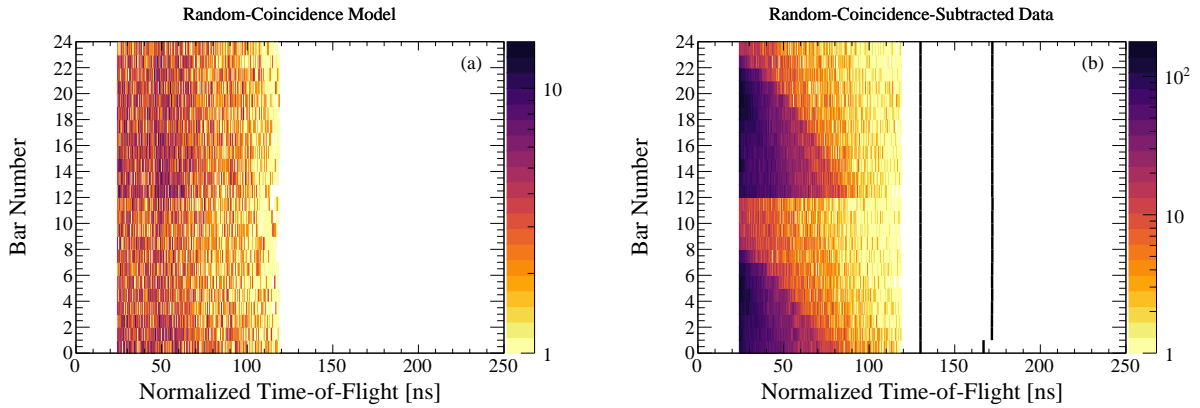
Figure 7.4: (a) Random coincidence background model for each LENDA bar for the 2.3290 Tm setting. (b) Data minus the random coincidence background for each LENDA bar for the 2.3290 Tm setting. The black lines indicate the LENDA bars used to create the background model.

than the rest of the LENDA bars because it was farther from the target (1.14 m). Then the data in this TOF_{1m} window were copied backwards to shorter times-of-flight. The original lab angle and light output were also copied to the new events.

After the random-coincidence background model was created, events with $TOF_{1m} >$ 119 ns or $TOF_{1m} < 24.3$ ns (corresponding to the maximum kinetic energy defined in Section 6.3.5.2) were removed.

Figure 7.4(a) shows the random-coincidence background model, and Figure 7.4(b) shows
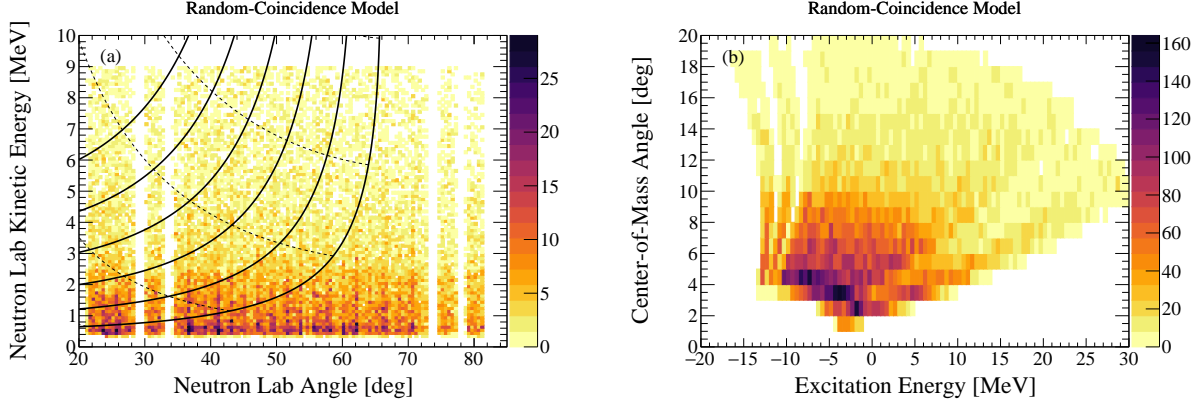
Figure 7.5: Random-coincidence model, N_{rand}, in the (a) lab frame and (b) the center-of-mass frame for the 2.3290 Tm setting.
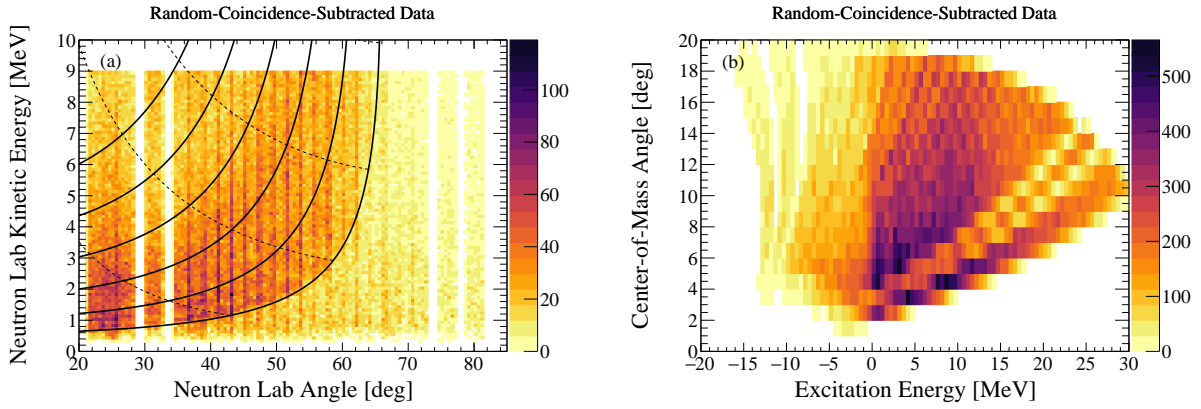
Figure 7.6: Raw data minus random-coincidence model, $N_{raw} - N_{rand}$, in (a) the lab frame and (b) the center-of-mass frame for the 2.3290 Tm setting.

the data with the random-coincidence background model subtracted. Although the model was created by copying events at long times to shorter times, the model had more counts at shorter times. This is due to the light-output cut, which is very restrictive at low kinetic energies, i.e. the cut removes more counts for longer times-of-flight. The random coincidence model is shown in the lab frame and center-of-mass frame in Figure 7.5, and the random-coincidence-subtracted data are shown in Figure 7.6. The random-coincidence background model introduced no systematic error.
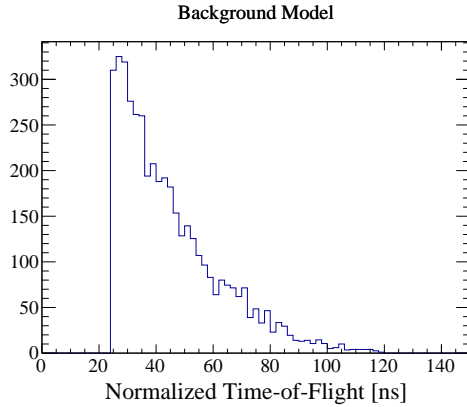
Figure 7.7: Beam-induced background model from NL08-NL11 for the 2.3290 Tm setting.

7.2.1.3 Beam-Induced Background from Other Reactions

When the beam impinged on the target, charge-exchange reactions were not the only re-actions that occurred. Indeed, the PID removed many other reaction channels, however, the PID could not remove non-charge-exchange reactions that yielded a ^{10}C in the S800 focal plane and a neutron in LENDA. The most significant component of this background in the ^{10}C settings was likely neutron knockout from ^{11}C (2.3290 Tm) or ^{12}N (2.4900 Tm). Any kind of breakup reaction could create background in the α-particle rigidity settings (2.8000 Tm and 3.0000 Tm).

According to the kinematics of the reaction, there were no charge-exchange neutrons beyond $65.5°$ given the cut $KE_n < 9$ MeV. The bars NL08-NL11 occupied these backward angles (indicated by the black lines in Figure 7.4(b)) and therefore had no charge-exchange events, so they were used to create the background model. The resulting background model shape is shown in Figure 7.7.

The background model shape was scaled such that the total counts below $E_x = 0$ MeV

would be equal to zero:

$$N_{bg} = S_{bg} N_{bg}^{NL} \tag{7.14}$$

$$S_{bg} = \frac{N_{raw}^{Ex<0} - N_{rand}^{Ex<0}}{(N_{bg}^{NL})^{Ex<0}} \tag{7.15}$$

where N_{bg}^{NL} is the number of counts measured by NL08-NL11, S_{bg} is the scaling factor

for the background model, and N_{bg} is the number of counts in the final scaled background

model. $N_{raw}^{Ex<0}$, $N_{rand}^{Ex<0}$, and $(N_{bg}^{NL})^{Ex<0}$ are the number of counts below $E_x = 0$ MeV in the

TOF_{1m} spectra of each detector's raw data, random-coincidence background model, and non-

charge-exchange background model, respectively. The background model and background-

subtracted data are shown in Figures 7.8 and 7.9, respectively.

The uncertainty in the counts below $E_x = 0$ MeV gave the scaling factor some systematic

error $\sigma_{S_{bg}}^{sys}$, which was propagated to the error in N_{bg}, σ_{bg}^{sys}:

$$\sigma_{S_{bg}}^{sys} = \frac{1}{(N_{bg}^{NL})^{Ex<0}} \sqrt{N_{meas}^{Ex<0} + N_{rand}^{Ex<0} + (N_{bg}^{NL})^{Ex<0} S_{bg}^2} \tag{7.16}$$

$$\sigma_{bg}^{sys} = N_{bg} \sigma_{S_{bg}}^{sys} \tag{7.17}$$

7.2.1.4 Background Subtraction Result

The background-subtracted measured counts N_{meas} was calculated as:

$$N_{meas} = N_{raw} - N_{foil} - N_{rand} - N_{bg} \tag{7.18}$$

Projections of the raw data and background models onto the excitation-energy axis are shown

in Figure 7.10, and projections of the background-subtracted data are shown in Figure 7.11.
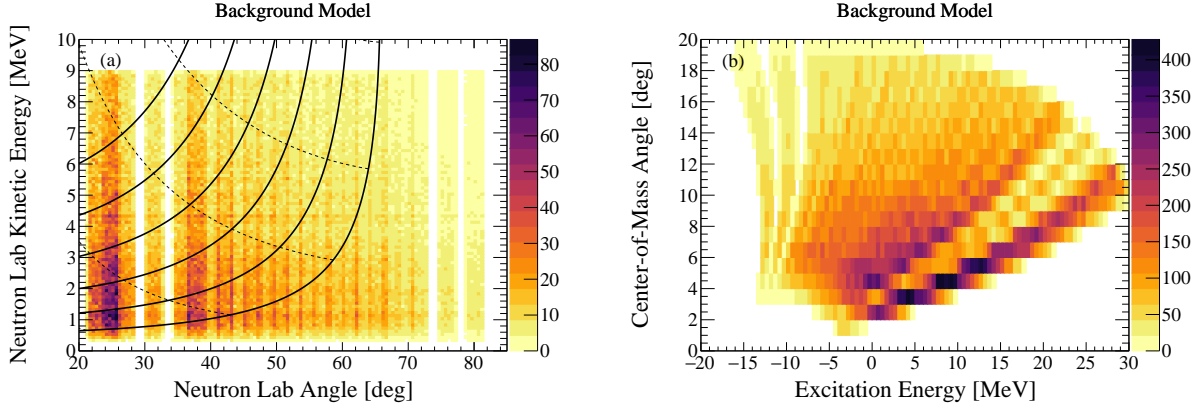
Figure 7.8: Background model, N_{bg}, in (a) the lab frame and (b) the center-of-mass frame for the 2.3290 Tm setting.
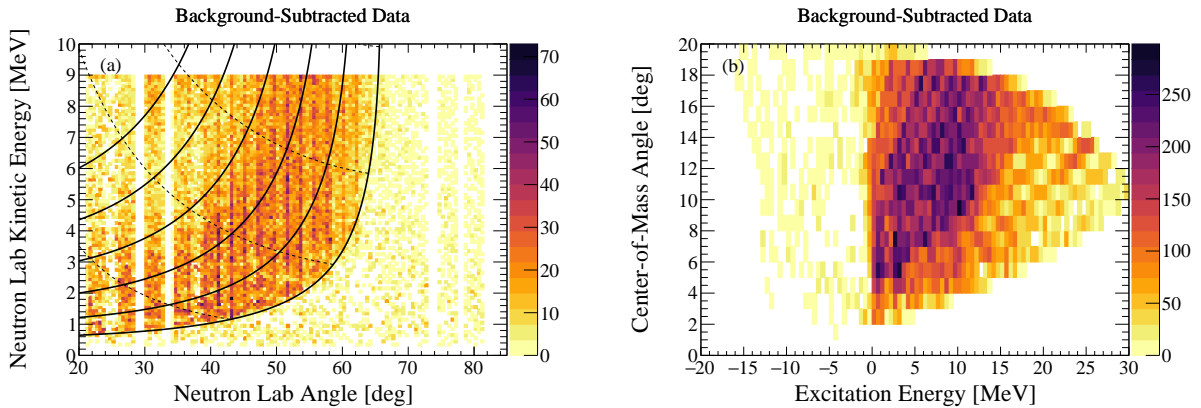
Figure 7.9: Background-subtracted data, N_{meas}, in (a) the lab frame and (b) the center-of-mass frame for the 2.3290 Tm setting.

Note that a continuum background component from quasi-free reactions has not been subtracted. Based on other charge-exchange reactions with light nuclei, this contribution is small at the low excitation energies of interest in this work. Additionally, the continuum contribution is not forward peaked, so any small contribution that is present will be filtered out in the Multipole Decomposition Analysis (Section 8.2.1).

The error from the light-output maximum cut (Section 6.3.5.3) was evaluated at this point in the analysis. The scaling factor of this cut was varied by ± 0.1, and the background subtraction was repeated. The ± 0.1 was an estimate of how distinctly the LO_{max} boundary could be discerned in the data. The error in N_{meas} from the scaling factor was calculated
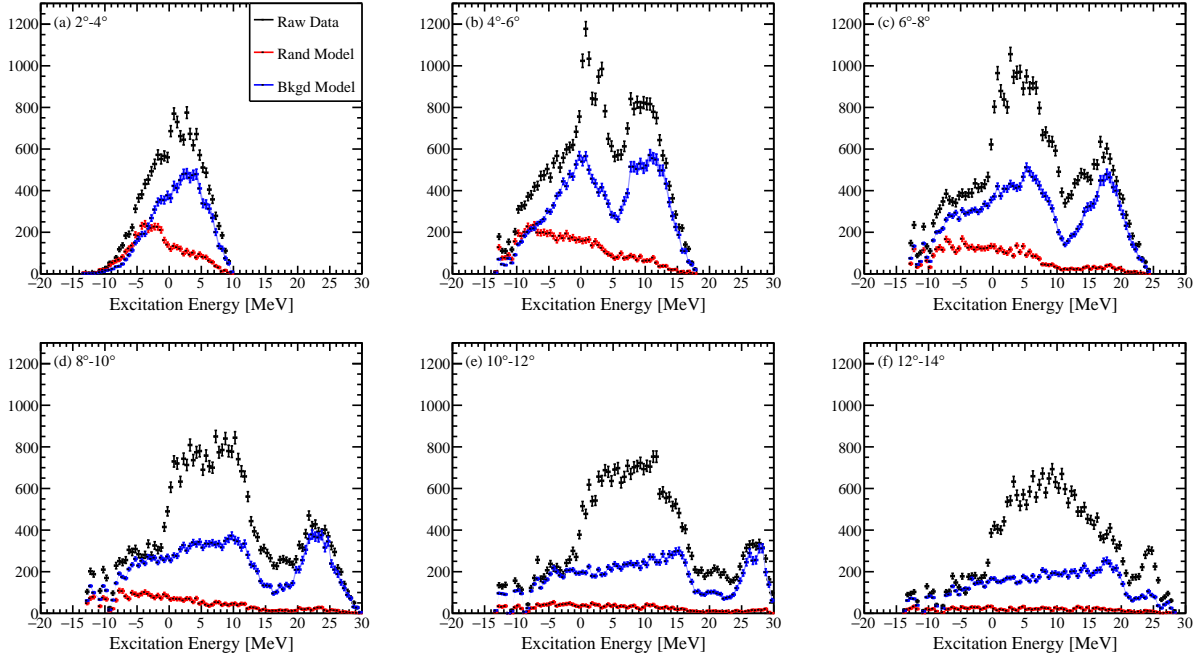
Figure 7.10: Excitation-energy spectra of the raw data N_{raw} (black), random coincidences N_{rand} (red), and other background N_{bg} (blue) for the 2.3290 Tm setting. Light blue bands indicate systematic error in the background model.
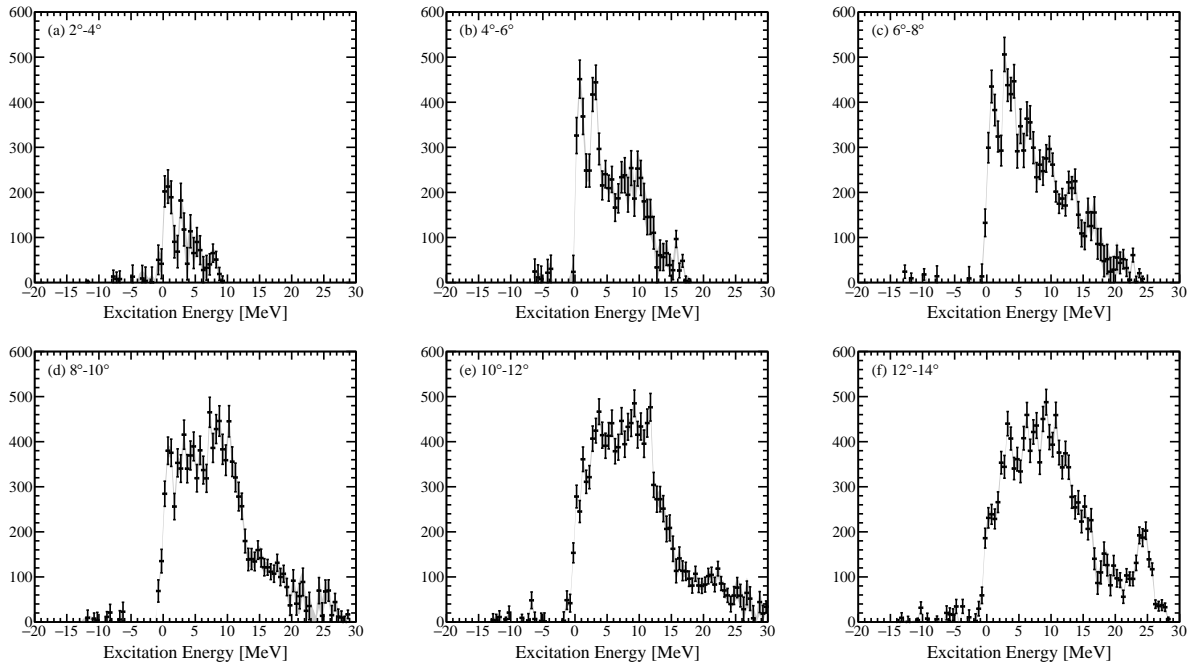
Figure 7.11: Background-subtracted excitation-energy spectra, N_{meas} for the 2.3290 Tm setting. Gray bands indicate systematic error.

as:

$$\sigma_{meas}^{LOcut} = \frac{1}{2} \left(\left| N_{meas}^{+0.1} - N_{meas} \right| + \left| N_{meas}^{-0.1} - N_{meas} \right| \right) \tag{7.19}$$

where $N_{meas}^{\pm 0.1}$ is the number of measured counts obtained from the analysis with the scaling factor increased/decreased by 0.1.

The only contribution to the systematic error in N_{meas} from the background subtraction was that from the beam-induced background, σ_{bg}^{sys} (Eq. 7.17). The error contributions from the background subtraction σ_{bg}^{sys} and from the light-output cut σ_{meas}^{LOcut} were added in quadrature to get the total N_{meas} systematic error:

$$\sigma_{meas}^{sys} = \sqrt{(\sigma_{bg}^{sys})^2 + (\sigma_{meas}^{LOcut})^2} \tag{7.20}$$

7.2.2 LENDA and S800 Acceptance

The result of the background subtraction was the number of reactions actually measured in the experiment. The next step was to correct measured counts for all the ways a reaction might not be measured, including the efficiency of the detectors and various cuts applied to the data. In this section, the acceptance of LENDA and the S800 is calculated and used to determine the LENDA+S800-acceptance-corrected counts.

The Geant4 simulation (Section 7.2.2.1) was used to do this correction. First, the reaction was simulated with a uniform excitation-energy distribution (Section 7.2.2.2). The same cuts that were applied to the experimental data were also applied to the simulated data. Next, the LENDA+S800 acceptance was calculated from the simulated data. Then the experimental data were corrected by dividing the data by the acceptance.

A second iteration of this correction was done because the acceptance correction depended on the input distribution in the simulation (Section 7.2.2.3). To use the most accurate input possible, the corrected experimental counts found in the previous step were used as input for the simulation, multiplied by 10 to get good statistics. Then the procedure described above was repeated to get the acceptance-corrected counts used in the analysis. Last, the error in the acceptance due to uncertainties in the simulation was evaluated (Section 7.2.2.4).

7.2.2.1   Geant4 Simulation

The Geant4 Simulation Toolkit is a toolkit for simulating "the passage of particles through matter" [119]. The beam energy and profile discussed in Sections 6.1.4 and 6.1.5 were used to define the beam in the simulation. The liquid hydrogen target was simulated as a cylinder made of liquid hydrogen with the density given in Section 7.4, and a Kapton foil was placed at either end of the cylinder. The LENDA detectors were modeled as rectangular prisms made of hydrogen and carbon with a ratio of H:C=1.104 and a density of 1.023 g/cm^3, according to the BC-408 scintillator specifications [121]. The target was placed at the origin, and the LENDA bars were placed around it according to the laser tracker measurements discussed in Section 6.3.1.

When the beam impinged on the target in the simulation, the simulation randomly selected a z-position within the target as the location of the charge-exchange reaction. Upon passing the determined z-position, the beam particle was destroyed and the ejectile and recoil particles were created according to relativistic two-body kinematics. The ^{11}N or ^{12}O ejectile was created in a state with $E_x = 0 - 30$ MeV at intervals of 0.1 MeV.

The decay mechanisms of ^{12}O and ^{11}N are not well-established. Nothing is known experimentally above $E_x = 7$ MeV in ^{10}C, and the branching ratios for levels between 3 and

7 MeV are also not well-established. Therefore simple decay schemes were assumed in the simulation. The error introduced from these simplified decay schemes is evaluated in Section 7.2.2.4. In the ^{10}C rigidity settings' simulations, the states decayed by one-proton (^{11}N) or two-proton (^{12}O) emission to the ground state of ^{10}C.

The decay is more complicated for the α-particle rigidity settings because ^{10}C can decay through many channels that yield $2\alpha+2p$, including ^{9}B$+p$, ^{8}Be$+2p$, ^{6}Be$+\alpha$, or ^{5}Li$+\alpha+p$. In this simulation, states with $E_x(^{12}O) < 2.3$ MeV decayed by one-proton emission to ^{11}N[g.s.], and states with $E_x(^{12}O) \geq 2.3$ MeV decayed by one-proton emission to ^{11}N[2.7 MeV]. States with $E_x(^{11}N) < 2.7$ MeV decayed to ^{10}C[g.s.], which did not decay further. States with $E_x(^{11}N) \geq 2.7$ MeV decayed by two-proton emission to ^{9}B[g.s], which decayed by one-proton to ^{8}Be[g.s.], which finally decayed to 2α. See the level schemes in Figure 7.12.

7.2.2.2 First Iteration LENDA+S800 Acceptance Correction

The LENDA+S800 acceptance accounts for events lost due to the imperfect LENDA intrinsic and geometric efficiencies and due to the finite S800 momentum and angular acceptances; it does not account for loss due to focal-plane detector efficiencies, other cuts, or DAQ dead time. These other sources of loss will be discussed in Section 7.2.3. The first-iteration acceptance $\epsilon_{LENDA+S800}^{1st}$ was estimated from the simulation as the ratio of the number of simulated output events $N_{Sim\ out}^{1st}$ to the number of simulated input events $N_{Sim\ in}^{1st}$:

$$\epsilon_{LENDA+S800}^{1st} = \frac{N_{Sim\ out}^{1st}}{N_{Sim\ in}^{1st}} \tag{7.21}$$

The first iteration of the acceptance correction was done with a uniform ^{11}N or ^{12}O excitation-energy spectrum. The simulated input was smeared to match the resolution of
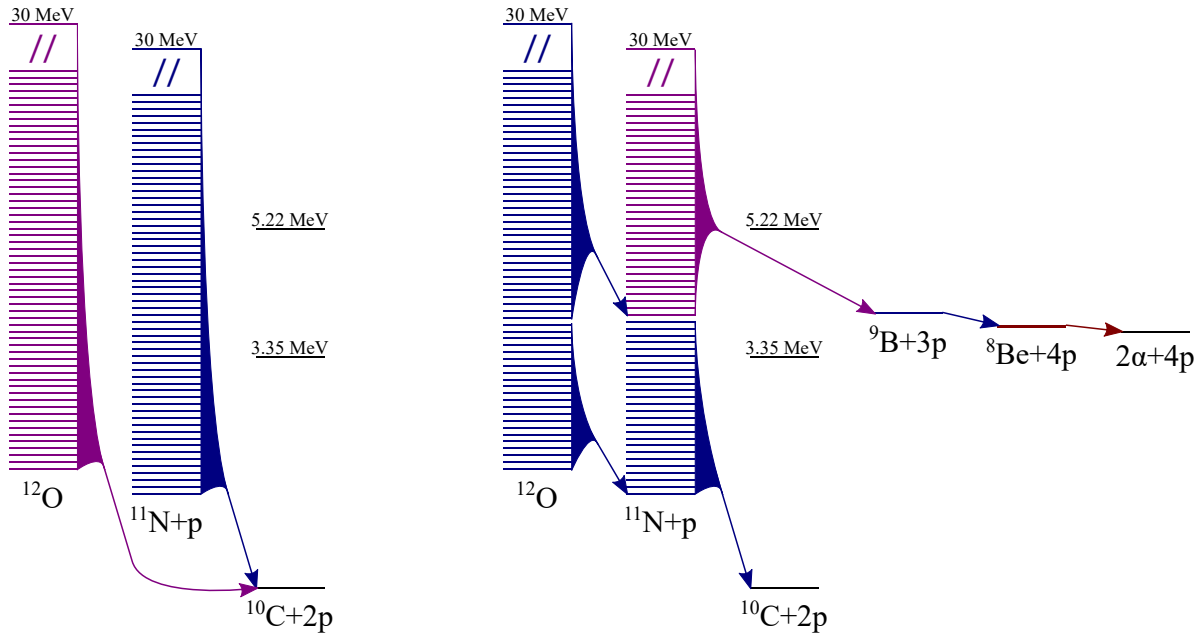
Figure 7.12: Simulated decay scheme for the ^{10}C rigidity settings (left) and α-particle rigidity settings (right). Branching ratios for every state are 100% to the indicated daughter state. This scheme is simplified from reality for the purposes of the simulation.
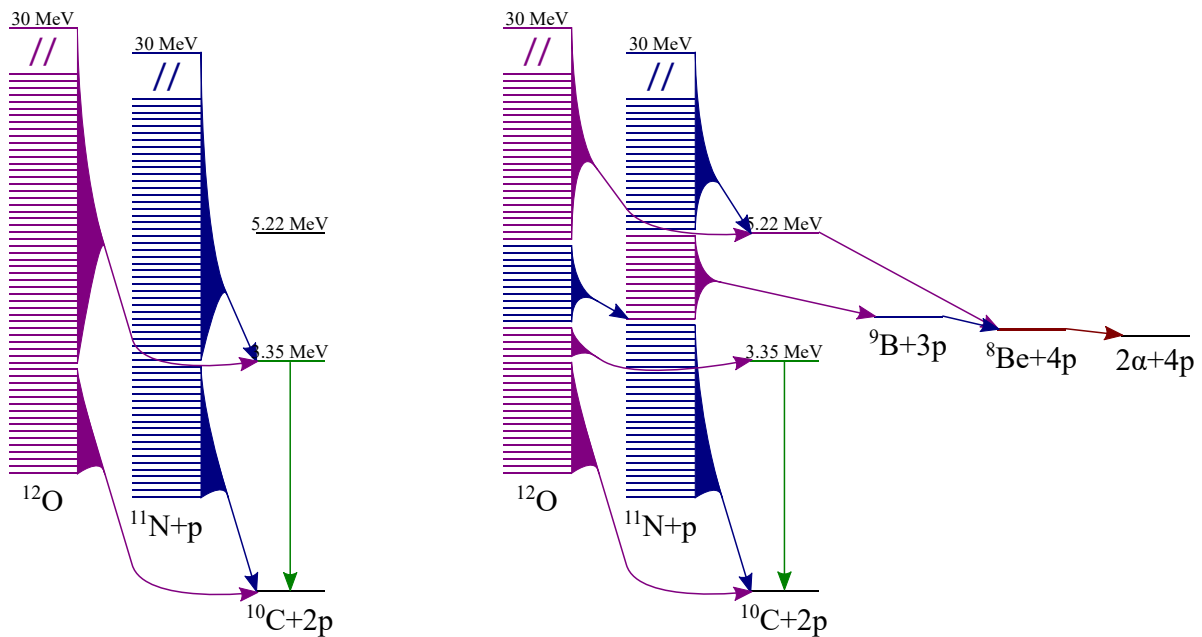
Figure 7.13: Alternative simulated decay scheme for the ^{10}C settings (left) and α settings (right) for error evaluation. Branching ratios for every state are 100% to the indicated daughter state. This scheme is simplified from reality for the purposes of the simulation.
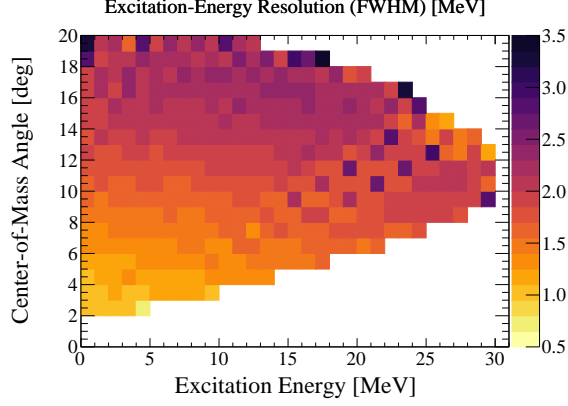
Figure 7.14: Simulated E_x resolution for the 2.3290 Tm rigidity setting.

the output. The resolution as a function of excitation energy and center-of-mass scattering angle was found from the simulated output data, shown in Figure 7.14 for the 2.3290 Tm rigidity setting. The resolution at higher excitation energies was distorted by the holes in the LENDA acceptance, so the input was smeared as a function of angle only using the resolutions at $E_x = 0$ MeV for the ^{10}C settings and $E_x = 5$ MeV for the α settings.

Figure 7.15 shows the smeared simulated input $N^{1st}_{Sim\ in}$, Figure 7.16 shows the simulated output $N^{1st}_{Sim\ out}$, and Figure 7.17 shows the acceptance $\epsilon^{1st}_{LENDA+S800}$. Then the first-iteration LENDA+S800-acceptance-corrected counts, shown in Figure 7.18, was calculated as:

$$(N'_{rxn})^{1st} = \frac{N_{meas}}{\epsilon^{1st}_{LENDA+S800}} \tag{7.22}$$

7.2.2.3 Second Iteration S800+LENDA Acceptance Correction

Due to spatial limitations around the beamline, the LENDA acceptance had holes between SL02-03 and SL03-04. The holes can be seen in the lab-frame kinematics plots, Figure 7.1. The holes caused distortions to $\epsilon_{LENDA+S800}$, and these distortions were mitigated by doing
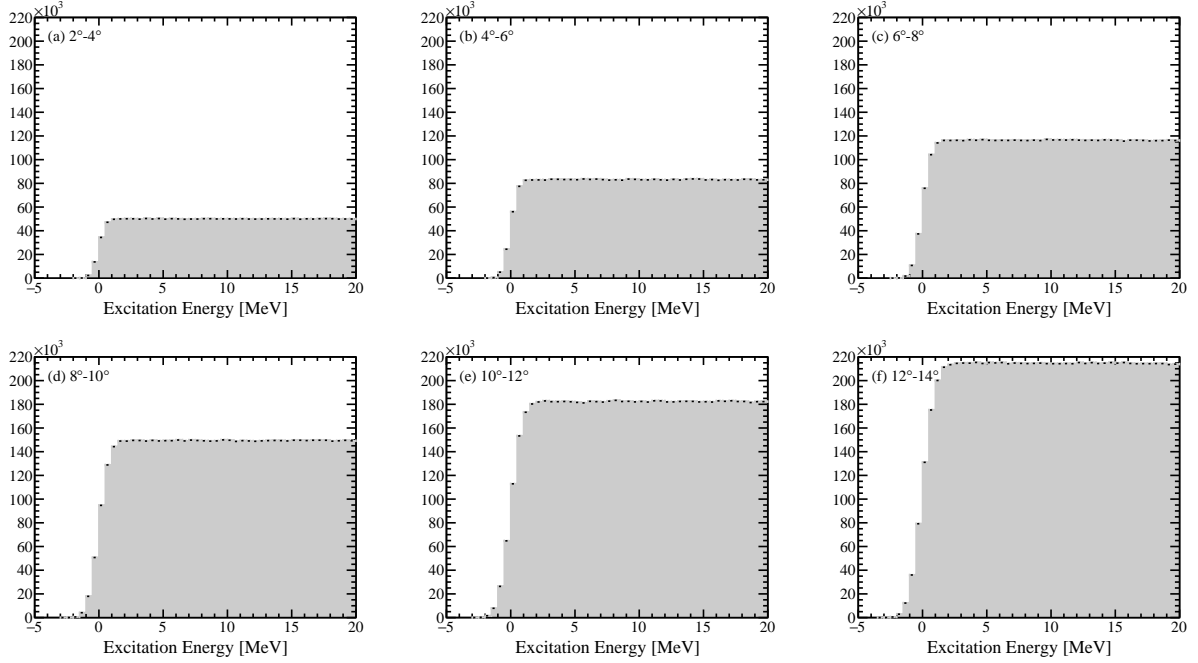
Figure 7.15: First-iteration simulated input, smeared, $N_{Sim\,in}^{1st}$.
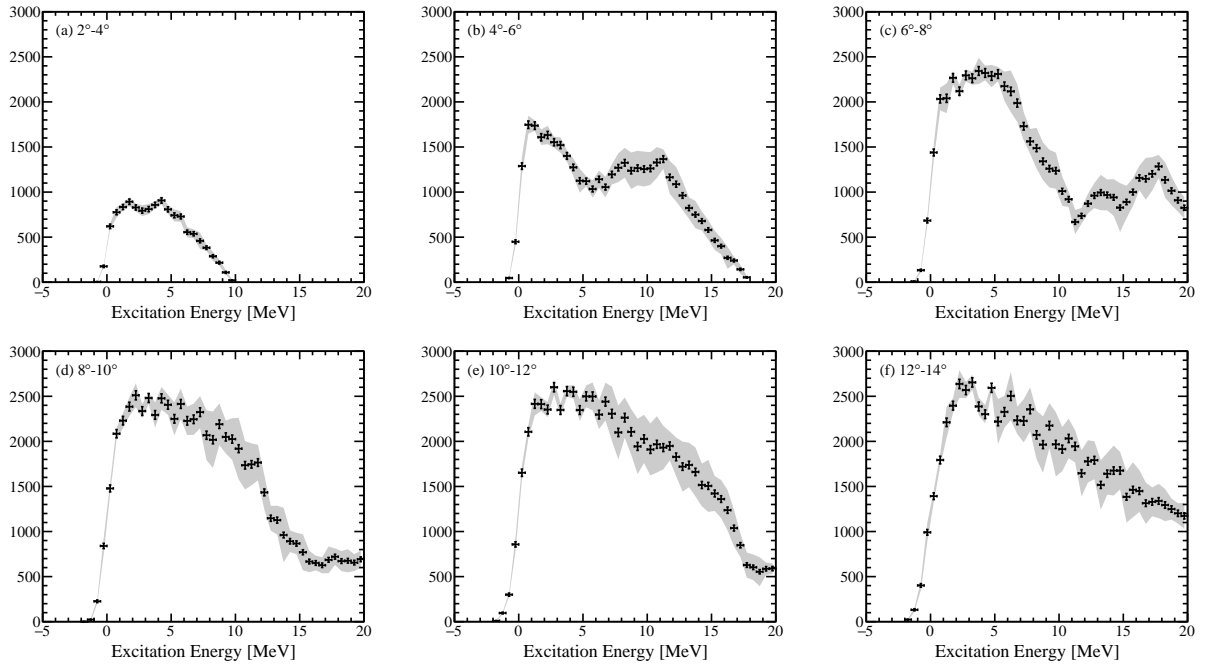
Figure 7.16: First-iteration simulated output, $N_{Sim\,out}^{1st}$.

127
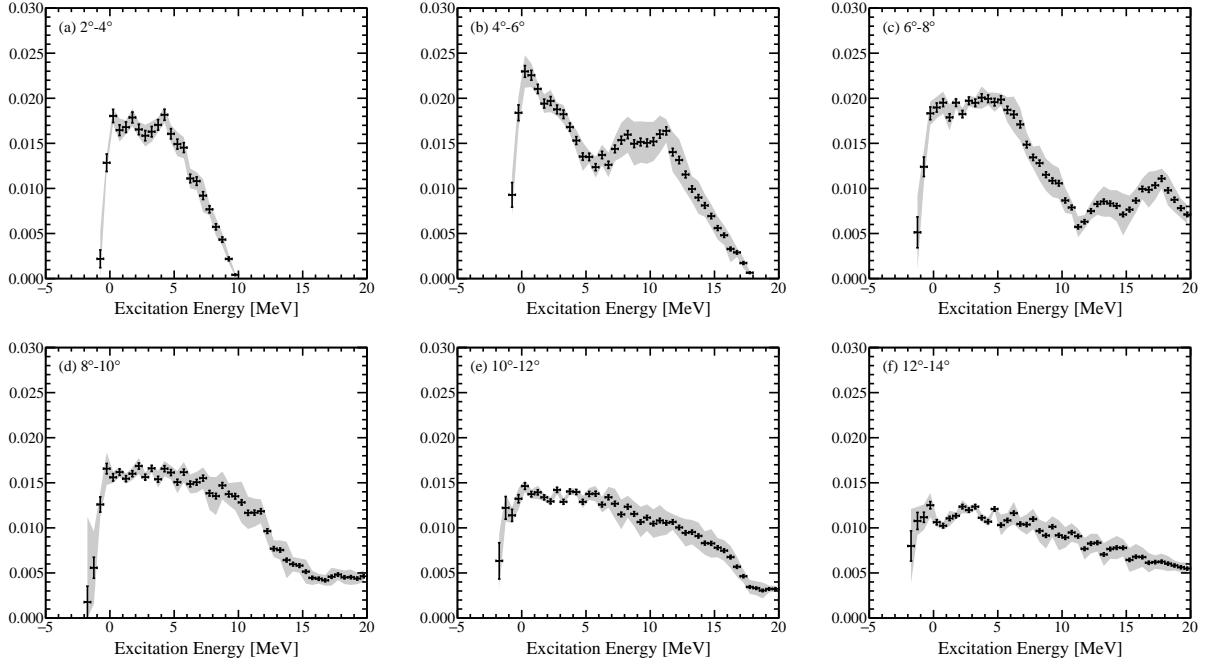
Figure 7.17: First-iteration simulated acceptance, $\epsilon^{1st}_{LENDA+S800}$.
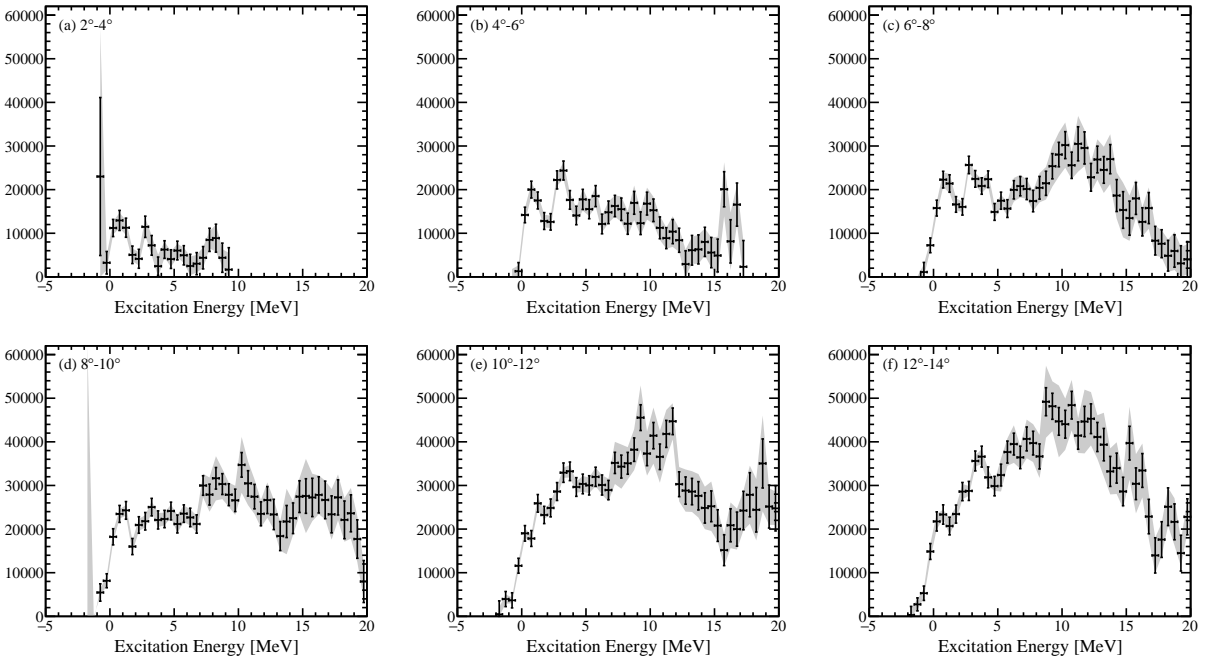
Figure 7.18: First-iteration LENDA+S800 acceptance-corrected counts, $(N'_{rxn})^{1st}$.

a second iteration of the LENDA+S800-acceptance correction. A toy model illustrating why a second iteration is necessary is given in Appendix A. $(N'_{rxn})^{1st}$ from the previous section was used as input for a second iteration of the simulation, and the process was repeated:

$$\epsilon_{LENDA+S800} = \frac{N_{Sim\ out}}{N_{Sim\ in}} \tag{7.23}$$

$$N'_{rxn} = \frac{N_{meas}}{\epsilon_{LENDA+S800}} \tag{7.24}$$

where $N_{Sim\ in}$ is $(N'_{rxn})^{1st}$ smeared (Figure 7.19), and $N_{Sim\ out}$ is the second-iteration output (Figure 7.20). $\epsilon_{LENDA+S800}$ is shown in Figure 7.21, and the LENDA+S800-acceptance-corrected counts, N'_{rxn}, are shown in Figure 7.22. A second iteration was not done for the α-particle rigidity settings due to poor statistics.

7.2.2.4 LENDA+S800 Acceptance Error

The LENDA+S800 acceptance was defined by LENDA's intrinsic and geometric efficiencies and the S800 momentum and angular acceptances. LENDA's intrinsic efficiency is defined by both the physics of the neutron interacting with the scintillator and the light-output threshold; a higher neutron scattering cross section means a higher intrinsic efficiency, and a higher light-output threshold means a lower intrinsic efficiency. The simulation has been benchmarked against data and other codes, and minor adjustments have been made to ensure consistency [92, 93, 94], so the error from the Geant4 physics models was small compared to the error from the light-output threshold.

LENDA's geometric efficiency was defined by the LENDA bars' positions, i.e. the bars' angles and distances from the target. The geometric efficiency is not very sensitive to the distances; moving the LENDA bars from 1 m to 1 m+1 mm decreases their solid angle
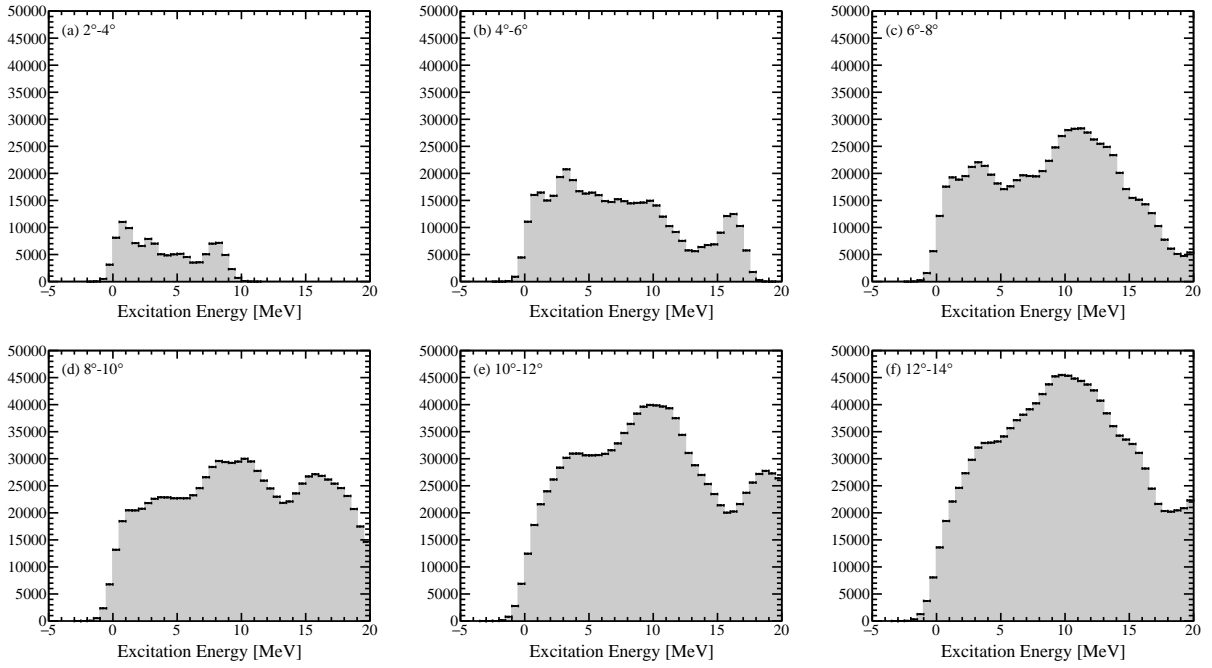
Figure 7.19: Second-iteration simulated input, smeared, $N_{Sim\,in}$.
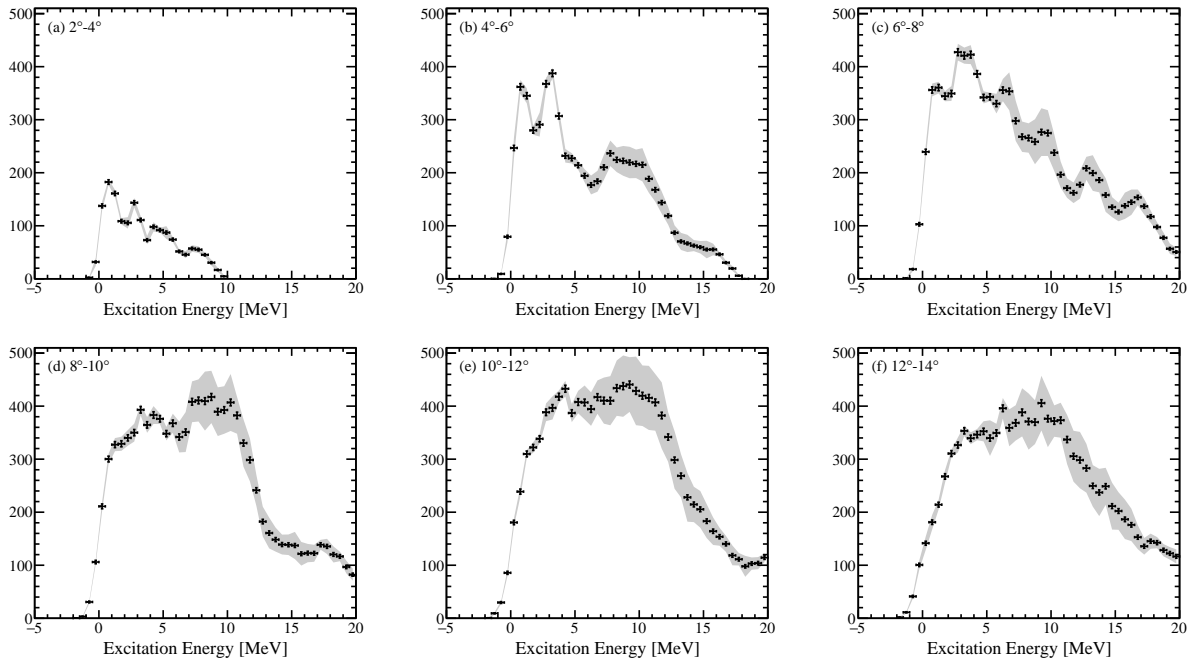
Figure 7.20: Second-iteration simulated output, $N_{Sim\,out}$.
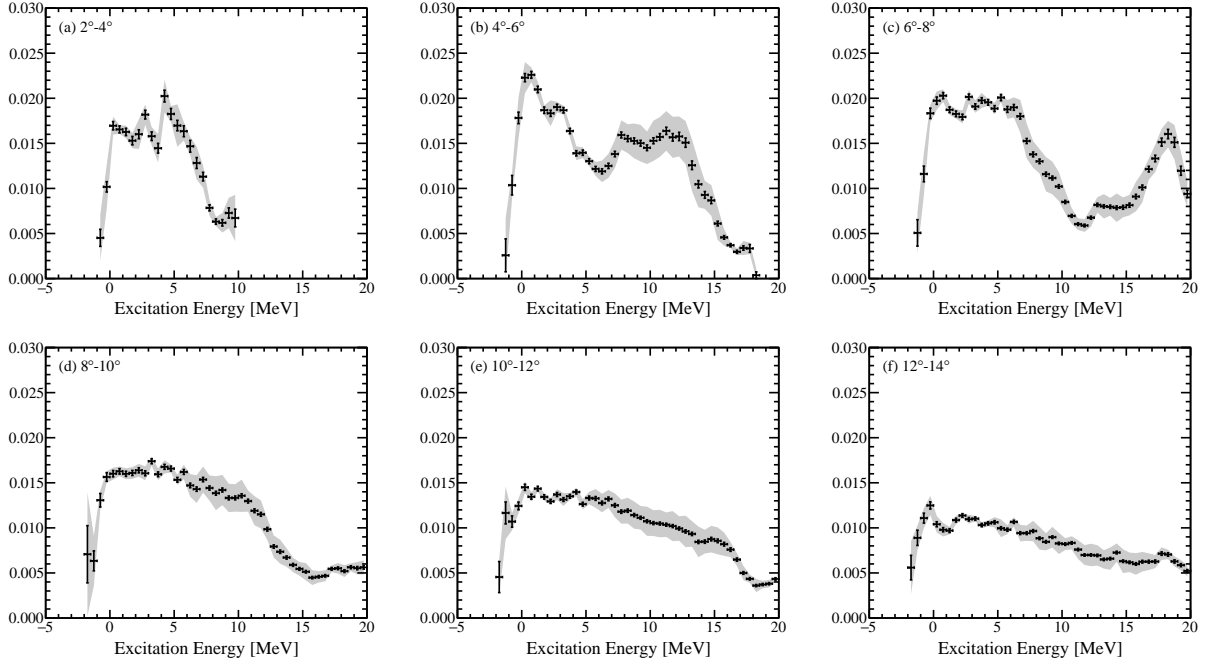
Figure 7.21: Second-iteration simulated acceptance, $\epsilon_{LENDA+S800}$.
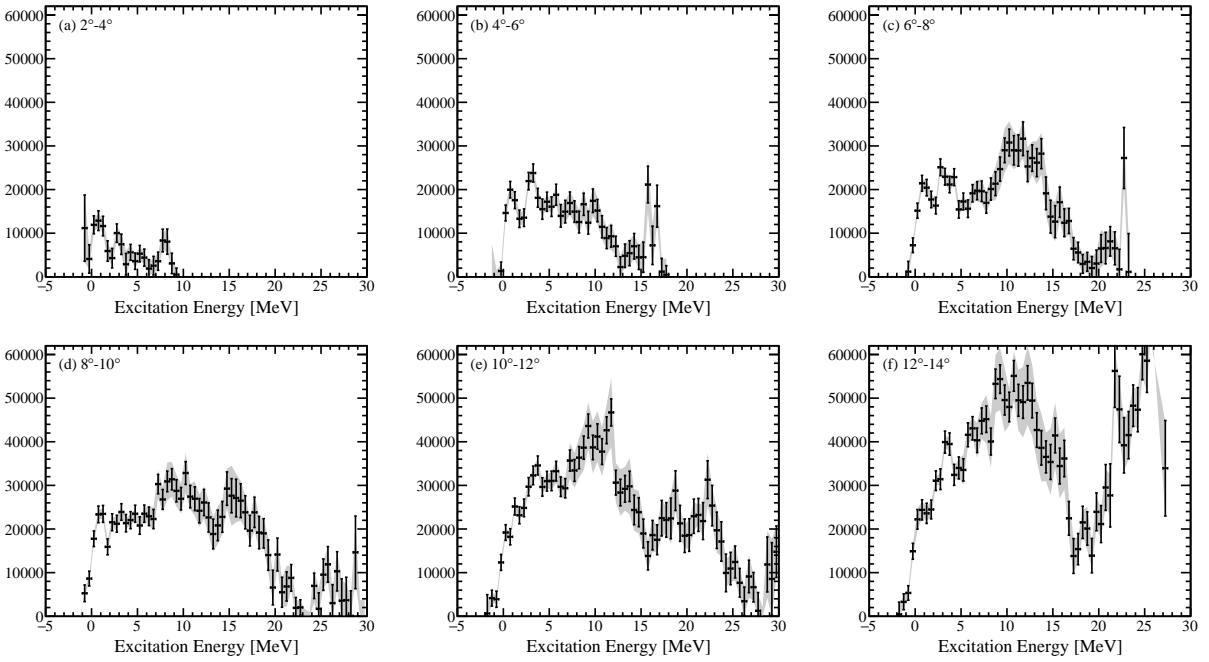
Figure 7.22: Second-iteration LENDA+S800 acceptance-corrected counts, N'_{rxn}.

131

from 0.1800 sr to 0.1796 sr, a negligible reduction of about 0.2%. Therefore only the angle uncertainty was propagated.

The S800 angular and momentum acceptances were well-known from the data. Recall that the S800 acceptance defined the ranges of reaction product angles and momenta that could reach the S800 focal plane. The momentum and angular distributions of the final products depended on how the particles react and decay. Therefore the kinematics in the simulation affected the number of reaction products measured. The kinematics of the charge-exchange reaction are well-defined, but the subsequent decays are not, so the reaction product decay was a source of error.

Therefore the simulation had three sources of error:

- LENDA light-output threshold

- LENDA position

- Reaction product decay

These errors were quantified by changing the simulation input parameters, re-running the simulation, and propagating the effect to N'_{rxn}.

The magnitude of the light-output gain drifts was estimated from the change in light-output calibrations done before and after the experiment. First, the uncalibrated light output that corresponded to the 65 keVee threshold was calculated using the pre- and post-experiment calibration parameters. Then the difference between the two uncalibrated values was multiplied by the calibration slope to get the change in units of keVee. The result is shown in Figure 7.23, and the standard deviation was 1 keVee, excluding NL12, which broke before the post-calibration data were taken (but after the experiment ended). Therefore the
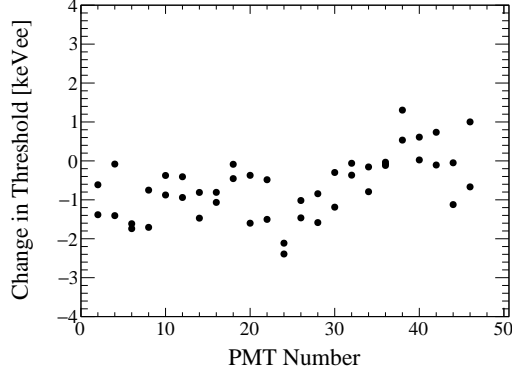
Figure 7.23: Change in LENDA light-output threshold from before to after the experiment.

simulation was repeated with the light-output threshold set to 64 keVee and 66 keVee to estimate the error due to the light-output gain drifts.

The uncertainty in the LENDA angle was $0.0572°$ based on the laser tracker measurement (1 mm on a circle with a 1 m radius), and the simulation was repeated with the LENDA bars all shifted forward or backward by $0.0572°$. Although shifting the LENDA bars does not impact the magnitude of the LENDA efficiency, it does change the shape of the efficiency, so evaluating this source of error is important.

Finally, the decay scheme was changed to estimate the error from uncertainties in the decay channels. In the alternative decay scheme, for the ^{10}C rigidity settings, states with $E_x(^{12}O) < 1.8$ MeV decayed by 2-proton emission to ^{10}C[g.s.], and states with $E_x(^{12}O) \geq 1.8$ MeV decayed by 2-proton emission to ^{10}C[3.354 MeV]. States with $E_x(^{11}N) < 2.1$ MeV decayed by proton emission to ^{10}C[g.s.], and states with $E_x(^{11}N) \geq 2.1$ MeV decayed by two-proton emission to ^{10}C[3.354 MeV]. Any state above $E_x = 3.354$ MeV in ^{10}C decayed by particle emission to $2\alpha+2p$, so no other states in ^{10}C needed to be included for these simulations.

Again, the α-particle rigidity settings were more complicated. For ^{12}O: $E_x(^{12}O) < 1.8$ MeV states decayed by two-proton emission to ^{10}C[g.s.], $1.8 \leq E_x(^{12}O) < 2.3$ MeV

states decayed by one-proton emission to ^{10}C[3.354 MeV], $2.3 \leq E_x(^{12}O) < 3.5$ MeV states decayed by one-proton emission to ^{11}N[2.7 MeV], and $3.5 \leq E_x(^{12}O)$ MeV states decayed by two-proton emission to ^{10}C[5.22 MeV]. For ^{11}N: $E_x(^{11}N) < 2.7$ MeV states decayed by one-proton emission to ^{10}C[g.s.], $2.7 \leq E_x(^{11}O) < 4.0$ MeV states decayed by two-proton emission to ^{9}B[g.s.], 4.0 MeV $\leq E_x(^{11}N)$ states decayed by one-proton emission to ^{10}C[5.22 MeV]. The ^{10}C[5.22 MeV] and ^{9}B[g.s.] states decayed by two- and one-proton emission to ^{8}Be, which decayed to 2α. See the level schemes in Figure 7.13.

The results of the systematic error simulations (second iteration) are shown in Figure 7.24. The uncertainty from the decay scheme was generally the most important contribution. The systematic error in the simulation output was estimated as:

$$\sigma_{Sim\,out}^{sys} = \sqrt{\sigma_{LO}^2 + \sigma_{Angle}^2 + \sigma_{DecayScheme}^2} \tag{7.25}$$

where

$$\sigma_{LO} = \frac{1}{2}\left(\left|N_{Sim\,out}^{+1keVee} - N_{Sim\,out}\right| + \left|N_{Sim\,out}^{-1keVee} - N_{Sim\,out}\right|\right) \tag{7.26}$$

$$\sigma_{Angle} = \frac{1}{2}\left(\left|N_{Sim\,out}^{+1mm} - N_{Sim\,out}\right| + \left|N_{Sim\,out}^{-1mm} - N_{Sim\,out}\right|\right) \tag{7.27}$$

$$\sigma_{DecayScheme} = \left|N_{Sim\,out}^{Decay2} - N_{Sim\,out}\right| \tag{7.28}$$

Then the systematic error in $\epsilon_{LENDA+S800}$ was:

$$\sigma_{LENDA+S800}^{sys} = \frac{\sigma_{Sim\,out}^{sys}}{N_{Sim\,in}} \tag{7.29}$$
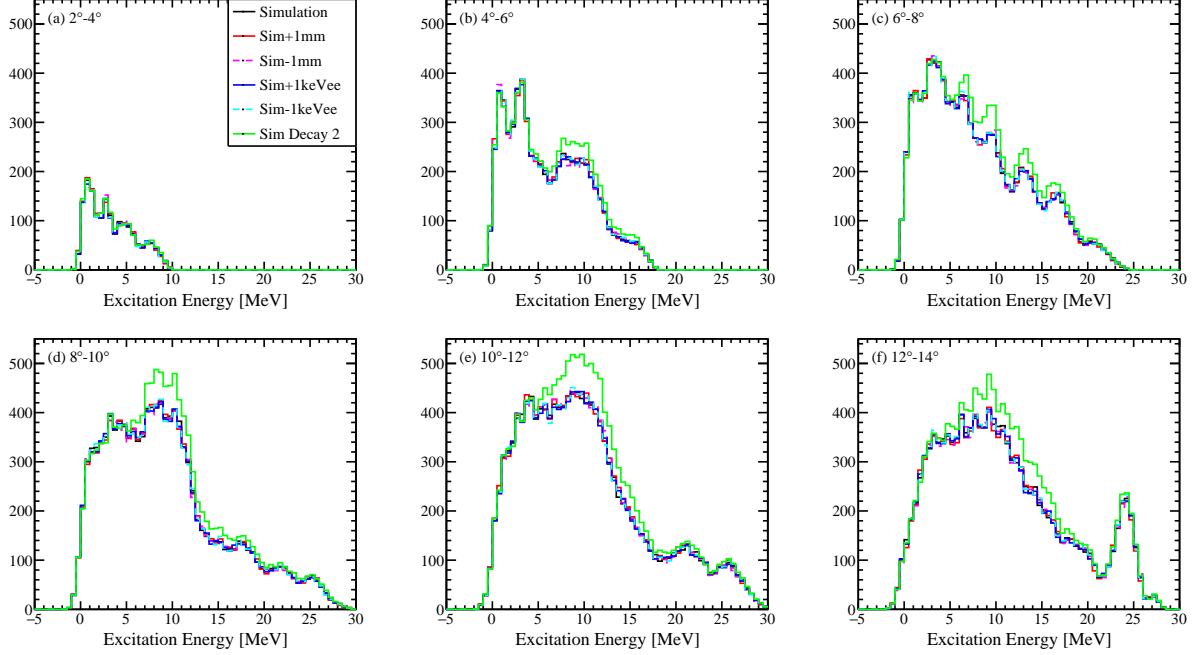
Figure 7.24: Second-iteration simulation output for error evaluation.

And the systematic error in N'_{rxn} was:

$$(\sigma'_{rxn})^{sys} = \frac{1}{\epsilon_{LENDA+S800}}\sqrt{(\sigma_{meas}^{sys})^2 + (\sigma_{\epsilon_{LENDA+S800}}^{sys})^2(N'_{rxn})^2} \qquad (7.30)$$

7.2.3 Reaction Product Measurement Efficiencies

In the previous section, the measured counts N_{meas} were corrected for the LENDA efficiency and S800 acceptance to get N'_{rxn}. In this section, N'_{rxn} is corrected for all the other ways reactions might not be measured to get the total number of reactions N_{rxn}. Other ways reactions were lost included the cuts applied in Ch. 6, the efficiencies of the S800 focal-plane detectors, and the DAQ live time. These efficiencies were found in previous sections and are summarized in Table 7.1 for convenience. Finally, the number of reactions that occurred

N_{rxn} was calculated:

$$N_{rxn} = \frac{N'_{rxn}}{\epsilon_{obj}\epsilon_{RF}\epsilon_{beamID}\epsilon_{CRDC}\epsilon_{IC}\epsilon_{scint}\epsilon_{PID}\epsilon_{mult}\epsilon_{DAQ}} \qquad (7.31)$$

where

N'_{rxn} = number of measured neutrons, corrected for LENDA and S800 acceptance

$\epsilon_{obj/RF}$ = efficiency of the TOF_{RF} and TOF_{obj} gates

ϵ_{beamID} = efficiency of the beam identification gates

ϵ_{CRDC} = CRDCs efficiency

ϵ_{IC} = ionization chamber efficiency

ϵ_{Scint} = focal-plane scintillator efficiency

ϵ_{PID} = efficiency of the PID gates

ϵ_{mult} = efficiency of LENDA multiplicity cut

ϵ_{DAQ} = DAQ live time

All ϵ in this section had uncertainties that were small compared to the uncertainty in N'_{rxn} and were therefore neglected. Then the error in N'_{rxn} was propagated to get the systematic error in N_{rxn}:

$$\sigma_{rxn}^{sys} = \frac{(\sigma'_{rxn})^{sys}}{\epsilon_{obj}\epsilon_{RF}\epsilon_{beamID}\epsilon_{CRDC}\epsilon_{IC}\epsilon_{scint}\epsilon_{PID}\epsilon_{mult}\epsilon_{DAQ}} \qquad (7.32)$$

The only efficiency that has not yet been discussed is the DAQ live time ϵ_{DAQ}. While the DAQ system was recording an event, it was "dead" and could not record a new event.

Table 7.1: Detector efficiencies and cuts for each rigidity setting.

	Section	2.3290 Tm	2.4900 Tm	2.8000 Tm	3.0000 Tm
$\epsilon_{obj/RF}$	6.1.1	100 %	100 %	100 %	100 %
ϵ_{beamID}	6.1.1	<100 %	<100 %	<100 %	<100 %
ϵ_{CRDC}	6.1.2	97 %	97 %	23 %	18 %
ϵ_{IC}	6.2.4	100 %	100 %	100 %	100 %
ϵ_{Scint}	6.2.4	100 %	100 %	100 %	100 %
ϵ_{PID}	6.2.4	<100 %	99 %	98 %	99 %
ϵ_{mult}	6.3.5.1	83 %	84 %	86 %	81 %
ϵ_{DAQ}	7.2.3	96 %	98 %	97 %	97 %

The fraction of events lost due to the DAQ dead time was calculated from the *Live.Trigger* and *Raw.Trigger* in the S800 scalers files:

$$\epsilon_{DAQ} = \frac{\sum_{run} \frac{(Live.Trigger)_{run}}{(Raw.Trigger)_{run}} \times t_{run}}{\sum_{run} t_{run}} \tag{7.33}$$

7.3   Beam Rate

The number of beam particles was calculated in three steps. First, the actual beam rate was calculated (Section 7.3.1). Then, ways that a beam particle might be lost were determined, and the actual beam rate was adjusted to take these losses into account (Section 7.3.2). Last, the beam purity was determined, and the beam rate of each species was calculated (Section 7.3.3).

7.3.1   Actual Beam Rate

The beam rate was measured by the S800 object detector, and these measurements were called the "scalers." The scalers rates were corrected for two effects to get the actual beam rate: a large beam spot and the beam bucket multiplicity.

The beam spot of a rare-isotope beam produced by projectile fragmentation is generally larger than that what can be achieved with stable beams. In this experiment, the secondary beam spot was larger than the active area of the object detector. The beam particles that did not hit the object detector's active area were not counted in the scalers. Data from the Full Cell Run (Run 198) of the unreacted beam setting were used to determine the fraction of beam particles that hit the active area of the object detector, f_{obj}. An $E_{IC} - TOF_{RF}$ PID gate on ^{11}C in the focal plane was applied to prevent the result from being skewed by bad events.

To find f_{obj}, a gate was first placed on events with good focal-plane scintillator energies E_{scint}, i.e. events where the beam particle reached the S800 focal plane. The fraction of particles that hit the object detector was taken as the fraction of those good-E_{scint} events that also had a good object time-of-flight TOF_{obj}:

$$f_{obj} = \frac{\text{Events with good } TOF_{obj} \text{ and } E_{scint}}{\text{Events with good } E_{scint}} = 81\% \qquad (7.34)$$

Due to the gate on good-E_{scint} events, this number does not include loss from imperfect transmission to the target. It also does not include loss from detector readout dead times because the rate in this run was very low.

In addition to the large beam spot, the scalers rate was also corrected for the bucket multiplicity. The primary beam was created in bunches with a certain frequency. Each primary beam bunch had many particles, and each primary beam particle had a small chance of being fragmented into the secondary beam particle of interest when it impinged on the fragmentation target. The result was that most beam bunches yielded no particles, some

yielded one particle, a few yielded two particles, etc. The number of secondary particles created from the primary beam bunch is called the bucket multiplicity.

The object detector readout's dead time was about 30 ns, and the RF period was about 42 ns. The scalers could count two beam particles in a single bucket if one arrived at the beginning of the bucket and another arrived at the end, but only one count was recorded per beam bucket most of the time. As a result, the number of counts recorded by the object detector was less than the actual number of beam particles. The severity of this effect increased as a function of beam rate.

The bucket-multiplicity effect was calculated from Poisson statistics.[1] First, for a beam rate r, the probability of getting k particles in a bucket is given by the Poisson distribution:

$$P(k \text{ particles in bucket given rate } r) = \frac{(rt)^k e^{-rt}}{k!} \tag{7.35}$$

Next, the probability to measure each particle is f_{obj}. The probability of measuring j particles given k total particles in the bucket is:

$$P(j \text{ measured particles given } k \text{ particles in bucket}) = \binom{j}{k}(1 - f_{obj})^{k-j}(f_{obj})^j \tag{7.36}$$

Then the total probability of measuring a count for any bucket is:

$$P(j > 0 \text{ measured particles given rate } r) =$$

$$\sum_{k, 0 < j \leq k} P(k \text{ particles in bucket given rate } r) \times$$

$$P(j \text{ measured particles given } k \text{ particles in bucket}) \tag{7.37}$$

---

[1]Please note that this a corrected version of the beam-bucket multiplicity calculation in Appendix C of Ref. [94].
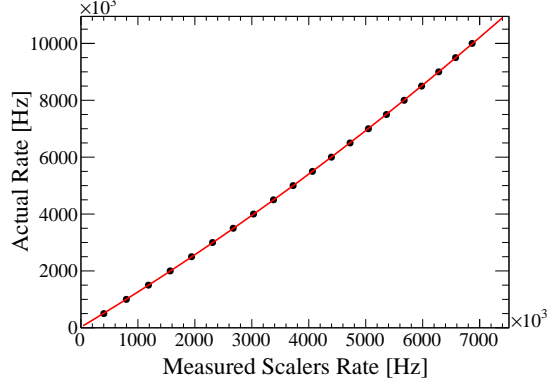
Figure 7.25: The black points are the measured scalers rate R_{scal} calculated from the actual beam rates R_{scal}^{corr}. The red line is a second-degree polynomial fit to the points. The fit was used to calculate R_{scal}^{corr} from R_{scal}.

Finally, the measured scalers rate R_{scal}, with units given in brackets, is:

$$R_{scal} = \frac{P(j > 0 \text{ measured particles given rate } r)[\text{counts}]}{[\text{bucket}]} \times \frac{1}{t \ [\text{seconds/bucket}]} \qquad (7.38)$$

Solving analytically for r is not possible, so instead $R_{scal}(r)$ was calculated for many points over the R_{scal} region of interest, and the points were fit to a second-degree polynomial $r(R_{scal})$, Figure 7.25. With the fit parameters a, b, and c, the actual beam rate $R_{scal}^{corr} = r$ was calculated from the scalers rate measured by the object detector R_{scal}:

$$R_{scal}^{corr}(R_{scal}) = a(R_{scal})^2 + bR_{scal} + c \qquad (7.39)$$

7.3.2 Beam Loss

After the actual beam rate R_{scal}^{corr} was calculated, the losses from that actual rate were determined. There were two sources of loss: a missing object time-of-flight TOF_{obj} and imperfect beam transmission from the object to the target.

140
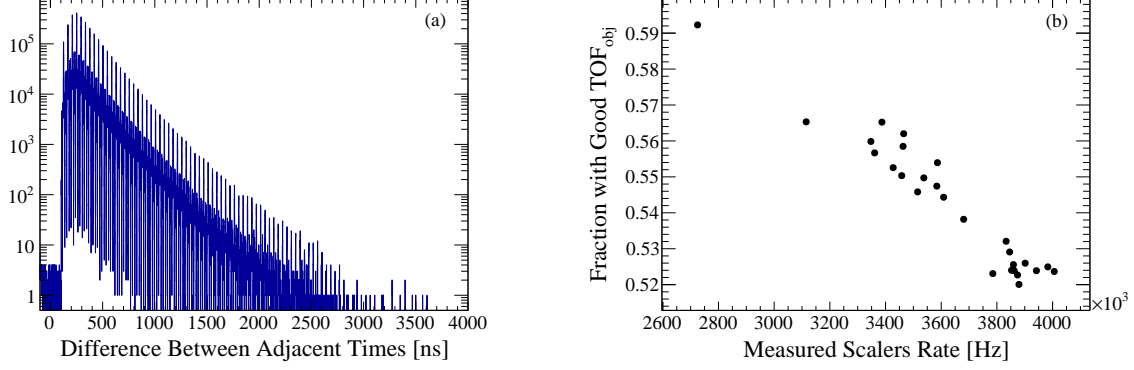
Figure 7.26: (a) Difference between adjacent object times for Run 232 (2.3290 Tm). The interval distribution of a random process is an exponential decay function, and this is reflected in the data. Additionally, this plot shows the structure of the beam (peaks at 42 ns intervals) and the variable dead time of the Multi-Hit TDC (gradual drop off from 235 ns to 100 ns). (b) f_{obj}^{run} for each run in the 2.3290 Tm rigidity setting.

As discussed previously, TOF_{obj} is critical for several steps of the analysis, and events without TOF_{obj} were discarded. A multi-hit TDC module recorded the object time used to calculate TOF_{obj}. Of course, if the beam particle did not hit the object detector, then the TDC did not record the time, and this effect was calculated above. Additionally, the TDC module had a variable dead time of about $100 - 235$ ns. If a beam particle was preceded by another particle in the previous $100 - 235$ ns, then the TDC did not record TOF_{obj} for that beam particle, and this is illustrated in Figure 7.26(a). This was a significant effect, and its severity increased as a function of beam rate.

Whether an event was missing TOF_{obj} due the beam particle not hitting the object detector's active area or due to the TDC module being "dead," the focal-plane scintillator still measured the reaction product as long as the beam particle was transmitted to the target. Therefore the fraction of events with a good TOF_{obj} was calculated as:

$$f_{obj}^{run} = \frac{\text{Events with good } TOF_{obj} \text{ and } E_{scint}}{\text{Events with good } E_{scint}} \tag{7.40}$$

141

f_{obj}^{run} is similar to f_{obj}, but calculated for the ^{10}C and α-particle data instead of the unreacted-beam data. The rates were much higher for the ^{10}C and α-particle rigidity settings, so both the effects of the large beam spot and the dead time were included in this number. f_{obj}^{run} was calculated with $E_{IC} - TOF_{RF}$ PID gates on ^{10}C or α-particles applied.

Note that the f_{obj} correction in the previous section added back the beam particles lost due to not hitting the active area of the target to the measured scalers rate. Now the f_{obj}^{run} correction removes those particles, plus particles lost due to the dead time. The result is an effective beam rate that only includes beam particles that can induce a CE reaction that can be measured–i.e. have a TOF_{obj}–which is what we want for the cross-section calculation. In other words, if the readout and TDC dead times were both negligible, then f_{obj} and f_{obj}^{run} would cancel, and the scalers rate could be used as measured (but still with a correction for transmission to the target, discussed next).

The f_{obj}^{run} for runs in the 2.3290 Tm rigidity setting are shown in Figure 7.26(b). f_{obj}^{run} is clearly correlated with the measured scalers rate. As the rate increases, the dead time effect becomes more severe, and more events are lost. If f_{obj}^{run} is extrapolated to a rate of zero, then f_{obj} is recovered because there is no dead time effect when the rate is very small, leaving only the rate-independent beam-spot effect.

Beam particles were also lost due to incomplete transmission to the target because of imperfect ion optics. Events with a good TOF_{obj} in data from the Empty Cell Run (Run 188) of the unreacted beam setting were used to calculate the beam transmission ϵ_{trans}. By definition, these events were not affected by the large beam spot effect or the dead time because these effects cause TOF_{obj} to not be recorded. If TOF_{obj} was recorded, then the only other way a beam particle could have been lost was from incomplete beam transmission. The transmission to the target was the ratio of the number events measured in the object
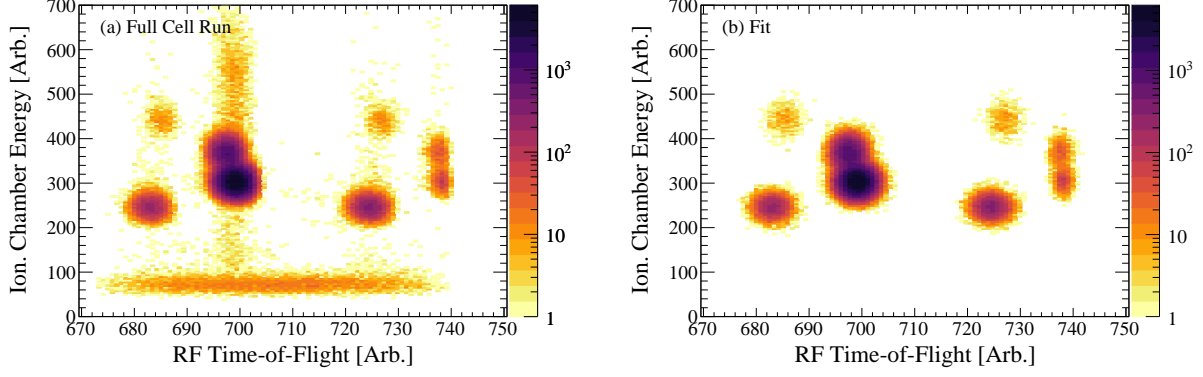
Figure 7.27: (a) $E_{IC} - TOF_{RF}$ PID used for beam identification. (b) Fit of (a).

detector to the number of events measured in the S800 focal plane:

$$\epsilon_{trans} = \frac{\text{Number of events in the S800 focal plane}}{\text{Number of events in the object detector}} = 77\% \qquad (7.41)$$

7.3.3 Beam Purity

After the actual beam rate was calculated and losses determined, the last step was to calculate the purity of each species in the beam. The beam purity was determined by sending the beam into the focal plane in the unreacted-beam rigidity setting and measuring the ratio of each beam particle. The Full Target Cell Run (Run 198) was used. The Empty Target Cell Run (Run 188) was not used because the beam changed slightly between these two runs while the cell was filling.

The beam particles were identified with the $E_{IC} - TOF_{RF}$ PID. The PID plot was fit with 2D Gaussian surfaces since the ^{12}N and ^{11}C peaks overlapped. Figure 7.27 shows the data and the fit. The volume V under a 2D Gaussian surface with amplitude A and x,y-standard deviations $\sigma_{x,y}$ is:

$$V = 2\pi A \sigma_x \sigma_y \qquad (7.42)$$

143

Table 7.2: Beam purity.

Beam Particle	ϵ_{purity}
^{11}C	78 %
^{12}N	14 %
^{10}B	7 %
^{13}O	< 1 %

Then the purity of each beam species was taken as the ratio of the volume under the surface V to the total volume V_{total}:

$$\epsilon_{purity} = \frac{V}{V_{total}} \tag{7.43}$$

The results are given in Table 7.2.

Finally, the effective number of beam particles N_{beam} was calculated as:

$$N_{beam} = \sum_{run} R_{run}^{corr} t_{run} \times f_{obj}^{run} \times \epsilon_{trans} \times \epsilon_{purity} \tag{7.44}$$

where

$$R_{run}^{corr} = \text{actual rate}$$

$$t_{run} = \text{run duration}$$

$$f_{obj}^{run} = \text{fraction of events with good } TOF_{obj}$$

$$\epsilon_{trans} = \text{beam transmission from the object to the target}$$

$$\epsilon_{purity} = \text{beam purity}$$

The resulting N_{beam} are given in Table 7.3.

Table 7.3: Effective beam counts N_{beam}.

Rigidity Setting [Tm]	Beam Particle	N_{beam}
2.3290	^{11}C	2.5×10^{11}
2.4900	^{12}N	5.4×10^{11}
2.8000	^{11}C	2.8×10^{10}
3.0000	^{12}N	2.2×10^{11}

7.3.4 Beam Rate Error

The error in N_{beam} was estimated from the fluctuations in the ratio of the reaction-product rate in the focal plane to the beam rate. Figure 7.28 shows this ratio as a function of run number. The beam slightly changed throughout the experiment, causing the beam spot or transmission to change and hence the beam rate to drift. Data from the 2.3290 Tm rigidity setting gated on ^{10}C was used to estimate the uncertainty from these effects. The 2.4900 Tm setting had the blocker in, which complicated measuring the rate of particles in the focal plane. The 2.8000 Tm and 3.0000 Tm settings were complicated by the possibility of measuring two α-particles in the focal plane. The standard deviation, about 8.4%, was used as the N_{beam} error:

$$\sigma_{beam}^{sys} = 0.084 \times N_{beam} \tag{7.45}$$

7.4 Target Density

The target areal number density N_{tgt} included both the liquid hydrogen and the hydrogen in the Kapton foils [94]:

$$N_{tgt} = \frac{\rho_{LH_2} t_{LH_2} N_A}{MM_H} + \frac{\rho_{Kapton}^H t_{Kapton} N_A}{MM_H} \tag{7.46}$$

145
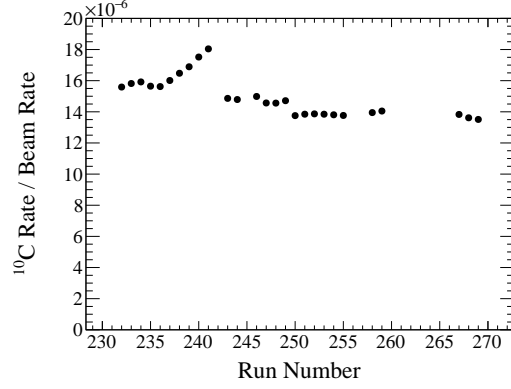
Figure 7.28: Ratio of the ^{10}C rate in the focal plane to the beam rate for the 2.3290 Tm runs. The standard deviation of this ratio is about 8.4%, which was used as the error in the beam rate.

where

$$\rho_{LH_2} = \text{density of the liquid hydrogen}$$

$$\rho_{Kapton}^{H} = \text{density of hydrogen in the Kapton foil}$$

$$t_{LH_2/Kapton} = \text{thickness of the liquid hydrogen/Kapton foil}$$

$$N_A = \text{Avogadro's number}$$

$$MM_H = \text{molar mass of hydrogen}$$

The thickness of each Kapton foil was 125 μm, so $t_{foil} = 250$ μm. The hydrogen density in Kapton is [122]:

$$\rho_{Kapton}^{H} = \rho_{Kapton} \times w_{Kapton}^{H} = 1.42 \text{ g/cm}^2 \times 2.64\% = 0.0374 \text{ g/cm}^3 \qquad (7.47)$$

ρ_{LH_2} and t_{LH_2} were deduced using the Geant4 simulation and the energy lost by the beam in the liquid hydrogen, $KE_{loss} = KE_{empty} - KE_{full}$. KE_{empty} is the energy of the beam after it passed through the Kapton foils only, measured by the S800 in the Empty

146

Cell Run (Run 188), and KE_{full} is the energy of the beam after it passed through both the Kapton foils and the liquid hydrogen, measured by the S800 in the Full Cell Run (Run 198). Two different methods were attempted to find ρ_{LH_2} and t_{LH_2}:

1. Varying the bulge (Section 7.4.1): ρ_{LH_2} was fixed to the value calculated from the equation of state. Then t_{LH_2} was varied in the simulation until KE_{loss} was reproduced. This method was not successful but is included for completeness.

2. Varying the density (Section 7.4.2): t_{LH_2} was fixed to 7 mm, i.e. the bulge was fixed to zero. Then ρ_{LH_2} was varied in the simulation until KE_{loss} was reproduced. This method was used for this analysis.

7.4.1   Varying the Bulge

Although the nominal liquid-hydrogen thickness is $t_{LH_2} = 7$ mm, the Kapton foils are very thin and bulge outwards when the cell is filled with liquid. This bulging makes the target an unknown amount thicker than 7 mm. In this section, the bulge of the target was varied in the simulation until KE_{loss} was reproduced. The liquid-hydrogen density was fixed to the value calculated from the temperature and pressure measured during the experiment.

First, the pressure and temperature measurements were corrected. The pressure was corrected by matching the pressure measured when the target cell was filled with air to atmospheric pressure. The resulting correction scaling factor was 0.88. The measured temperature was corrected by applying an offset to match the measured hydrogen liquid-gas
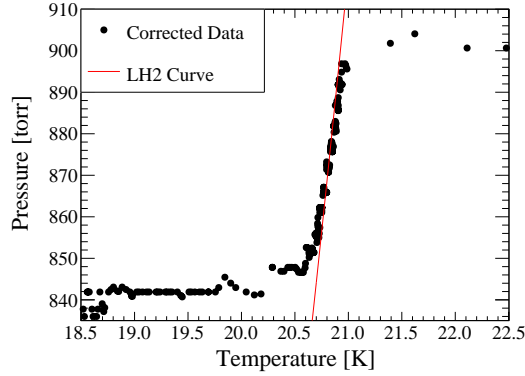
Figure 7.29: Measured liquid-hydrogen pressure vs. temperature. The black circles are the corrected data, and the red solid line is the known liquid-gas curve. The temperature offset was 0.3 K. The slope of the liquid-gas curve was slightly steeper than the data because the phase change occurred quickly and the hydrogen was not in equilibrium during the phase change.
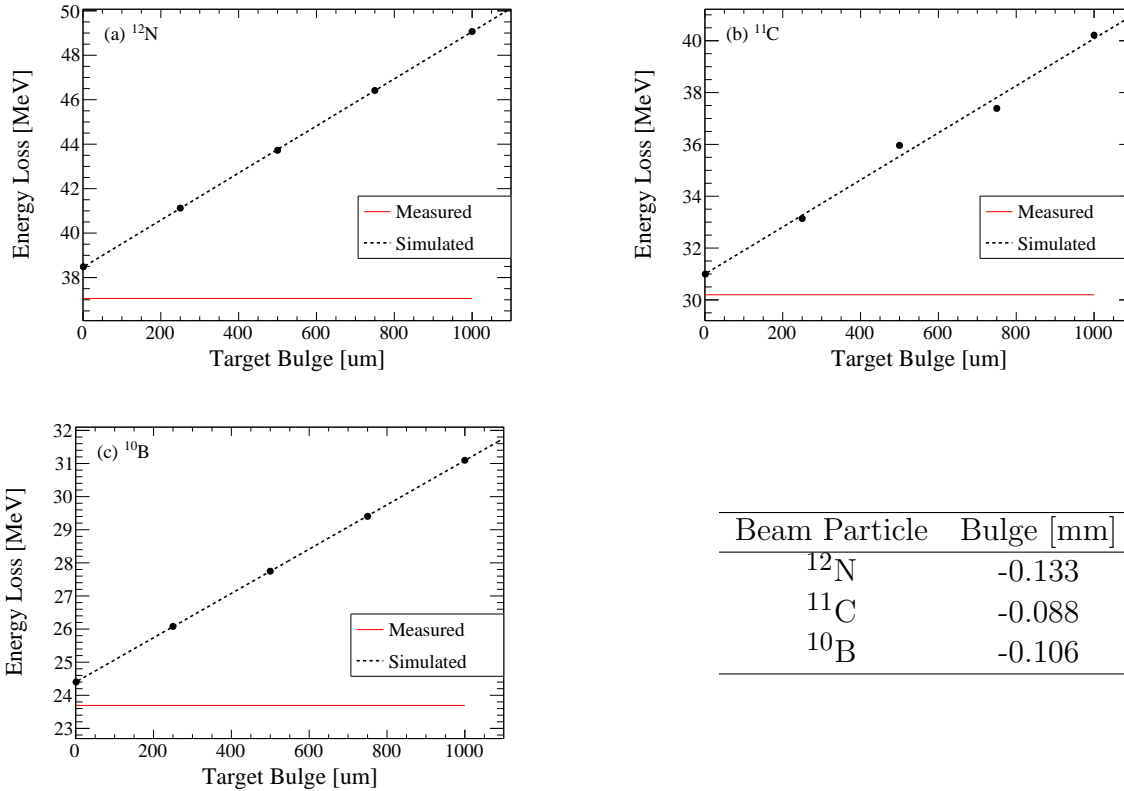
Beam Particle	Bulge [mm]
^{12}N	-0.133
^{11}C	-0.088
^{10}B	-0.106

Figure 7.30: Energy loss in the target vs. the bulge size measured with a (a) ^{12}N beam, (b) ^{11}C beam, and (c) ^{10}B beam. The black points are the simulated energy loss, and the dashed black line is a fit to the black points. The solid red line is the measured energy loss. The "actual" bulge size should be the point where the red and black lines intersect.

148

curve to the known curve [logger_e17018.kumac]:

$$T[\text{K}] = 0.0112(P[\text{torr}])^4 + 0.0132(P[\text{torr}])^3 - 5.0914(P[\text{torr}])^2 + 38.64(P[\text{torr}]) + 52.453$$

$$(7.48)$$

The resulting correction offset was 0.3 K. The corrected data and liquid-gas curve are shown in Figure 7.29.

The average pressure of the target during the Full Cell Run (Run 198) was 832 torr, and the average temperature was 16.4 K. According to the equation of state [123], this corresponds to a density of $\rho_{LH2}^{EOS} = 75.0$ mg/cm^3. (*This is not the density actually used for the analysis.*) In this simulation, the target density was fixed to ρ_{LH2}^{EOS}, and the bulge was varied from 0 mm to 1 mm. The resulting KE_{loss} is shown in Figure 7.30.

The energy losses were fit to a line, and the point where the line intersects the measured energy loss should have been the target bulge. The result, however, was a negative bulge for all three beam species, which is not physical. Therefore this method was not used to determine the target density and thickness.

7.4.2   Varying the Density

Rather than fixing the density and varying the bulge, the opposite approach was pursued. The bulge was fixed to zero, and the liquid hydrogen density was varied from $68 - 76$ mg/cm^3 in the simulation. The results are shown in Figure 7.31. The average density from the KE_{loss} of the ^{12}N, ^{11}C, and ^{10}B beams was $\rho_{LH2} = 72.7(3)$ mg/cm^3.
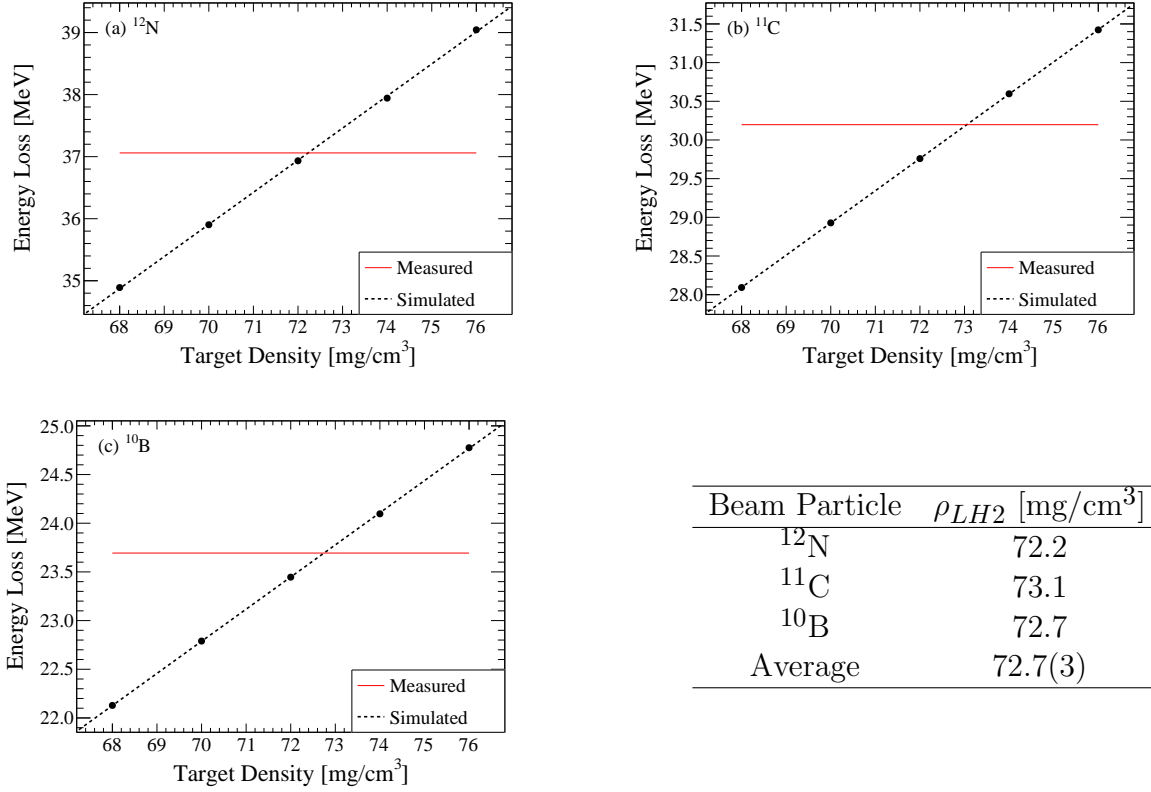
Figure 7.31: Energy loss in the target vs. the target density measured with a (a) ^{12}N beam, (b) ^{11}C beam, and (c) ^{10}B beam. The black points are the simulated energy loss, and the dashed black line is a fit to the black points. The solid red line is the measured energy loss. The point where the red and black lines intersect was used as actual target density.

7.4.3 Target Thickness Error

The Kapton thickness t_{Kapton} and density ρ^H_{Kapton} have negligible error. Because the liquid hydrogen density was calculated assuming a thickness of exactly $t_{LH2} = 7$ mm, the only error to propagate is that of the target density. Then the error in the target areal number density N_{tgt} was taken as:

$$\sigma^{sys}_{tgt} = \sigma_{\rho_{LH2}} \frac{t_{cell} N_A}{MM_H} \tag{7.49}$$

7.5 Cross Section

Finally, the differential cross sections were calculated:

$$\frac{d\sigma}{d\Omega} = \frac{N_{rxn}}{10^{-24}\Delta\Omega N_{beam} N_{tgt}} \text{ barn/sr} \tag{7.50}$$

Figure 7.32 shows the resulting cross sections for the 2.3290 Tm data. Two prominent peaks can be observed around 1 MeV and 3 MeV. The height of these peaks decreases as the angle increases. This forward-peaking behavior indicates that they are associated with $\Delta L = 0$ and correspond to GT transitions. Because these states are populated by GT transitions from the ground state of ^{11}C ($J^{\pi} = \frac{3}{2}^{-}$), they can be identified as the first $\frac{1}{2}^{-}$ state in ^{11}N at about 1 MeV and the first $\frac{3}{2}^{-}$ state at about 3 MeV. The broad structure at higher excitation energies is likely a combination of states associated with different angular momentum transfers.

The 2.8000 Tm data appear to be mostly background and will be discussed in Section 8.4. No kinematic lines were visible in the 2.4900 Tm and 3.0000 Tm data. The lack of kinematic lines suggests that the observed counts were mostly background, so this data could not be used to study ^{12}O.

The number of reactions N_{rxn}, the number of beam particles N_{beam}, and the target areal number density N_{tgt} all contributed to the systematic error of the cross section:

$$\sigma^{sys}_{\frac{d\sigma}{d\Omega}} = \frac{d\sigma}{d\Omega}\sqrt{\left(\frac{\sigma^{sys}_{rxn}}{N_{rxn}}\right)^2 + \left(\frac{\sigma^{sys}_{beam}}{N_{beam}}\right)^2 + \left(\frac{\sigma^{sys}_{tgt}}{N_{tgt}}\right)^2} \tag{7.51}$$
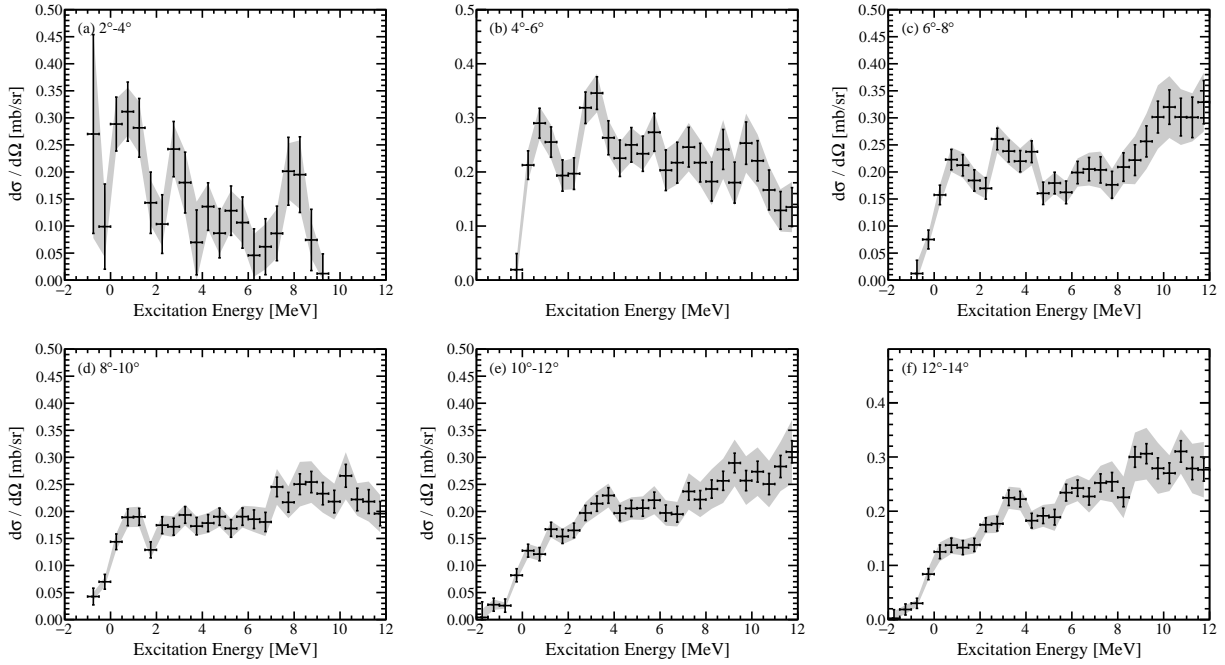
Figure 7.32: Cross sections for different angular bins for the 2.3290 Tm data. Gray bands indicate systematic error.

Chapter 8

$B(\mathbf{GT})$ Extraction

In this chapter, the charge-exchange cross section is used to extract the Gamow-Teller transition strength, $B(\mathrm{GT})$. First, the unit cross section, or the proportionality constant that connects the charge-exchange cross section to $B(\mathrm{GT})$, was determined using the factorization given in Ref. [68] (Section 8.1). Next, a Multipole Decomposition Analysis (MDA) was used to extract the $\Delta L = 0$ component from the measured cross section, and the $\Delta L = 0$ component was extrapolated to zero momentum transfer (Section 8.2). Then $B(\mathrm{GT})$ was extracted using the proportionality relationship (Section 8.3) [68]. Last, the $2\alpha+3p$ decay channel was investigated, and its contribution to $B(\mathrm{GT})$ was estimated (Section 8.4).

8.1 Unit Cross Section

The unit cross section $\hat{\sigma}_{GT}$ is the constant of proportionality between the charge-exchange cross section and $B(\mathrm{GT})$. In other words, it is the cross section per unit $B(\mathrm{GT})$. $\hat{\sigma}_{GT}$ can be obtained in several ways, including:

1. Measuring the β-decay half-life and charge-exchange cross section

2. Interpolating measured $\hat{\sigma}_{GT}$ of neighboring nuclei

3. Calculating the theoretical cross section and $B(\mathrm{GT})$

4. Using the factorized expression in Ref. [68]
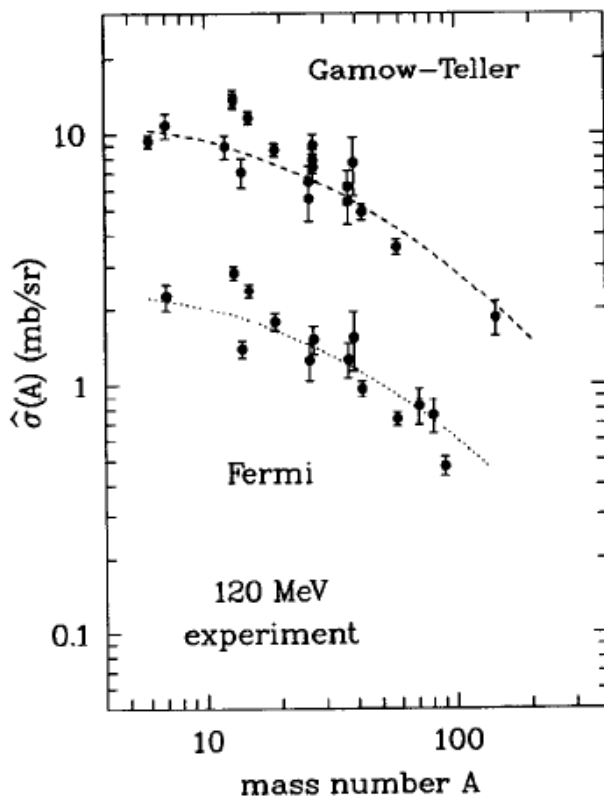
Figure 8.1: Measured unit cross sections as a function of mass number A, taken from Ref. [68]. The dashed lines can be used to estimate $\hat{\sigma}$ where β-decay data are not available.

Each method is discussed for completeness, but only method (4) was used for the actual analysis.

First, the ideal method of obtaining $\hat{\sigma}_{GT}$ is extracting it from experiments. If the β-decay half-life and charge-exchange cross section have been measured for the same transition, then $\hat{\sigma}_{GT}$ is:

$$\hat{\sigma}_{GT} = \frac{[d\sigma/d\Omega(q=0)|_{\Delta L=0}]_{charge-exchange}}{B(\mathrm{GT})_{\beta-decay}} \tag{8.1}$$

This method cannot be used for $^{11}\mathrm{C} \rightarrow {}^{11}\mathrm{N}$ because there are no states in $^{11}\mathrm{N}$ that β-decay.

154
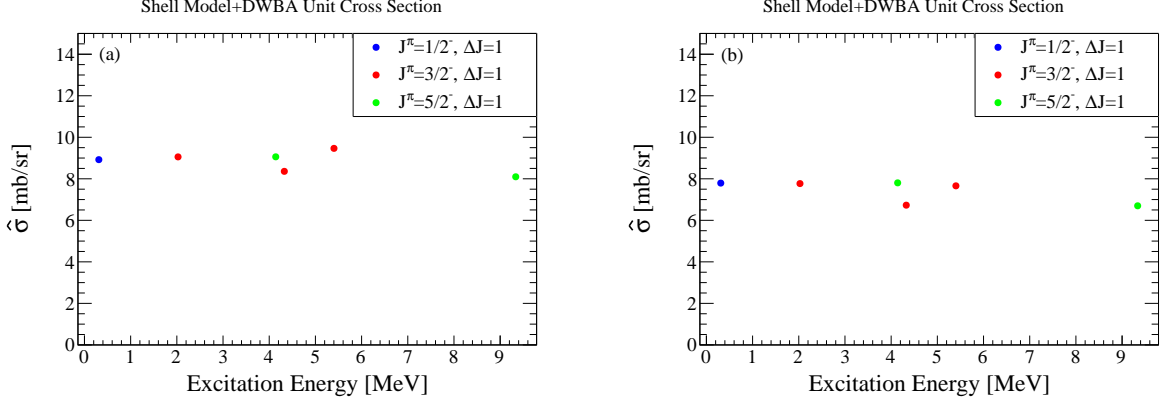
Figure 8.2: (a) Unit cross sections calculated from DWBA cross sections and shell-model $B(\text{GT})$'s. States with $B(\text{GT})_{Shell\ Model} < 0.01$ are not shown. (b) Same as (a), with binding energies lowered from -1.0 MeV to -0.1 MeV. The result is about a 10% reduction in $\hat{\sigma}_{GT}$.

If β-decay data are not available, then a unit cross section can be obtained by interpolating measured unit cross sections from neighboring nuclei. Figure 8.1 [68] shows such an interpolation. The value of the unit cross section at $A = 11$ is about 9.1 mb/sr.

The third method to obtain a unit cross section is to take the ratio of the theoretical charge-exchange cross section and $B(\text{GT})$:

$$\hat{\sigma} = \frac{\left[(d\sigma/d\Omega)_{q=0}\right]_{DWBA}}{B(\text{GT})_{Shell\ Model}} \tag{8.2}$$

Oxbash was used to find $B(\text{GT})_{Shell\ Model}$, and DW81 was used to find $\left[(d\sigma/d\Omega)_{q=0}\right]_{DWBA}$. The results are shown in Figure 8.2. The quenching factor from Eq. 3.3 was applied to $B(\text{GT})_{Shell\ Model}$. The unit cross section obtained from this method was about 9 mb/sr. Although the absolute magnitudes of the DWBA calculations were not quite reliable enough to use this method, the small spread of $\hat{\sigma}_{GT}$ between states confirms that the unit cross section is independent of the final spin J_f, justifying the use of one unit cross section for all final states.

Fourth, Ref. [68] demonstrates that the unit cross section can be factorized:

$$\hat{\sigma} = K(E_p, \omega) N^D(q, \omega) |J_{\sigma\tau}|^2 \tag{8.3}$$

where

$$K(E_p, \omega) = \frac{E_i E_f}{\hbar^2 c^2 \pi^2} \frac{k_f}{k_i} \text{ is the kinematical factor}$$

$$N^D(q, \omega) = \frac{\sigma(DW; q, \omega)}{\sigma(PW)} \text{ is the distortion factor}$$

$$J_{\sigma\tau} = \text{the volume integral of the nucleon-nucleus interaction}$$

The kinematical factor $K(E_p, \omega)$ is straightforward to calculate, and the volume integral $J_{\sigma\tau}$ is relatively well-known from both calculations and measurements (e.g. Ref. [124] and references therein). The distortion factor $N^D(q, \omega)$ is the ratio of the distorted wave to the plane wave.

The factorized expression was used to obtain $\hat{\sigma}_{GT} = 8.4$ mb/sr for this analysis. This value was taken from Ref. [57], where $B(\text{GT})$ was extracted from $^{11}\text{B}(n,p)$ at $E_n = 96$ MeV. The distortion factor was calculated to be 0.450, and $J_{\sigma\tau}(0) = 180$ MeV/fm^3 from Ref. [124].

Ref. [57] did not provide an error, so the standard deviation of unit cross sections from neighboring nuclei in the $A = 10 - 13$ region (Table 8.1) was used as an estimate of the error. The standard deviation is about 1 mb/sr. Unit cross sections from reactions at higher energies were included in this estimate; although $J_{\sigma\tau}$ and N^D generally decrease and K generally increases at higher energies, these effects are small and even somewhat cancel, so these unit cross sections can still be used to estimate the uncertainty in $\hat{\sigma}_{GT}$. Therefore the unit cross section used in this analysis was $\hat{\sigma}_{GT} = 8.4(10)$ mb/sr.

Table 8.1: (n,p) and (p,n) unit cross sections for $A = 10 - 13$. These data were used to estimate the error in the unit cross section.

Reference	Reaction	E_n or E_p [MeV]	$\hat{\sigma}_{GT}$ [mb/sr]
Jackson *et al.* [125]	$^{12}\text{C}(n,p)^{12}\text{B}$	198	9.42(31)
Jackson *et al.* [125]	$^{13}\text{C}(n,p)^{13}\text{B}$	198	10.97(56)
Taddeucci *et al.* [126]	$^{11}\text{B}(p,n)^{11}\text{C}$	160	9.22(55)
Sorenson *et al.* [127]	$^{12}\text{C}(n,p)^{12}\text{B}$	65-250	$\approx 9.5(4)$ at $E_n = 95$ MeV
Sorenson *et al.* [127]	$^{13}\text{C}(n,p)^{13}\text{B}$	65-250	$\approx 9.5(5)$ at $E_n = 95$ MeV
Ringbom *et al.* [57]	$^{10}\text{B}(n,p)^{10}\text{Be}$	96	7.6
Ringbom *et al.* [57]	$^{11}\text{B}(n,p)^{11}\text{Be}$	96	8.4

8.2 The $q = 0$ Cross Section

To extract $B(\text{GT})$, the $\Delta L = 0$ component of the cross section must be extrapolated to zero momentum transfer ($q = 0$, where $\mathbf{q} = \mathbf{k_f} - \mathbf{k_i}$), where both the scattering angle and Q-value are zero. The $\Delta L = 0$ cross section at $0°$ was extracted via a Multipole Decomposition Analysis (MDA) (Section 8.2.1), and that result was extrapolated to $Q = 0$ by using a scaling factor obtained from the Distorted Wave Born Approximation (DWBA) calculations (Section 8.2.2).

8.2.1 Multipole Decomposition Analysis

As discussed in Chapter 4, a Multipole Decomposition Analysis (MDA) is method of extracting the individual angular momentum transfer (ΔL) components from the measured cross section. In an MDA, the experimental angular distribution is fit to the following equation:

$$\frac{d\sigma}{d\Omega} = C_0 \left[\frac{d\sigma}{d\Omega}\right]_{DWBA}^{\Delta L=0} + C_1 \left[\frac{d\sigma}{d\Omega}\right]_{DWBA}^{\Delta L=1} + C_2 \left[\frac{d\sigma}{d\Omega}\right]_{DWBA}^{\Delta L=2} + \cdots \qquad (8.4)$$

where $\left[\frac{d\sigma}{d\Omega}\right]_{DWBA}^{\Delta L}$ are the theoretical ΔL shapes and $C_{\Delta L}$ are the fit parameters.

The data were divided into 0.5-MeV excitation-energy bins, and the MDA fits for six

selected bins are shown in Figure 8.3. The ΔL shapes were calculated in the Distorted Wave Born Approximation (DWBA) as described in Chapter 4, but with an excitation energy matching that of each bin.

The angular distributions were smeared before they were used in the MDA. In this experiment, the excitation-energy resolution worsened at higher scattering angles, distorting the angular distributions. These distortions could cause certain ΔL components to be favored in the MDA. To mitigate the distortions, the excitation-energy spectra for each angular bin were smeared so that the resolution everywhere matched the worst resolution. The smeared angular distributions were constructed from these smeared excitation-energy spectra. Note that the center-of-mass angle resolution was generally better than $1.5°$ (FWHM), so uncertainty in the center-of-mass angle did not significantly distort the angular distributions.

The MDA fit range was $4° - 14°$, and only the $\Delta L = 0, 1$ shapes were used. The $\Delta L = 1, 2$ shapes were too similar in the $4° - 14°$ region, and the statistics were too poor to use three ΔL shapes in the fit. The fit with $\Delta L = 0, 1$ yielded a better reduced χ^2 value than $\Delta L = 0, 2$.

The MDA results are shown in Figure 8.4. $\Delta L = 0$ dominates at low excitation energies, and $\Delta L = 1$ dominates at higher excitation energies. The main result of the MDA is the $\Delta L = 0$ component of the measured cross section (the green lines in Figure 8.3) at $0°$:

$$\left[\frac{d\sigma}{d\Omega}(Q = Q, 0°) \right]_{exp}^{\Delta L = 0} = C_0 \left[\frac{d\sigma}{d\Omega}(Q = Q, 0°) \right]_{DWBA}^{\Delta L = 0} \tag{8.5}$$
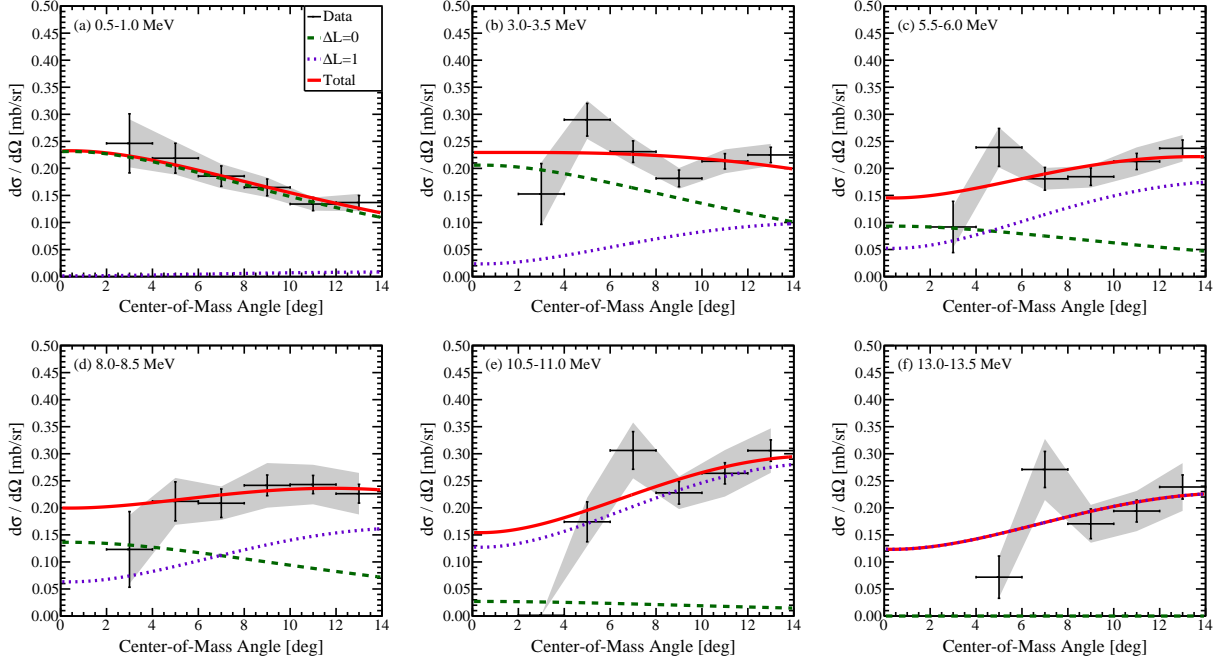
Figure 8.3: MDA fits for a few selected excitation-energy bins.
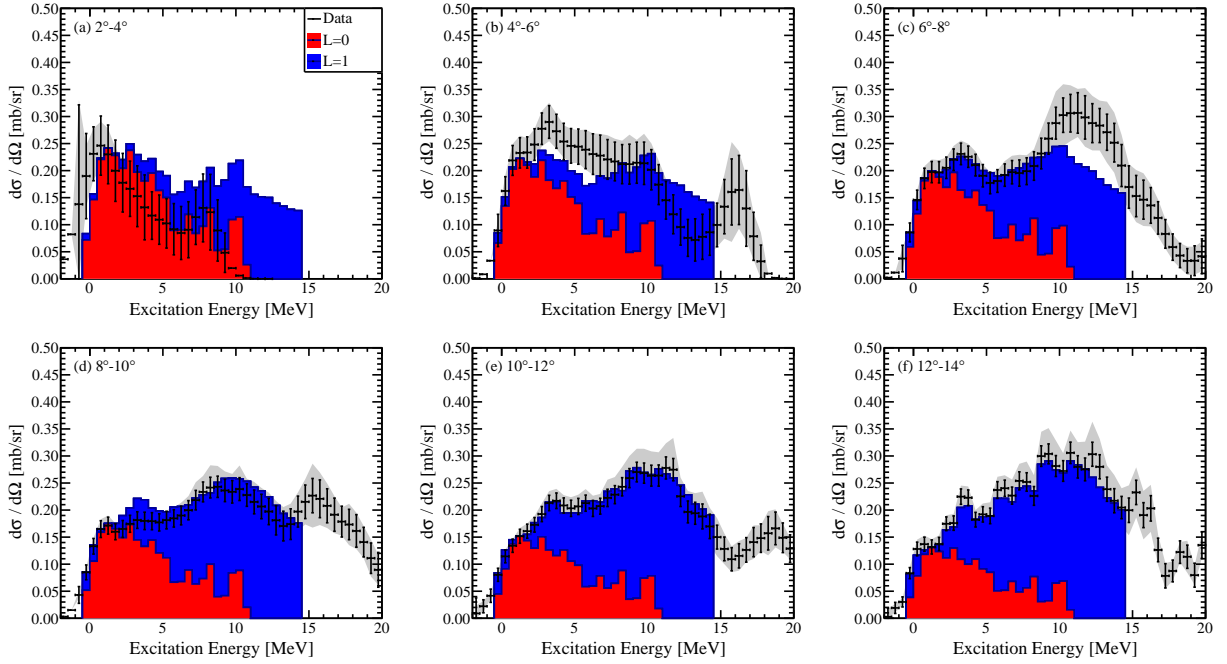
Figure 8.4: Cross sections broken down into their ΔL components according to the MDA results.
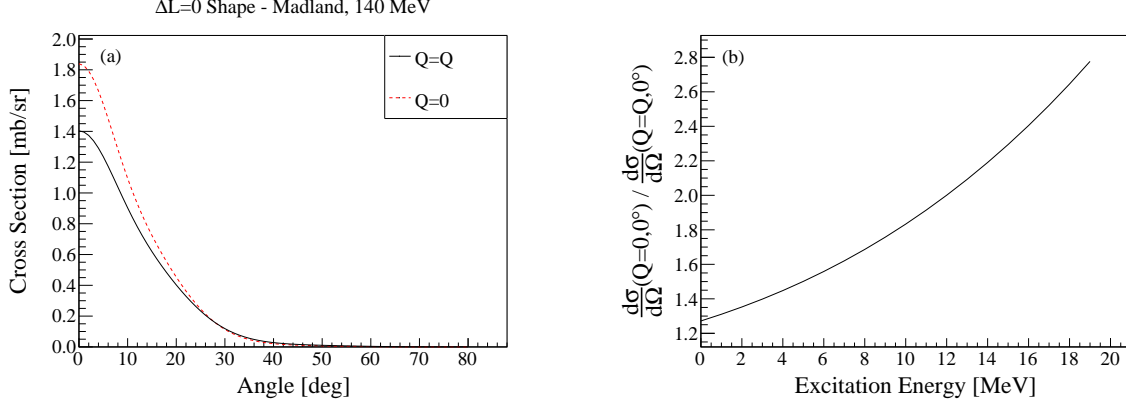
Figure 8.5: (a) $\Delta L = 0$ shape calculated with $Q = 0$ (red) and $Q = Q$ (black). The ratio of the two at zero degrees was used to extrapolate to zero energy transfer. (b) Zero energy transfer scaling factor as a function of excitation energy.

8.2.2 Extrapolation to $Q = 0$

Next, the $\Delta L = 0$ cross section at $0°$ was extrapolated to $Q = 0$. In general, as the energy transfer in a reaction (Q-value or excitation energy) increases, the cross section goes down. This effect is demonstrated for $^{11}C(p,n)$ by the DWBA calculations shown in Figure 8.5(a). The calculations were used to estimate the magnitude of the decrease, shown in Figure 8.5(b). The cross section decreases by a factor of about 1.3 for $E_x = 0$ MeV, and the factor grows as the excitation energy increases. The final $q = 0$ cross section was calculated as the scaling factor multiplied by the MDA result from the previous section:

$$
\frac{d\sigma}{d\Omega}(q = 0)\bigg|_{\Delta L=0} = \left[\frac{\frac{d\sigma}{d\Omega}(Q = 0, 0°)}{\frac{d\sigma}{d\Omega}(Q = Q, 0°)} \right]_{DWBA} \times \left[\frac{d\sigma}{d\Omega}(Q = Q, 0°) \right]_{exp}^{\Delta L=0} \tag{8.6}
$$

The systematic error from the MDA and $Q = 0$ extrapolation were small relative to the error from the measured cross section. The only source of statistical error was the uncertainty of the MDA C_0 coefficient, which comes from the ROOT fitting algorithm.

In addition to the double differential cross sections, the angle-integrated cross sections

between $4° - 6°$ for the $\frac{1}{2}^-$ and $\frac{3}{2}^-$ states were also extracted. The angle-integrated cross section of each state was calculated from a fit of the low-excitation-energy region for the $4° - 6°$ angular bin. Each state was modeled as a Voigt function, which is the convolution of a Gaussian distribution G with a Lorentzian distribution L. This function models a state at excitation energy E_0 with intrinsic width Γ smeared with experimental resolution σ:

$$G(E; E_0, \sigma) = \frac{1}{\sqrt{2\pi}\sigma} e^{-(E-E_0)^2/2\sigma^2} \tag{8.7}$$

$$L(E; E_0, \Gamma) = \frac{1}{\pi} \frac{\Gamma/2}{(E - E_0)^2 + \Gamma^2/4} \tag{8.8}$$

$$V(E; E_0, \sigma, \Gamma) = (G * L)(E; E_0, \sigma, \Gamma) \tag{8.9}$$

The fit function was:

$$f_{fit}(E; A_1, A_2, A_3) = A_1 V(E; E_1, \sigma_1, \Gamma_1) + A_2 V(E; E_2, \sigma_2, \Gamma_2) + A_3 V(E; E_3, \sigma_3, \Gamma_3) \tag{8.10}$$

where E_i, σ_i, Γ_i are the energies, resolutions, and widths, respectively, of the known states i. σ_i were fixed to the experimental resolutions found from the simulation, and E_i and Γ_i were fixed to the excitation energies and widths given in Ref. [128] (Table 8.2). The three fit parameters A_i are the amplitudes of each Voigt function. The third peak $\left(\frac{5}{2}^-\right)$ was included only to estimate the background under the $\frac{3}{2}^-$ state. The systematic error in A_i was estimated by repeating the fit with the cross section plus and minus the systematic errors. The statistical error in A_i came from the fitting algorithm in ROOT. The fit is shown in Figure 8.6.

The cross section of each state was taken as the integral of the fit, A_i (normalized ac-

Table 8.2: ENSDF adopted values [128]. Note that the three measurements of the $\left(\frac{5}{2}^{-}\right)$ width differ too significantly to justify even using an average, so 0 keV was simply used as the width in the fit.

State	E_x [MeV]	Γ [keV]
$\frac{1}{2}^{-}$	0.730(70)	600(100)
$\frac{3}{2}^{-}$	2.860(70)	340(40)
$\left(\frac{5}{2}^{-}\right)$	4.420(70)	0
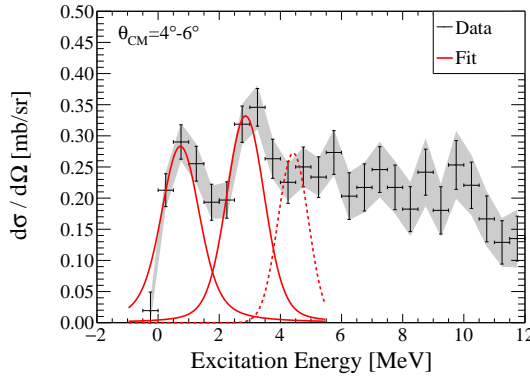
Figure 8.6: Fit to extract the total cross section for the $\frac{1}{2}^{-}$ and $\frac{3}{2}^{-}$ states in ^{11}N. The third peak is included only as a background model.

cording to the histogram binning), multiplied by a scaling factor $f_{\Delta L=0}$ (0.97 for the $\frac{1}{2}^{-}$ state and 0.84 for the $\frac{3}{2}^{-}$ state) to only include the $\Delta L = 0$ part of the cross section:

$$\left[\frac{d\sigma}{d\Omega}(Q = Q, \theta_{CM})\right]_{exp}^{\Delta L=0} = f_{\Delta L=0}A_i \tag{8.11}$$

As seen in Figure 8.3, the measured cross section exceeds the MDA result in the $4° - 6°$ bin. This excess is likely due to acceptance effects. The magnitude of the effect was estimated by repeating the same analysis for the $6° - 8°$ bin. The difference between the results served as an estimate of this uncertainty, and the systematic error bars were increased accordingly.

To extrapolate the $\Delta L = 0$ cross section for the individual states to zero degrees, the experimental cross section was multiplied by the ratio of the DWBA cross sections at $\theta = 0°$

and $\theta = \theta_{CM}$. Then that was extrapolated to $Q = 0$ in the same manner as before:

$$\frac{d\sigma}{d\Omega}(q=0)\Big|_{\Delta L=0} = \left[\frac{\frac{d\sigma}{d\Omega}(Q=0,0°)}{\frac{d\sigma}{d\Omega}(Q=Q,0°)}\right]_{DWBA} \times \left[\frac{\frac{d\sigma}{d\Omega}(Q=Q,0°)}{\frac{d\sigma}{d\Omega}(Q=Q,\theta_{CM})}\right]_{DWBA} \times \left[\frac{d\sigma}{d\Omega}(Q=Q,\theta_{CM})\right]_{exp}^{\Delta L=0} \quad (8.12)$$

8.3 $B(\mathbf{GT})$ Results

The resulting $\frac{d\sigma}{d\Omega}(q=0)\Big|_{\Delta L=0}$ from Eqs. 8.6 and 8.12 were divided by the unit cross section to get $B(\text{GT})$:

$$B(GT) = \frac{\frac{d\sigma}{d\Omega}(q=0)\Big|_{\Delta L=0}}{\hat{\sigma}_{GT}} \quad (8.13)$$

The resulting $B(\text{GT})$ spectrum is shown in Figure 8.7(a), and the cumulative spectrum is shown in Figure 8.7(b). The $B(\text{GT})$ for each state and the cumulative $B(\text{GT})$ up to 10 MeV are:

- $B(GT)\left[\frac{1}{2}^-\right] = 0.18 \pm 0.01(stat) \pm 0.03(sys)$

- $B(GT)\left[\frac{3}{2}^-\right] = 0.18 \pm 0.01(stat) \pm 0.04(sys)$

- $\sum_{E_x=0 \text{ MeV}}^{10 \text{ MeV}} B(GT) = 0.61 \pm 0.03(stat) \pm 0.12(sys)$

The largest uncertainty in Eq. 8.13 is interference from the $\Delta L = 2, \Delta S = 1$ component. This component can constructively or destructively interfere with $\Delta L = 0, \Delta S = 1$ (both are $\Delta J^\pi = 1^+$), so their contribution cannot be removed by an MDA. The $\Delta L = 2, \Delta S = 1$ component is mediated mainly by the tensor-τ component of the effective interaction, and its effect on the cross section was estimated by switching off the tensor parts of the Franey
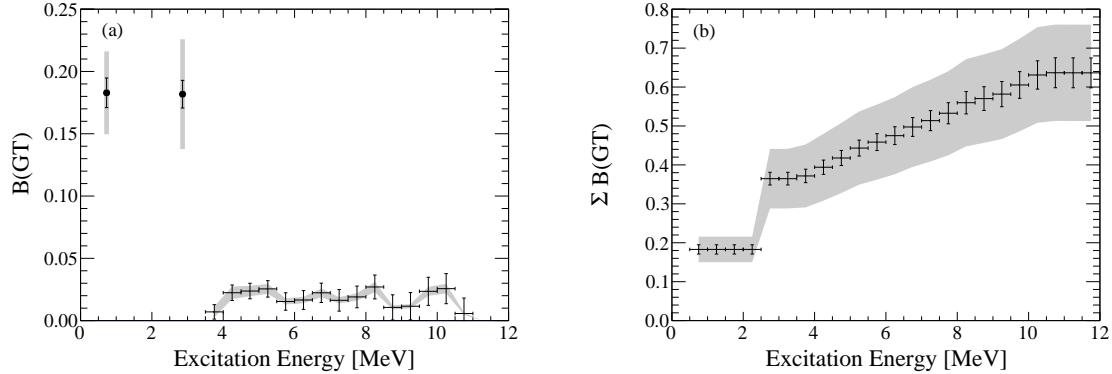
Figure 8.7: (a) Measured $B(GT)$ distribution. (b) Cumulative $B(GT)$ distribution. Gray bands indicate systematic error.

and Love effective interaction in the DW81 code. The cross section changed by no more than 5%, which is small relative to the other systematic errors in this experiment.

8.4 $2\alpha+3p$ Decay Channel Contribution to $B(GT)$

Only the ^{10}C$+p$ final state data have been considered so far, but ^{11}N can also decay to $2\alpha+3p$ above $E_x \approx 2.7$ MeV (see Figure 7.12). If there is a non-zero branching ratio to this decay channel, then the $B(GT)$ result from the ^{10}C$+p$ data would be too small. However, the direct (p,n) reaction populates proton-particle neutron-hole states in ^{11}N, and the decay by proton emission to ^{10}C$+p$ is expected to be the preferred decay channel.

Nevertheless, α-particles were measured in the S800 focal plane (2.8000 Tm) to study this alternative decay channel. The excitation-energy spectra are shown in Figure 8.8. The angular distributions are very strongly forward peaked, much more so than expected from a charge-exchange reaction, indicating that the data are mostly background. No significant signal above background was observed below 4 MeV. This is consistent with Refs. [56] and [129], which have shown that the $\frac{3}{2}^-$ state and all states below it decay to ^{10}C, and that branching to the $2\alpha+3p$ decay channels appears at higher excitation energies.
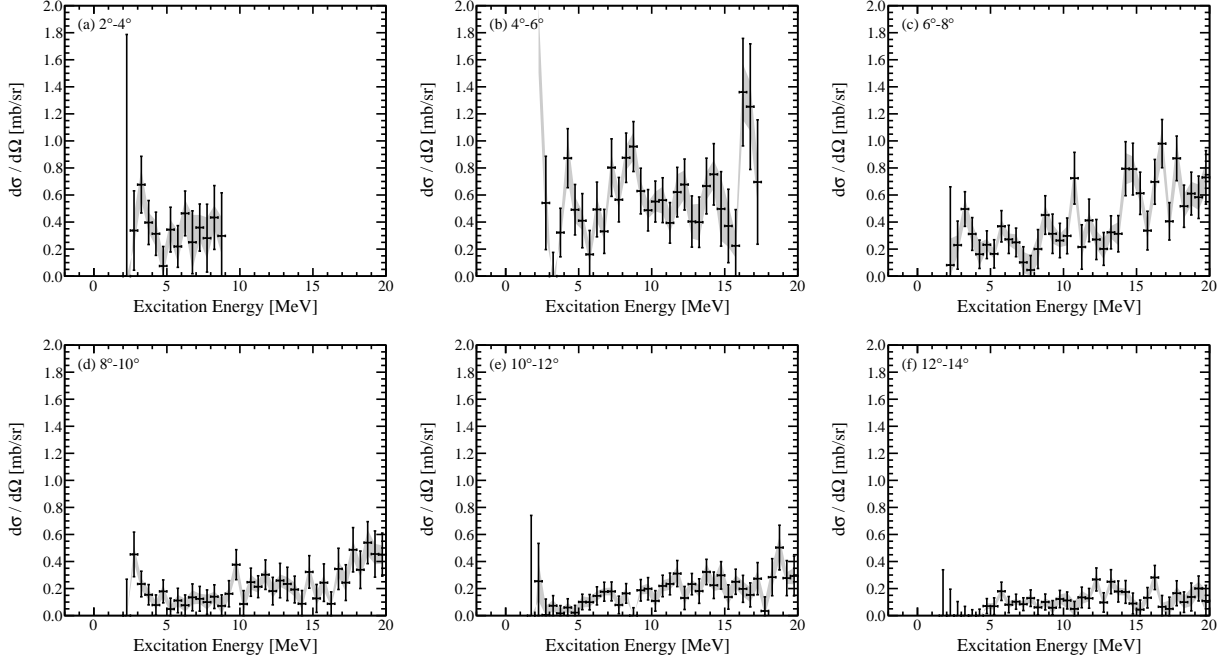
Figure 8.8: Cross section for ^{11}C$(p,n)^{11}$N$\rightarrow 2\alpha + 3p$ data. Gray bands indicate systematic error.

At higher excitation energies, only an upper limit of 65% of the ^{10}C$+p$ channel could be determined. However, separating the signal from the background was difficult, and the actual yield from the $2\alpha+3p$ channel is probably significantly lower. Extracting the $\Delta L = 0$ yield from the $2\alpha+3p$ data was not possible given the background, so this channel was excluded from the analysis.

Chapter 9

Discussion

The Gamow-Teller transition strengths are presented in Table 9.1, along with theoretical calculations and experimental results from mirror ^{11}B(n,p)-type experiments. Figure 9.1 also shows a comparison of the present experimental results to the theoretical calculations. The shell-model calculations were done in Oxbash as described in Section 2.1. Recall that a quenching factor of $q^2 = 0.69$ (Eq. 3.3) was applied to the shell-model B(GT) values. The experimental B(GT) results agree with the shell-model calculations for both the individual states and for the cumulative strength up to 10 MeV. However, as discussed in Section 8.4, additional GT strength in the ^{11}N$\rightarrow 2\alpha + 3p$ channel could not be excluded.

Variational Monte Carlo (VMC) calculations for both the proton- and neutron-rich cases were performed by Garrett King and collaborators at Washington University in St. Louis as described in Section 2.2. The VMC results are consistent with both the present experimental results and the shell-model calculations. The VMC results are also very similar for both the ^{11}C$\rightarrow^{11}$N and the mirror ^{11}B$\rightarrow^{11}$Be cases, suggesting that isospin symmetry holds.

Note that no additional scaling or quenching factors were applied to the VMC results. The VMC calculations inherently include correlations outside the p-shell model space, such as sd-shell correlations and α-clustering effects, which reduce the strength compared to the calculations without such correlations. Additionally, note that the VMC uncertainties given in Table 9.1 are statistical only. Uncertainty due to the choice of interaction was estimated

Table 9.1: Comparison of the present experimental $B(GT)$ results to theoretical calculations and to mirror (n,p)-type experiments.

	$B(GT)\left[\frac{1}{2}^{-}\right]$	$B(GT)\left[\frac{3}{2}^{-}\right]$	$\sum_{Ex=0 \text{ MeV}}^{10 \text{ MeV}} B(GT)$
^{11}C$(p,n)^{\dagger}$	$0.18(1)^{stat}(3)^{sys}$	$0.18(1)^{stat}(4)^{sys}$	$0.61(3)^{stat}(12)^{sys}$
Shell Model†	0.2061	0.2259	0.5950
VMC ^{11}C$\rightarrow^{11}$N†	$0.2050(7)^{\ddagger}$	$0.180(1)^{\ddagger}$	-
VMC ^{11}B$\rightarrow^{11}$Be†	$0.2012(4)^{\ddagger}$	$0.175(1)^{\ddagger}$	-
^{11}B(n,p) [57]	-	-	0.75(8)
^{11}B$(d,^{2}$He$)$ [58]	$\approx 0.34^{*}$	$\approx 0.33^{*}$	-
^{11}B$(t,^{3}$He$)$ [59]	0.23(5)	0.17(5)	-

†This work.

‡Errors shown are statistical only. Model uncertainties contribute an additional 10% error. See text for details.

*From Figure 3(a) of Ref. [58].

to be $2 - 4\%$ in a previous study of GT matrix elements with all available NV2+3 model classes [32]. If a conservative 5% model uncertainty is assumed, then the resulting uncertainty in $B(GT)$ is about 10%.

The shell-model calculations are able to reproduce the parity inversion of the ground state, and the calculated excitation energies of the $\frac{1}{2}^{-}$ and $\frac{3}{2}^{-}$ states are in reasonable agreement with the ENSDF values. The VMC calculations did not yield excitation energies; a VMC calculation for the ground state will be necessary to determine whether the VMC method can reproduce the parity inversion.

In addition to theoretical calculations, the present experimental results were also compared to $B(GT)$ values obtained from mirror ^{11}B(n,p)-type experiments. First, the ^{11}B(n,p) reaction was measured at the Svedberg Laboratory in Uppsala, Sweden [57]. Although the excitation-energy resolution was too poor (3.5-4.5 MeV (FWHM)) to extract strengths for individual states, the cumulative $B(GT)$ up to 10 MeV was 0.75(8). The ^{11}B$(d,^{2}$He$)$ reaction was measured at the RIKEN Accelerator Research Facility [58], and the ^{11}B$(t,^{3}$He$)$ reaction was measured at the National Superconducting Cyclotron Laboratory at Michigan
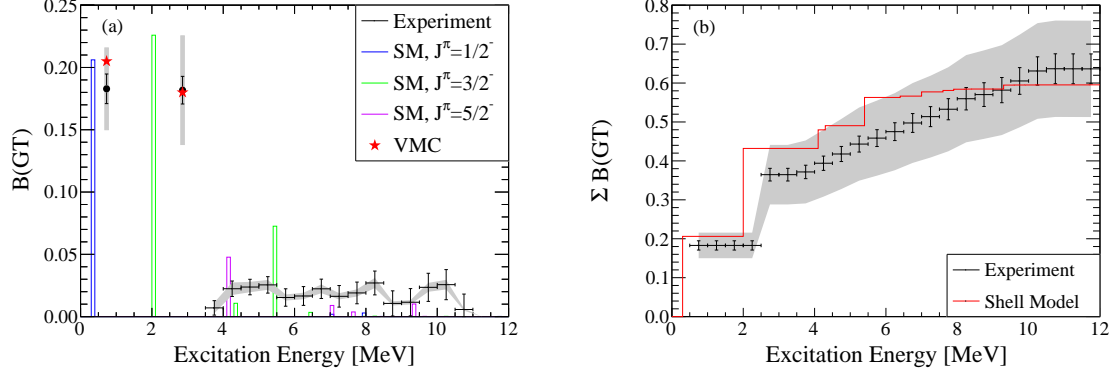
Figure 9.1: (a) Comparison of the data (black, with gray bands indicating systematic error) to the shell-model calculations (blue, green, purple) and VMC calculations (red stars). (b) Measured cumulative $B(GT)$ distribution (black, with gray bands indicating systematic error) compared to the shell-model calculation (red).

State University [59]. Both groups extracted $B(GT)$ for the $\frac{1}{2}^-$ and $\frac{3}{2}^-$ states, but the $(d,^2\text{He})$ results are significantly larger than the $(t,^3\text{He})$ results and are consistent with the shell-model calculations without quenching. Under the assumption of isospin symmetry, the present $^{11}\text{C}(p,n)$ results are consistent with the (n,p) results and the $(t,^3\text{He})$ results. Again, the VMC calculations predict very similar GT transition strengths for the transitions to the $\frac{1}{2}^-$ and $\frac{3}{2}^-$ states in ^{11}N and ^{11}Be, supporting the isospin symmetry assumption.

Chapter 10

Large LENDA: The LENDA

Extension

An array of large plastic scintillators was added to LENDA to increase the overall efficiency of the detector array. These detectors were originally built at Fermilab in the 1980s, then given to the University of Notre Dame, and finally passed along to Michigan State University (MSU) in 2016 (Section 10.1). As part of this thesis work, the detectors were refurbished and characterized once they arrived at MSU (Section 10.2), and they were used to supplement the existing LENDA bars in the experiment (Section 10.3).

10.1   Large LENDA History

This detector array was originally designed and built at Fermilab as part of the TOF2 hodoscope [130]. The purpose of this system was to provide π, K, and p identification at momenta up to about 2 GeV/c. The detectors are BC-408 plastic scintillators with dimensions of 152×15.2×5.1 cm. The geometry of the detectors was determined by the space limitations of the spectrometer room at Fermilab. The required timing resolution was defined by the expected timing separation between the hadrons in experiments.

The TOF2 scintillators were coupled to two different types of light guides: a standard straight guide at the top and a bent guide at the bottom. A bent light guide was necessary

because a standard light guide and PMT would not fit between the bottom of the scintillator and the floor. Each light guide was coupled to an Amperex XP-2020 PMT. The PMTs were shielded by μ-metal and soft iron shields. The PMT base design was based on a modified-dynode Mark III design. The TOF2 detectors were originally wrapped with an opaque static shielding material.

The timing resolution was characterized in several ways. First, the timing resolution was characterized at Fermilab Lab F with a $\approx$100 GeV/c muon beam. The walk-corrected time-of-flight resolution was 250 ps (FWHM).

Second, the timing resolution was characterized in the A2 test beam at Brookhaven National Lab. Positive and negative hadron beams with momenta 0.8-4.0 GeV/c were used. The resolution was again measured to be 250 ps (FWHM).

Third, the timing resolution for each phototube was characterized by sending UV laser light directly into the detector. The timing resolution was 160 ps (FWHM) for each photo-tube, which corresponds to a time-of-flight resolution of 180 ps. This represents the resolution under ideal conditions, and the 250 ps resolution is more representative of what is achievable in an experiment.

Finally, the detectors were used in Fermilab experiment E735 at the C0 collision region of the Tevatron I collider. The detectors measured charged hadrons created in proton-antiproton collisions. The width of the π peak ($1.1 \geq p_\pi \geq 1.16$ GeV/c) was about 280 ns, consistent with the characterization measurements.

Several years later, the detectors were moved to the University of Notre Dame for use in reaction studies with radioactive beams [131]. The array was repurposed for one-neutron-transfer reaction measurements to investigate the exceptionally large ^{6}He breakup cross

section. These measurements required a highly efficient neutron detector array for low-energy neutrons.

At Notre Dame, the detectors were unwrapped and polished. They were rewrapped with Teflon tape, aluminum foil, black tape, and the original static shielding material, in that order, from inside to outside. The curved light guides were replaced by standard light guides. All but nine of the original Amperex XP2020 phototubes were replaced by Amperex XP2262B phototubes.

The timing resolution was characterized with a collimated ^{60}Co source. The resolution of the top-bottom PMT time difference was 800 ps (FWHM). This result is consistent with the 250 ps (FWHM) Fermilab result because the ^{60}Co γ-ray energies are much less than the hadron energies at Fermilab.

Finally, the detector array was donated to the NSCL Charge-Exchange Group at MSU in 2016. Our goal is to use them to measure $\approx$1-10 MeV neutrons in (p,n) charge-exchange experiments.

10.2   Refurbishment

When the detectors arrived at the NSCL, they were refurbished. Alyssa Davis contributed significantly to the work presented in this section. First, the PMT bases, which were previously unlabeled, were labeled and permanently assigned to their own PMT. The detector was covered with a black felt blanket to mitigate any light leaks, and a ^{22}Na spectrum was taken to ensure the detector worked with its assigned bases.

The original static shielding material was removed and discarded because it had small holes from 30 years of wear and tear. As a replacement, the detectors were wrapped in
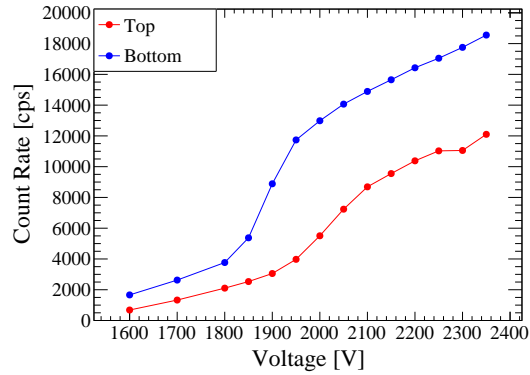
Figure 10.1: LL05 counting curves. These curves were used to find the optimum voltage for each PMT.

an extra layer of black electrical tape. After wrapping, the detector's background rate was measured without the blanket to check for light leaks. If the background rate did not change as the lights were turned on and off, then the detector had no light leaks.

After the detector was re-wrapped, the PMTs were optimized. The gain and focus knobs on the PMT bases were adjusted to maximize the signal amplitude and secured with tape. Then a counting curve was taken with each PMT to determine the optimum voltage. The counting curves for the LL05 PMTs are shown in Figure 10.1. The counting curves did not show a flat plateau as is usually expected, but rather exhibited a shallow positive slope, possibly due to noise. The optimum voltage was taken as the point just after the slope changes from steep to shallow, e.g. 2000 V for the bottom PMT of LL05 shown in Figure 10.1. Starting with the optimum voltage, the PMTs were gain-matched as much as possible. Note that the gains of the PMTs varied significantly, preventing good gain-matching across all detectors.

Then commissioning measurements were done. ^{241}Am, ^{252}Cf, ^{22}Na, ^{137}Cs, and ^{60}Co light-output spectra were taken to verify that the response of each detector was reasonable. These spectra are shown for LL05 in Figures 10.2(a-e). A light-output calibration was done

with ^{22}Na, ^{137}Cs, and ^{241}Am, shown for LL05 in Figure 10.2(f). Although these detectors have rather poor light-output resolution, the light-output calibration was still nicely linear.

The position was calibrated by placing the ^{22}Na source at five different locations along the bar. The position was calculated in two ways. First, the position was determined from the time difference between the top and bottom PMTs. This is shown in Figure 10.3(a).

Second, the position was calculated from the light output of each PMT. The signal is attenuated as it travels through the scintillator, so a smaller signal indicates that the scintillating event occurred farther from the PMT. Hence the relative size of the top and bottom signals contains position information. The signal size, LO, at the end of the detector where the PMT is:

$$LO = LO_0 e^{-x/\lambda} \tag{10.1}$$

where LO_0 is the initial size of the signal, x is the distance it traveled through the scintillator, and λ is the mean free path. If x is the distance from the top PMT and L is the length of the detector, then the light output in each PMT is:

$$LO_{top} = LO_0 e^{-x/\lambda} \tag{10.2}$$

$$LO_{bottom} = LO_0 e^{-(L-x)/\lambda} \tag{10.3}$$

The position is proportional to the natural log of the ratio of the top and bottom light outputs:

$$\frac{LO_{top}}{LO_{bottom}} = e^{(-2x+L)/\lambda}$$
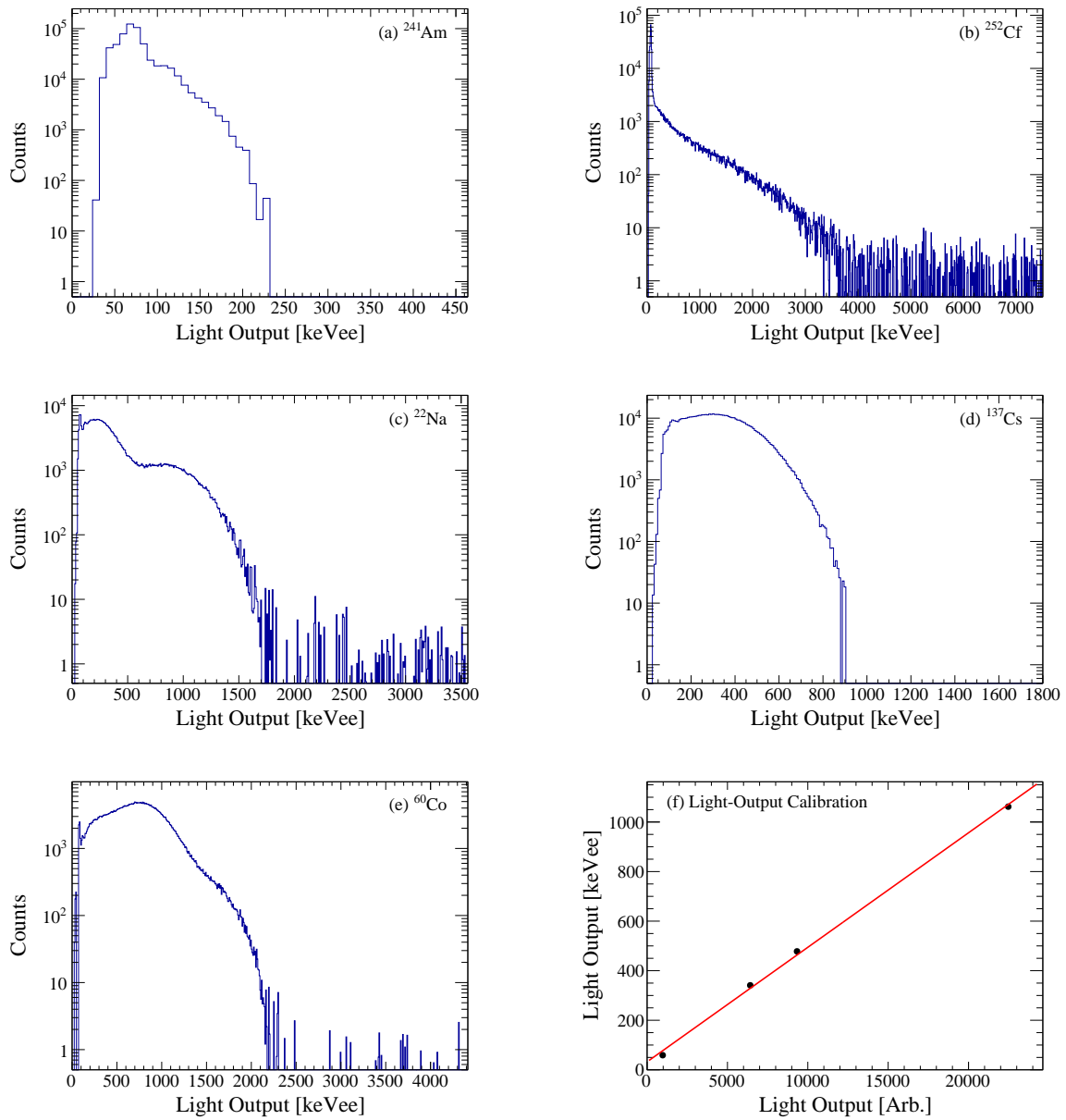
Figure 10.2: (a-e) LL05 light output spectra. (f) LL05 commissioning light-output calibration.
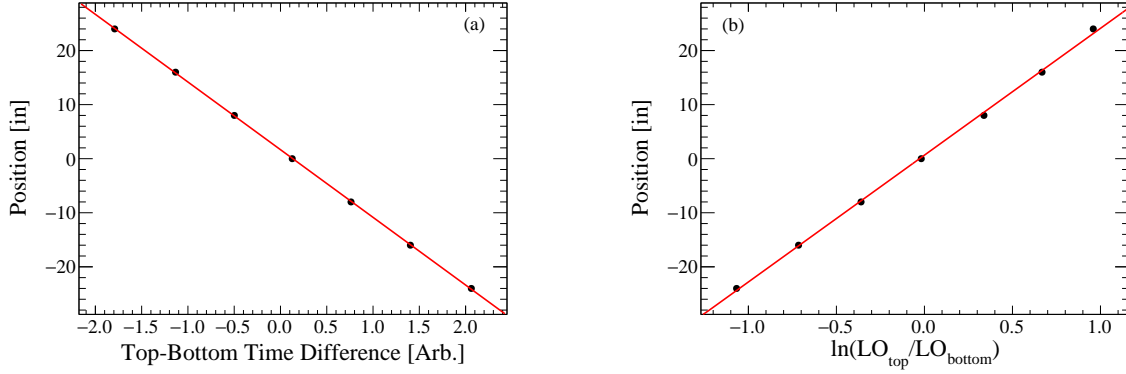
Figure 10.3: (a) LL05 position calibration with the top-bottom time difference. (b) LL05 position calibration with the top-bottom light-output difference.

$$ln\frac{LO_{top}}{LO_{bottom}} = \frac{-2x + L}{\lambda}$$

$$x \propto \ln\frac{LO_{top}}{LO_{bottom}} \tag{10.4}$$

The position calibration using this method is shown in Figure 10.3(b).

Last, the time-of-flight resolution was measured with the ^{60}Co source. The LENDA bar SL02 provided the reference time. The Large LENDA bar was placed horizontally, and SL02 was placed vertically 50 in away. The centers of each bar were aligned. The source was suspended halfway between each bar. ^{60}Co was chosen because it emits two relatively high-energy γ rays in coincidence, 1.173 MeV and 1.332 MeV. The LL05 light output vs. the time-of-flight is shown in Figure 10.4(a). The Compton edges can be seen around 1 MeV. The resulting time-of-flight resolution as a function of LL05 light output is shown in Figure 10.4(b). The time-of-flight resolution presented here includes the resolution of SL02. A time-of-flight resolution of about 1.5 ns (FWHM) was achieved for the higher light outputs.
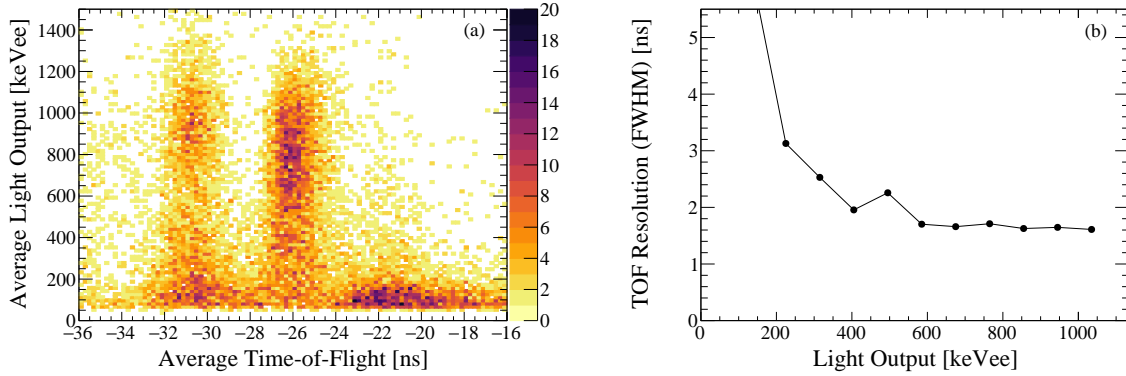
Figure 10.4: (a) LL05 average light output vs. average time-of-flight. SL02 was used as the reference time. (b) LL05 time-of-flight resolution (including the reference detector SL02 resolution) as a function of light output.

10.3   In the Experiment

The Large LENDA bars were used in the experiment with the goal of increasing the efficiency of the existing LENDA array. They were placed roughly 3 m from the target in the angle range $\theta_{LL} \approx 38° - 78°$, where θ_{LL} is the azimuthal angle with the beam line as the z-axis. Large LENDA was placed to the right of the beamline (from the beam's point of view). Figure 5.9 shows a photo of the experimental setup.

Unfortunately, due to difficulties in background subtraction, the Large LENDA array could not be used in the main analysis of the experimental data. However, their light-output calibration (Section 10.3.1) and time-of-flight corrections (Section 10.3.2) are given here as a proof-of-principle demonstration for future experiments with less background.

10.3.1   LL Light Output Calibration

The Large LENDA bars were calibrated just like their North and South LENDA counterparts as described in Section 6.3.2, and just like their commissioning measurements described in Section 10.2. Again, the sources used were ^{241}Am, ^{137}Cs, and ^{22}Na. The energy spectra are

shown in Figure 10.5 for LL05T. Unlike North and South LENDA, the first ^{241}Am peak at 26 keVee is not visible in the Large LENDA bars, so only the 60 keVee photopeak was used for the calibration. The light-output resolution is also worse in Large LENDA than in North and South LENDA, so the location of the Compton Edge is more uncertain. However, the light-output calibration was still nicely linear within uncertainties, as shown in Figure 10.6 for LL05T.

A few of the Large LENDA detectors–LL04, LL09, and LL11–performed poorly in the experiment and should be checked before use in future experiments. In particular, the ^{241}Am photopeak was not at all visible in LL04, was barely visible in LL09, and was relatively small in LL11. The Compton edges of the other sources in LL04, LL09, and LL11 were comparable to all of the other bars.

10.3.2   LL Timing Resolution

The Large LENDA time-of-flight was corrected in the same way as North and South LENDA, as described in Section 6.3.4. The same focal-plane corrections were applied to correct for *E1 up* correlations with xfp and afp. Jitter corrections were applied to correct the γ flash to 0 ns. The Large, North, and South LENDA jitter corrections are shown in Figure 10.7. Then a walk correction was applied, as illustrated in Figure 10.8.

The resulting time-of-flight resolution is shown as a function of light output in Figure 10.9. Like North and South LENDA, the Large LENDA time-of-flight resolution approaches 1 ns (FWHM) at high light outputs. However, the resolution is worse than North and South LENDA at lower light outputs.
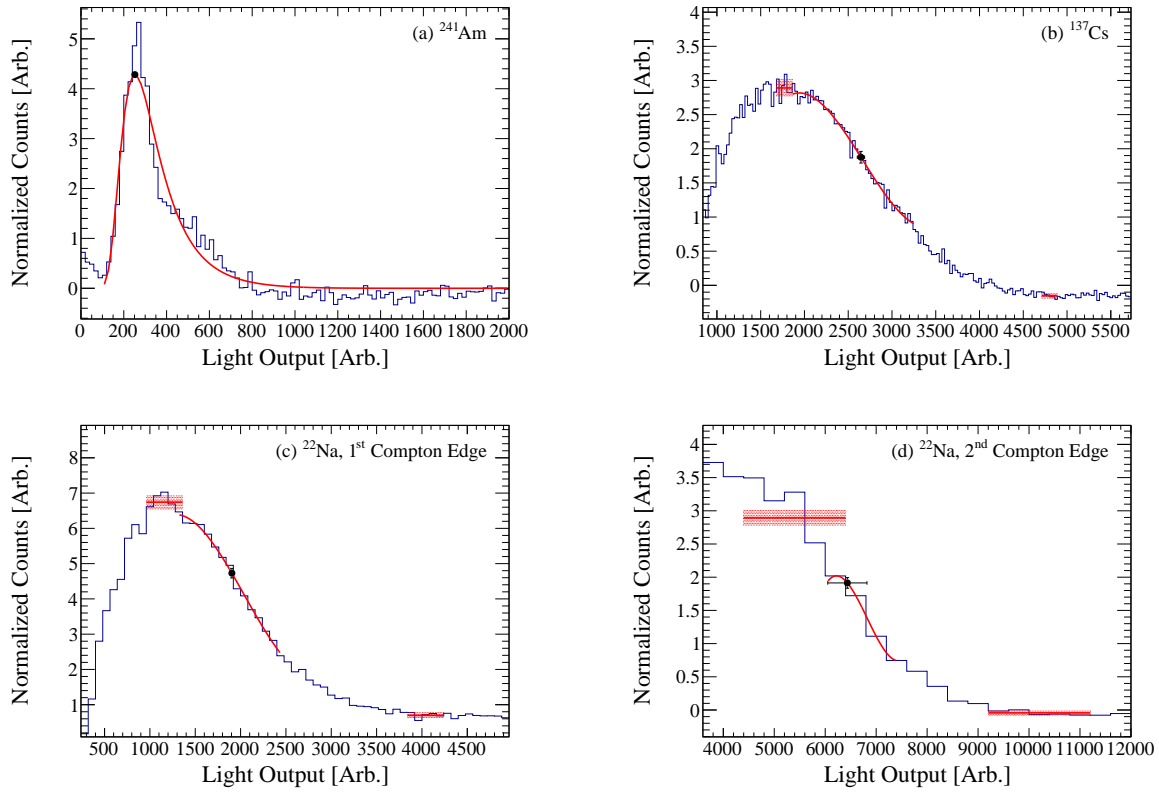
Figure 10.5: Energy spectra for LL05T energy calibrations. The red curves are the fits, and the black points indicate the photopeak or Compton edge location. The red rectangles show the uncertainty in the maximum and minimum used to determine the 2/3 maximum for the Compton edge.
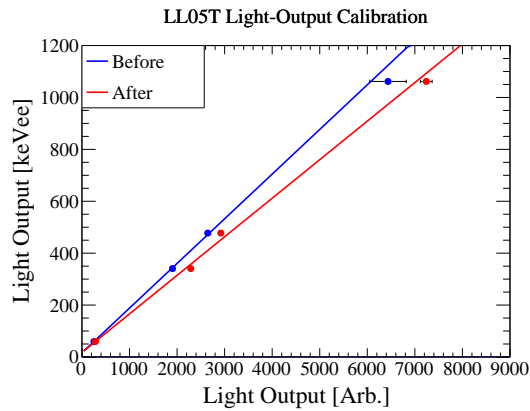
Figure 10.6: Energy calibrations for the LL05T PMT before (blue) and after (red) the experiment.
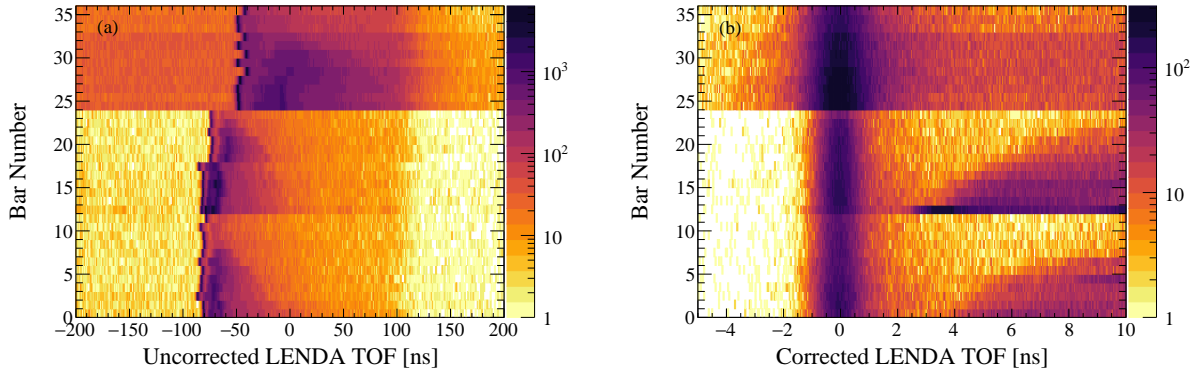
Figure 10.7: LENDA time-of-flight spectra (a) before and (b) after the jitter correction for the first set of 2.3290 Tm runs. Bar Numbers 0-11 are North LENDA, 12-23 are South LENDA, and 24-35 are Large LENDA.
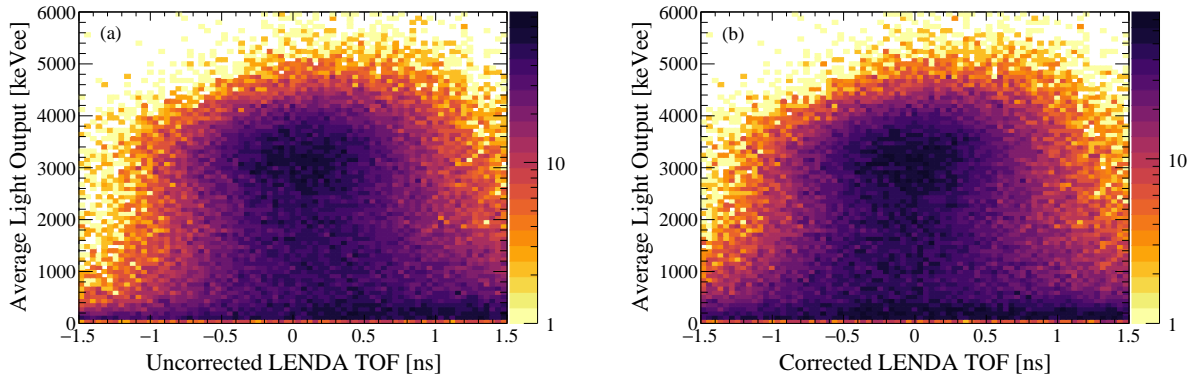
Figure 10.8: Large LENDA light output vs. time-of-flight (a) before and (b) after the walk correction.
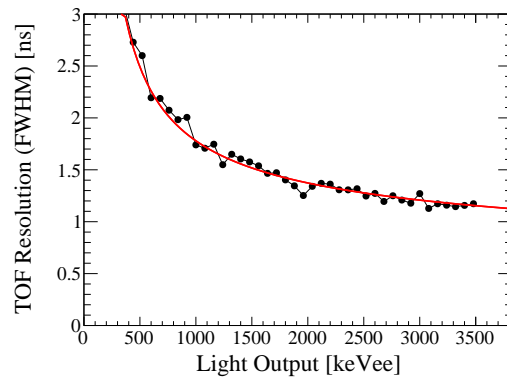
Figure 10.9: Large LENDA timing resolution as a function of the light output.

Chapter 11

Digital Filter Algorithm for Dark Count Rate Reduction in Silicon Photomultipliers

Oak Ridge National Laboratory (ORNL) provides world-class neutron scattering facilities that enable materials research relevant to many applications. To maximize the breadth of research and scientific output at these facilities, new neutron detector technologies must be developed.

A prototype neutron detector was built at ORNL. The prototype detector, illustrated in Figure 11.1, consists of two 5 cm x 5 cm sheets of Eljen EJ-426HD ZnS(Ag):^{6}LiF scintillator that sandwich a 25 x 25 array of Kuraray Y-11(200)M wavelength shifting (WLS) fibers. The front scintillator has a thickness of 0.32 mm, and the back scintillator has a thickness of 0.50 mm. The fibers have a 1 mm diameter and are spaced 2.15 mm apart. Each fiber is read out by an ON Semiconductor MICROFC-10035-SMT-TRI silicon photomultiplier (SiPM).

Briefly, the detector operates as follows. An incident neutron creates a burst of photons when it interacts with the scintillator. The photons propagate through the scintillator to the WLS fibers, and the fibers transport the photons to the SiPMs. The SiPMs convert the photons to an electronic signal that can be processed.
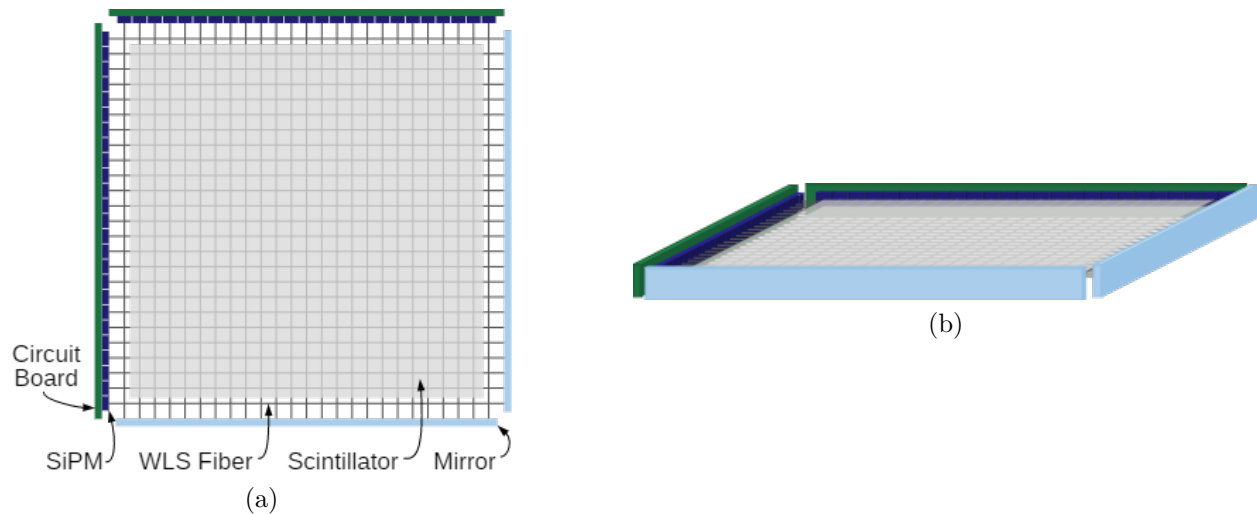
Figure 11.1: (a) Top and (b) side view illustrations of the prototype neutron detector. The detector consists of two sheets of ZnS(Ag):^{6}LiF scintillator that sandwich an array of wavelength-shifting (WLS) fibers. The fibers are read out by silicon photomultipliers (SiPMs).

This design is similar to the design of detectors currently in use at the Spallation Neutron Source at ORNL, with the exception that the current design uses photomultiplier tubes (PMTs) to read out the WLS fibers. It is desirable to increase the area and fiber density of the next generation neutron detectors to increase the geometric neutron detection efficiency and position resolution. However, due to the high cost of PMTs, scaling the current detector design is prohibitively expensive. SiPMs, on the other hand, are much cheaper than PMTs and would allow for efficient scaling of WLS fiber detectors.

The SiPMs, however, have not been used in this type of detector before because they have a large dark count background. This dark count background comes from thermal electrons in the active volume and obscures the neutron signal. In this work, a simulation of the prototype detector response was developed, and the simulation was used to optimize a digital filter algorithm that can distinguish the electronic signature of a neutron from the large dark count background.

Section 11.1 describes the model of the SiPM response to a single photon, and Section 11.2
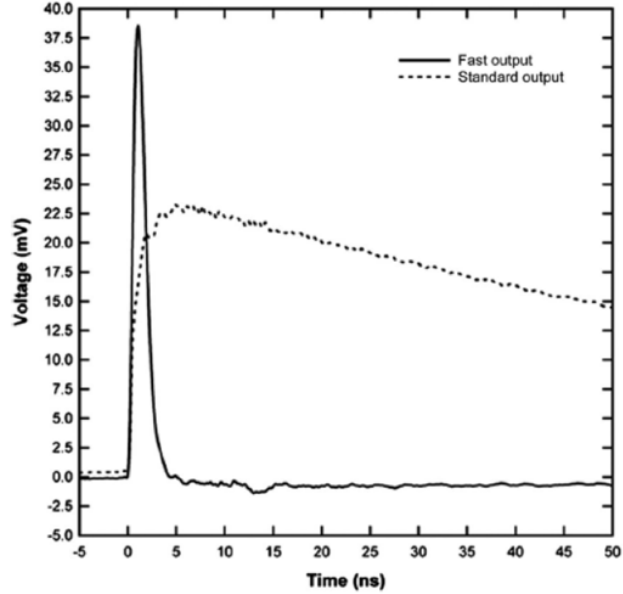
Figure 11.2: Silicon photomultiplier single-photon response [132]. The standard output is used in this case.

explains how the model is used to simulate the dark count background in the detector. Section 11.3 describes the model of the scintillator response to incident neutrons and gamma rays, and Section 11.4 explains how those models are used to simulate neutron and gamma data in the detector. Last, the digital filter algorithm is described in Section 11.5, and the optimization of the algorithm using the simulated data is given in Section 11.6.

11.1 SiPM Single-Photon Response

The SiPM's single-photon response is shown in Figure 11.2. Note that the SiPM response to a thermal electron is identical to that of a real photon. Because the data acquisition system samples the SiPM output only every 10 ns, the standard response is used for the prototype detector. Eq. 11.1 gives the model for this pulse.

$$V(t) = -0.200443t + 24.658287 - \frac{5.452290}{t} \tag{11.1}$$

182
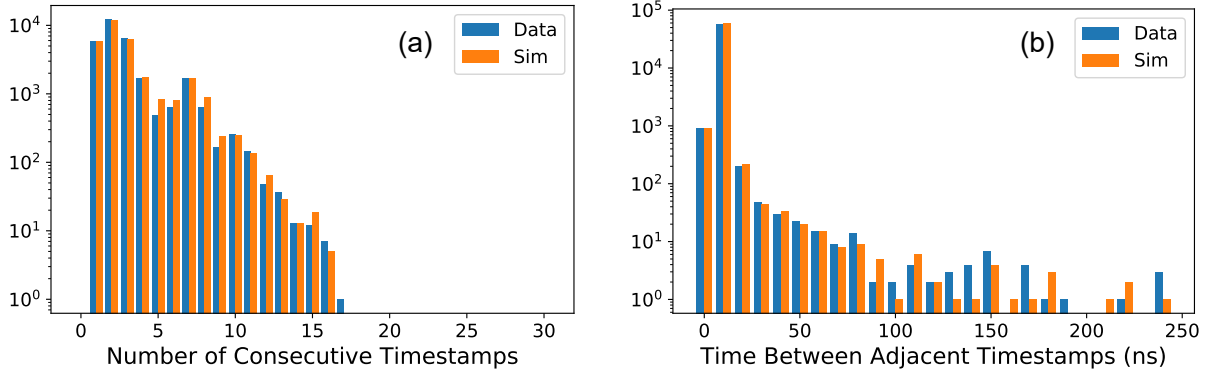
Figure 11.3: (a) The number of consecutive timestamps and (b) the time between adjacent timestamps were used to find the parameters of the dark count background simulation.

11.2   Dark Count Background

To simulate the dark count background, SiPM pulses are generated at random time intervals with a certain rate according to Poisson statistics. The pulse is given a height according to a certain distribution. Then an afterpulse may be generated after the initial pulse according to some probability. Therefore the parameters of the dark count background simulation are:

- Dark count rate

- SiPM pulse height distribution

- Probability of afterpulsing

- Time to afterpulse

These parameters were deduced using background data from the prototype detector. The dark count rate was determined by counting the number of events that do not have any events in the preceding 1 μs. The pulse height distribution was estimated by reproducing the distribution of the number of consecutive timestamps, Figure 11.3(a). The afterpulsing parameters were estimated by reproducing the time between adjacent timestamps, Figure 11.3(b).

The detector output is a series of timestamps. The data acquisition system reads the SiPM output every 10 ns. If the output exceeds a certain discriminator threshold, then the

183
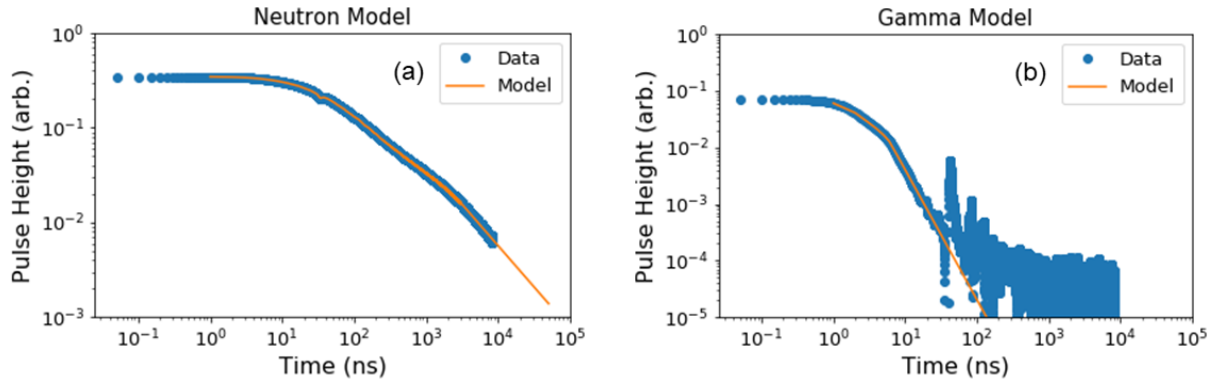
Figure 11.4: Average scintillator response with model for (a) neutrons and (b) gamma rays.

timestamp is recorded. The simulation works the same way: the SiPM output is sampled every 10 ns, and if the output is greater than a user-defined discriminator threshold, then the timestamp is recorded.

11.3   Scintillator Neutron and Gamma Responses

The neutron and gamma responses of the scintillator were measured with ^{252}Cf and ^{60}Co, respectively. The scintillator was coupled directly to a photomultiplier tube to maximize photon collection. Many pulses were averaged to get the neutron and gamma response shapes. The measured shapes and models are shown in Figure 11.4. The pulses are modeled as the measured value at every ns except at large times, where the model is a power law extrapolation.

11.4   Neutron and Gamma Data

Neutron and gamma data are generated in a manner similar to the dark count background. Random time intervals with a certain rate are generated to represent incident neutrons or gamma rays. For each incident neutron or gamma ray, a certain number of photons reach
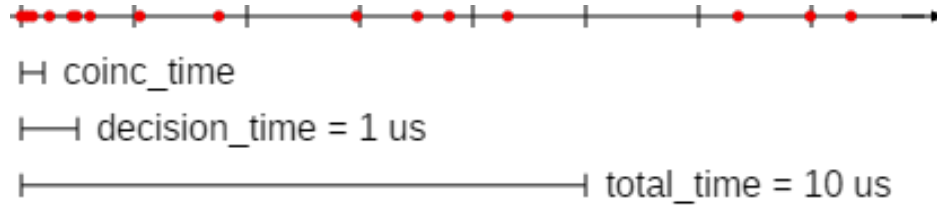
Figure 11.5: Illustration of the digital filter algorithm. The red points represent the recorded timestamps of the detector output. See text for details.

the SiPM. For each photon, a time is randomly drawn from the neutron or gamma pulse shapes shown in Figure 11.4. For each time, a SiPM pulse and possibly an afterpulse are generated as described in Section 11.2.

The complete simulated detector data are created by combining simulated dark count background, neutron, and gamma data.

11.5   Digital Filter Algorithm

The digital filter algorithm is illustrated in Figure 11.5. It uses three windows to separate neutron events from gamma events and dark count background. The first window has a length of *coinc_time*. If at least *min_coinc* timestamps occur in this window, then the algorithm continues to count for a second window of length *decision_time*. If at least *min_neutron* timestamps occur in this window, then the algorithm continues to count for a third window of length *total_time*. If at least *total_counts* timestamps occur in this window, then the event counts as a neutron. The first window is the initial trigger. The purpose of the second window is to eliminate triggers on the dark count background, and the purpose of the third window is to eliminate triggers on gamma rays.

As shown in Figure 11.4, the neutron pulse is very long, and photons from the neutron interaction in the scintillator may arrive after the end of the *total_time* window. In order

185

to prevent double-counting of a single neutron event, the algorithm continues to count for another *total_time* window every time the *total_count* is exceeded.

11.6   Filter Parameter Optimization

The quality of the filter algorithm was determined by how well it maximized the neutron detection efficiency and minimized the false neutron detection rate. The simulated input detector parameters were:

- Background count rate = 1,500 cps
- Discriminator threshold = 500
- Neutron pulse size = 20 photons/pulse
- Neutron pulse rate = 1,000 cps
- Gamma pulse size = 5 photons/pulse
- Gamma pulse rate = 10,000 cps

The following filter parameter space was explored. Note that *decision_time* and *total_time* are held constant to keep the parameter space manageable, but they can also be varied in future studies.

- $min\_coinc = 3 - 8$
- $coinc\_time = 100 - 750$ ns
- $min\_neutron = 4 - 14$
- $decision\_time = 1$ μs
- $total\_counts = 20 - 35$
- $total\_time = 10$ μs
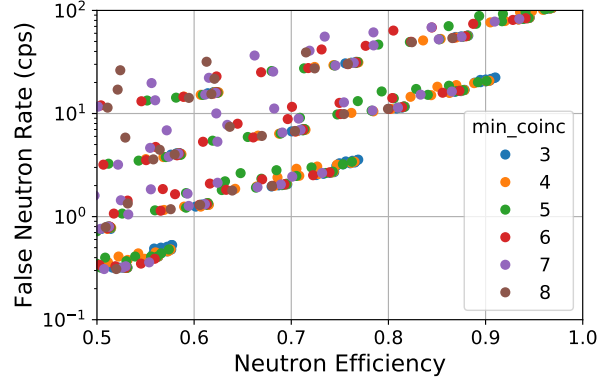
Figure 11.6: Performance of the filter algorithm. Each point represents one set of filter parameters. The best parameter sets maximize the neutron efficiency and minimize the false neutron rate.

Figure 11.6 shows the resulting detector performance for each parameter set. The optimum filter parameters maximize neutron efficiency while minimizing the false neutron rate.

Figures 11.7(a-c) show only filter parameter sets with $min\_coinc = 4$. This shows that a longer $coinc\_time$, a smaller $min\_neutron$, or a smaller $total\_counts$ generally yields better efficiency, but also a higher false neutron rate. Filter parameter sets with other values of min_coinc show a similar trend.

The optimum filter parameter sets are shown in Figure 11.7(d). The achievable efficiency is determined by the maximum allowable false neutron rate, which is defined by the experiment requirements.

Next, the input detector parameters were varied. Figure 11.8(a) shows the optimum filter parameters for various neutron pulse sizes. For a pulse size of 10 photons/pulse, achieving a neutron efficiency of >50% and a false neutron rate of <100 cps with this filter algorithm is not possible. However, the results are greatly improved for 30 photons/pulse.

Figure 11.8(b) shows the optimum filter parameters for various neutron rates. The performance improves as the rate decreases. With a neutron count rate of 100,000 cps, achieving a neutron efficiency of >50% and a false neutron rate of <100 cps is not possible.
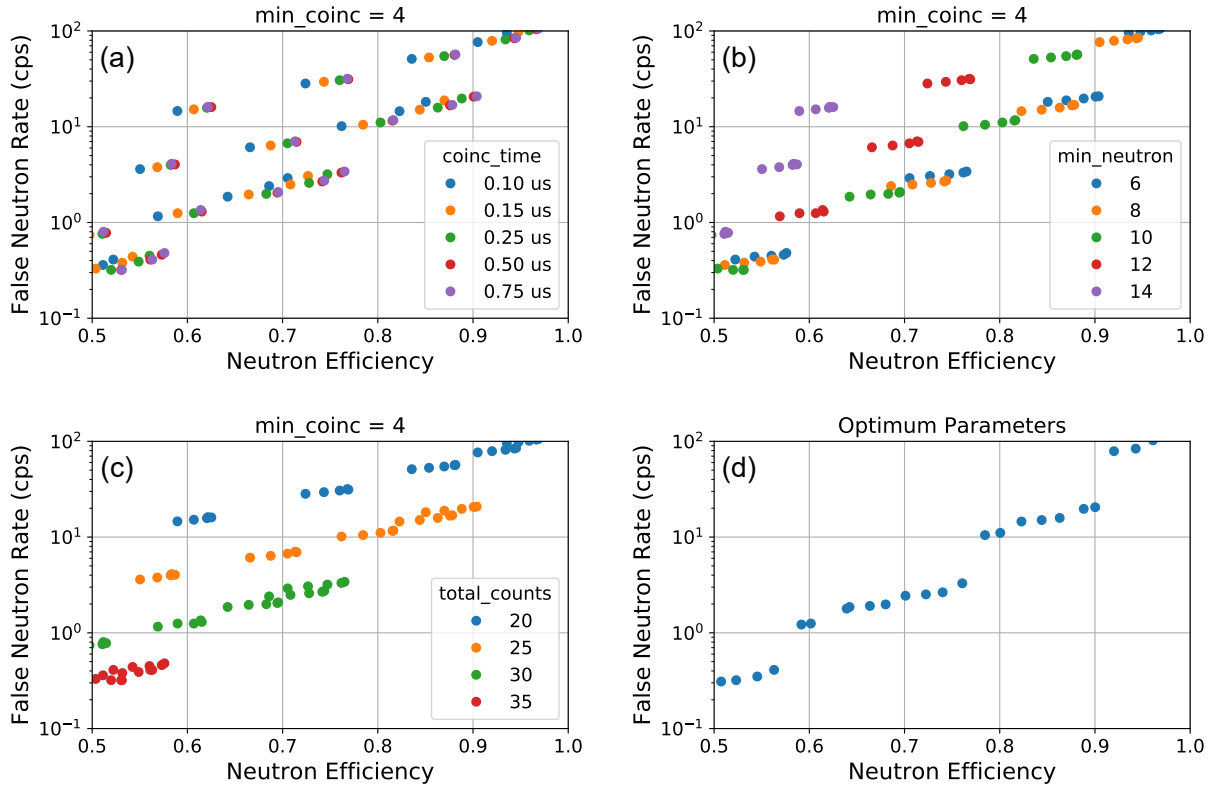
Figure 11.7: (a-c) Performance of filter for parameter sets with $min\_coinc = 4$ only. (d) Performance of the filter algorithm for optimum parameter sets only.

Although the dark count background rate was determined empirically from detector data, only one SiPM was used. It is likely that different SiPMs will have different dark count background rates. Figure 11.8(c) shows the optimum filter parameters for various dark count background rates. Noise rates between 1,000-5,000 cps do not significantly affect the performance of the filter algorithm.

Figure 11.8(d) shows the optimum filter parameters for various gamma rates. Above about 1,000 cps, gamma rays significantly diminish the filter algorithm performance. Below this value, the performance is limited by the dark count background.
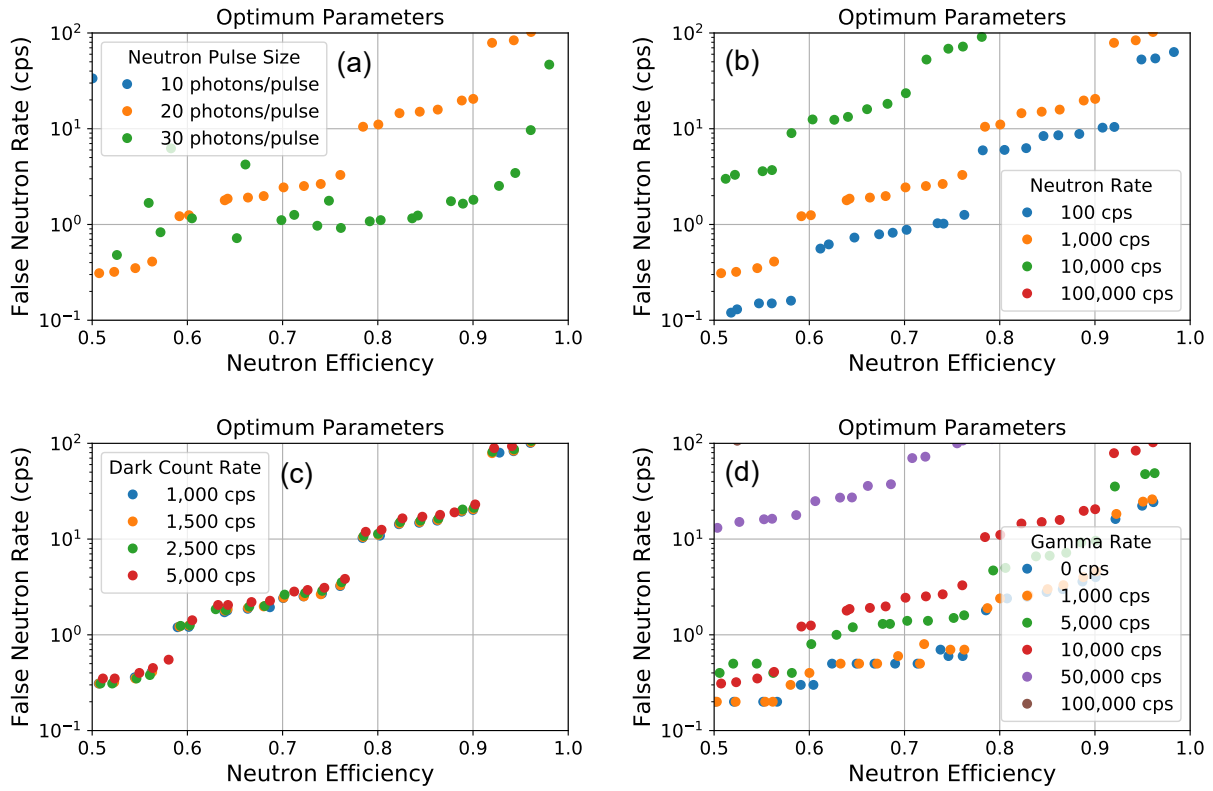
Figure 11.8: Performance of filter for various (a) neutron pulse sizes, (b) neutron rates, (c) dark count background rates, and (d) gamma rates.

Chapter 12

Conclusion

In conclusion, the Gamow-Teller transition strength $B(\text{GT})$ has been extracted from the $^{11}\text{C}(p,n)^{11}\text{N}$ reaction in inverse kinematics. Both shell-model and *ab-initio* Variational Monte Carlo (VMC) calculations reproduce $B(\text{GT})$ for transitions to the first $\frac{1}{2}^-$ state and first $\frac{3}{2}^-$ state in ^{11}N well. The shell-model calculations are also consistent with the cumulative $B(\text{GT})$ strength up to 10 MeV in ^{11}N. Additionally, under the assumption of isospin symmetry, the results are consistent with the $B(\text{GT})$ extracted from (n,p) and $(t,^3\text{He})$ measurements to the mirror states in ^{11}Be. Both the experimental and theoretical results indicate that the unbound nature of ^{11}N does not significantly alter the structure from what is expected for bound p-shell nuclei.

Looking forward, the accuracy of the *ab-initio* $B(\text{GT})$ value could be improved by performing a Green's Function Monte Carlo (GFMC) propagation rather than VMC. GFMC calculations typically quench the GT matrix element by 2% to 3% from the VMC value, but this would still be in good agreement with the data. A GFMC $B(\text{GT})$ calculation for these transitions could confirm this expectation. Work is already underway at Washington University in St. Louis to obtain GT matrix elements from GFMC for $A \geq 11$ with the NV2+3 interactions.

Experimentally, this work has demonstrated the feasibility of extracting $B(\text{GT})$ from the (p,n) charge-exchange reaction in inverse kinematics with proton-rich rare-isotope beams.

However, the background was very large, generally exceeding half of the measured counts, even after cleaning (Figure 7.10). Future efforts would benefit from better ways to estimate and eliminate background. The background from γ rays could be greatly reduced by employing neutron detectors with pulse-shape discrimination capabilities, and a project to develop an array of such detectors is underway at the Facility for Rare Isotope Beams (FRIB).

Large LENDA is an array of large neutron detectors that is currently available for use. As part of this work, these detectors were refurbished and shown to function as expected. They can be used in future (p,n) experiments or other experiments resulting in intermediate-energy $(1-10 \text{ MeV})$ neutrons, provided that the background is sufficiently small.

Finally, an algorithm for reducing the dark count rate in silicon photomultipliers (SiPMs) was implemented and tested with a prototype neutron detector at Oak Ridge National Laboratory. SiPMs are not sensitive to magnetic fields like PMTs are, and they can be used near large magnets such as those planned for installation at FRIB.

APPENDIX

APPENDIX A

Acceptance Correction with Holes

In this appendix, a toy model is used to illustrate the complications that arise when the experimental acceptance has holes. In this toy model, let's say that we are interested in the excitation-energy region $E_x = 0 - 10$ MeV. The efficiency of our toy model experiment is 10% everywhere, except for a small hole from 3.5-4.0 MeV where the efficiency is 0%. This is illustrated in Figure A.1. The resolution of our toy model is 0.1 MeV everywhere.

Now assume we don't actually know the "true" efficiency of our toy model experiment from first principles. We can use a simulation to estimate the efficiency, and we simulate 10^7 events with a uniform excitation-energy distribution. The efficiency is the output divided by the smeared input. Our experimental binning is 1 MeV so that no bin has zero acceptance. The input, smeared input, output, and efficiency are shown in Figure A.2.

The effect of the small hole is a $\approx$5% efficiency in the 3-4 MeV bin. The effect of the

Figure A.1: Toy model efficiency.

Figure A.2: (a) Simulation input. (b) Simulation input smeared. (c) Simulation output (d) Simulated efficiency. Note the 3-4 MeV bin has an efficiency of almost exactly 5%.

0.1 MeV resolution can be seen in the output as well. The 0-1 MeV and 9-10 MeV bins have less output counts because some counts are smeared to below 0 MeV or above 10 MeV. Smearing the input corrects this effect, and the efficiency of the first and last bins is accurate.

Next, we can do the "experiment" by "measuring" a Gaussian distribution with a mean of $E_x = 2$ MeV and a standard deviation of $\sigma_{E_x} = 2$ MeV. The measured spectrum shows the low acceptance in the 3-4 MeV bin. The reconstructed spectrum is the ratio of the measured spectrum to the efficiency found above. Both spectra are shown in Figure A.3.

In the 3-4 MeV bin, the reconstructed value is smaller than the true value. On this Gaussian curve, more events occur between 3.0-3.5 MeV, where the hole is, than between 3.5-4.0 MeV. Only the events between 3.5-4.0 MeV are measured. Because the simulation we

194
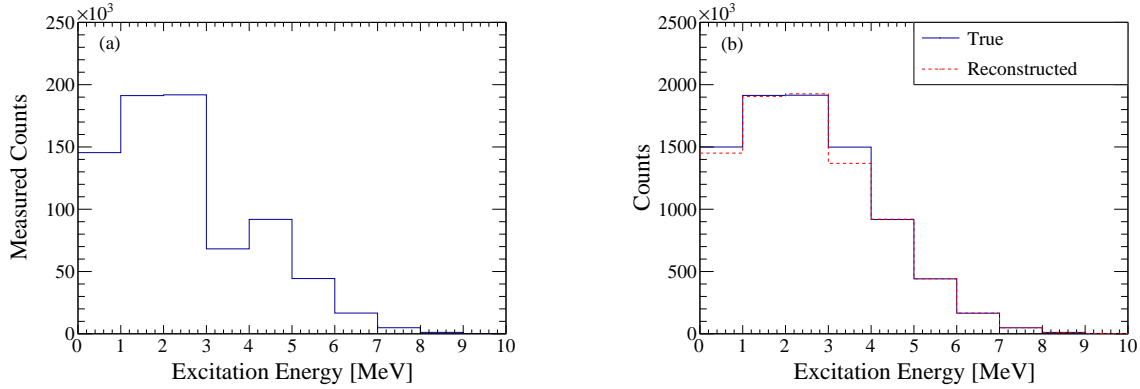
Figure A.3: (a) Measured experimental counts. (b) True counts (blue) and reconstructed counts (red).

used to estimate the efficiency was uniform, the acceptance of that bin was approximately 5%. But now, with only the data from 3.5-4.0 MeV, we are insensitive to anything between 3.0-3.5 MeV. The value of the 3-4 MeV bin is twice what is in 3.5-4.0 MeV, and therefore it is too small.

This effect can be corrected by simulating the true E_x distribution. If the Gaussian curve is used as the simulation input, then the bins are weighted exactly right, and the effect goes away. The new input, smeared input, output, and efficiency are shown in Figure A.4. The corrected reconstruction is shown in Figure A.5. This is why a second iteration of the analysis is done in Section 7.2.2.3.
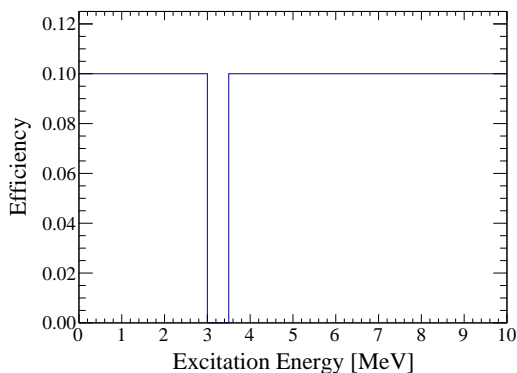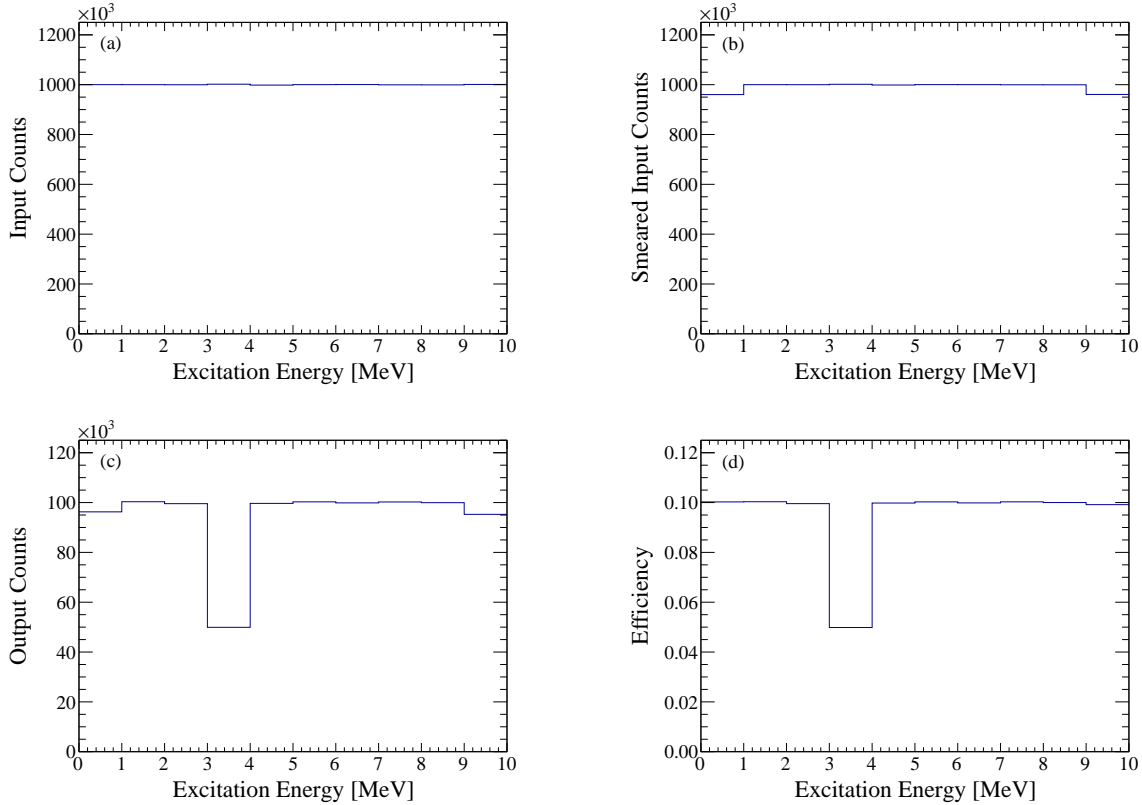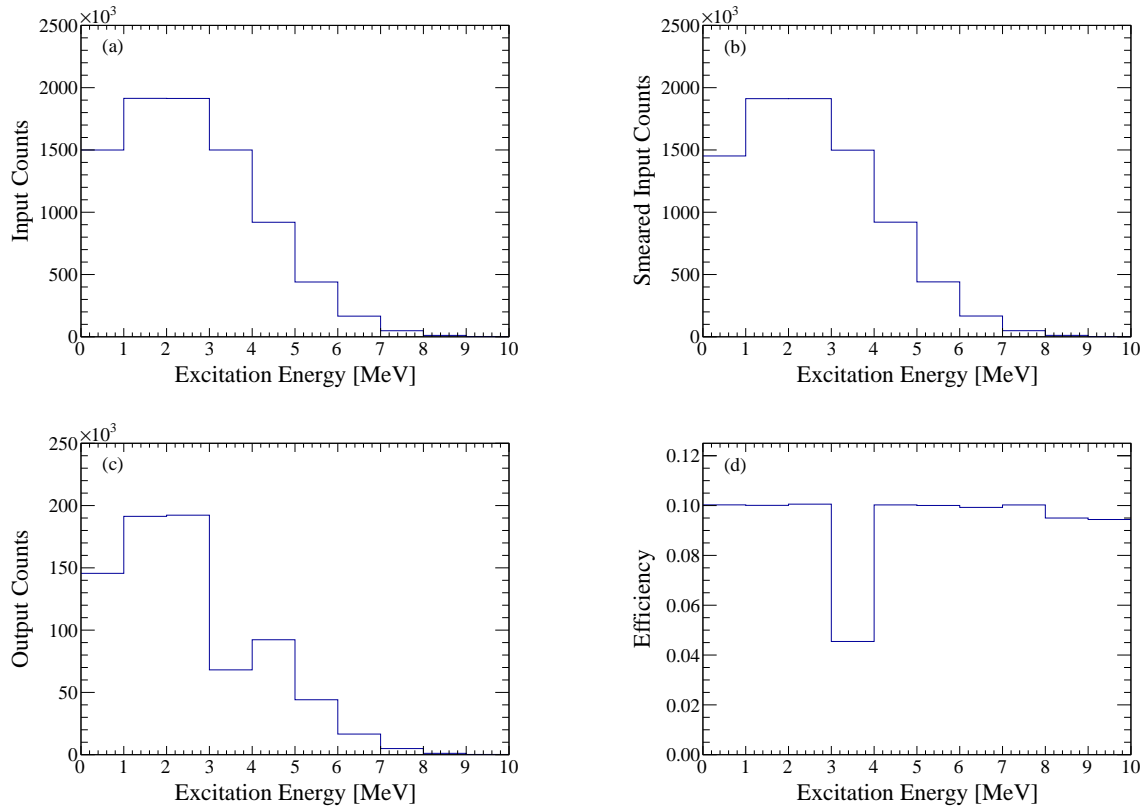
Figure A.4: (a) Simulation input. (b) Simulation input smeared. (c) Simulation output (d) Simulated efficiency. Note the 3-4 MeV bin has a lower efficiency of about 4.5% compared to Figure A.2(d).
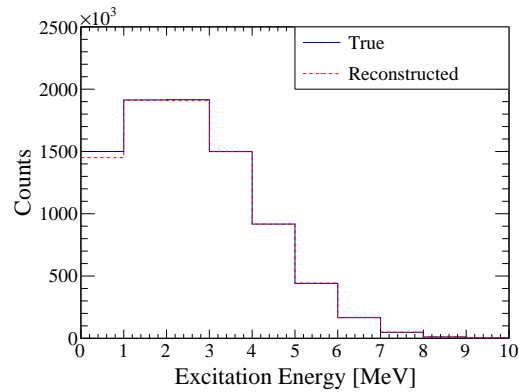
Figure A.5: True counts (blue) and corrected reconstructed counts (red).

REFERENCES

REFERENCES

[1] H. Geiger, "On the Scattering of the α-Particles by Matter," *Proceedings of the Royal Society of London. Series A, Containing Papers of a Mathematical and Physical Character*, vol. 81, no. 546, pp. 174–177, 1908.

[2] H. Geiger and E. Marsden, "On a diffuse reflection of the α-particles," *Proceedings of the Royal Society of London. Series A, Containing Papers of a Mathematical and Physical Character*, vol. 82, no. 557, pp. 495–500, 1909.

[3] H. Geiger, "The scattering of α-particles by matter," *Proceedings of the Royal Society of London. Series A, Containing Papers of a Mathematical and Physical Character*, vol. 83, no. 565, pp. 492–504, 1910.

[4] E. Rutherford, "LXXIX. The scattering of α and β particles by matter and the structure of the atom," *The London, Edinburgh, and Dublin Philosophical Magazine and Journal of Science*, vol. 21, no. 125, pp. 669–688, 1911.

[5] H. Geiger and E. Marsden, "LXI. The laws of deflexion of a particles through large angles," *The London, Edinburgh, and Dublin Philosophical Magazine and Journal of Science*, vol. 25, no. 148, pp. 604–623, 1913.

[6] A. S. Eddington, *The Internal Constitution of Stars*. Cambridge University Press, 1926.

[7] W. C. Röntgen, "On a new kind of rays," *Science*, vol. 3, no. 59, pp. 227–231, 1896.

[8] National Research Council, *Nuclear Physics: Exploring the Heart of Matter*. National Academies Press, 2013.

[9] G. Gamow, "Mass defect curve and nuclear constitution," *Proceedings of the Royal Society of London. Series A, Containing Papers of a Mathematical and Physical Character*, vol. 126, no. 803, pp. 632–644, 1930.

[10] M. G. Mayer, "On closed shells in nuclei. II," *Physical Review*, vol. 75, no. 12, p. 1969, 1949.

[11] O. Haxel, J. H. D. Jensen, and H. E. Suess, "On the 'magic numbers' in nuclear structure," *Physical Review*, vol. 75, no. 11, p. 1766, 1949.

[12] K. S. Krane, *Introductory Nuclear Physics*. John Wiley & Sons, Inc., 1988.

[13] I. Tanihata, "Neutron halo nuclei," *Journal of Physics G: Nuclear and Particle Physics*, vol. 22, no. 2, p. 157, 1996.

[14] B. Jonson, "Light dripline nuclei," *Physics Reports*, vol. 389, no. 1, pp. 1–59, 2004.

[15] I. Tanihata, H. Savajols, and R. Kanungo, "Recent experimental progress in nuclear halo structure studies," *Progress in Particle and Nuclear Physics*, vol. 68, pp. 215–313, 2013.

[16] B. Blank and M. Płoszajczak, "Two-proton radioactivity," *Reports on Progress in Physics*, vol. 71, no. 4, p. 046301, 2008.

[17] M. Pfützner, M. Karny, L. V. Grigorenko, and K. Riisager, "Radioactive decays at limits of nuclear stability," *Rev. Mod. Phys.*, vol. 84, pp. 567–619.

[18] D. H. Wilkinson and D. E. Alburger, "Beta Decay of ^{11}Be," *Physical Review*, vol. 113, no. 2, p. 563, 1959.

[19] I. Talmi and I. Unna, "Order of Levels in the Shell Model and Spin of ^{11}Be," *Physical Review Letters*, vol. 4, no. 9, p. 469, 1960.

[20] A. Kramida, Y. Ralchenko, J. Reader, and NIST ASD Team, "NIST Atomic Spectra Database (ver. 5.9)." https://www.nist.gov/pml/atomic-spectra-database, 2021.

[21] National Nuclear Data Center (NNDC) at Brookhaven National Laboratory, "NuDat 3.0." https://www.nndc.bnl.gov/nudat3/.

[22] B. A. Brown, "Lecture Notes in Nuclear Structure Physics." National Superconducting Cyclotron Laboratory and Department of Physics and Astronomy, Michigan State University, E. Lansing, MI 48824, 2017.

[23] R. F. Casten, *Nuclear Structure from a Simple Perspective*. Oxford University Press Inc., New York, 1990.

[24] C. Iliadis, *Nuclear Physics of Stars*. Wiley-VCH Verlag GmbH & Co. KGaA, Boschstr. 12, 69469 Weinheim, Germany, 2008.

[25] A. de Shalit and I. Talmi, *Nuclear Shell Theory*. Academic Press, New York and London, 1963.

[26] B. A. Brown, "The nuclear shell model towards the drip lines," *Progress in Particle and Nuclear Physics*, vol. 47, no. 2, pp. 517–599, 2001.

[27] B. A. Brown, "The nuclear configuration interations method," in *International Scientific Meeting on Nuclear Physics-Basic concepts in Nuclear Physics: theory, experiments, and applications*, pp. 3–31, Springer, 2018.

[28] B. A. Brown, A. Etchegoyen, N. S. Godwin, W. D. M. Rae, W. A. Richter, W. E. Ormand, E. K. Warburton, J. S. Winfield, L. Zhou, and C. H. Zimmerman, "OXBASH."

[29] E. K. Warburton and B. A. Brown, "Effective interactions for the 0p1s0d nuclear shell-model space," *Physical Review C*, vol. 46, no. 3, p. 923, 1992.

[30] T. Sebe and J. Nachamkin, "Variational buildup of nuclear shell model bases," *Annals of Physics*, vol. 51, no. 1, pp. 100–123, 1969.

[31] R. R. Whitehead, "A numerical approach to nuclear shell-model calculations," *Nuclear Physics A*, vol. 182, no. 2, pp. 290–300, 1972.

[32] G. B. King, L. Andreoli, S. Pastore, M. Piarulli, R. Schiavilla, R. B. Wiringa, J. Carlson, and S. Gandolfi, "Chiral effective field theory calculations of weak transitions in light nuclei," *Physical Review C*, vol. 102, no. 2, p. 025501, 2020.

[33] J. Carlson, S. Gandolfi, F. Pederiva, S. C. Pieper, R. Schiavilla, K. E. Schmidt, and R. B. Wiringa, "Quantum Monte Carlo methods for nuclear physics," *Reviews of Modern Physics*, vol. 87, no. 3, p. 1067, 2015.

[34] J. E. Lynn, I. Tews, S. Gandolfi, and A. Lovato, "Quantum Monte Carlo methods in nuclear physics: recent advances," *Annual Review of Nuclear and Particle Science*, vol. 69, pp. 279–305, 2019.

[35] S. Gandolfi, D. Lonardoni, A. Lovato, and M. Piarulli, "Atomic nuclei from quantum Monte Carlo calculations with chiral EFT interactions," *Frontiers in Physics*, vol. 8, p. 117, 2020.

[36] E. Epelbaum, H.-W. Hammer, and U.-G. Meißner, "Modern theory of nuclear forces," *Reviews of Modern Physics*, vol. 81, no. 4, p. 1773, 2009.

[37] R. Machleidt and D. R. Entem, "Chiral effective field theory and nuclear forces," *Physics Reports*, vol. 503, no. 1, pp. 1–75, 2011.

[38] M. Piarulli, L. Girlanda, R. Schiavilla, R. N. Pérez, J. Amaro, and E. R. Arriola, "Minimally nonlocal nucleon-nucleon potentials with chiral two-pion exchange including Δ resonances," *Physical Review C*, vol. 91, no. 2, p. 024003, 2015.

[39] M. Piarulli, L. Girlanda, R. Schiavilla, A. Kievsky, A. Lovato, L. E. Marcucci, S. C. Pieper, M. Viviani, and R. B. Wiringa, "Local chiral potentials with Δ-intermediate states and the structure of light nuclei," *Physical Review C*, vol. 94, no. 5, p. 054007, 2016.

[40] A. Baroni, L. Girlanda, A. Kievsky, L. E. Marcucci, R. Schiavilla, and M. Viviani, "Tritium β decay in chiral effective field theory," *Physical Review C*, vol. 94, no. 2, p. 024003, 2016. [Erratum: A. Baroni, L. Girlanda, A. Kievsky, L. E. Marcucci, R. Schiavilla, and M. Viviani (2017).].

[41] A. Baroni, L. Girlanda, A. Kievsky, L. E. Marcucci, R. Schiavilla, and M. Viviani, "Erratum: Tritium β decay in chiral effective field theory [Phys. Rev. C 94, 024003 (2016)]," *Physical Review C*, vol. 95, no. 5, p. 059902, 2017.

[42] A. Baroni, R. Schiavilla, L. E. Marcucci, L. Girlanda, A. Kievsky, A. Lovato, S. Pastore, M. Piarulli, S. C. Pieper, M. Viviani, *et al.*, "Local chiral interactions, the tritium Gamow-Teller matrix element, and the three-nucleon contact term," *Physical Review C*, vol. 98, no. 4, p. 044003, 2018.

[43] W. Benenson, E. Kashy, D. H. Kong-A-Siou, A. Moalem, and H. Nann, "$T = \frac{3}{2}$ states in mass-11 nuclei," *Physical Review C*, vol. 9, no. 6, p. 2130, 1974.

[44] V. Guimaraes, S. Kubono, and M. Hosaka, "Structure of light proton-rich nuclei on the drip-line," tech. rep., Tokyo Univ., 1994.

[45] L. Axelsson, M. J. G. Borge, S. Fayans, V. Z. Goldberg, S. Grévy, D. Guillemaud-Mueller, B. Jonson, K. M. Källman, T. Lönnroth, M. Lewitowicz, *et al.*, "Study of the unbound nucleus ^{11}N by elastic resonance scattering," *Physical Review C*, vol. 54, no. 4, p. R1511, 1996.

[46] A. Azhari, T. Baumann, J. Brown, M. Hellström, J. H. Kelley, R. A. Kryger, D. J. Millener, H. Madani, E. Ramakrishnan, D. E. Russ, *et al.*, "Proton decay of states in ^{11}N," *Physical Review C*, vol. 57, no. 2, p. 628, 1998.

[47] A. Lépine-Szily, J. Oliveira Jr, A. Ostrowski, H. Bohlen, R. Lichtenthaler, A. Blazevic, C. Borcea, V. Guimarães, R. Kalpakchieva, V. Lapoux, *et al.*, "Spectroscopy of the Unbound Nucleus ^{11}N by the ^{12}C(^{14}N,^{15}C)^{11}N Transfer Reaction," *Physical Review Letters*, vol. 80, no. 8, p. 1601, 1998.

[48] A. Lépine-Szily, J. M. Oliveira, A. N. Ostrowski, H. G. Bohlen, R. Lichtenthaler, A. Blazevic, C. Borcea, V. Guimarães, R. Kalpakchieva, V. Lapoux, *et al.*, "Study of Excited Levels of the Unbound Nucleus ^{11}N," *Acta Physica Polonica B*, vol. 30, no. 5, p. 1441, 1999.

[49] H. T. Fortune, D. Koltenuk, and C. K. Lau, "Energies and widths of low-lying levels in ^{11}Be and ^{11}N," *Physical Review C*, vol. 51, no. 6, p. 3023, 1995.

[50] F. C. Barker, "Comment on 'Energies and widths of low-lying levels in ^{11}Be and ^{11}N'," *Physical Review C*, vol. 53, no. 3, p. 1449, 1996.

[51] J. M. Oliveira Jr, A. Lépine-Szily, H. G. Bohlen, A. N. Ostrowski, R. Lichtenthäler, A. Di Pietro, A. M. Laird, G. F. Lima, L. Maunoury, F. de Oliveira Santos, *et al.*, "Observation of the ^{11}N Ground State," *Physical Review Letters*, vol. 84, no. 18, p. 4056, 2000.

[52] K. Markenroth, L. Axelsson, S. Baxter, M. J. G. Borge, C. Donzaud, S. Fayans, H. O. U. Fynbo, V. Z. Goldberg, S. Grévy, D. Guillemaud-Mueller, *et al.*, "Crossing the dripline to ^{11}N using elastic resonance scattering," *Physical Review C*, vol. 62, no. 3, p. 034308, 2000.

[53] V. Guimarães, S. Kubono, F. C. Barker, M. Hosaka, S. C. Jeong, I. Katayama, T. Miyachi, T. Nomura, M. H. Tanaka, Y. Fuchi, *et al.*, "Spectroscopic study of the unbound ^{11}N nucleus," *Brazilian Journal of Physics*, vol. 33, no. 2, pp. 263–266, 2003.

[54] E. Casarejos, C. Angulo, P. J. Woods, F. C. Barker, P. Descouvemont, M. Aliotta, T. Davinson, P. Demaret, M. Gaelens, P. Leleux, *et al.*, "Low-lying states in the unbound ^{11}N nucleus," *Physical Review C*, vol. 73, no. 1, p. 014319, 2006.

[55] A. Kumar, R. Kanungo, A. Calci, P. Navrátil, A. Sanetullaev, M. Alcorta, V. Bildstein, G. Christian, B. Davids, J. Dohet-Eraly, *et al.*, "Nuclear force imprints revealed on the elastic scattering of protons with ^{10}C," *Physical Review Letters*, vol. 118, no. 26, p. 262502, 2017.

[56] T. B. Webb, R. J. Charity, J. M. Elson, D. E. M. Hoff, C. D. Pruitt, L. G. Sobotka, K. W. Brown, J. Barney, G. Cerizza, J. Estee, *et al.*, "Particle decays of levels in ^{11,12}N and ^{12}O investigated with the invariant-mass method," *Physical Review C*, vol. 100, no. 2, p. 024306, 2019.

[57] A. Ringbom, J. Blomgren, H. Condé, K. Elmgren, N. Olsson, J. Rahm, T. Rönnqvist, O. Jonsson, L. Nilsson, P. U. Renberg, *et al.*, "The ^{10,11}B$(n,p)^{10,11}$Be reactions at $E_n = 96$ MeV," *Nuclear Physics A*, vol. 679, no. 3-4, pp. 231–250, 2001.

[58] T. Ohnishi, H. Sakai, H. Okamura, T. Niizeki, K. Itoh, T. Uesaka, Y. Satou, K. Sekiguchi, K. Yakou, S. Fukusaka, *et al.*, "Study of spin-isospin excitations in ^{11}Be via the $(d,^2$He$)$ reaction at 270 MeV," *Nuclear Physics A*, vol. 687, no. 1-2, pp. 38–43, 2001.

[59] I. Daito, H. Akimune, S. M. Austin, D. Bazin, G. P. A. Berg, J. A. Brown, B. S. Davids, Y. Fujita, H. Fujimura, M. Fujiwara, *et al.*, "Gamow-Teller strengths from $(t,^3$He$)$ charge-exchange reactions on light nuclei," *Physics Letters B*, vol. 418, no. 1-2, pp. 27–33, 1998.

[60] F. Osterfeld, "Nuclear spin and isospin excitations," *Reviews of Modern Physics*, vol. 64, no. 2, p. 491, 1992.

[61] J. Rapaport and E. Sugarbaker, "Isovector excitations in nuclei," *Annual Review of Nuclear and Particle Science*, vol. 44, no. 1, pp. 109–153, 1994.

[62] M. Ichimura, H. Sakai, and T. Wakasa, "Spin–isospin responses via (p,n) and (n,p) reactions," *Progress in Particle and Nuclear Physics*, vol. 56, no. 2, pp. 446–531, 2006.

[63] Y. Fujita, B. Rubio, and W. Gelletly, "Spin–isospin excitations probed by strong, weak and electro-magnetic interactions," *Progress in Particle and Nuclear Physics*, vol. 66, no. 3, pp. 549–606, 2011.

[64] R. Meharchand, R. G. T. Zegers, B. A. Brown, S. M. Austin, T. Baugher, D. Bazin, J. Deaven, A. Gade, G. F. Grinyer, C. J. Guess, *et al.*, "Probing Configuration Mixing in ^{12}Be with Gamow-Teller Transition Strengths," *Physical Review Letters*, vol. 108, no. 12, p. 122501, 2012.

[65] R. Meharchand, *Spectroscopy of ^{12}Be using the ($^{7}Li,^{7}Be$) reaction in inverse kinematics.* PhD thesis, Michigan State University, ProQuest LLC. 789 East Eisenhower Parkway, P.O. Box 1346, Ann Arbor, MI 48106-1346, 2011.

[66] A. Arima, "History of giant resonances and quenching," *Nuclear Physics A*, vol. 649, no. 1-4, pp. 260–270, 1999.

[67] W. T. Chou, E. K. Warburton, and B. A. Brown, "Gamow-Teller beta-decay rates for $A \leq 18$ nuclei," *Physical Review C*, vol. 47, no. 1, p. 163, 1993.

[68] T. N. Taddeucci, C. A. Goulding, T. A. Carey, R. C. Byrd, C. D. Goodman, C. Gaarde, J. Larsen, D. Horen, J. Rapaport, and E. Sugarbaker, "The (p,n) reaction as a probe of beta decay strength," *Nuclear Physics A*, vol. 469, no. 1, pp. 125–172, 1987.

[69] D. F. Jackson, *Nuclear Reactions.* Methuen & Co Ltd, 1970.

[70] I. J. Thompson and F. M. Nunes, *Nuclear reactions for astrophysics: principles, calculation and applications of low-energy reactions.* Cambridge University Press, 2009.

[71] M. N. Harakeh and A. van der Woude, *Giant Resonances: Fundamental High-Frequency Modes of Nuclear Excitation.* Great Clerendon Street, Oxford OX2 6DP: Oxford University Press, 2001.

[72] J. D. Anderson and C. Wong, "Evidence for charge independence in medium weight nuclei," *Physical Review Letters*, vol. 7, no. 6, p. 250, 1961.

[73] J. D. Anderson, C. Wong, and J. W. McClure, "Isobaric states in nonmirror nuclei," *Physical Review*, vol. 126, no. 6, p. 2170, 1962.

[74] C. D. Goodman, S. M. Austin, S. D. Bloom, J. Rapaport, and G. R. Satchler, *The (p,n) Reaction and the Nucleon-Nucleon Force.* Plenum Press, New York, 1980.

[75] S. D. Bloom, J. D. Anderson, W. F. Hornyak, and C. Wong, "Spin-Spin Interaction and the Reaction O^{18}(p,n)F^{18}," *Physical Review Letters*, vol. 15, no. 6, p. 264, 1965.

[76] J. D. Anderson, C. Wong, and V. A. Madsen, "Charge exchange part of the effective two-body interaction," *Physical Review Letters*, vol. 24, no. 19, p. 1074, 1970.

[77] W. R. Wharton and P. T. Debevec, "Study of the (Li^6,He^6) reactions," *Physical Review C*, vol. 11, no. 6, p. 1963, 1975.

[78] R. R. Doering, A. Galonsky, D. M. Patterson, and G. F. Bertsch, "Observation of giant Gamow-Teller strength in (p,n) reactions," *Physical Review Letters*, vol. 35, no. 25, p. 1691, 1975.

[79] C. D. Goodman, C. A. Goulding, M. B. Greenfield, J. Rapaport, D. E. Bainum, C. C. Foster, W. G. Love, and F. Petrovich, "Gamow-Teller matrix elements from $0°(p,n)$ cross sections," *Physical Review Letters*, vol. 44, no. 26, p. 1755, 1980.

[80] K. Langanke and G. Martínez-Pinedo, "Nuclear weak-interaction processes in stars," *Reviews of Modern Physics*, vol. 75, no. 3, p. 819, 2003.

[81] K. Langanke, G. Martinez-Pinedo, and R. G. T. Zegers, "Electron capture in stars," *Reports on Progress in Physics*, 2021.

[82] M. D. Cortina-Gil, P. Roussel-Chomaz, N. Alamanos, J. Barrette, W. Mittig, F. Auger, Y. Blumenfeld, J. M. Casandjian, M. Chartier, V. Fekou-Youmbi, *et al.*, "Search for the Signature of a Halo Structure in the $p(^6\text{He},^6\text{Li})n$ Reaction," *Physics Letters B*, vol. 371, no. 1-2, pp. 14–18, 1996.

[83] M. D. Cortina-Gil, A. Pakou, N. Alamanos, W. Mittig, P. Roussel-Chomaz, F. Auger, J. Barrette, Y. Blumenfeld, J. M. Casandjian, M. Chartier, *et al.*, "Charge-exchange reaction induced by ^{6}He and nuclear densities," *Nuclear Physics A*, vol. 641, no. 3, pp. 263–270, 1998.

[84] J. Brown, D. Bazin, W. Benenson, J. Caggiano, M. Fauerbach, M. Hellström, J. Kelley, R. Kryger, R. Pfaff, B. Sherrill, *et al.*, "Measurement of the $^1\text{H}(^6\text{He},^6\text{Li})n$ reaction in inverse kinematics," *Physical Review C*, vol. 54, no. 5, p. R2105, 1996.

[85] Z. Li, W. Liu, X. Bai, Y. Wang, G. Lian, Z. Li, and S. Zeng, "First observation of neutron–proton halo structure for the 3.563 MeV 0+ state in ^{6}Li via $^1\text{H}(^6\text{He},^6\text{Li})n$ reaction," *Physics Letters B*, vol. 527, no. 1-2, pp. 50–54, 2002.

[86] S. Shimoura, T. Teranishi, Y. Ando, M. Hirai, N. Iwasa, T. Kikuchi, S. Moriya, T. Motobayashi, T. Murakami, T. Nakamura, *et al.*, "Charge exchange reaction of the neutron-halo nucleus ^{11}Li," *Nuclear Physics A*, vol. 616, no. 1-2, pp. 208–214, 1997.

[87] T. Teranishi, S. Shimoura, Y. Ando, M. Hirai, N. Iwasa, T. Kikuchi, S. Moriya, T. Motobayashi, H. Murakami, T. Nakamura, *et al.*, "Isobaric analog state of ^{11}Li," *Physics Letters B*, vol. 407, no. 2, pp. 110–114, 1997.

[88] S. Shimoura, T. Teranishi, Y. Ando, M. Hirai, N. Iwasa, T. Kikuchi, S. Moriya, T. Motobayashi, T. Murakami, T. Nakamura, *et al.*, "Isobaric analog state of ^{11}Li," *Nuclear Physics A*, vol. 630, no. 1-2, pp. 387–393, 1998.

[89] S. Takeuchi, S. Shimoura, T. Motobayashi, H. Akiyoshi, Y. Ando, N. Aoi, Z. Fü, T. Gomi, Y. Higurashi, M. Hirai, *et al.*, "Isobaric analog state of ^{14}Be," *Physics Letters B*, vol. 515, no. 3-4, pp. 255–260, 2001.

[90] Y. Satou, T. Nakamura, N. Fukuda, T. Sugimoto, Y. Kondo, N. Matsui, Y. Hashimoto, T. Nakabayashi, Y. Okumura, M. Shinohara, *et al.*, "Invariant mass spectroscopy of ^{19,17}C and ^{14}B using proton inelastic and charge-exchange reactions," *Nuclear Physics A*, vol. 834, no. 1-4, pp. 404c–407c, 2010.

[91] Y. Satou, T. Nakamura, Y. Kondo, N. Matsui, Y. Hashimoto, T. Nakabayashi, T. Okumura, M. Shinohara, N. Fukuda, T. Sugimoto, *et al.*, "^{14}Be(p,n)^{14}B reaction at 69 MeV in inverse kinematics," *Physics Letters B*, vol. 697, no. 5, pp. 459–462, 2011.

[92] M. Sasano, G. Perdikakis, R. G. T. Zegers, S. M. Austin, D. Bazin, B. A. Brown, C. Caesar, A. L. Cole, J. M. Deaven, N. Ferrante, *et al.*, "Gamow-Teller Transition Strengths from ^{56}Ni," *Physical Review Letters*, vol. 107, no. 20, p. 202501, 2011.

[93] M. Sasano, G. Perdikakis, R. G. T. Zegers, S. M. Austin, D. Bazin, B. A. Brown, C. Caesar, A. L. Cole, J. M. Deaven, N. Ferrante, *et al.*, "Extraction of Gamow-Teller strength distributions from ^{56}Ni and ^{55}Co via the (p,n) reaction in inverse kinematics," *Physical Review C*, vol. 86, no. 3, p. 034324, 2012.

[94] S. I. Lipschutz, *The (p,n) charge-exchange reaction in inverse kinematics as a probe for isovector giant resonances in exotic nuclei.* PhD thesis, Michigan State University, ProQuest LLC. 789 East Eisenhower Parkway, P.O. Box 1346, Ann Arbor, MI 48106-1346, 2018.

[95] M. Kobayashi, K. Yako, S. Shimoura, M. Dozono, N. Fukuda, N. Inabe, D. Kameda, S. Kawase, K. Kisamori, T. Kubo, *et al.*, "Spin-Isospin Response of the Neutron-Rich Nucleus ^{8}He via the Reaction in Inverse Kinematics," in *Proceedings of the Conference on Advances in Radioactive Isotope Science (ARIS2014)*, p. 030089, 2015.

[96] J. Yasuda, M. Sasano, R. G. T. Zegers, H. Baba, W. Chao, M. Dozono, N. Fukuda, N. Inabe, T. Isobe, G. Jhang, *et al.*, "Inverse kinematics (p,n) reactions studies using the WINDS slow neutron detector and the SAMURAI spectrometer," *Nuclear Instruments and Methods in Physics Research Section B: Beam Interactions with Materials and Atoms*, vol. 376, pp. 393–396, 2016.

[97] J. Yasuda, M. Sasano, R. G. T. Zegers, H. Baba, D. Bazin, W. Chao, M. Dozono, N. Fukuda, N. Inabe, T. Isobe, *et al.*, "Extraction of the Landau-Migdal Parameter

from the Gamow-Teller Giant Resonance in ^{132}Sn," *Physical Review Letters*, vol. 121, no. 13, p. 132501, 2018.

[98] L. Stuhl, M. Sasano, J. Gao, Y. Hirai, K. Yako, T. Wakasa, D. S. Ahn, H. Baba, A. I. Chilug, S. Franchoo, *et al.*, "Study of spin-isospin responses of radioactive nuclei with the background-reduced neutron spectrometer, PANDORA," *Nuclear Instruments and Methods in Physics Research Section B: Beam Interactions with Materials and Atoms*, vol. 463, pp. 189–194, 2020.

[99] C. B. Hinke, M. Böhmer, P. Boutachkov, T. Faestermann, H. Geissel, J. Gerl, R. Gernhäuser, M. Górska, A. Gottardo, H. Grawe, *et al.*, "Superallowed Gamow–Teller decay of the doubly magic nucleus ^{100}Sn," *Nature*, vol. 486, no. 7403, pp. 341–345, 2012.

[100] Program DWBA70, R. Schaeffer and J. Raynal (unpublished); extended version DW81 by J. R. Comfort (unpublished).

[101] D. G. Madland, "Progress in the development of global medium-energy nucleon-nucleus optical model potentials," *arXiv preprint nucl-th/9702035*, 1997.

[102] P. Schwandt, H. O. Meyer, W. W. Jacobs, A. D. Bacher, S. E. Vigdor, M. D. Kaitchuck, and T. R. Donoghue, "Analyzing power of proton-nucleus elastic scattering between 80 and 180 MeV," *Physical Review C*, vol. 26, no. 1, p. 55, 1982.

[103] M. A. Franey and W. G. Love, "Nucleon-nucleon t-matrix interaction for scattering at intermediate energies," *Physical Review C*, vol. 31, no. 2, p. 488, 1985.

[104] J. R. Comfort and B. C. Karp, "Scattering and reaction dynamics for the ^{12}C+p system," *Physical Review C*, vol. 21, no. 6, p. 2162, 1980.

[105] P. A. Závodszky, B. Arend, D. Cole, J. DeKamp, M. Doleans, G. Machicoane, F. Marti, P. Miller, J. Moskalik, W. Nurnberger, *et al.*, "Design, construction, and first commissioning results of superconducting source for ions at NSCL/MSU," *Review of Scientific Instruments*, vol. 79, no. 2, p. 02A302, 2008.

[106] F. Marti, P. Miller, D. Poe, M. Steiner, J. Stetson, and X. Y. Wu, "Commissioning of the coupled cyclotron system at NSCL," in *AIP Conference Proceedings*, vol. 600, pp. 64–68, American Institute of Physics, 2001.

[107] D. J. Morrissey, B. M. Sherrill, M. Steiner, A. Stolz, and I. Wiedenhoever, "Commissioning the A1900 projectile fragment separator," *Nuclear Instruments and Methods in Physics Research Section B: Beam Interactions with Materials and Atoms*, vol. 204, pp. 90–96, 2003.

[108] A. Stolz, M. Behravan, M. Regmi, and B. Golding, "Heteroepitaxial diamond detectors for heavy ion beam tracking," *Diamond and related materials*, vol. 15, no. 4-8, pp. 807–810, 2006.

[109] DuPont, "Kapton® Polyimide films." https://www.dupont.com/electronic-materials/kapton-polyimide-film.html.

[110] D. Bazin, J. A. Caggiano, B. M. Sherrill, J. Yurkon, and A. Zeller, "The S800 spectrograph," *Nuclear Instruments and Methods in Physics Research Section B: Beam Interactions with Materials and Atoms*, vol. 204, pp. 629–633, 2003.

[111] J. Pereira, "The NSCL S800 spectrograph." https://wikihost.nscl.msu.edu/S800Doc/doku.php, November 2020.

[112] G. F. Knoll, *Radiation detection and measurement*. John Wiley & Sons, 2010.

[113] G. Perdikakis, M. Sasano, S. M. Austin, D. Bazin, C. Caesar, S. Cannon, J. M. Deaven, H. J. Doster, C. J. Guess, G. W. Hitt, *et al.*, "LENDA: A low energy neutron detector array for experiments with radioactive beams in inverse kinematics," *Nuclear Instruments and Methods in Physics Research Section A: Accelerators, Spectrometers, Detectors and Associated Equipment*, vol. 686, pp. 117–124, 2012.

[114] S. Lipschutz, R. G. T. Zegers, J. Hill, S. N. Liddick, S. Noji, C. J. Prokop, M. Scott, M. Solt, C. Sullivan, and J. Tompkins, "Digital data acquisition for the Low Energy Neutron Detector Array (LENDA)," *Nuclear Instruments and Methods in Physics Research Section A: Accelerators, Spectrometers, Detectors and Associated Equipment*, vol. 815, pp. 1–6, 2016.

[115] XIA LLC, "Pixie-16: 16-channel PXI Digital Pulse Processor for Nuclear Spectroscopy." https://xia.com/dgf_pixie-16.html.

[116] S. Lipschutz, S. Noji, and J. Pereira, "R00TLe." https://github.com/slipschutz/R00TLe.

[117] R. Brun and F. Rademakers, "ROOT - An object oriented data analysis framework," *Nuclear Instruments and Methods in Physics Research Section A: Accelerators, Spectrometers, Detectors and Associated Equipment*, vol. 389, no. 1-2, pp. 81–86, 1997.

[118] M. Berz, K. Joh, J. A. Nolen, B. M. Sherrill, and A. F. Zeller, "Reconstructive correction of aberrations in nuclear particle spectrographs," *Physical Review C*, vol. 47, no. 2, p. 537, 1993.

[119] S. Agostinelli, J. Allison, K. Amako, J. Apostolakis, H. Araujo, P. Arce, M. Asai, D. Axen, S. Banerjee, G. Barrand, *et al.*, "GEANT4–a simulation toolkit," *Nuclear*

Instruments and Methods in Physics Research Section A: Accelerators, Spectrometers, Detectors and Associated Equipment, vol. 506, no. 3, pp. 250–303, 2003.

[120] D. P. Sanderson, "A 3-D Coordinate System for the NSCL," *9th International Workshop on Accelerator Alignment*, September 2006.

[121] Saint Gobain, "BC-400,BC-404,BC-408,BC-412,BC-416 Premium Plastic Scintillators." https://www.crystals.saint-gobain.com/sites/imdf.crystals.com/files/documents/bc400-404-408-412-416-data-sheet.pdf, 2021.

[122] NIST, "Composition of KAPTON POLYIMIDE FILM." https://physics.nist.gov/cgi-bin/Star/compos.pl?matno=179.

[123] NIST, "Thermophysical Properties of Fluid Systems." https://webbook.nist.gov/chemistry/fluid/.

[124] N. Olsson, H. Condé, E. Ramström, T. Rönnqvist, R. Zorro, J. Blomgren, A. Håkansson, G. Tibell, O. Jonsson, L. Nilsson, *et al.*, "The ^{12}C$(n,p)^{12}$B reaction at $E_n = 98$ MeV," *Nuclear Physics A*, vol. 559, no. 3, pp. 368–400, 1993.

[125] K. P. Jackson, A. Celler, W. P. Alford, K. Raywood, R. Abegg, R. E. Azuma, C. K. Campbell, S. El-Kateb, D. Frekers, P. W. Green, *et al.*, "The (n,p) reaction as a probe of Gamow-Teller strength," *Physics Letters B*, vol. 201, no. 1, pp. 25–28, 1988.

[126] T. N. Taddeucci, R. C. Byrd, T. A. Carey, D. E. Ciskowski, C. C. Foster, C. Gaarde, C. D. Goodman, E. Gülmez, W. Huang, D. J. Horen, *et al.*, "Gamow-Teller transition strengths from the ^{11}B$(p,n)^{11}$C reaction in the energy range 160–795 MeV," *Physical Review C*, vol. 42, no. 3, p. 935, 1990.

[127] D. S. Sorenson, X. Aslanoglou, F. P. Brady, J. R. Drummond, R. C. Haight, C. R. Howell, N. S. P. King, A. Ling, P. W. Lisowski, B. K. Park, *et al.*, "Energy dependence of the Gamow-Teller strength in p-shell nuclei observed in the (n,p) reaction," *Physical Review C*, vol. 45, no. 2, p. R500, 1992.

[128] J. H. Kelley, E. Kwan, J. E. Purcell, C. G. Sheu, and H. R. Weller, "Energy levels of light nuclei $A = 11$," *Nuclear Physics A*, vol. 880, pp. 88–195, 2012.

[129] R. J. Charity, L. G. Sobotka, T. B. Webb, and K. W. Brown, "Two-proton decay from α-cluster states in ^{10}C and ^{11}N," *Physical Review C*, vol. 105, no. 1, p. 014314, 2022.

[130] S. Banerjee, P. D. Beery, N. N. Biswas, N. M. Cason, V. P. Kenney, J. M. LoSecco, A. P. McManus, J. Piekarz, and S. R. Stampke, "Design and performance of a time-of-flight system for particle identification at the Fermilab collider," *Nuclear Instruments and Methods in Physics Research Section A: Accelerators, Spectrometers, Detectors and Associated Equipment*, no. 1, pp. 121–133, 1988.

[131] J. J. Kolata, H. Amro, M. Cloughesy, P. A. DeYoung, J. Rieth, J. P. Bychowski, and G. Peaslee, "A large segmented neutron detector for reaction studies with radioactive beams near the Coulomb barrier," *Nuclear Instruments and Methods in Physics Research Section A: Accelerators, Spectrometers, Detectors and Associated Equipment*, vol. 557, no. 2, pp. 594–598, 2006.

[132] Semiconductor Components Industries, LLC, "How to Evaluate and Compare Silicon Photomultiplier Sensors." Publication Order Number: TND6262/D, September 2018.